Cape Peninsula
University of Technology

# MODELING AND CONTROL OF A DUAL-MODE GRID-INTEGRATED RENEWABLE ENERGY SYSTEM

**by**

**HALTOR MATAIFA**

**Thesis submitted in fulfilment of the requirements for the degree**

**Master of Technology:** **Electrical Engineering**

**in the Faculty of Engineering**

**at the Cape Peninsula University of Technology**

**Supervisor:** Prof. R. Tzoneva
**Co-supervisor:** Mr. Carl Kriger

**Bellville**
December 2015

## DECLARATION

I, Haltor Mataifa, declare that the contents of this dissertation/thesis represent my own unaided work, and that the dissertation/thesis has not previously been submitted for academic examination towards any qualification. Furthermore, it represents my own opinions and not necessarily those of the Cape Peninsula University of Technology.

**Signed** **Date**

## ABSTRACT

From the electric power generation perspective, the last three decades have been characterized by sustained growth in the amount of Distributed Power Generation (DPG) systems integrated into the electric grid. This trend is anticipated to continue, especially in light of the widespread acceptance of the many benefits envisaged in the increase of renewable-based power generation.

The potential for grid-integrated DPG systems to significantly contribute to electric power supply reliability has consistently attracted extensive research in recent times, although concerns continue to be raised over their adverse impact on the normal grid operation at high penetration levels. These concerns largely stem from the limited controllability of most DPG systems, which tend to exhibit large output impedance variation, and non-deterministic power output characteristics. There has therefore also been a growing need to develop effective control strategies that can enhance the overall impact of the DPG systems on the grid operation, thus improving their synergistic properties, and probably also enabling an even higher penetration level into the utility grid.

In line with this identified need, this thesis discusses the modeling and controller design for an inverter-based DPG system with the capability to effectively operate both in grid-connected and autonomous (*i.e.* independent of the utility grid) operational modes. The dual-mode operation of the DPG is made possible by incorporating into the inverter interface control scheme the means to ensure seamless transition of the DPG between the grid-connected and autonomous modes of operation. The intention is to have a grid-integrated inverter-based DPG system whose operation approximates that of an online Uninterruptible Power Supply (UPS) system, in that it is able to sustain power supply to the local load in the absence of the grid supply, which would be desirable for critical loads, for which the level of power supply reliability guaranteed by the grid often falls short of the requirements. The work developed in this thesis considers three of the aspects associated with grid-integrated DPG systems that are equipped with autonomous-mode operation capability.

Firstly, the dynamic modeling and Maximum Power Point Tracking (MPPT) control of Photovoltaic (PV) and Wind Energy Conversion (WEC) systems is addressed. An adequate understanding of the dynamic characteristics and control strategies of these primary energy sources is essential to the study of grid-integrated DPG systems.

The next aspect considered is the design of the control strategies for the grid-mode as well as autonomous-mode operation of the DPG-inverter, which are addressed separately, along with all the control-related aspects associated with each respective operational mode.

Lastly, once the grid-mode and autonomous-mode controllers have been designed, the aspect of ensuring seamless transition between the grid-connected and autonomous operational

modes is dealt with. Attention is particularly given to the factors that may affect the dynamics associated with the mode transition from the grid-mode to the autonomous mode, and methods are proposed to realize the desired seamless transition strategy.

The results of the extensive computer simulations conducted to evaluate the performance of the developed models and algorithms demonstrate that the designed control strategy enables the inverter-based DPG to effectively inject high-quality current into the grid when operating in the grid-mode, to sustain power supply to a local load in the event of the loss of the grid (*i.e.* autonomous operation), and to seamlessly switch between the two modes of operation as necessitated by the system conditions.

As the penetration level of DPG systems into the electric power system steadily rises, their importance to assuring a reliable electric power supply system is likewise going to increase. The study of effective control strategies for DPG systems to enhance their synergistic properties (in conjunction with the grid), as discussed in this thesis, is in this respect very relevant, and certainly merits the research efforts it continues to attract.

Keywords: *Distributed Generation; renewable energy; inverter control; dual-mode operation; seamless transition; current-mode control; voltage-mode control*.

## ACKNOWLEDGEMENTS

**I wish to thank:**

- The Executive Management of the Centre for Substation Automation and Energy Management Systems (CSAEMS), for the immense privilege accorded to me to be a member of the CSAEMS, and to conduct my research under their capable stewardship during the past four years. It has been a tremendously enriching experience, with far-reaching benefits.
- My principal advisor, Prof. Raynitchka Tzoneva, for her immeasurable contribution to the successful completion of this research project. The depth of my indebtedness toward her cannot possibly be conveyed by any set of words.
- Mr. Shahien Behardien, Mr. Carl Kriger, Dr. Senthil Krishnamurthy (members of the CSAEMS) and Dr. Atanda Raji, all who have (in some way) made significant contributions to the work done in connection with this thesis, and whose mentorship I have developed great appreciation for.
- Dr. Alexander Apostolov (PAC World), Dr. Bruce Rigby (etalumi**S**e), and Mr. Patrick Cost (ABB Europe), all external professionals whose contributions to the CSAEMS's research activities over the years have enriched the scope and output of this research project.
- All the members of the CSAEMS for their good workmanship, and their inspirational attitude toward the research activities of the centre.
- All others not mentioned by name who have in some way rendered support to the work done in connection with this thesis.

***Non scholae, sed vitae discimus***
**[Seneca, ca. 62 A.D.]**

The financial assistance of the National Research Foundation towards this research is acknowledged. Opinions expressed in this thesis and the conclusions arrived at, are those of the author, and are not necessarily to be attributed to the National Research Foundation.

## DEDICATION

To all my dear family members, whose unconditional love, extraordinary patience and unwavering support have made the most challenging times during my study period bearable; and to Jehovah God Almighty, the source of my life, of all my strength and of my capabilities.

## TABLE OF CONTENTS

## LIST OF FIGURES

## LIST OF TABLES

## GLOSSARY OF TERMS

| Acronym | Definition/Explanation |
|---|---|
| BESS | Battery Energy Storage System |
| CAES | Compressed-Air Energy Storage |
| CAN | Control Area Network |
| CB-SPWM | Carrier-Based Sinusoidal Pulse Width Modulation |
| CCD | Coordinated Controller Design |
| CHP | Combined Heat and Power generation |
| CIGRÉ | Conseil International des Grands Réseaux Électriques (International Council on Large Electric Systems) |
| CSI | Current-Source Inverter |
| DER | Distributed Energy Resource |
| DG | Distributed Generation |
| DFIG | Doubly-Fed Induction Generator |
| DLC | Double-Layer Capacitor (supercapacitor) |
| DPG | Distributed Power Generation |
| DSP | Digital Signal Processor |
| dSPACE | Digital Signal Processing And Control Engineering |
| EES | Electrical Energy Storage |
| EPRI | Electrical Power Research Institute |
| FAA | Federal Aviation Administration |
| FFT | Fast Fourier Transform |
| FLC | Fuzzy Logic Control |
| GA | Gradient Approximation (algorithm) |
| HAWT | Horizontal-Axis Wind Turbine |
| HDPG | Hybrid Distributed Power Generation |
| LCL (filter) | Inductor-Capacitor-Inductor passive filter |
| LCOE | Levelized Cost Of Energy |
| LQG | Linear Quadratic Gaussian (regulator) |
| LQR | Linear Quadratic Regulator |
| MC | Micro-source Controller |
| MCFC | Molten-Carbonate Fuel Cell |
| MPC | Model Predictive Controller |
| MPP(T) | Maximum Power Point (Tracking) |
| NaNiCl | Sodium Nickel Chloride (battery) |
| NaS | Sodium Sulphur (battery) |
| NDZ | Non-Detection Zone |
| NOCT | Nominal Operating Cell Temperature |
| PAFC | Phosphoric-Acid Fuel Cell |
| PCC | Point of Common Coupling (of DG with the grid) |
| PEMFC | Proton-Exchange-Membrane Fuel Cell |
| P(I)(D) | Proportional-(Integral)-(Derivative) regulator |
| PLECS | Piecewise Linear Electrical Circuit Simulation |
| PLL | Phase-Lock Loop circuit |
| PMSG | Permanent Magnet Synchronous Generator |
| PR | Proportional-Resonant (regulator) |
| PSCAD/EMTDC | Power Systems Computer Aided Design/Electromagnetic Transients with DC |
| PSF | Power Signal Feedback |
| PWM | Pulse Width Modulation |
| PV | Photovoltaic |
| P&O | Perturb & Observe (MPPT algorithm) |

| | |
|---|---|
| RCC | Ripple Correlation Control (MPPT algorithm) |
| RSCAD | Real-time Simulator Computer Aided Design |
| RTDS | Real-Time Digital Simulator |
| SCIG | Squirrel-Cage Induction Generation |
| SEPIC | Single-Ended Primary Inductor Converter |
| SERI | Solar Energy Research Institute |
| SMES | Super-Conducting Magnetic Energy Storage |
| SNG | Synthetic Natural Gas |
| SOCI | Second-Order Generalized Integrator |
| SOFC | Sulphur-Oxide Fuel Cell |
| SVPWM | Space Vector Pulse Width Modulation |
| SRF-PLL | Synchronous Reference Frame PLL circuit |
| THD | Total Harmonic Distortion |
| TSR | Tip-Speed Ratio |
| UPS | Uninterruptible Power Supply |
| VAWT | Vertical-Axis Wind Turbine |
| VCO | Voltage-Controlled Oscillator |
| VOC | Voltage-Oriented Control |
| VSI | Voltage-Source Inverter |
| WEC(S) | Wind Energy Conversion (System) |
| WTS | Wind Turbine System |

## LIST OF MATHEMATICAL SYMBOLS

| Symbol | Definition/Explanation |
|---|---|
| $\alpha_{sc}$ | PV cell short-circuit current temperature coefficient |
| $\beta$ | Wind turbine rotor blade pitch angle |
| $\beta_{oc}$ | PV cell open-circuit voltage temperature coefficient |
| $C_p$ | Wind turbine power coefficient |
| $C_x$ | Circuit capacitance ($x$-subscript indicates that the definition is generic) |
| $D_m$ | Wind turbine drive-train mutual damping coefficient |
| $\delta_{PLL}$ | PLL circuit tracked phase deviation |
| $\lambda$ | Wind turbine tip-speed ratio |
| $\lambda_{PLL}$ | Lagrangian multiplier for the PLL circuit loop filter optimization |
| $\xi$ or $\varsigma$ | Closed-loop system damping coefficient |
| $e_x$ | Tracking error signal ($x$-subscript indicates that the definition is generic) |
| $f_o$ | Nominal line frequency |
| $f_{res}$ | LCL filter resonant frequency |
| $f_s$ | Sampling frequency (for system discretization) |
| $f_{sw}$ | PWM switching frequency |
| $H_g$ | Wind turbine generator inertia constant |
| $H_T$ | Wind turbine rotor inertia constant |
| $I_{mpp}$ | PV module current at MPP |
| $I_{ph}$ | PV photo-generated current |
| $I_{pv}$ | PV module output current |
| $K_i$ | Integral gain value |
| $K_p$ | Proportional gain value |
| $K_s$ | Wind turbine shaft stiffness constant |
| $L_x$ | Circuit inductance ($x$-subscript indicates that the definition is generic) |
| $m_a$ | Inverter amplitude modulation ratio |
| $\overline{m}_{abc}$ | Inverter averaged switching function |
| $n_{id}$ | Diode ideality factor |
| $p$ | Number of magnetic poles of the electrical machine |
| $P_{mpp}$ | PV module power generated at the MPP |
| $P_{pv}$ | Generated power of the PV module |
| $P_T$ | Power extracted by the wind turbine from the wind power |
| $P_w$ | Power available in the wind stream |
| $P_x$ | Active power ($x$-subscript indicates that the definition is generic) |
| $Q_x$ | Reactive power ($x$-subscript indicates that the designation is generic) |
| $R_x$ | Circuit resistance ($x$-subscript indicates that the definition is generic) |

| | |
|---|---|
| $S(f)$ | Wind turbulence spectral density function |
| $T_e$ | Current controller computational time delay |
| $T_g$ | Wind turbine generator torque |
| $T_s$ | Sampling period (for system discretization) |
| $T_T$ | Wind turbine aerodynamic torque |
| $V_{DC}$ | DC-link (inverter input) voltage |
| $V_{LLrms}$ | Line to line rms voltage of the electric grid |
| $V_{mpp}$ | PV module terminal voltage at MPP |
| $V_{pv}$ | PV module terminal voltage |
| $V_T$ | PV cell thermal voltage |
| $v_w$ | Wind velocity |
| $\rho$ | Air density |
| $\theta$ | Grid voltage phase angle |
| $\theta_g$ | Wind turbine generator rotor angular position |
| $\theta_m$ | Lead compensator maximum phase contribution |
| $\theta_T$ | Wind turbine rotor angular position |
| $\tau_x$ | Time constant (of a component or a system) |
| $\psi$ | Permanent-magnet-induced stator winding flux of the PMSG |
| $\omega_c$ | PR compensator relative bandwidth |
| $\omega_g$ | Wind turbine generator rotor angular velocity |
| $\omega_m$ | Lead compensator geometric mean frequency |
| $\omega_{nPLL}$ | PLL circuit closed-loop bandwidth |
| $\omega_o$ | Nominal angular line frequency |
| $\omega_{res}$ | LCL filter angular resonant frequency |
| $\omega_T$ | Wind turbine rotor angular velocity |
| $\omega_{sw}$ | PWM angular switching frequency |
| $x_{abc}$ | Instantaneous value of a three-phase quantity (voltage, current, power, or impedance) |
| $X_{abc}$ | Amplitude of a three-phase quantity (voltage, current, power, or impedance) |
| $x_d$ , $x_q$ | d-, q-axis components of a parameter (voltage, current, power, or impedance) expressed in the rotating reference frame |
| $X_{rms}$ | RMS value of an AC quantity (voltage, current or power) |

# CHAPTER 1

# THESIS INTRODUCTION AND RESEARCH OBJECTIVES

## 1.1. Introduction

The scope of usage and need for reliable electric power supply have both greatly increased since it was first used to power such loads as lighting and telecommunication towards the end of the 19th century (Wheeler *et al.*, 2015). The importance of reliable electric power supply became even more evident in the early 1970s, as volatile fuel prices steadily threatened the global energy security as well as power supply reliability (Hirsh *et al.*, 2005). Since then, much effort has been made to promote Distributed Power Generation (DPG), seen almost universally as a vital means to partially allaying energy security concerns, enhancing the reliability of electric power supply, and diminishing the adverse ecological impacts of electric power generation and consumption. As a result of this development, the power generation sector has in the last three decades been characterized by sustained growth in the amount of DPG systems integrated into the electric power grid, a trend that is anticipated to continue into the foreseeable future.

The advocacy of a greater contribution from distributed (especially renewable) power generation to all new generation capacity is nearly unanimous, virtually everywhere. As mentioned above, the DPG industry as it stands today sprung almost entirely out of energy security concerns, with the sober realization that the accessibility of fossil fuels (as the most important sources of energy) was limited not only by their uneven global distribution, but also by their finite nature (Wang, 2005). Such limitations, on the contrary, could hardly be attributed to such renewable energy sources as Photovoltaic (PV) and Wind Energy Conversion (WEC) systems.

More than just partly address energy security concerns, increased renewable-based DPG has also been perceived as providing an opportunity to reduce green-house gas emissions stemming from electric power generation, thus improving the environmental footprint of electric power generation and consumption. Greater flexibility, relative to conventional power generation, is one other positive aspect of DPG that is often highlighted. In this respect, DPG systems typically present a more feasible means of providing remote power supply (*i.e.* to locations where economical or other factors may make providing grid power prohibitive); they may provide additional new generation at significantly lower capital cost; and they may also allow achieving higher power supply efficiencies by virtue of the possibility to install them closer to the end-users (thus cutting out transmission losses). The list of the benefits expounded for increased DPG can indeed be made as long as one intends. And there is quite a large body of work discussing the various aspects related to the present and possible future

significance of distributed generation (see for example Sun & Zhang, 2012; Martin, 2009; van Werven *et al.*, 2005; Pepermans *et al.*, 2003; & Dondi *et al.*, 2002).

DPG is also non-conventional, however, differing from centralized generation in many respects. For instance, the weather dependence of some renewable power generation systems (such as PV and WEC systems) gives them an intermittent power generation characteristic, which necessitates the use of some form of interface for the conditioning of the generated power, so that it is compatible with the grid (or isolated load) requirements in terms of voltage magnitude and frequency. It also exhibits faster dynamics at the interface to the grid, with low inertia (if inverter-based), which is in direct contrast with the characteristics typical of the centralized, synchronous generator-based power generation. It is not surprising, therefore, that a rising amount of grid-integrated distributed generation is associated with concerns over the possible adverse implications on the normal operation of the grid (Dulău *et al.*, 2014). Most of these concerns largely have to do with the limited controllability of most DPG systems, and the quality of power injected into the grid via the interface. Consequently, the growth of DPG has elicited much interest in the development of effective control strategies that can enhance the overall impact of the DPG systems on the normal operation of the grid, thus improving their synergistic properties, and enabling greater contribution from DPG systems to the provision of secure and reliable electric power supply (Liserre *et al.*, 2010).

The work discussed in this thesis is aligned with the objective of developing these effective control strategies for the DPG system interface. In the following sections of this chapter, the problem being addressed in this thesis is identified, along with the specific intended objectives of the research, the methodology used, the scope of the research work, and the envisaged research outputs, among other factors related to this research, to contextualize the work presented in the rest of the thesis.

## 1.2. Problem identification

Integrating DPG systems into the electric power grid is seen as a way to enhance their potential to contribute more to electric power supply reliability, as mentioned in the previous section. Some DPG systems (such as Combined Heat and Power (CHP), Fuel-Cell & small Hydro Power (HP) systems) offer the generation flexibility that may be exploited in such ancillary grid services as load leveling, peak shaving, frequency control and reactive power support (CIGRE, 2000). At the same time, though, the grid-integration of distributed generation in fact constitutes the introduction of non-conventionally generated power into the electric power grid.

Most DPG systems are interfaced to the grid by means of power electronics (inverters), which are generally needed to condition the generated power, to be of the appropriate voltage magnitude and frequency, and thus make it compatible with the corresponding grid quantities.

This is especially the case for Photovoltaic (PV) and Fuel-Cell energy sources that generate Direct-Current (DC) power, variable-frequency Wind Energy Conversion (WEC) systems, and Microturbines, both of which generate alternating (AC) power at frequencies incompatible with the grid frequency.

There are a number of issues associated with the inverter-interfaced grid-integrated DPG systems. The impact on the grid power quality can be highlighted as an example of those issues. Power electronic interfaces are often cited as a potential source of significant harmonic currents, which certainly have a degrading effect on the grid power quality (Pepermans *et al.*, 2003). Inverter-interfaced DPG systems may also interfere with the normal operation of the grid protection functions, by virtue of their adding significant (active and/or reactive) power to the network, without contributing much to the fault current (Keller & Kroposki, 2010). Then there is also the safety-related concern of the grid-integrated DPG system continuing to energize a part of the grid in the absence of the grid supply, which ideally has to be avoided (Martin, 2009). These are just a few of the reasons why grid codes stipulate stringent requirements for grid-integrated DPG systems, in the interest of preserving the integrity of the electric grid supply system.

From the discussion above, it can be succinctly stated that the problem faced here, with respect to realizing reliable electric power supply, is that there is a desire to increase the participation of Distributed Power Generation in the fulfillment of the functions of the electric grid, but this is to some extent inhibited by the grid-integration issues that mainly result from their non-conventional nature (Awad *et al.*, 2008). Research into the development of means to circumvent these grid-integration issues thus merits consideration, in order to enhance the supportive role of the DPG in realizing a reliable electric grid power supply (Liserre *et al.*, 2010; Carnieletto *et al.*, 2009).

## 1.3. Problem statement

The main problem addressed in this thesis is how to realize the grid-integration of inverter-interfaced DPG systems in a way that enhances their overall impact on the desired operation of the grid.

Current standards for the grid integration of DPG stipulate requirements that restrict the operation of the DPG in the absence of the grid supply, mainly due to safety and power quality concerns (IEEE 1547-2003). It is partly for this reason that most control schemes suggested today for interfacing DPG systems only focus on either their grid-mode or stand-alone mode operation. This, however, severely limits the ability of the DPG systems to contribute to power supply reliability. With the ever-increasing contribution of distributed generation to the overall generation capacity, simply operating the distributed generation when the grid is available amounts to under-exploiting these sources of power supply.

It would be desirable to have DPG systems that are able to operate both in the grid-connected and autonomous (*i.e.* in the absence of the grid supply) modes, especially in cases where there are critical loads, for which the level of power supply reliability guaranteed by the grid does not suffice (Carnieletto *et al.*, 2009). The problem thus encompasses the investigation of the means to achieve this dual-mode operation of the DPG system.

## 1.4. Research aim and objectives

This thesis is mainly aimed at developing an effective control strategy for an inverter interface for a renewable-based Distributed Power Generation system that is intended to operate in two modes: grid-connected and autonomous. The control strategy should ensure that safety and power quality requirements are satisfied in both operational modes by:

- the effective control of the current injected into the grid when operating in grid mode;
- the effective regulation of the load voltage magnitude and frequency, while meeting the load current demand, when operating autonomously;
- ensuring the quick detection of the occurrence of grid anomalies that may necessitate the disconnection of the DPG system from the grid, as stipulated by the grid-code requirements (*i.e.* islanding detection); and
- ensuring the seamless transition of the DPG system's operational mode, between the grid-connected and autonomous modes.

A 15 kVA grid-interactive three-phase inverter, interfacing the DPG system to a $400 V_{rms}$ distribution network, is considered in this work. The work focuses on the theoretical analysis and design of the DPG system, from the primary energy sources and their individual controllers, to the control scheme for the main grid interface. The research aim, as outlined above, is achieved by addressing the following objectives:

1. review of the main Distributed Energy Resource (DER) technologies that form the backbone of the Distributed Power Generation systems;
2. review of previous work related to the control of the DPG-inverter, and the commonly used inverter current controllers;
3. modeling of the Photovoltaic (PV) and Wind Energy Conversion (WEC) systems, as the primary energy sources of the DPG system;
4. design of controllers for the Maximum Power Point Tracking (MPPT) control of the PV and WEC sources;
5. development of the inverter plant model for controller design, as well as the parameter design and dynamic performance analysis of the interface filter;
6. design of the controller for the grid-mode operation of the inverter-interfaced DPG system, including a method for the synchronization of the inverter output voltage with the grid voltage;

7. design of the controller for the autonomous-mode operation of the inverter-interfaced DPG system, as well as the islanding detection logic, to ensure the fast detection of the loss of the grid supply;
8. design of an algorithm to ensure the smooth operational mode transition of the inverter-interfaced DPG system, both from grid-connected to autonomous operational mode and vice versa; and
9. performance analysis of the designed control strategy by means of some representative simulation case studies, to evaluate the performance of the designed control strategy against the requirements specified in the research aim.

## 1.5. Hypothesis

This research work is conducted on the presumption that improvements can be made to the commonly used control strategies for inverter-interfaced grid-integrated distributed generation systems, which can significantly enhance their role in ensuring higher power supply reliability than that guaranteed by the grid supply. By developing control strategies that consider the operation of the DPG both when connected to the grid and in the absence of the grid, they can be made to behave more like online Uninterruptible Power Supply (UPS) systems. Conventional online UPS systems tend to be costly to implement, but that cost is warranted by the need for uninterrupted power supply to certain critical loads. Dual-mode DPG systems, operating as envisaged in the framework of this research, can fulfill the functions of the online UPS systems, except at possibly much lower costs than the premium costs that have to be incurred in running the conventional UPS systems.

## 1.6. Delimitation of the research

The topic of developing control methods for the conditioning of the output power of DPG systems is undoubtedly a broad one, and it is thus necessary to define the scope within which this research work is carried out. In the two sub-sections that follow, the tasks that lie within the scope of this work are outlined first, followed by those that are beyond the scope of this research (and may be considered in future as extensions to the work presented in this thesis).

### 1.6.1. Within the scope of the thesis

1. the theory of the principle aspects of the considered primary energy sources (*i.e.* PV & WEC systems) is discussed, their models are developed for computer simulation, and their MPPT control is addressed;
2. linear controllers are considered for the control strategy development of the inverter interface for the modeled DPG system;
3. a small-scale inverter interface (*i.e.* 15 kVA), integrated into a low-voltage distribution network, is considered in this thesis;

4. the performance of the developed DPG system is analyzed mainly for steady-state, idealized grid operating conditions; and
5. the focus of the thesis is on the theoretical analysis, design, and computer simulation of the mathematical models and the associated controllers for the DPG system.

### 1.6.2. Beyond the scope of the thesis

1. The detailed discussion and modeling of primary distributed energy sources is confined to the PV and WEC systems; there are many candidate distributed resources, but their consideration is limited to a brief discussion of their main principles of operation and the technologies associated with them;
2. the incorporation of energy storage as part of power management in the autonomous-mode operation of the DPG system is not considered in this thesis;
3. Non-linear controllers (and other advanced control techniques, such as adaptive and optimal control) are beyond the scope of the work covered in this thesis;
4. the detailed analysis of the response of the DPG system to grid abnormal conditions (such as various short-circuit fault conditions), and other features of the DPG system such as voltage ride-through, are beyond the scope of the work covered in this thesis; and
5. the experimental (*i.e.* practical) implementation of the designed DPG system and associated controllers is also beyond the scope of the work covered in this thesis, and is considered for follow-up work.

## 1.7. Motivation for the research work

Electric power supply *reliability* remains one of the most desirable characteristics of the electric power system. This, together with the desire to reduce the dependence on the finite and geographically unevenly distributed fossil fuels in the generation of electric power, has been the main driving force behind the steady increase in grid-integrated Distributed Power Generation, as mentioned in Section 1.1. However, it can be said that the full potential of these generation sources to contribute to power supply reliability is to a significant extent still underexploited, mainly on account of the quite restrictive grid code requirements, which tend to limit the flexibility of operation of the grid-integrated DPG systems, in an effort to preserve the integrity of the electric grid, and thus secure its reliable operation.

A review of previous related work has revealed that in most cases DPG systems are considered either in terms of their grid-connected or stand-alone operation, and rarely the flexible operation in both modes. Making a fuller exploitation of the potential of the grid-integrated DPG, however, requires more than just ensuring their effective operation when connected to the grid. If they are so designed as to effectively operate even in the absence of the grid supply, they may play a greater role in providing higher-reliability power supply than that obtainable from the grid supply, which is especially desirable for sensitive loads, for

which even momentary power interruptions are intolerable (Chen, 2011; Carnieletto *et al.*, 2009).

The investigative study carried out in the framework of this research was motivated by the strive towards such control strategies as can enable the versatile operation of the grid-integrated DPG systems, while satisfying the safety and power quality requirements, irrespective of the mode of operation. Such DPG control and operation is perceived as the key to enhancing its role in participating in the provision of secure, reliable power supply, with minimal adverse impacts (Reznik, 2013; Chen, 2011; Carnieletto *et al.*, 2009; Awad *et al.*, 2008).

## 1.8. Assumptions made in the research

The work conducted in this thesis is very much of a theoretical nature, and builds on the work of previous researchers. In carrying out the research work, therefore, some of the assumptions made are that:

- where models developed by other researchers (mathematical or otherwise) have been used, they represent the corresponding physical phenomena to an acceptable level of accuracy;
- for the models and algorithms developed in this work, provided that well-established concepts and theories are employed in developing them, they can be validated by appropriate means (computer simulations considered in this case), so as to qualify their usage in further analyses;
- the models and other tools provided in the simulation platform (Matlab/Simulink in this case) enable the representation of the power system phenomena relevant to the studies carried out in this work, as well as the model design and algorithm development, to the appropriate level of accuracy; this then allows both the implementation of the designed models and algorithms, as well as the results obtained from the simulation analyses, to be treated as sufficiently representative of the corresponding physical phenomena; and
- although idealized conditions are assumed for the distributed generation system design and analysis, the developed methods can with appropriate modifications be adapted to more realistic system operating conditions, for instance for the experimental implementation, such that this work is still of practical import.

## 1.9. Research methodology

Research into control methods for Distributed Power Generation system interfaces necessitates the gaining of knowledge from quite a number of discrete disciplines. Adequate familiarity with the principal concepts of *electric power generation*, *power system theory*, *power electronics*, *control theory*, and *system modeling and simulation* is required, and must be appropriately integrated into a research project of this sort. The research thus has to

encompass a study of these various fields to acquire the relevant knowledge, and an analysis of the existing solutions to the studied problem by means of reviewing the relevant previous work, after which the analysis and design tasks intended for the current work can be carried out, and the results evaluated.

The methodology followed in this work can thus be outlined as follows.

### 1.9.1. Model development

Based on the preliminary study of the previous work and the relevant knowledge gained from the study of the related fields as mentioned above, models for the studied system are to be developed and implemented in Matlab/Simulink. The *SimPowerSystems* Toolbox (in Simulink) provides models and tools for representing all the relevant parts of the electric power grid, as well as the tools for the physical modeling of the primary energy sources. Commonly used mathematical models for these energy sources could thus be implemented in the simulation environment, and their validity evaluated against the results obtained by previous researchers.

### 1.9.2. System design and algorithm development

In line with the objectives of the research as outlined in Section 1.4, control algorithms are to be developed, and other system parameters determined for the various parts of the DPG system. This encompasses:

- The design of parameters for the filter interface, whose function is to attenuate low-frequency ripple and high-frequency harmonics (due to switching) from the inverter output voltage and current, and thus plays an important role in ensuring that the inverter output power meets the minimum power quality requirements;
- the analysis of the best way to devise a control strategy that satisfies the design requirements of the seamless dual-mode operation of the DPG system; this has to take into account the distinct control and operational objectives of the two operational modes;
- the design of the controllers, along with the relevant auxiliary functionalities, such as the inverter synchronization circuit and the islanding detection logic; and
- the design of control logic to implement control strategy switching as well as smooth operational mode transition, thus resulting in an integrated control strategy for the versatile operation of the grid-integrated DPG system.

### 1.9.3. System simulation and performance analysis

With the focus on the steady-state operation of the power system, a number of simulation cases are to be conducted, to evaluate the performance of the designed controllers, in terms of the control strategy's ability to enable the effective dual-mode operation of the inverter-interfaced grid-integrated distributed power generation system. The simulation cases have to

be chosen so as to provide for the testing of all the functionalities included in the developed control strategy. A discussion of the simulation results accompanies each simulation case, and a summary of the main results is also included in the concluding chapter of the thesis.

## 1.10. Main research outputs

The main outputs resulting from this research are:

- a detailed discussion of the theory, mathematical modeling, and MPPT control of the Photovoltaic (PV) and Wind Energy Conversion (PV) systems;
- a holistic approach to the design of a control strategy for a dual-mode grid-interactive inverter; this includes the development of an LCL filter-based inverter plant model for controller design, the discussion of the interface filter requirements and control objectives for the dual-mode inverter operation, and the detailed parameter design and dynamic response analysis of the LCL filter for interfacing the inverter to the grid (as well as to the autonomous load);
- an integrated control strategy for the dual-mode inverter operation, comprising two separate controllers for the respective (*i.e.* grid-connected & autonomous) operational modes, a seamless operational mode transition and controller switching algorithm, an inverter synchronization circuit, and an islanding detection logical function;
- several adequately analyzed representative simulation cases that evaluate the performance of the designed control strategy, to determine its suitability for the envisaged function of operating the DPG-inverter in dual mode.

The results of this research as presented in this thesis may serve an especially significant pedagogical function. Efforts have been made to discuss the theoretical concepts and design procedures for the considered systems in a logical and systematic way, such that the work presented in this thesis may be of special interest to researchers in the field of grid-integrated Distributed Power Generation systems. Moreover, references are provided for the large body of the previous work consulted in the course of working on this thesis, which can also be useful to researchers in the field. The practical application of the results of the research is none-the-less significant, and is envisaged for follow-up work.

## 1.11. Thesis outline

The various chapters of the thesis are so arranged as to collectively adequately address the problem that forms the basis for the work discussed in this thesis work, and in the process of doing so, to satisfy the research aim and the associated objectives. Eight chapters make up this thesis, and the main aspects addressed in each of them are as specified below.

Chapter 2 contains a review of the previous work related to the research project presented in this thesis. The study of the previous work focuses mainly on inverter-interfaced grid-

integrated distributed generation systems, with regards to the commonly used control techniques and integration strategies.

Chapter 3 presents a brief overview of the various DER technologies that form the backbone of the DPG systems, in terms of their principal characteristics and technological developments. The integrated operation of DERs as Hybrid Distributed Power Generation (HDPG) systems is also briefly discussed, as an observed future trend in the quest to improve the performance characteristics of DPG systems.

Chapter 4 covers the discussion of the theory of Photovoltaic (PV) and Wind Energy Conversion (WEC) systems, their mathematical models, and the commonly used methods for the MPPT control of these intermittent primary energy sources. The developed mathematical models are implemented in Matlab/Simulink, and their performances are evaluated to ascertain their suitability for the intended functions.

Chapter 5 deals with the development of the inverter plant model for the current controller design task. Models are presented for both the (inverter input) DC-link voltage and the (inverter output) AC-side current dynamics, to facilitate the design of a dual-loop inverter current controller for the grid-mode operation of the inverter. The chapter also addresses the parameter design and dynamic response analysis of the LCL filter for interfacing the inverter to the grid (and to the autonomous load).

In Chapter 6, the current-mode controller for the grid-mode operation of the inverter is designed, along with a Phase-Lock Loop (PLL) circuit for synchronizing the inverter output voltage with the grid voltage. The chapter also contains a number of simulation case studies to analyze how the well the designed controller does in satisfying the design objectives for the grid-mode operation of the inverter.

In Chapter 7, the voltage-mode controller for the autonomous-mode operation of the inverter is designed, together with an active islanding detection logical function, to ensure the quick detection of the grid anomalies for which the inverter-interfaced grid-integrated DPG system is required to disconnect from the grid. The algorithm to ensure the seamless operational mode transition of the dual-mode DPG-inverter is also presented in this chapter. A number of simulation case studies are presented, and the simulation results analyzed in light of the control objectives to be satisfied in the autonomous-mode operation of the DPG system, and also considering the smooth transition between the grid-connected and autonomous operational modes.

Chapter 8 concludes the thesis with a summary of the main results of the research work presented in this report. Suggestions are also made for possible extensions to the work conducted in this thesis.

Following the concluding chapter, the work consulted in this thesis work is referenced, and an appendix of additional relevant material (such as additional theoretical information and some computer codes used in the simulations) is provided.

## 1.12. Conclusion

The work presented in this thesis is a result of the investigative research project done in the framework of the development of effective control strategies for grid-integrated Distributed Power Generation systems. This chapter served to contextualize the research that has been conducted, by stating the problem that the research work seeks to address, the aim of the research, the envisaged research outcomes, and the methodology followed in working towards achieving the research objectives, among a few other factors relevant to this research work. The context for the presentation of the subject matter discussed in this thesis is further set by outlining the work covered in each of the remaining thesis chapters.

The following chapter contains an overview of the literature review conducted as part of this thesis work, which was deemed relevant to this research project. The main focus of the literature review was on the methods for the modeling and controller design for PV and WEC systems, as well as the control of the DPG-inverter, both when injecting power into the grid and when operating independently of the grid.

# CHAPTER 2

# REVIEW OF THE MODELING AND CONTROL OF INVERTER-BASED DISTRIBUTED POWER GENERATION SYSTEMS

## 2.1. Introduction

Electric power generation from distributed energy resources is presently a very active field of research. This can be viewed as a clear reflection of the general view of both the academia and the industry regarding the role of Distributed Power Generation (DPG) in the electric power supply system. It is generally held that DPG has a key role to play in the provision of secure, reliable and efficient electric power supply, both now and into the future. Thus extensive research has been (and continues to be) carried out, the main aim being to enhance the conversion of the energy available in the distributed (especially renewable) energy sources to useful electric power, and to effectively condition the thus generated power, so as to make it compatible with the end-user requirements.

The objective of this chapter is to present and discuss some relevant information gathered from the review of the previous work concerned with the modeling and control of distributed power generation systems, with the consideration being confined to the inverter-based distributed generators. The chapter is organized as follows.

As a way of introducing the topic of Distributed Power Generation, Section 2.2 provides a brief discussion of the shortcomings in the traditional centralized power generation that prompted the earnest consideration of Distributed Power Generation as a significant alternative (or at least supplement) to the centralized generation. The technical issues associated with the increasing amount of the grid-integrated DPG and the needed developments necessitated by this growth of DPG are also briefly discussed.

The main approach taken in reviewing the previous work by other authors that is of relevance to this project has been briefly outlined in Section 2.3.

Section 2.4 is concerned with the literature review on the modeling of Photovoltaic (PV) and Wind Energy Conversion (WEC) systems, as well as the Maximum Power Point Tracking (MPPT) control of these energy sources so as to optimize the energy yield.

The previous work related to the control of the inverter in its role as an interface and power conditioning device for DPG sources is discussed in Section 2.5, where attention is given to the commonly used topologies and control techniques, and the future trend for the DPG inverter control.

Then in Section 2.6, attention is drawn to the previous work regarding the dual-mode control of the grid-interactive inverter (*i.e.* one that is able to operate both in grid-connected mode and autonomous mode). The control requirements for the dual-mode control of the inverter and the

different techniques used to achieve these requirements are among the aspects considered in the literature review.

Table (2.1) provides a condensed view of the previous work that has been reviewed or consulted in working on this thesis. The graphical depiction of the same information is shown in Figure (2.1). Although not all the sources in the graph have been published strictly in the context of DPG systems, the graph may still serve to illustrate a clear trend with regard to the intensity of research activities in the field of distributed power generation.

**Table 2.1: Summary of the referenced work.**

| Source | Year of publication | No. of sources consulted |
|---|---|---|
| Gardner | 1967 | 1 |
| Wasynczuk *et al.* | 1981 | 1 |
| Frohr & Orttenburger; Hersch & Zweibel; Schoeman & van Wyk; SERI; | 1982 | 4 |
| Anderson & Bose Hughes; | 1983 | 2 |
| Lorenz & Lawson; | 1987 | 1 |
| Kawabata *et al.*; | 1990 | 1 |
| Ängquist & Lindberg; Leithead *et al*; | 1991 | 2 |
| Holtz; | 1992 | 1 |
| DeWinkel & Lamopree; Thiringer & Linders; | 1993 | 2 |
| Lorenzo; Novak *et al.* | 1994 | 2 |
| Chen & Chu; Novak *et al*; | 1995 | 2 |
| Midya *et al*; | 1996 | 1 |
| EERE; King *et al*; O'Kane & Fox; Trykozko; Wichert; | 1997 | 5 |
| Kazmierkowski & Malesani; Swiegers & Enslin; | 1998 | 2 |
| Brambilla *et al*; CIRED WG4; Gow & Manning; | 1999 | 2 |
| Chung; CIGRE; Ding & Buckeridge; Friedman; Hansen *et al*; IEEE Std. 929-2000; Jenkins *et al.*; Kim & Hwang; Price; Ropp *et al.*; | 2000 | 10 |
| Ackermann *et al.*; Chambers; Directive 2001/77/EC; Green; Muljadi & Butterfield; Neacsu; UL std 1741; van Rooij; Walker; | 2001 | 9 |
| Ackermann & Knyazkin; Barsali *et al.*; Dondi *et al.*; Green; Hudson *et al.*; IEA; Lasseter; Tirumala *et al.*; Yuan *et al.*; | 2002 | 9 |
| Brand *et al.*; Castañer & Markvart; Dell'Aquila *et al.*; Hohm & Ropp; IEEE *std*. 1547; Loh *et al.*; Milosevic; Nigim & Hegazi; Pepermans *et al.*; Prodanovic & Green; Salami & Davis; Slootweg *et al*; Strauss & Engler; Twining & Holmes; | 2003 | 14 |
| Blaabjerg *et al.*; Hethessy *et al*; Lasseter & Paigi; Marwali & Keyhani; Nise; Ogata; Teodorescu *et al*; Xue *et al.*; Xiao *et al.*; Xiao & Dunford; Xu *et al.*; Ye *et al.*; Zeineldin *et al.*; | 2004 | 13 |
| Ackermann; Azmy & Erlich; De Mesmaeker *et al.*; Femia *et al.*; Hirsh *et al.*; Kariniotakis *et al*; Liserre *et al.*; Timbus *et al.*; van Werven & Scheepers; Zeineldin *et al.*; | 2005 | 10 |
| Blaabjerg *et al.*; CanREA; Carrasco *et al.*; Esram *et al*; European Technology Platform; Evyu; Leithead & Dominguez; Li *et al*; Lopes *et al.*; Lupu *et al*; Kroposki *et al.*; Purchala *et al.*; Patel; RTDS Technologies; Teodorescu *et al.*; van Gerwen; von Meier; WADE; Wang; | 2006 | 19 |
| Ahmed *et al.*; Araújo *et al.*; Dingguo & Zhixin; Esram & Chapman; Fox *et al.*; Mackiewicz; Mäki *et al.*; Martinez; Omari *et al.*; Sera *et al.*; | 2007 | 10 |
| Awad *et al.*; Bajracharya *et al.*; Cleveland; Eskom; Gao & Iravani; House of Commons; Mahat *et al.*; Sharma & Agarwal; IEEE *std*. P1547.2; Kramer *et al.*; Sera *et al.*; | 2008 | 11 |
| Apostolov; Barakati *et al*; Bellini *et al*; Carnieletto; Coelho *et al*; Gellings; Gonzalez *et al*; Heydt *et al.*; Hunt; Huskey *et al.*; IET; Maknouninejad *et al.*; Martin; Martinez & Marrtin-Arnedo; Monreal *et al.*; Sozer & Torrey; Pao & Johnson; Suryanarayanan & Mitra; Timbus *et al.*; Villalva *et al.*; Vlad *et al*; Ying-Yi *et al*; | 2009 | 22 |

| | | |
|---|---|---|
| Ding *et al*; EPRI; Eskom; Firouzi; Flin; Hassan & Radman; Jenkins *et al.*; Kalmikov & Dykes; Khatri; Keller & Kroposki; Kim *et al*; Liserre *et al.*; Pena & Medina; Wang *et al.*; Yadzani & Iravani; | 2010 | 15 |
| Arnold; Burton *et al.*; Chen; Cultura II & Salameh; DeBrito *et al*; Enerweb; Higgins *et al.*; IEC; Lasseter; Kachhiya *et al*; Kesraoui *et al*; Lettl *et al.*; Maknouninejad *et al.*; Mauri *et al.*; Nehrir *et al.*; Salhi & El-Bachtri; Singh & Santoso; Teodorescu *et al.*; Ustun *et al.*; | 2011 | 19 |
| Ali *et al.*; Elmer & Riffat; FAA; Gomathy *et al*; Gupta & Kumar; Liu *et al*; Rocabert *et al.*; Rogner; Schubel & Crossley; Wang *et al.*; Sun & Zhang; | 2012 | 11 |
| Abdeddaim & Betka; Babu & Arulmozhivarman; Di Piazza & Vitale; Hansen *et al*; Massawe; Reznik; Srinivas & Reddy; Teja; Zhou *et al*; | 2013 | 9 |
| Bisoyi *et al*; Dulău *et al.*; Kiran *et al.*; Louzazni & Aroudam; Óskardottir; Ragheb; Santosh *et al*; Srinivas *et al.*; Tian *et al.*; Weiler; | 2014 | 10 |
| Benadli *et al.*; Boukhezzar & Siguerdidjane; Dida & Benattous; Li *et al.*; Liu *et al.* | 2015 | 5 |

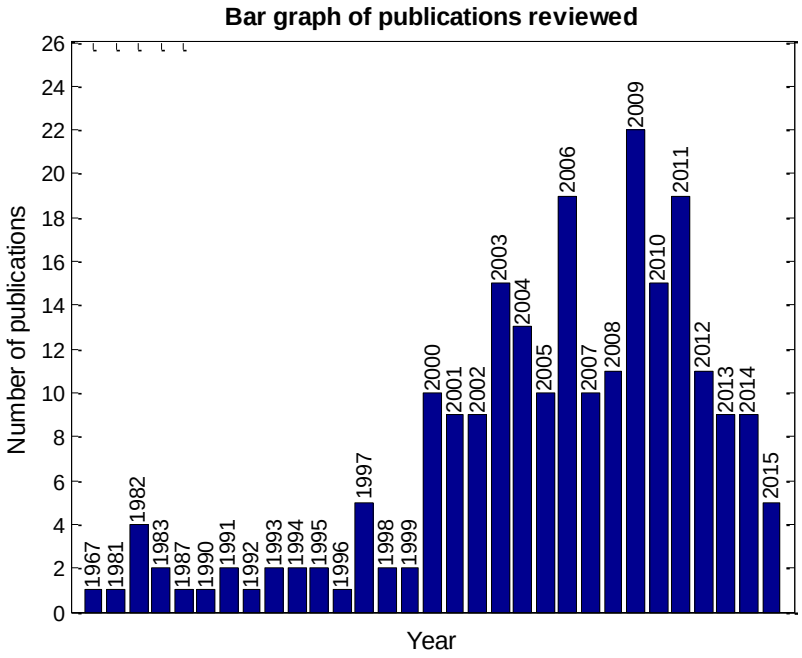


**Figure 2.1:** **Bar graph depiction of the reviewed publications.**

## 2.2. Developments in electric power generation

### 2.2.1. Traditional power generation

Electric power generation started out as decentralized generation systems located within close proximity to the loads, and generating little more than the power demand of the local loads (Weiler, 2014). With time, though, the trend towards bulk, centralized power generation gained preference due to a number of reasons, some of which can be stated as (Martin, 2009; Hirsh *et al.*, 2005; Hughes, 1983):

- the economies of scale gained by the application of innovative steam turbine and Alternating-Current (AC) technologies, leading to significantly reduced costs of large-scale power generation;
- developments that enabled large-scale power generation from fossil fuels such as coal and petroleum;

- the growth in the industrial demand for electric power that promoted bulk generation; and
- the establishment of a largely monopolistic electric power supply industry, with only a few big role players, resulting in the diminished economic viability of small-scale power generation.

This trend held sway for much of the 20th century, and showed little sign of taking recourse. The stagnation in generation technology improvements that became evident in the 1960s, combined with the "energy crisis" of the 1970s, however, brought about a noticeable "paradigm shift" with respect to electric power generation (Hirsh *et al.*, 2005).

### 2.2.2. Emergence of Distributed Generation

Small-scale decentralized power generation (commonly referred to simply as DG) came to be seen in a new light, as presenting a solution to some of the shortcomings that were identified in the large-scale, centralized generation. And over the past few decades, the number of reasons provided in advocacy of DG has been on the increase. Among others can be mentioned (Martin, 2009; Pepermans *et al.*, 2003; IEA, 2002 & Dondi *et al.*, 2002):

- the desire to diversify the primary energy mix as a way of reducing the dependence on fossil fuels for power generation, thus enhancing energy security;
- the desire to reduce the adverse ecological impacts of fossil fuel-based power generation;
- the potential for reducing the transmission losses (which considerably degrade power supply efficiency) by having (distributed) generation that is located in close proximity with the load;
- the greater economical feasibility of DG to provide remote power supply (to areas where extending the grid supply would be uneconomical); and
- the opportunity to use flexible, controllable distributed resources for providing ancillary services to the grid, such as voltage regulation, frequency control, reactive power support, and other services relevant to the effective operation of the grid, at reduced cost.

As a result of the numerous factors in support of DG (only a sample of which is outlined above), the past few decades have been characterized by sustained growth in the contribution of the DG to new generation capacity (Ali *et al.*, 2012).

This growth of DG is generally perceived in a positive light, and is even considered by most to be an essential component of the future energy systems that are well-equipped to deal with the ever-increasing energy demand in an economical and sustainable way (Liserre *et al.*, 2010). At the same time, much concern continues to be expressed regarding the possible adverse impacts

of the increasing percentage of grid-integrated DG on the normal operation of the grid. Most grid-integrated DG tends to be connected to distribution networks (Eurelectric, 2013). These networks have traditionally been designed to deliver power from the transmission side to the consumers, usually with minimal monitoring and active control, an operational philosophy that is based mainly on the presumption of unidirectional (and reasonably predictable) power flow in the network. A significant presence of DG in the distribution network, however, tends to change not only the power flow, but also the voltage control, reactive power, and capacity management characteristics of the network, with considerable implications on the normal operation of the network (Eurelectric, 2013; Jenkins *et al.*, 2010).

Thus, much as distributed generation promises many positive benefits with respect to supporting the electric power grid's principal function of delivering secure, reliable electric power in a sustainable, efficient and economical way, it also necessitates certain technical requirements that are needed to enhance the overall impact of the DG on the effective operation of the electric grid (Awad *et al.*, 2008).

### 2.2.3. Requirements for the effective grid integration of distributed generation

Two of these requirements brought about by the sustained increase in grid-integrated DG can be highlighted here. Firstly, the change of the operational philosophy of the electric power supply (especially the distribution) systems from passive (having only minimal monitoring and control capabilities) to an actively managed power distribution network, with more elaborate monitoring and control functions, is considered to be an essential requirement for accommodating the increasing amount of grid-integrated DG (Eurelectric, 2013). Moreover, the active management of the distribution network could also improve the efficiency, reliability and power quality characteristics of the network, thus better meeting the energy requirements of the end-users.

Secondly, the development of advanced power conversion and control algorithms for DPG systems is another factor considered to be very essential to enhancing the DPG's overall impact on the electric power system. In this regard, the technological advancements being made in power electronics as well as computational technologies are in effect a necessity for practically realizing the desired advancements in the power conversion and control techniques for DPG systems (Reznik, 2013; Liserre *et al.*, 2010).

The work discussed in this thesis is more closely aligned with the second requirement for achieving the desired optimal contribution to reliable and secure electric power supply from distributed energy resources, which is to enhance the power conversion and controllability of the DPG systems. The modeling and controller design for small-scale PV and WEC systems is considered, with the objective of optimizing their energy yield by means of appropriate MPPT control, as well as developing control strategies to enable their versatile operation (*i.e.* both in

the presence and absence of the grid power supply). This could serve to improve their synergistic characteristics, in terms of providing necessary ancillary services to the grid, and help to enhance the reliability of electric power supply (Gao & Iravani, 2008; Zeineldin *et al.*, 2005; Nigim & Hegazi, 2003; Tirumala *et al.*, 2002).

## 2.3. Literature review approach

The literature review is considered under three main sub-headings, which are:

1. primary energy source modeling and control;
2. DPG-inverter interface control; and
3. dual-mode grid-inverter control.

Extensive use of online sources has been made in working on this thesis. So the discussion of the literature review on each of the above-listed sub-topics begins with a list of the key phrases used in the online search for the related previous work. This is followed by an outline of the main areas of interest that form the basis for the comparative analysis and discussion of the reviewed work. The main aspects of each of the reviewed works are presented in tabulated form for each of the sub-topics, followed by a brief discussion of the main points to be drawn from the review and their relevance to the current work.

The first of these sub-topics is considered in the following section.

## 2.4. PV and WEC systems modeling and MPPT control

PV and WEC systems are nonconventional forms of power generation that exhibit characteristics significantly different from those of the traditional, synchronous machine-based power generation systems that form the basis for large-scale electric power generation. It is thus essential to study their power generation characteristics and their likely behavior when integrated into the grid (Kariniotakis *et al.*, 2005). Mathematical models representing the steady-state and dynamic characteristics of these energy conversion systems are useful tools that facilitate this analysis.

A large amount of publications addressing the modeling and control of PV and WEC systems has been encountered in the process of reviewing the previous work on this topic, demonstrating that it is an aspect of DPG systems that has attracted much attention from researchers, especially in recent years. An exhaustive discussion of this broad topic is certainly impracticable in the context of this chapter; therefore, the discussion of the reviewed previous work has been confined to highlighting the important considerations in the modeling and MPPT control of these systems.

### 2.4.1. Review of the existing literature

The key phrases used in the online search for literature under the topic: “PV and WEC systems modeling and MPPT control”, were:

- *renewable energy;*
- *distributed generation modeling;*
- *photovoltaic power generation;*
- *wind energy generation systems;*
- *maximum power point tracking;*
- *PV MPPT; and*
- *wind turbine MPPT control.*

Some information from the reviewed literature is presented in Table (2.2), briefly outlining a comparative analysis of the various works based on the:

- *principal focus of the work;*
- *energy source considered;*
- *methodology used; and*
- *algorithm(s) implemented.*

**Table 2.2:** PV and WEC systems modeling and MPPT control.

| Source | Principal focus of the work | Energy source considered | Methodology used | Algorithm(s) implemented | Comments |
|---|---|---|---|---|---|
| Dida & Benattous, 2015 | Discusses the modeling and controller design for a Doubly-Fed Induction Generator (DFIG)-based Wind Energy Conversion (WEC) system, using a fuzzy logic Maximum Power Point Tracking (MPPT) controller. | Wind | Modeling of the WEC system, the generator, and the power electronic converter interface are discussed, after which the controller design for the WEC system is presented. | Proportional-Integral (PI)-based DC-link voltage regulation; and fuzzy logic-based optimal tip-speed ratio control of the wind turbine for MPPT operation. | The proposed control strategy for the DFIG-based WEC system has high complexity by virtue of its use of a multilevel back-to-back converter in the rotor circuit and an intelligent (fuzzy logic) controller. The motivation is that superior steady-state and dynamic response are achieved, along with better power quality, compared with conventional configurations and control strategies. |
| Benadli *et al.*, 2015 | Discusses the modeling and controller design for a grid-connected PV power generation system that makes use of a two-stage power electronic converter topology. | Photovoltaic. | Simulation models for the PV generator and the Voltage Source Inverter (VSI) are discussed first, followed by the development of the controllers used in the study. | Proportional-Integral (PI) compensator for DC-link voltage regulation; and synchronous-reference frame (dq)-based PI controller as well as sliding-mode controller for the inverter output current regulation. | The work mainly looks at the comparison of the performance of the dq-PI current controller and the sliding-mode current controller; the sliding-mode controller is reported to achieve superior steady-state and dynamic performance, although at the cost of higher complexity, which is generally associated with more difficult and costlier implementation. |
| Santosh *et al.*, 2014 | Presents the design and simulation of a standalone PV system that uses a Single-Ended Primary Inductance Converter (SEPIC) as the PV interface to the load, controlled by an MPPT controller. | Photovoltaic | The modeling of the PV electrical model, the interface converter and the MPPT controller are all presented, as the main components of the considered system. The design and simulation of the fuzzy logic-based PV MPPT controller is also discussed in detail. | Perturb-and-Observe (P&O) and Fuzzy logic-based PV MPPT control algorithms. | The paper discusses the positive characteristics of the SEPIC converter that make it a suitable alternative to the buck-boost converter for PV battery charging systems, and the positive characteristics of the fuzzy logic-based MPPT control are also discussed. |
| Hansen *et al.*, 2013 | Critical performance analysis of the various methods in the PV model parameter estimation | Photovoltaic | Experimentally measured PV current-voltage (IV) data combined with computer simulations, to derive the model parameters that minimize the error between the predicted IV curves and the measured ones | Iterative numerical techniques are used extensively for the model parameter estimation and model solution, although not explicitly specified | The paper reports that a single-diode PV model is able to model IV curves for a wide range of irradiance and temperature conditions, and for a variety of technologies, but the parameter estimation technique plays a significant role, and many techniques suffer from systematic errors that often cause the divergence of the model results. |

| | | | | | |
|---|---|---|---|---|---|
| Abdeddaim & Betka, 2013 | Presents the design of controllers for a grid-connected variable-speed WEC system so as to achieve optimal aerodynamic performance. | Wind | The WEC system that is considered is based on the DFIG, interfaced to the grid via a back-to-back converter. Firstly, the modeling of the various subsystems of the WEC system is discussed; then the controller design is presented, followed by the analysis of the simulation results. | Fuzzy-logic-plus PI-based MPPT control, and sliding mode control-based active and reactive power output regulation of the WEC system | Due to the inherent uncertainties in the WEC system's power yield, the authors suggest the use of nonlinear, robust control to achieve improved control performance. The suggested dual-loop control strategy based on nonlinear controllers is reported to yield good simulation results. |
| Gupta & Kumar, 2012 | Discusses the modeling of a WEC system based on a fixed-pitch wind turbine model, using a Permanent-Magnet Synchronous Generator (PMSG). | Wind | The modeling of the various subsystems of the WEC system is discussed in detail, and the complete system is implemented in Matlab/Simulink, and the performance analyzed from the simulation results. | Dq frame-based PI control of both the generator- and grid-side converters of the WEC system. The control system allows electrical and mechanical dynamics control (generator-side), as well as real- and reactive power output regulation (grid-side). | The work covers all the aspects of the modelling of a WEC system incorporating the aerodynamic, mechanical, electrical, and control subsystems, although the principal focus is on the modelling of the PMSG. The performance of the modelled system is considered mainly in terms of the output power quality of the WEC system. |
| Gomathy *et al.*, 2012 | Discusses the Matlab/Simulink implementation of a PV model, and the Perturb-and-Observe (P&O) and Incremental Conductance (IncCond) techniques for PV MPPT control | Photovoltaic | A (single-diode) PV model is implemented in Matlab/Simulink, and then used for the study of the P&O and IncCond MPPT algorithms. | Fixed-step P&O, fixed-step IncCond and variable-step IncCond algorithms. | Although the P&O and IncCond MPPT algorithms are among the most widely used techniques, they have significant drawbacks. The paper considers particularly the use of a variable step size for the IncCond method as a way of improving its performance. |
| Kesraoui *et al.*, 2011 | Presents a simple MPPT technique for a variable-speed PMSG-based WEC system, and discusses the simulation results of a Matlab/Simulink implementation of the suggested technique. | Wind | An MPPT algorithm for a fixed-pitch variable-speed WEC system based on the suitable regulation of the DC-link voltage is considered. The control attempts to minimize the derivative of the turbine's mechanical power output with respect to the DC-link voltage. The WEC system modeling and controller design are presented, and the simulation results discussed. | A step-and-search (or perturb-and-observe) algorithm for the MPPT control of the WEC system; variable DC-link voltage perturbation is used as a means of tracking the optimal operating point of the WEC system. | Rather than base the MPPT algorithm on the (wind and rotor) speed measurements, the paper suggests the use of a search algorithm that uses knowledge of the wind turbine's electrical characteristics. The avoidance of measurements may imply some positive characteristics of the WEC system's control dynamics. |
| Cultura II & Salameh, 2011 | Presents the detailed design and simulation of a PMSG-based wind turbine system, which may be useful in predicting the performance of an actual wind turbine generator system. | Wind | Models of the wind turbine, the PMSG, and power electronic converter interfaces (as the main system components) are developed and implemented in a simulation | N/A | The simulation results of the implemented WEC system are reported to exhibit good agreement with the field data acquired from an actual installed system, and |

| | | | | | |
|---|---|---|---|---|---|
| | | | environment. Simulation results are discussed in terms of their agreement with the data obtained from an actual installed system. | | demonstrate that the suggested model could be used for performance prediction of similar wind turbine generation systems. |
| Salhi & El-Bachtri, 2011 | Presents a direct duty ratio MPPT controller that uses a PI-fuzzy controller. | Photovoltaic | Modeling of the various components of the PV generation system, including the PV model, the interface converter, and the fuzzy logic control. | PI-Fuzzy controller for the direct duty ratio control of the PV boost converter interface | The fuzzy logic control is presented as an alternative MPPT technique; its main advantage is that it does not need an exact mathematical model of the plant, and has relatively easy implementation. The fuzzy control rules may be specific to a given design, however, such that each design case requires its own set of rules. |
| Kim *et al.*, 2010 | Presents the modeling and analysis of a grid-connected variable-speed WEC system in PSCAD/EMTDC, and proposes an algorithm for the maximum power extraction control of the WEC system. | Wind | The modeling of the various components of the WEC system (wind turbine, synchronous generator, back-to-back converter, and controller) is discussed, and the developed models are validated by means of dynamic computer simulations. | Dq-frame decoupled control of the WEC system output active and reactive power, by means of regulating the d- and q-axis components of the WEC system output current. | The proposed model of the WEC system takes into account the transfer of the generated power to the grid under dynamic conditions, and mainly focuses on the response of the WEC system controllers to the dynamic variations. |
| Ding *et al.*, 2010 | Develops detailed dynamic models for a grid-connected PV generation system, with Battery Energy Storage (BESS), and including the various power electronic converter interfaces and their control | PV and BESS | Models of the PV and Battery Energy Storage systems that are available from literature are implemented in Matlab/Simulink, together with their power electronic converter interfaces and the corresponding controllers. Some simulation cases are then conducted, to ascertain the validity of the implemented models | P&O MPPT control of the PV array output; battery charge/discharge regulator circuit; and decoupled active/reactive power control of the inverter interface for the PV/BESS hybrid system | The work's focus is on the dynamics of the operation of a grid-connected PV/Battery hybrid system. The simulation case studies are chosen so as to test both the steady-state and dynamic operating conditions. |
| Ying-Yi *et al.*, 2009 | Discusses the MPPT control of a direct-drive, PMSG-based variable-speed WECS system using various Gradient Approximation (GA) algorithms | Wind | A review of existing literature on the MPPT control of WEC systems is addressed first; then the proposed GA-based MPPT techniques are discussed in detail. Simulation results of implementing the proposed algorithms are also discussed in terms of the benefits and drawbacks | Three MPPT techniques based on GA are discussed: a full-sensor control method, a rule-based method, and an adaptive-duty-ratio method. The control variable for the MPPT control is chosen to be the duty ratio of the DC-DC (buck-boost) converter. | The MPPT control of (especially low-power) WEC systems should ideally be simple and of low cost, while substantially improving the power yield of the WEC system. The paper suggests that the proposed adaptive-duty-ratio method-based gradient approximation satisfies these conflicting objectives. |
| Barakati *et al.*, 2009 | Discusses the MPPT control of a Squirrel-Cage Induction Generator (SCIG)-based WEC system, having a | Wind | The mathematical models of the main subsystems of the WEC system are briefly described, | Two MPPT techniques are discussed; the mechanical-speed sensor-less Power | The paper draws relevant attention to the implementation aspects of the MPPT algorithms that have been |

| | | | | | |
|---|---|---|---|---|---|
| | Matrix Converter (MC)) front-end, and proposes a sensor-less Power Signal Feedback (PSF) MPPT technique. | | followed by a brief overview of common MPPT techniques for WEC systems, drawing attention to both their desirable characteristics and drawbacks. The proposed MPPT controllers are then discussed, followed by simulations to analyze the effectiveness of the suggested techniques. | Signal Feedback (PSF), and Perturb and Observe (P&O) techniques. | discussed, highlighting that a given control technique's complexity and implementation cost are important considerations, in addition to it's effectiveness in satisfying the control objectives. |
| Vlad *et al.*, 2009 | Discusses the MPPT control of a direct-drive PMSG-based low-power WEC system, and suggests a control strategy to improve the closed-loop dynamics. | Wind | A brief review of some common MPPT techniques for WEC systems (with emphasis on their limitations) is followed by a discussion of the modeling of the considered WEC system and the control strategies studied. A comparative analysis of the control strategies is then made by means of simulations and experimental studies. | Two MPPT control algorithms are considered; one based on the Linear Quadratic Optimal Regulator (LQR), and another on an anticipative control structure, suggested by the authors. | Optimal tip-speed ratio-based MPPT control of the WEC system has the drawback that it requires the use of the measured wind speed, which tends induce significant torque variations in the control system. The authors thus suggest a control strategy that takes into account the undesirable effects of the wind speed disturbance in the control system. |
| Gonzalez *et al*., 2009 | Discusses the dynamic modeling and controller design for a small-scale WEC system, with the emphasis being on the stable operation of the system in two main regions, the linear-power and constant-power control regions | Wind | The modeling of the wind turbine and the PMSG are discussed, and frequency response analysis done on the developed models, before designing controllers to stabilize and enhance the dynamic response of the WEC system. | Perturb & Observe MPPT control of the wind turbine; simplified extended Kalman filter for wind turbine position and speed estimation; and dq-frame PI turbine torque and speed control | The paper focuses on the dynamic behavior of the WEC system, and the variable-structure power management and control strategy suggested is intended to ensure the enhanced dynamic operation of the WEC system in both the linear- and constant-power regions of the wind turbine system's characteristic. |
| Villalva *et al.*, 2009 | Proposes a method for determining the unknown model parameters of a single-diode PV cell model using only the PV cell data provided in manufacturer datasheets, to facilitate PV array modeling in Power Electronic simulations for PV energy conversion | Photovoltaic | Taking into account temperature and irradiance effects, the pn junction diode-based mathematical model of the PV cell is used in conjunction with manufacturer-provided PV module data to determine the unknown model parameters which provide the best fit of the model to the experimentally obtained data | An iterative numerical process is used to determine the PV cell model parameters that minimize the difference between the simulated and experimentally obtained peak power | In addition to the PV array model development, a brief theory of the physics of PV generation is also included in the paper, as well as the influence of atmospheric conditions on the PV energy yield, which may be helpful to those with little knowledge of PV energy conversion |
| Sera *et al.*, 2007 | Presents a single-diode, five-parameter model of the PV cell that is developed exclusively on the basis of manufacturer-provided datasheet parameters, and takes into account the temperature and | Photovoltaic | The five-parameter single-diode model parameters are determined by formulating the PV cell characteristic equation for each of the salient-point (*i.e.* short-circuit, | A numerical iterative method is employed in the solution of the derived equations, to obtain the model parameters; the | The paper reports that a sufficiently accurate model of the PV cell can be developed that is purely based on manufacturer datasheet parameters; the benefit of the approach lies in the |

| | | | | | |
|---|---|---|---|---|---|
| | irradiance dependence of the model parameters | | open-circuit and maximum power point) parameters, and solving them simultaneously | Newton-Raphson method is used to solve the nonlinear PV cell characteristic equation | avoidance of experimental data collection over a lengthy period for the model development |
| Dingguo & Zhixin, 2007 | Discusses the modeling and controller design for a DFIG-based variable-speed WEC system, to enable operation in all regions of the wind turbine's power characteristic curve. | Wind | A three-mass model of the WEC system based on the DFIG is considered. A dual-loop control strategy is then discussed and developed, for the speed-torque control of the WEC system in the optimal-power-coefficient region, and pitch control in the reduced-power-coefficient region. | Speed control based on loop shaping and feed-forward compensation; pitch control using fixed pitch-angle-scheduling based on wind speed measurements. | The controller design approach takes into account both the optimal power extraction (in the below-rated-speed region) and mechanical load curtailing (in the above-rated-speed region), to essentially enhance the dynamic operation of the WEC system across the system's entire operating region. the controllers chosen are of moderate complexity. |
| Lupu *et al.*, 2006 | Proposes a multi-variable power-regulation control strategy for a variable-speed WEC system that ensures proper output power regulation and mechanical load reduction above the rated output of the machine. | Wind | With the focus being on the control of the variable-speed WEC system in the power regulation (above-rated) region, commonly used control techniques are briefly reviewed, with attention drawn to their main drawback. The suggested multi-variable control strategy that addresses the main drawback is then presented, along with simulations to assess its effectiveness. | Nonlinear dynamic state feedback torque control combined with linear blade angle control is developed for the power regulation control of the variable-speed WEC system. | WEC systems exhibit multiple operating regimes, each region of operation having in turn multiple, often conflicting control objectives. The paper's emphasis is on devising a control strategy that satisfies the two main objectives of the WEC system control in the above-rated operating region, which are power limitation below the rated value, and transient load reduction. A multi-variable control strategy is proposed to satisfy these objectives. |
| Li *et al.*, 2006 | Considers the optimal control of a grid-interactive DFIG-based variable-speed WEC system, such that both the power yield is maximized, and the generator stator active power losses are minimized, for improved overall system efficiency. | Wind | The modeling of the DFIG-based WEC system is addressed first, followed by the presentation of the proposed control strategy. Decoupled control of the stator active and reactive power outputs is used as the basis for the MPPT control and active-power-loss-minimization of the WEC system. | An optimal control strategy for the decoupled control of the stator active and reactive power regulation is developed; the active and reactive power regulations are used for the MPPT control and the active power loss minimization respectively. | The authors propose a control strategy that not only seeks to maximize the WEC system's energy yield below rated output, but also to improve the overall system efficiency by taking the machine's active losses into account in the controller design, and basing the design on an accurate electrical model of the DFIG. |
| Leithead & Domininguez, 2006 | Presents a control strategy for a variable-speed pitch-regulated wind turbine that is aimed at decoupling the generator speed and tower load control loops, in an effort to effectively alleviate the wind turbine's transient loads while ensuring | Wind | The factors influencing the control performance and transient load alleviation of large wind turbines in the above-rated operating region are discussed, and the design objectives for wind turbine control systems outlined. Then the proposed strategy | A Coordinated Controller Design (CCD) approach is developed, to simultaneously achieve effective generator speed control and tower fatigue load reduction of the considered large wind turbine in the above-rated operating region. | A good overview of the requirements for wind turbine control to satisfy the operational objectives across the turbine's operating range is provided, and, along with representative dynamic models of the various control loops, forms a good basis for the |

| | | | | | |
|---|---|---|---|---|---|
| | satisfactory power output regulation, in the above-rated region of the turbine's operation. | | for addressing the two main control objectives for the wind turbine's operation in the above-rated region is presented. | | analysis and controller design task. Further, the suggested CCD approach seeks to achieve improved control performance by modifying the conventional controller without substantially increasing the controller's complexity. |
| Esram *et al.*, 2006 | Development and experimental verification of the Ripple Correlation Control (RCC)-based dynamic MPPT technique | Photovoltaic | The mathematical analysis and design of the proposed MPPT technique is firstly dealt with, and the various practical-implementation-related aspects discussed, before presenting the experimental implementation and results analysis. | Various ways of implementing the discussed RCC-based MPPT technique are suggested; the chosen technique for implementation takes into account the computational burden and component costs. | The desirable characteristics of MPPT control are discussed in detail, and the various aspects of the suggested technique are highlighted that make it suitable for satisfying many of these characteristics; particularly, very good dynamic response is mentioned as a major advantage of this technique. |
| Xiao *et al.*, 2004 | Presents a simplified computer simulation model that accurately reproduces the current-voltage characteristics of a PV cell based on several different materials. | Photovoltaic | A manufacturer-datasheet-based approach to determining the parameters of the single-diode model of the pn-junction PV cell is used. | N/A | The work focuses on developing a simplified model that avoids the computational burden associated with solving the nonlinear model of the PV, but which nonetheless adequately depicts the important electrical characteristics of the PV cell |
| Slootweg *et al.*, 2003 | Presents the development and analysis of a generic model for variable-speed wind turbines that can be incorporated into power system dynamics simulation studies, to facilitate the study of the impact on the grid of large-scale grid-integrated wind power generation. | Wind | After presenting the general approach to the modeling of variable-speed wind turbines, the main subsystems that make up a variable-speed wind turbine are discussed in greater detail, and then simulation results of implementing the proposed model in a power system simulation software package are presented and discussed. | N/A | In order for the proposed model to be integrated into a power system simulation software package, and to be generic for the various variable-speed wind turbine types, it is designed to only represent the fundamental voltage and current components, with a minimum number of parameters. The reported simulation results agree well with manufacturer-provided data, nonetheless. |
| Green, 2002 | Discussion of the fundamental physical principles underlying PV energy conversion, and how these act as limiting factors to the practically realizable PV energy conversion efficiency. | Photovoltaic | Discussion of the various stages of PV energy conversion development, which have been a direct result of the gradual clearer understanding that has been gained of the underlying principles of the photovoltaic effect. | N/A | The paper gives a fairly detailed account of the microscopic processes that form the basis for PV energy conversion, and the progress in PV converter device design that has been accomplished as a result of the clearer understanding of these processes. |
| Walker, 2001 | Implements an electrical model of the PV cell in Matlab, and uses it to compare the matching efficiencies of three different | Photovoltaic | The PV cell is modeled as a current source in parallel with a diode; a model of moderate complexity is | N/A | A critical evaluation of the various interfacing options of the PV array to the load is made, with focus on the |

| | | | | | |
|---|---|---|---|---|---|
| | interfacing options for the PV array to the load. | | adopted, which is nonetheless sufficiently accurate for the intended study (of PV interface converter topologies). | | relative performance of the buck and boost converters; the boost converter is said to have slight advantages over the buck converter. |
| Muljadi & Butterfield, 2001 | Discusses the rotor speed control of a variable-speed WEC system by means of pitch and generator load control, so as to maximize the energy capture in the medium-wind-speed region, and to minimize the wind turbine loads in the high-wind-speed operating region of the WEC system. | Wind | The behavior of a pitch-controlled, DFIG-based WEC system is analyzed in terms of energy yield and power limitation, in comparison with the constant-speed wind turbine system; the implementation of the strategy used to control the WEC system in the two main operating regions is then discussed. | Pitch angle adjustment and generator load control are used to maximize energy yield under partial-load conditions, and to limit the aerodynamic torque under full-load conditions of the WEC system. | The practical aspects of the aerodynamic power control of a pitch-controlled, variable-speed WEC system are highlighted, and how they affect the control strategy design and operating threshold setting. In particular, the size of the WEC system and the ratings of the generator and power converter affect the pitch rate and generator load control. |
| Hansen *et al.*, 2000 | Development of simple mathematical models for the main components of a stand-alone PV generation system, simulation analysis, and model validation against experimental data measurements. | Photovoltaic | Use of simple mathematical models available in published literature, along with measured data on a pilot PV installation, to develop a modular-structure model library for stand-alone PV generation characterization. | Readily available mathematical models (from literature) for the various system components. | The work develops a library of simple mathematical models of the principal elements of a stand-alone PV system, providing a critical analysis of the developed models in light of the comparison of simulation results with measurements from the pilot system. |
| Gow & Manning, 1999 | Development of a circuit-based simulation model of a PV array, especially useful in Power Electronics analysis and design for PV energy conversion systems. | Photovoltaic | Formulation of analytical expressions relating the PV cell model parameters to the ambient conditions from experimental data, and numerical solution of the expressions. | The Levenberg-Marquardt curve-fitting technique is used to derive the model parameters, and the Newton-Raphson method is used for the model solution. | The developed model uses the double-diode representation of the pn-junction PV cell operating characteristics, with the level of accuracy that befits component-level modeling. The irradiance and temperature effects on all model parameters are also accounted for. |
| Brambilla *et al.*, 1999 | Presents a PV array dynamic MPPT control technique that has improved immunity to the adverse effects of the array parasitic capacitance | Photovoltaic | The proposed dynamic MPPT method is based on the RCC technique, and presents an alternative computation technique so as to diminish the power-sinking effects of the array parasitic capacitance. | A computational method making use of high- and low-pass filters to extract the current and voltage ripple components for the MPPT implementation is presented, and simulation results from implementing the algorithm are discussed. | The paper's (stated) contribution is the consideration of how the intrinsic capacitance of the PV array affects the performance of the dynamic RCC-based MPPT technique, and suggesting a way to improve the technique's performance. |
| Swiegers & Enslin, 1998 | Proposes a simple, low-cost but efficient integrated MPPT | Photovoltaic | Design and experimental implementation of the suggested integrated | A dual-loop algorithm is used, where the outer loop sets the reference PV output voltage, based on the empirically established ratio of the maximum- | The main objective of the work is to devise an MPPT method that improves the PV energy yield at minimal |

| | | | | | |
|---|---|---|---|---|---|
| | controller for a PV panel, which can additionally perform battery voltage regulation and short-circuit protection. | | MPPT controller, and discussion of the experimental results. | power-point voltage to the open-circuit voltage of the PV panel, while the inner loop tracks the reference value set by the outer loop. | additional cost to the PV generation system. The additional cost of implementing the suggested technique is reported to be about 2.8% of the used PV panel, in the case considered in the paper. |
| King *et al.*, 1997 | Description of effective methods for the determination of the temperature coefficients of PV cells, modules and arrays. | Photovoltaic | Analysis of the test methods used in the temperature coefficient characterization of PV modules and arrays, to establish the factors affecting the accuracy of the determined values. | N/A | The significance of the correct thermal modeling of PV generation systems is explained; further, the factors influencing the accuracy of the determined temperature coefficients are discussed, as well as suggestions for improving the measurement accuracy. |
| Midya *et al.*, 1996 | Proposes a dynamic method for the MPPT control of a PV generator that is based on the natural switching ripple of the PV generator's output voltage and current (*i.e.* the RCC technique). | Photovoltaic | The commonly used MPPT techniques for PV systems are critically analyzed, after which the proposed method is presented, with details of the operating principals and practical realization. | PV MPPT technique that considers the dynamic measures of the PV voltage and current ripples as natural perturbations that can be used for the MPPT, by means of the duty ratio control of the PV interface converter. | The practical limitations of the commonly used perturbation-based MPPT methods are highlighted, and the benefits of the proposed method discussed in detail. The operating limitations of the suggested method are also highlighted. |
| Novak *et al*., 1995 | Presents the physical modeling, system identification and controller design for a variable-speed, fixed-pitch, Horizontal-Axis Wind Turbine (HAWT), with the aim of the controller design being to maximize the power yield while restricting the dynamic mechanical loads of the turbine. | Wind | A number of system identification techniques are used on an existing wind turbine installation, to derive the physical model of the drive-train system, which is then used in the controller design task. The structural design of the turbine is taken into account in the model derivation, as it affects the model dynamics. | A number of linear and nonlinear controllers for the speed and torque control of the wind turbine have been discussed and designed, including nonlinear tracking controllers, the Linear Quadratic Gaussian controller, and Proportional controllers. | An accurate model of the system is essential for the controller design. Obtaining a moderately complex yet sufficiently accurate drive-train model is highlighted as a significant challenge, mainly due to the non-availability of accurate manufacturer data. This often necessitates the use of system identification for the purpose of obtaining accurate estimates of the key model parameters, as is done in the paper. |
| Thiringer & Linders, 1993 | Considers the variable-speed control of a fixed-pitch wind turbine to ensure both optimal energy yield in the below-rated and wind turbine load reduction in the above-rated operating region of the turbine. | Wind | Details and the theory of operation of the wind power generation system considered in the study are provided, after which the design aspects of the rotor speed and electrical power control strategy proposed in the paper are discussed. This is followed by static and | An electrical output power control strategy with a deadbeat characteristic is developed, and uses an estimation (rather than measurement) of the wind speed, on the basis of the generator electrical power | The practical aspects of the variable-speed control of fixed-pitch wind turbines are highlighted well in the paper; further, the analysis of the studied case shows that while taking the limitations of such operation into account, a fixed-pitch wind turbine can be made to effectively operate at |

| | | | | | |
|---|---|---|---|---|---|
| | | | dynamic performance analyses of the system, subject to the devised control strategy. Conclusions are then made of the main outcomes of the study. | output and the turbine rotor speed. | variable speed, and thus achieve both improved energy yield and reduced mechanical loads in comparison with fixed-speed operation. |
| Leithead *et al.*, 1991 | Discusses the role and objectives of control systems in the operation of large constant- and variable-speed wind turbines across the entire operating range (*i.e.* from cut-in to above-rated speed). | Wind | A comprehensive discussion of the factors affecting the dynamic response of a large wind turbine, the significant stresses it is subjected to through the turbulent component of the input wind spectrum, and the role played by the control system in shaping the wind turbine dynamics, is presented. Particularly, the importance of active pitch control for power limitation is well-elaborated on. | N/A | The paper clearly shows how the wind turbine control system seeks to shape the turbine's dynamic and steady-state response, reduce the transient loads, maximize the energy capture, and smoothen the generated power, all while ensuring minimal control action. Comment is also made on how the design philosophy of wind turbines affects their structural dynamic behavior, and the necessity of taking this into account in controller design. |
| Hersch & Zweibel, 1982 | A nontechnical introduction to PV generation systems, covering the physics of PV cell operation as well as the system-level design of PV systems. | Photovoltaic | Theoretical explanation of the fundamental principles of the PV generation and energy conversion system. | N/A | The work is addressed to a wide audience, and covers all the relevant aspects of PV generation in sufficient detail. |

### 2.4.2. Discussion

The literature that has been reviewed regarding the modeling and control of PV and WEC systems reveals that there are various different factors that need to be taken into account in the analysis and design of these systems, and generally authors tend to address some specific topic of their choice. The discussion of the reviewed (tabulated) literature as it applies to PV generation systems' modeling and control is discussed below separately from that of the WEC systems, this approach being motivated by the significant disparity that exists in the characteristics of these two primary energy sources.

#### 2.4.2.1. PV system modeling and control

It can be seen from the reviewed literature that some of the important aspects that constitute the study of PV generation systems are (1) the determination of an adequately accurate mathematical model of the electrical characteristics of the PV generator, (2) control techniques to enhance the PV power yield (Maximum Power Point Tracking, MPPT), as well as (3) the consideration of the power-conditioning converter interface unit.

Looking at the modeling aspect, the most commonly considered mathematical model of a PV generator is the one based on the semiconductor pn-junction diode, in which the PV generator is represented as a solar irradiance-dependent current source in parallel with two diodes (Gow & Manning, 1999) or (rather more commonly) one diode (e.g. Benadli *et al.*, 2015; Ding *et al*, 2010; Walker, 2001). It is also common to incorporate shunt and series parasitic resistances to represent active power losses in the device. The resultant model is a nonlinear relation between the PV current yield and the terminal voltage, and exhibits strong dependence on atmospheric conditions (irradiance, temperature) as well as the characteristics of the pn junction (parasitic capacitance and resistances, ideality factor). Model parameter estimation forms a vital component of the determination of the PV generator's mathematical model, mainly because not all the relevant model information is provided in PV module manufacturer datasheets. The determination of the unknown PV model parameters can be either experimental (requiring tests on an installed PV module over a sufficiently lengthy period of time) or analytical (using numerical simulations coupled with PV module manufacturer-provided data). For its relative convenience and simplicity, most researchers advocate the use of the analytical approach (Villalva *et al.*, 2009; Sera *et al*., 2007; Hansen *et al*, 2000). Hansen *et al* (2013) concluded in their investigation that a single-diode PV model may be adequately accurate for most PV system study purposes, and although most parameter estimation techniques suffer from systematic errors that may significantly affect the model accuracy, consideration of the parameters' thermal dependencies, among other factors, could enhance the model accuracy (see also King *et al.*, 1997).

MPPT control is another vital aspect in the study of PV generation systems, and this has to do with two main reasons. The first is that the PV generator is an inherently low-efficiency energy generator (Green, 2002), such that extracting the maximum possible power from it is essential to improving its economic feasibility. The second is that the PV power yield is a highly nonlinear function of the operating voltage (which in turn changes with variations in atmospheric conditions), and exhibits one optimal point for given atmospheric conditions (Hersch & Zweibel, 1982). Thus many techniques have been studied to realize the MPPT control of the PV generator, and it can be stated that due to the nonlinearity of the PV power yield (essentially precluding the application of linear control theory), the techniques are to a large extent heuristic (Santosh *et al.*, 2014; Salhi & El-Bachtri, 2011) or based on the knowledge of the PV characteristic curve (Gomathy *et al.*, 2012; Ding *et al.*, 2010; Swiegers & Enslin, 1998). The prominent among the many suggested techniques are the Perturb-and-Observe (Ding *et al.*, 2010), Incremental Conductance (Gomathy *et al.*, 2012), Ripple Correlation Control (Esram *et al.*, 2006), and Fuzzy Logic Control-based (Santosh *et al.*, 2014). The conceptual operation of these and other common MPPT techniques is further discussed in the section on PV MPPT control in Chapter 4. The various methods certainly differ as regards accuracy, complexity, dynamic performance, efficiency and other factors. With the desire to keep enhancing the PV energy generator performance, research into improved PV MPPT control is expected to produce further MPPT techniques.

The third aspect, the consideration of the power converter as a power conditioning and interface unit for the PV generator, is directly related to the topic of MPPT, because MPPT control is implemented via the converter interface. In this respect, Walker (2001) compared the performance of the buck and boost converters, to establish the relative merits of the two options. According to the reported results, the boost converter exhibits slightly better performance, although the performance difference between the two also shows some dependence on the irradiance level. Santosh *et al* (2014) considered the use of the Single-Ended Primary Inductor Converter (SEPIC) for use as a battery charge regulator (as opposed to the more commonly used buck-boost converter), the main motivation being the fact that the polarity of the output voltage corresponds to that of the input voltage.

The three aspects considered above certainly do not cover everything about PV energy generators, and were only selected for their direct relevance to the work considered in this thesis.

#### 2.4.2.2. WEC system modeling and control

A WEC system is quite complex, with numerous subsystems, such as the aerodynamic, mechanical, electrical, and control subsystems. Coupled with the potentially turbulent environmental conditions under which it periodically may have to operate (having to

withstand all forms of wind regimes), the dynamic modeling and control of the WEC system commands a high level of investigative research, and the breadth of the available literature on the topic attests to this.

WEC systems are mainly either of the horizontal-axis (Horizontal-Axis Wind Turbine, HAWT) or the vertical-axis (Vertical-Axis Wind Turbine, VAWT) types. The HAWT variant dominates the commercially available systems (Leithead *et al.*, 1991), and forms the basis for the WEC systems considered in this thesis.

Similar to the PV generation system, the WEC system can also be analyzed in terms of dynamic mathematical modeling for energy yield analysis (additionally with mechanical characteristics), maximum power extraction (or optimal) control, as well as power conditioning and interfacing to the electric power grid.

The consideration of the modeling of WEC systems has to take into account the many variations that exist. The various commonly implemented topologies may be distinguished by means of such characteristics as the form of aerodynamic design (fixed-pitch or pitchable), and the concept used for the turbine rotor speed (constant-speed or variable-speed). They can also be differentiated by the form of drive-train (direct-drive or gearbox-incorporated), the type of generator used (synchronous or asynchronous) and the form of interface to the electric grid (directly connected, partial-power electronics or full power electronics) (Carrasco *et al.*, 2006). These various configurations affect the type of analysis and control mechanisms that can be applied to a given variant. Discussion here is thus more or less generic, and is oriented towards the reviewed literature.

As the reviewed literature demonstrates, the modeling and controller design for WEC systems tend to be significantly intertwined. As clarified by a number of researchers (Leithead & Dominguez, 2006; Novak *et al.*, 1995; Leithead *et al.*, 1991), this close connection mainly has to do with the fact that a control system is always designed with respect to a specific plant, and a sufficiently accurate model of the plant is a prerequisite for an effective controller design task. With the great variety of WEC systems that exist, along with their complex, multi-variable nature, system modeling invariably has to be coupled to controller design.

The multi-objective nature of the control of (especially large) WEC systems is exemplified by the work of Leithead *et al* (1991), who showed that the control system is fundamentally intended to shape the wind turbine's dynamic and steady-state response, reduce transient loads, maximize the energy capture, and smoothen the generated power, at the same time ensuring the optimal expenditure of the control energy. The authors considered the modeling and control requirements of both constant- and variable-speed wind-turbines, and their analysis showed that the variable-speed operation leads to relatively improved electrical and mechanical load regulation.

Interest for the variable-speed operation of WEC systems has continued to grow, especially for large wind turbines, such that it has been considered even for fixed-pitch turbines, which generally work on the constant-rotor-speed concept, as considered for instance by Novak *et al* (1995) as well as Thiringer and Linders (1993). Despite the limitations of this control concept, the researchers reported improved overall performance relative to the fixed-speed operation concept.

Often the differentiating factor for the commonly studied WEC systems is the type of generator used, and in this sense, many researchers have looked at the WEC system based on the Doubly-Fed Induction Generator (DFIG)(Dida & Benattous, 2015; Abdeddaim & Betka, 2013; Dingguo & Zhixin, 2007; Li *et al.*, 2006), the Permanent Magnet Synchronous Generator (PMSG)(Gupta & Kumar, 2012; Cultura II & Salameh, 2011; Kim *et al.*, 2010; Ying-Yi *et al.*, 2009), and the Squirrel-Cage Induction Generator (SCIG) (Barakati *et al.*, 2009; Teodorescu *et al.*, 2004).

From this fraction of previous work on WEC systems that has been looked at, it is evident that the pertinent considerations in the modeling and controller design (the topology notwithstanding) are the representation in the plant model of all the characteristics that are relevant to the control objectives of interest, and the judicious choice of the control strategy among the numerous approaches that are available.

#### 2.4.2.3. PV and WEC systems modeling and MPPT control in this thesis

The review of the previous work conducted in this section has direct relevance to this thesis. In Chapter 4, models of both PV and WEC systems are developed to facilitate simulation studies of renewable energy systems, in line with the objectives of this thesis. The relevance of the work reviewed here will take the form of guiding the modeling and controller design process, in terms of the various choices that have to be made.

In the case of the PV generation system, for instance, modeling involves the choice of the mathematical model to use and the method for the unknown parameter estimation, the design of the MPPT controller, and the choice of the converter interface, all of which will be aided by the insight gained from this review.

The study of the WEC system involves the choice of the aerodynamic design, the type of drive-train, the type of electric generator, the operational concept for the turbine rotor speed, the type of interface to the electric grid, and the control approach, among other factors, for the topology to be considered. Here again, the work reviewed in this section will be helpful in the treatment of the WEC system modeling and analysis.

Distributed Power Generation (DPG) systems (such as the renewable sources considered in this thesis) are invariably interfaced to the load by means of Power Electronic converters (such

as the inverter), and most of the power conditioning and control of the DPG is carried out via the control of the inverter. The following section thus looks at the previous work related to the control of inverters as power conditioning interfaces for DPGs.

## 2.5. Control of the Distributed Power Generation inverter interface

### 2.5.1. Review of the existing literature

The key phrases used in the online search for literature under the topic: "Control of the Distributed Power Generation inverter interface", were:

- *inverter control techniques;*
- *inverter current control;*
- *inverter voltage control;*
- *grid inverter filter design;*
- *grid inverter functionalities; and*
- *grid inverter synchronization.*

Some information from the reviewed literature is presented in Table (2.3), briefly outlining the aspects of interest in the context of the work presented in this thesis, based on the:

- *principal focus of the work;*
- *input to the inverter;*
- *aspects of the inverter control considered;*
- *control technique considered; and*
- *implementation of the considered technique.*

**Table 2.3:** Control of the DPG-inverter interface

| Source | Principal focus of the work | Input to the inverter (if specific) | Aspect(s) of the inverter Control considered | Control technique(s) Considered | Implementation of the Considered technique (if any) | Comments |
|---|---|---|---|---|---|---|
| Liu *et al.*, 2015 | Discusses the control of paralleled inverter-based DPG systems in an islanded microgrid based on Model Predictive Controllers (MPC), in order to achieve improved current sharing of the units in the microgrid. | Constant DC voltage. | Inverter output current regulation. | Model Predictive Control. | Simulations have been conducted in the Matlab/PLECS software package to evaluate the performance of the suggested controller. | Proper current sharing of paralleled inverters in a microgrid is an issue for which many different solutions have been suggested in literature. The authors in this paper propose the use of an MPC, which allows the optimal selection of a control action among some candidates so that the desired system state trajectory is achieved. |
| Louzazni & Aroudam, 2014 | Proposes the state feedback linearization and pole placement-based control of a single-stage grid-connected inverter-based PV power generation system with MPPT control. | Photovoltaic | PV MPPT, inverter input DC-link voltage, and inverter output current regulation. | Incremental Conductance (IncCond) MPPT, and inverter current regulation by state feedback control. | Matlab/Simulink simulations. | PV generation in conjunction with the interface inverter is a highly nonlinear system; the authors thus suggest the input-output linearization and pole placement approach to achieve improved dynamic characteristics of the inverter output current regulation; the IncCond-based PV MPPT control is also used to improve the DC-link voltage dynamic characteristics. |
| Zhou *et al.*, 2013 | Presents a control strategy for three-phase grid-connected LCL inverters based on the instantaneous power theory, and makes use of a positive-sequence voltage detector rather than a Phase-Lock Loop (PLL). | Photovoltaic | Inverter output current control; and grid voltage vector detection. | Control structure based on instantaneous power theory, implemented in the stationary (*i.e.* αβ) reference frame, using Proportional-Resonant (PR); compensators; also an algorithm for the positive-sequence voltage vector detection based on a double resonant filter. | Simulation in Matlab/Simulink | The proposed control strategy is intended to simplify the complexity of the control structure by avoiding PLL-based grid voltage phase angle detection, and the decoupling and feed-forward compensation associated with the commonly used synchronous reference frame-based inverter control. Good transient and steady-state response is reported to have been achieved, even under distorted grid conditions. |

| | | | | | | |
|---|---|---|---|---|---|---|
| Rocabert *et al.*, 2012 | Considers an overview of the structures and control techniques for grid-interactive microgrids at different hierarchical levels, and discusses the present and future potential for microgrids to provide grid support services. | Not specified. | Grid-connected current-mode control, stand-alone voltage-mode control, and grid-synchronization. | Synchronous reference frame PI control, stationary reference frame Proportional plus Resonant (PR) control, and droop control (generic discussion). | N/A | The grid services desired from microgrids in future power systems (such as islanded-mode operation) are discussed in terms of the required enabling technological developments, such as the integration of energy storage into microgrids, active demand management, and enhanced microgrid controllability and monitoring. |
| Liu *et al.*, 2012 | Presents a design method for obtaining the optimal PI gain parameter values for the PV grid inverter current regulation. | Photovoltaic | Inverter input DC-link voltage and output AC current control. | Voltage-Oriented Control (VOC) in a dual-loop scheme, with outer-loop DC-link voltage and inner-loop AC current control, using optimally determined PI compensator gain parameters. | Simulations carried out in the Real-Time Digital Simulator (RTDS). | The work focuses on the issue of the optimal setting of PI gain parameters to ensure effective control system performance under varying operating conditions and parameter variations. Optimal dominant-pole placement based on the desired natural frequency criteria is used as the guideline for the PI gain parameter setting. |
| Sozer & Torrey, 2009 | Discusses the generic aspects of the modeling and control of grid-interactive inverters for renewable power generation. | Not specified | MPPT control; inverter grid synchronization; anti-islanding protection; inverter output current regulation; and Pulse Width Modulation (PWM) signal generation. | PLL-based grid synchronization; frequency and voltage shift-based anti-islanding detection algorithms; synchronous reference frame PI inverter current control; stand-alone voltage-mode control; and Sinusoidal and Space Vector Pulse Width Modulation techniques, discussed generically. | N/A | The paper presents a generic treatment of the main aspects of the modeling and control of inverters for interfacing renewable power generation, highlighting pertinent implementation aspects, such as the signal processing requirements for the digital implementation of the control algorithms. |
| Maknouninejad *et al.*, 2009 | Presents a controller design procedure for single- and three-phase grid-connected inverters implemented in the stationary (αβ) reference frame, PR compensators. | Not specified | Output active and reactive power regulation | αβ-frame PR control | Simulations carried out in Simulink to test the suggested controllers with harmonic compensation. | The αβ-frame PR inverter current control is recommended as an alternative to the dq-frame PI compensation, as it leads to a less complex control structure, with improved power quality performance under non-ideal grid conditions. |
| Timbus *et al.*, 2009 | Presents the evaluation of some linear controllers for the current control of inverter-based grid- | Variable input power (such as PV or | Grid-connected mode current control. | Natural (*i.e.* abc) reference frame control; synchronous frame PI; stationary frame PR; and | Experimental evaluation of all the considered | The performance of the linear controllers is considered in terms of power quality and their |

| | | | | | | |
|---|---|---|---|---|---|---|
| | connected DPG systems. | rectified wind power output), | | deadbeat control. | controllers has been carried out. | behavior under anomalous grid conditions (such as voltage ride-through); experimental results show the considered controllers to have comparable performance. |
| Ahmed *et al.*, 2007 | Presents the analysis of various passive filter configurations for interfacing grid-interactive inverters so as to realize the desired current harmonic attenuation of the injected grid current. | Not specified. | Harmonic content of the inverter output current. | Parameter design procedure for the LCL filter, taking into account the required current harmonics attenuation, inverter output power factor, and filter resonance damping. | Simulations have been carried out to evaluate the performance of the designed filter parameters. | The characteristics of the commonly used passive filters for grid-interactive inverters (L-, LC- & LCL filters) are discussed in terms of their suitability for satisfying the grid-code-stipulated power quality requirements for grid inverters. A design procedure for the LCL filter is also discussed in detail. |
| Teodorescu *et al.*, 2006 | Discusses the application of PR regulators and filters to the current/voltage control of the grid-connected converter, with a view to overcoming some known limitations of the commonly used PI compensator-based control implemented in the synchronous reference frame. | PV or any other renewable energy source. | Inverter current/voltage control; harmonic filtering; and PLL-based grid synchronization. | PR controller implemented in the stationary ($\alpha\beta$) reference frame. | The performance of the developed controllers has been verified by means of simulations as well as experimental implementation in a laboratory-scale microgrid set-up. | A variety of applications for the resonant (control) concept have been discussed in the paper, in addition to presenting two application examples: a single-phase PV inverter controller; and a three-phase microgrid power quality compensator. Further, the positive attributes that make the PR regulator perhaps the more favorable candidate than the dq-frame-based PI regulator have been clearly outlined. |
| Carrasco *et al.*, 2006 | Discusses the present and future role of Power Electronics in the grid-integration of renewable energy sources and energy storage technologies. | Renewable energy sources such as wind, PV fuel cell power, as well as various energy storage technologies. | Dependent on the primary energy source (for instance machine torque control and output power regulation in the case of a wind turbine system). | Several controllers have been discussed. | N/A | The almost indispensable role of Power Electronics in the development of the DPG field has been well-outlined in the paper, in terms of both the present capabilities and the desired future technological advancements. |
| Liserre *et al.*, 2005 | Proposes a systematic procedure for the LCL filter parameters' design for a three-phase active rectifier so as to obtain low current harmonic content, rapid dynamic response, and good | The converter is considered in rectification mode, with the AC-side connected to | Rectified output current control | Synchronous reference frame (dq)-based PI controllers. | Both dynamic simulations and experimental implementation have been conducted, to | The proposed LCL filter parameter design procedure incorporates such pertinent aspects as current ripple attenuation, resonance damping, impact on power factor, and |

| | | | | | | |
|---|---|---|---|---|---|---|
| | stability margin. | the grid, and the DC-side to a load. | | | evaluate the performance of both the designed controllers and the power quality of the filter. | inductor voltage drop. This facilitates a more comprehensive approach to the design of this vital component of the grid-inverter. |
| Timbus *et al.*, 2005 | Looks at the structures and main characteristics of commonly used grid synchronization techniques for grid-integrated DPG systems, along with suggesting methods to compensate for the adverse effects of grid disturbances on the synchronization. | DC input, either drawn from a DC source or obtained from the rectified output of an AC source. | Synchronization with the grid voltage. | Techniques implemented in both the stationary (αβ) and synchronous (dq) reference frame are discussed; the suggested algorithm seeks to minimize the grid anomalies' adverse effects by the suitable design of the compensation filter for the synchronization loop circuit. | The considered algorithms have been implemented in a laboratory set-up, which has been used to test the developed algorithms under various grid operating conditions. | Considerable emphasis has been placed on the influence of the dynamics of the synchronization loop filter, which has to be designed according to the main objective(s) of the synchronization. |
| Twining & Holmes, 2003 | Proposes a robust strategy for the current-mode control of an LCL filter-interfaced grid-connected Voltage-Source Inverter (VSI) to ensure the stability of the control system. | Constant DC input considered. | Inverter current control. | Dq reference frame-based dual-loop inverter current control, with outer-loop grid-current and inner-loop capacitor-current regulation. | Both simulations and experimental studies of the proposed control strategy have been carried out to evaluate its performance. | It is made clear in the paper that besides ensuring low-distortion injected grid current, control system stability (especially for LCL filter-interfaced converters) and robustness to grid voltage distortion are equally important considerations for the control of grid-connected converters. |
| Chung, 2000 | Presents the analysis and design of the PLL circuit for the grid-voltage phase-tracking for grid-interactive three-phase inverters, giving particular consideration to the effects of grid anomalies on the dynamic response of the PLL circuit. | Not considered. | Synchronization with the grid voltage. | Second-order PLL circuit making use of a PI compensator as the loop filter. | Dynamic simulations to test the effectiveness of the designed PLL circuit have been performed, followed by experimental analysis. | Since the PLL circuit is a tracking problem that imposes the conflicting objectives of fast dynamic response as well as good noise rejection, the author proposes the use of an optimization method that facilitates the realization of a good compromise between the two main objectives. The performance of the PLL circuit under grid abnormal conditions is well-treated as well. |
| Kazmierkowski & Malesani, 1998 | Presents a review of linear and nonlinear current control techniques for three-phase PWM inverters, and discusses new trends in intelligent control | Not specified | Current control | A variety of linear and nonlinear control techniques are discussed, covering stationary, synchronous and predictive deadbeat linear controllers, as well as hysteresis, | N/A | Inverter performance is highly dependent on the employed current control technique, and various applications prioritize different performance criteria. |

| | | | | | | |
|---|---|---|---|---|---|---|
| | techniques. | | | discrete modulation, online-optimized, Neural Network and Fuzzy Logic nonlinear controllers | | The paper discusses the commonly employed inverter current controllers in terms of their main characteristics and their applicability to various applications. |
| Kawabata *et al.*, 1990 | Presents the dead beat current and voltage control with (time-delay compensation) of the three-phase PWM VSI, implemented on a hybrid computer. | Not specified | Inverter terminal voltage and current regulation. | Dead beat predictive control, implemented using the inverter model expressed in the synchronous reference frame. | The proposed algorithms have been implemented on a hybrid computer platform for experimental evaluation. | The deadbeat control law for the PWM VSI output current regulation has the desirable characteristics of fast dynamic response and precise control. Good load disturbance rejection and immunity to the time-delay-induced current control errors have been realized in the proposed control strategy by means of load current prediction and computational delay compensation. |

### 2.5.2. Discussion

Before discussing the role of the inverter in Distributed Power generation (DPG) systems, it may be worth mentioning that one common classification for inverters, which depends on the inverter's terminal characteristics, is that of either the Voltage-Source Inverter (VSI)(virtually constant terminal voltage), or the Current-Source Inverter (CSI)(virtually constant output current). The VSI is the one that is more commonly used for DPG applications, the CSI being rather confined to specialized, high-power applications (Evyu, 2006). Thus this discussion is done with reference to the VSI.

#### 2.5.2.1. Considerations for the control of the DPG inverter

The inverter plays a very significant role in most DPG systems. Its primary function is usually identified as being a power conditioning interface unit; that is, it matches the DPG's power output to the load requirements, this being in terms of the voltage magnitude and frequency, as well as the current demand. This logically leads to the observation that the dynamics of the power derivation from the DPG as well as the quality of the power output are highly influenced by the performance of the inverter. Carrasco *et al* (2006) have comprehensively discussed both the present and future role of Power Electronic interfaces in the development of renewable energy generation. Their conclusion is that the recent growth witnessed in the renewable energy sector has been closely tied to Power Electronics technological advances. Further, the authors have highlighted the anticipated future trend in terms of the enabling capabilities of Power Electronics that will contribute to the continued growth of DPG.

The literature reviewed on the control of the inverter for interfacing DPG systems (hereafter referred to as the DPG-inverter) reveals that this encompasses quite a number of aspects.

Firstly, the objective of the DPG-inverter control may be to regulate either the output current or the terminal voltage, or perhaps both variables. This is usually dictated by the type of source with which the inverter is paralleled (as is often the case), whether it operates in parallel with the grid supply (grid-interactive mode) or in parallel with other inverters, independent of the grid (autonomous mode). In either case, the proper choice of the control strategy and the form of compensation should ensure that the control objectives are well-met (Kazmierkowski & Malesani, 1998).

Secondly, when working in parallel with other source(s), the inverter's terminal voltage (magnitude and frequency) has to be well-synchronized with the other source(s), in order not to induce anomalies into the common power supply. This is especially the case when the inverter operates in grid-interactive mode, where its terminal voltage has to be properly synchronized with the grid voltage (Timbus *et al.*, 2005).

Thirdly, since the inverter conditions the power at its input by means of high-frequency switching, effective filtering of high-frequency harmonics and low-frequency ripple is very

essential to ensuring an acceptable level of the inverter output power quality. Various types of passive filters are used for this purpose.

The discussion of the control of the DPG-inverter in this section is mostly oriented towards the grid-interactive operation. In Section 2.6, the characteristics of (and requirements for) the autonomous-mode operation are considered, when the review focuses on the dual-mode operation of the inverter.

The DPG-inverter invariably uses current-mode control when operating in the grid-interactive mode. This more easily enables the meeting of the grid-code requirements for the grid-interactive inverter (Rocabert *et al.*, 2012). The characteristics of the current-mode control that make it preferable to the voltage-mode control for the grid-mode inverter operation have been discussed by Kazmierkowski and Malesani (1998), highlighting such characteristics as the control of the instantaneous current waveform with high accuracy which, coupled with very good dynamic response characteristics (including good load disturbance rejection and low sensitivity to grid parameter variations) leads to high-quality injected grid power. Thus many researchers have considered a variety of current control algorithms for the grid-mode inverter operation. As discussed by Teodorescu *et al* (2011), the selection of the appropriate inverter current controller has to take into account both the controller performance (in terms of transient and steady-state response, stability, waveform quality, and robustness or sensitivity to model uncertainties and disturbance rejection) and the economical aspects (complexity of the control structure, and the ease and cost of implementation).

A variety of both linear and nonlinear controllers have been applied to the inverter current control. The grid-code power quality requirements are more easily achievable by means of linear controllers, however, and thus they are quite commonly employed, even with their relatively inferior dynamic characteristics (Kazmierkowski & Malesani, 1998). The commonly researched linear controllers are: synchronous reference frame-Proportional-Integral (dq-PI) compensator; stationary reference frame-Proportional-Resonant (αβ-PR) compensator; predictive deadbeat control (Liu *et al.*, 2012; Timbus *et al.*, 2009; Teodorescu *et al.*, 2006; Twining & Holmes, 2003; Kawabata *et al.*, 1990); instantaneous power theory (Zhou *et al.*, 2013); and state feedback control (Louzani & Aroudam, 2014). The comparative analysis of these controllers has been considered by some researchers (such as Timbus *et al.*, 2009; Kazmierkowski & Malesani, 1998), and the conclusion is that the difference may lie mainly in the complexity of implementation (that is, their dynamic performance is fairly comparable).

An overview of the methods of the grid-inverter synchronization and their main characteristics was considered by Timbus *et al* (2005), highlighting the significant influence of the loop filter (and thus the need for its proper design) in the accuracy of the phase-tracking circuit. The loop filter design was considered in further detail by Chung (2000), in the design of a PLL circuit

for the purpose of grid-voltage phase tracking. The author presented an optimization procedure for the loop filter design that permits the simultaneous addressing of the PLL circuit's conflicting design objectives of fast dynamic response and good noise rejection.

Then the issue of the selection of the appropriate filter interface and its parameter design has also been considered by many researchers, as a vital component of the DPG-inverter, which moreover influences the dynamic response characteristics of the inverter current control (Teodorescu *et al.*, 2011). In this regard, Liserre *et al* (2005) presented a systematic procedure for the parameter design of the LCL filter which takes into account all the pertinent aspects of the filter characteristics. The same task was addressed by Ahmed *et al* (2007), and the reviewed work shows that the LCL filter is generally the preferred choice for the grid-inverter interface, when compared with other passive filter configurations, such as the series-L filter and the LC filter (Teodorescu *et al.*, 2011).

#### 2.5.2.2. Control of the DPG inverter in this thesis

The modeling of (and controller design for) the DPG-inverter is a major component of the work covered in this thesis, making the literature review discussed in this section very relevant material.

In Chapter 5, the modeling of the inverter for current controller design is addressed, where the information reviewed on the appropriate choice of (and parameter design for) the interface filter is made extensive use of. The understanding acquired from the study of synchronization techniques for the grid-interactive inverter is applied in Chapter 6, where a brief discussion of the commonly used methods, along with the design of the PLL circuit (as the technique used in this thesis), is presented. Chapter 6 also addresses the current controller design for the grid-mode operation of the inverter, and there again the previous work on current control techniques reviewed in this thesis is made reference to.

As stated in Chapter 1, this thesis considers the control strategy design for the dual-mode operation of the DPG-inverter. So the final part of the literature review considers the requirements and techniques for the dual-mode control of the grid-interactive inverter, as discussed in the following section.

## 2.6. Dual-mode control of the grid-interactive inverter

### 2.6.1. Review of the existing literature

The key phrases used in the online search for literature under the topic: "Dual-mode control of the grid-interactive inverter", were:

- *dual-mode grid-tie inverter;*
- *control of grid inverter with islanded operation capability;*
- *safe islanding of grid-integrated distributed generation; and*
- *control strategies for versatile grid inverter operation.*

Some information from the reviewed literature is presented in Table (2.4), as a comparative analysis of the various works with regards to the:

- *principal focus of the work;*
- *aspects of the control considered;*
- *control mechanism used; and*
- *implementation of the considered mechanism.*

**Table 2.4:** Dual-mode control of the grid-interactive inverter.

| Source | Principal focus of the work | Aspects of the control considered | Control mechanism(s) Used | Implementation of the considered mechanism | Comments |
|---|---|---|---|---|---|
| Li *et al.*, 2015 | Presents an MPC-based strategy for the dual-mode control of a single-phase grid-connected inverter, to realize the effective operation of the system in both modes, as well as the seamless transfer between the modes. | Inverter output power regulation in grid mode; inverter terminal voltage magnitude and frequency control in islanded mode; synchronization with the grid; and seamless mode transition. | MPC control of the inverter output in the various operational modes; and Second-Order Generalized Integrator (SOCI)-based grid synchronization. | The performance of the proposed control strategy has been evaluated by means of both simulations (Matlab/Simulink) and hardware implementation (dSPACE hardware). | The authors consider the pertinent aspects of the operation of a dual-mode inverter, which are proper control in the respective operational modes, well-coordinated disconnection from and reconnection to the grid, as well proper synchronization in the grid-connected mode. |
| Tian *et al.*, 2014 | Presents a control strategy for the operation of a single-phase inverter in both grid-connected and stand-alone modes, with the capability to seamlessly transition between the two operational modes. | Inverter output current control, and transition control between grid- and stand-alone modes. | Multiple-loop control strategy, with the main outer loop controlled by a PR compensator, for inverter output current control (grid mode) and filter capacitor voltage regulation (stand-alone mode); and a mode transition strategy based on hysteresis current control. | Matlab/Simulink simulations as well as an experimental set-up have been used to test the proposed control strategy. The experimental test set-up considers a battery storage unit connected to an electric grid whose voltage magnitude can be adjusted to emulate voltage sag. | The proposed seamless transition control strategy for a dual-mode inverter aims to achieve smooth mode transition by means of fast load current control, as well as the minimization of the load voltage transients in the transition process. |
| Kiran *et al.*, 2014 | Discusses the state-space modeling of a single-phase grid-interactive inverter, and the design of a Quadratic Optimal Regulator for the dual-mode operation of the inverter. | Focus is on the stability of the control system in both grid-connected and stand-alone modes. | State feedback control by means of a linear quadratic optimal controller. | Matlab simulations. | The positive aspect of a quadratic optimal controller (as a grid inverter controller) as mentioned in the paper is that it enables taking into account the stability, transient and steady-state response of the control system, as well as the control energy expense in achieving the desired system response. The paper does discuss the design of a quadratic optimal controller, but dynamic simulations are not performed to analyze the performance of the proposed controller. |
| Srinivas & Reddy, 2013 | Discusses the design of control algorithms to enable the dual-mode operation of an inverter-based DPG system. | Inverter synchronization with the grid voltage; islanding phenomenon detection; intelligent load shedding; and | Dq-reference-frame PI-based regulation of the inverter output current (grid-connected mode) and the inverter terminal voltage | Matlab/Simulink simulations. | The paper addresses some of the aspects to be considered in the control of a dual-mode inverter, which are the use of the |

| | | | | | |
|---|---|---|---|---|---|
| | | inverter output power regulation. | (stand-alone mode). | | appropriate control mechanism in the two operational modes (with their different control objectives), synchronization in the grid-connected mode, islanding detection, as well as ensuring satisfactory power quality in the stand-alone operational mode. |
| Wang *et al.*, 2012 | Presents the control strategy design procedure for the master DPG-inverter in a master-slave microgrid configuration to ensure the microgrid's seamless transition between the grid-interactive and autonomous operational modes. | Current-mode control in the grid-connected mode; voltage-mode control in the autonomous mode; and the mode transition logic to ensure the smooth operational mode transition. | Multi-loop PI control in the synchronous (dq) reference frame, both for the current and voltage controllers. | Computer simulations in PSCAD/EMTDC. | The suggested control strategy for the microgrid with dual-mode operation capability uses two distinct controllers for the respective modes in which it operates. The use of different controllers necessitates compensating for the discrepancies in the controller reference values that exist immediately prior to the initiation of the mode transition process, and the authors propose a method to realize such compensation, as the main focus of their work. |
| Sharifzadeh & Jalilian, 2011 | Presents an approach to the small-signal dynamic stability analysis of an inverter-based DPG system with grid-connected and autonomous-mode operation capability. | Inverter output active power and voltage regulation. | Frequency droop control for active power regulation; voltage droop control for reactive power regulation. | Eigenvalue analysis by means of computer simulations. | A dual-mode grid-interactive inverter has three main modes of operation, if the transition interval from the one mode to the other is also considered. The stability of the control system is important in all the three modes, and the paper shows how the eigenvalue sensitivity analysis of the system can be used in the determination of controller parameters to ensure small-signal system stability. |
| Chen *et al.*, 2011 | Discusses the design and control of a multi-inverter grid-interactive microgrid to realize smooth mode transition of the microgrid between the grid-connected and | Precise inverter output current control; equal current sharing among the paralleled microgrid inverters; and smooth mode transition between the grid- | Grid-connected current-mode control by a single-loop PR regulator; autonomous voltage-mode control by a dual- (inner current and outer voltage) loop | Both computer simulations and experimental implementation have been conducted to evaluate the performance of the proposed control strategy. | The paper considers the grid-connected and autonomous-mode operation of a multi-parallel-inverter microgrid, as well as the transition between |

| | | | | | |
|---|---|---|---|---|---|
| | autonomous operational modes, to ensure uninterrupted power supply to the microgrid's critical load. | connected and autonomous operational modes. | control, using Proportional and PR regulators respectively. | | the two operational modes. A master-slave architecture is used in the microgrid, with communication via the Control Area Network (CAN) bus being used to realize current sharing among the inverters. A compensation technique of the master controller's reference values is suggested as a means to enable the microgrid's smooth mode transition. |
| Kim *et al.*, 2008 | Deals with the dynamic modeling and controller design for a PV-Wind-Battery hybrid DPG system, with power dispatch capability and ability to operate both in grid-connected and autonomous modes. | MPPT control of the renewable energy generators (PV, wind); battery charge/discharge regulation; grid inverter output power regulation; and supervisory control of the hybrid system. | Modified hysteresis control for battery charge/discharge regulation; power averaging control using a low-pass filter; dq-frame PI-based inverter current control; and MPPT control of the PV and wind energy generators. | The proposed dynamic models and control strategies have been simulated in the PSCAD/EMTDC software suite, as well as experimentally implemented, to evaluate their dynamic performance. | The proposed concept of a hybrid DG system with versatile power transfer is intended, among other things, to better support the grid by supplying stable, high-quality power in grid-connected mode, and improve the reliability of power supply to critical local loads in the absence of the grid power. Energy storage plays a significant role in enabling such operation of renewable-based generation. |
| Gao & Iravani, 2008 | Presents a voltage-mode control strategy for grid-connected and autonomous-mode operation of a Voltage-source Inverter (VSI), ensuring effective regulation of the instantaneous output power with current limiting in both modes, smooth mode transition between the operational modes, and inherent zero-Non-Detection-Zone (NDZ) islanding detection. | VSI output active and reactive power regulation; VSI synchronization with the grid voltage; and islanding detection. | Droop voltage magnitude and frequency control in both grid-connected and autonomous operational modes (corresponding to reactive and active power regulation respectively); PLL for synchronization; and positive voltage feedback for islanding detection. | Small-signal dynamic (eigen)-analysis in Matlab, and time-domain simulations in the PSCAD/EMTDC software package. | A significant issue with grid-interactive VSIs with autonomous-operation capability is the transients associated with mode transition, mainly due to the use of different control strategies in the two modes. The paper suggests the use of a single (voltage-mode) control strategy to avoid this; other features of the suggested method are inherent zero-NDZ islanding detection, current limiting, and ride-through capability. Moreover, small-signal dynamic stability analysis has also been performed, to aid the controller |

| | | | | | |
|---|---|---|---|---|---|
| | | | | | parameter setting. |
| Gu *et al.*, 2006 | Proposes a strategy for the dual-mode operation of a single-phase inverter system, with smooth transition between grid-connected and autonomous modes. | Grid-mode inverter current control; autonomous-mode inverter terminal voltage magnitude and frequency regulation; and a mode-transition procedure between the operational modes. | Three-level hysteresis current controller for the grid-mode current control; and a self-adaptive fuzzy logic voltage regulator for the autonomous-mode voltage regulation. | The proposed strategy has been implemented in a laboratory-scale experimental set-up, to evaluate its performance. | The proposed control strategy for the dual-mode inverter makes use of nonlinear controllers, and this is motivated by the desire to achieve superior dynamic response of the control system, such as robustness to parameter variations and good load disturbance rejection in the autonomous mode. |
| Lopes *et al.*, 2006 | Discusses and evaluates the control strategies and other requirements to enable a microgrid connected to the medium-voltage grid to successfully transition to (and operate stably in) stand-alone mode, either following a grid disturbance or as a planned event. | A hierarchical control strategy is considered for the microgrid, consisting mainly of supervisory control, as well as the direct control of the loads and micro-sources' power yield. | Frequency/power and voltage/reactive power droop control of the various micro-sources, coordinated by the supervisory controller. In lslanded mode, one or more inverters are voltage-controlled, also by droop characteristics, whereas the others are current-controlled. | A low-voltage test network has been implemented in Matlab/Simulink, to evaluate the performance of the suggested control strategies. | The simulation results reported in the paper demonstrate that a microgrid can successfully transition to autonomous operational mode (perhaps triggered by a grid fault). Effective load management (e.g. load shedding) and energy storage (state-of-charge) management are identified as key factors in the successful stand-alone operation of a microgrid. |
| Teodorescu & Blaabjerg, 2004 | Presents the development and practical test of a flexible control strategy to enable a small-scale variable-speed WEC system's operation in grid-connected and stand-alone modes. | WEC system's Generator- and grid-side converter control, the and strategy for the mode transition between grid-connected and stand-alone operation of the WEC stsem. | Flux vector control for the generator-side converter, decoupled dq-frame control for the grid-side converter, and phase comparison of grid-inverter terminal voltage and grid voltage (PLL-based) for loss-of-grid detection and eventual mode changeover | An experimental system emulating a WEC system has been built, with controllers implemented on a Digital Signal Processor (DSP). | The paper covers fairly comprehensively the various aspects of small-scale WEC systems modeling and lab-scale implementation, and thus serves as a good reference work for related wind energy generation studies. |
| Zeineldin *et al.*, 2004 | Presents a control strategy to realize the safe controlled islanding of an inverter-based DPG system, with the focus of the control strategy being on the maintenance of the islanded system's voltage magnitude and frequency within the stipulated nominal ranges. | Grid-mode inverter output current control; autonomous-mode inverter terminal voltage regulation; and islanding detection. | Both the current control and voltage regulation are implemented in the dq reference frame with PI compensators; a hybrid passive islanding detection algorithm (based on voltage magnitude, and current and voltage distortion measurements) is employed. | Simulations have been performed in the PSCAD/EMTDC software package to test the safe controlled islanded operation of the DPG system under the proposed control strategy. | The safe controlled islanded operation of a grid-interactive DPG system as discussed in the paper is intended to enable the fuller utilization of distributed generation, especially in contributing to electric power supply reliability. The suggested control strategy has been tested for different scenarios, to |

| | | | | | |
|---|---|---|---|---|---|
| | | | | | ascertain its ability to enable the desired dual-mode operation of the distributed generation system. |
| Loh *et al.*, 2003 | Investigates the choice of the (feedback current) variables for the multi-loop feedback control of Uninterruptible Power Supply (UPS) systems, in terms of their influence on the transient system response and power quality performance, and makes a proposition of the better-performing scheme based on the obtained simulation and experimental results. | Regulation of the inverter terminal voltage magnitude and frequency, in its role as a UPS. | A multi-loop control strategy, having an inner-loop current control (using a PID compensator) , and an outer-loop voltage regulator (using a PR compensator). | Both computer simulations (Matlab/Simulink) as well as a digital experimental implementation were conducted to evaluate the relative performances of the investigated multi-loop feedback control strategies. | The comparative analysis of the investigated inner-loop current control strategies (i.e. use of either filter inductor or capacitor current for feedback) mainly considers the extent of the influence of the load disturbances on the voltage harmonic distortion, besides the transient response performance of the control system. The authors report that, based on the obtained results, capacitor current feedback yields better performance for inverter multi-loop control in UPS systems. |
| Tirumala *et al.*, 2002 | Proposes a control algorithm for the smooth transfer of a grid-interactive inverter to the autonomous operational mode in the event of a grid fault, in order to maintain power supply to mission-critical loads in the absence of the grid supply. | The seamless transfer of the inverter's operational mode between grid-connected and stand-alone. | A systematic mode transition algorithm has been suggested that ensures a smooth voltage profile across the sensitive load, irrespective of the operational mode, and including during the transition process. | Simulations in SABER software and a hardware prototype implementation in dSPACE have been used to analyze the suggested algorithm's effectiveness in realizing the desired seamless mode transition. | It is emphasized in the paper that irrespective of the direction of mode transition, the algorithm should ideally ensure minimal load voltage transients in order to avoid excessive load current excursions. This requires proper synchronization of the inverter terminal voltage with that of the point-of-common-coupling, especially during the mode transition interval. |
| Barsali *et al.*, 2002 | Discusses the techniques for controlling paralleled distributed generation units without the need for high-bandwidth online communication for control purposes, so as to realize improved continuity of power supply (in the absence of the grid) at reasonable complexity and cost. | Inverter output power regulation in the grid-connected mode, and inverter terminal voltage magnitude/frequency regulation in the islanded operational mode. | Droop control characteristics based on the locally measured variables of the generation unit, implemented for both the grid-connected and islanded operational modes control. | Simulations have been conducted on a number of case studies to evaluate the performance of the suggested control approach. | The proposed droop-characteristic-based control of dispersed generators for power supply reliability enhancement is motivated by the need for a minimal-complexity control structure that nonetheless enables effective power sharing as well as voltage magnitude and frequency control. Simulation results of the considered cases |

| | | | | | |
|---|---|---|---|---|---|
| | | | | | support the effectiveness of the proposed approach. |
| Chen & Chu, 1995 | Discusses the implementation of current-mode and voltage-mode controllers in paralleled inverters making up a single-phase UPS system, in a master-slave configuration, with supervisory control. | Voltage-mode control is implemented in the (one) master inverter, which regulates the UPS's voltage magnitude and frequency; the other (two) parallel inverters are controlled to supply the UPS load demand, in current-mode control. | A phase-lead-lag compensator is used to regulate the master inverter's terminal voltage (which is the UPS voltage); current-mode-controlled inverters make use of load and voltage feed-forward compensation, along with appropriate loop-shaping, to realize fast tracking of the UPS' load current. | An experimental single-phase model of a UPS system consisting of three inverters (one voltage-mode, two current-mode controlled) has been set up to test the suggested control strategy. | The authors propose a topology for a UPS system comprised of paralleled inverters that is modular, and employs simple control techniques with no need for high-bandwidth online communication for control purposes, making it easily expandable. The supervisory controller plays an important role in this topology in ensuring the efficient and reliable coordinated operation of the paralleled inverters. |

### 2.6.2. Discussion

One of the most attractive characteristics of Distributed Power Generation (DPG) is its potential to improve the electric power supply reliability, and this is especially desirable for sensitive and mission-critical loads, for which even momentary grid supply interruptions may be intolerable (Barsali *et al.*, 2002; Tirumala *et al*, 2002).

DPG may better contribute to power supply reliability if designed for both grid-interactive and autonomous operation, as has been considered by many researchers, from the literature reviewed on this topic. The feasibility of such operation of the grid-interactive inverter heavily hinges on two important factors or requirements.

#### 2.6.2.1. Requirements and techniques for the dual-mode inverter control

The first requirement is related to the characteristics of the DPG, as far as its ability to meet the load demand in the absence of the grid supply. Lopes *et al* (2006) showed that this aspect (of the DPG successfully meeting the load demand autonomously) requires the incorporation of proper load management (such as load shedding), as well as energy storage with effective state-of-charge control, especially in the case of the intermittent renewable generation sources.

The second requirement is related to the control strategy used for the DPG-inverter, which then has to be so controlled that the DPG satisfies the operational requirements of both the grid mode and the autonomous mode, and to ensure the system's smooth transition between the two operational modes. The means of meeting this second requirement are considered in light of the literature that has been reviewed on the topic. In particular, the different approaches that have been explored to enable the seamless dual-mode operation of the grid-interactive DPG are examined from the literature, as a basis for the contribution to the field made in this thesis.

The main objective of the control of the grid-interactive DPG-inverter is to inject high-quality current into the grid. As mentioned in Section 2.5.2, current-mode control is the one that is more suitable for meeting this objective. On the other hand, the main control objective for the autonomous-mode operation is the proper regulation of inverter's terminal voltage magnitude and frequency, while being able to supply the demanded current within its rating. Meeting this objective requires that the inverter be controlled as a voltage source (Gao & Iravani, 2008). This disparity of the inverter control objectives in the two operational modes poses a challenge for the choice of the most appropriate control approach.

From the reviewed literature, the commonly used approach is to design two distinct controllers which are best suited to satisfying the control objectives of the respective operational modes, and to implement an algorithm that determines the control mode of the inverter on the basis of the grid conditions (Tian *et al.*, 2014; Srinivas & Reddy, 2013; Gut *et al.*, 2006; Teodorescu *et al.*, 2004). Tirumala *et al* (2002) emphasized that the most important consideration in a dual-

mode inverter control strategy that uses distinct controllers in the two operational modes is to ensure the maintenance of a reasonably uniform voltage profile across the load during the mode transition interval. This helps to suppress load current transients, and thus facilitates a smooth and successful mode transition. This in turn requires the fast detection of the grid conditions which should necessitate such a transition.

Some researchers have considered control strategies that avoid the need for control mode transition by designing a single controller that is valid for both operational modes, as exemplified by the work of Gao and Iravani (2008). When a multi-inverter grid-interactive dual-mode microgrid is considered, it is common to use the master-slave control architecture, which usually implies the need for the control mode transition of only one (the master) inverter, others being current-mode-controlled in either operational mode (Wang *et al.*, 2012; Chen *et al.*, 2010; Lopes *et al.*, 2006; Chen & Chu, 1995).

For the dual-mode microgrid, droop-based control has also been investigated, with the positive characteristic of imposing minimal communication requirements for control purposes among the paralleled inverters (Lopes *et al.*, 2006; Zeineldin *et al.*, 2004; Barsali *et al*., 2002). The droop control of inverters suffers from the short-fall of diminished accuracy of current control, which may have adverse implications for the grid-mode operation.

#### 2.6.2.2. Dual-mode control of the grid inverter in this thesis

The reviewed literature on the requirements and approaches for the dual-mode control of the DPG-inverter brings to the fore not only the capabilities required of the candidate control strategy, but also the relative merits of the approaches commonly used to realize the control strategy. The insight gained from this review is applied in Chapter 7, in which the seamless mode transition control of the DPG-inverter is treated.

## 2.7. Conclusion

The previous work that has been reviewed as the basis for this thesis work has been discussed in this chapter.

Starting with a discussion of the developments in the electric power system in the latter decades of the $20^{th}$ century as a precursor to the establishment of the distributed power generation sector as is known today, the chapter went on to discuss the modeling and controller design for Photovoltaic (PV) and Wind Energy Conversion (WEC) systems, which are the two most widely studied renewable energy sources, and are anticipated to play an increasingly pivotal role in the drive towards cleaner and more sustainable energy supply.

Since distributed generation makes extensive use of power electronic interfaces, a review of the control of the DPG-inverter was also discussed.

The final part of this literature review was particularly focused on the requirements and control strategies for the dual-mode (grid-connected and autonomous-mode) operation of the grid-interactive inverter, in line with the main objective of this thesis work.

The following chapter discusses an overview of Distributed Energy Resources (DER), in terms of their main characteristics and the technological developments associated with them.

# CHAPTER 3

# DISTRIBUTED ENERGY RESOURCE (DER) TECHNOLOGIES

## 3.1. Introduction

Distributed Power Generation (DPG) distinguishes itself from large-scale, centralized power generation in quite a number of ways. One such way is that while the latter is largely based on a few, high-energy-density primary energy sources (such as fossil fuels, nuclear energy and large-scale hydro power), the former is built upon a great variety of relatively smaller-scale Distributed Energy Resource (DER) technologies, which include some fossil fuel-based technologies, various renewable energy sources, and a variety of energy storage technologies. An overview of the main fossil fuel-based as well as renewable-based energy resource technologies is depicted in Figure (3.1) (van Gerwen, 2006), which also indicates the typical sizes and applications of the various technologies. Figure (3.2) shows the overview of the various electrical energy storage technologies (IEC, 2011).

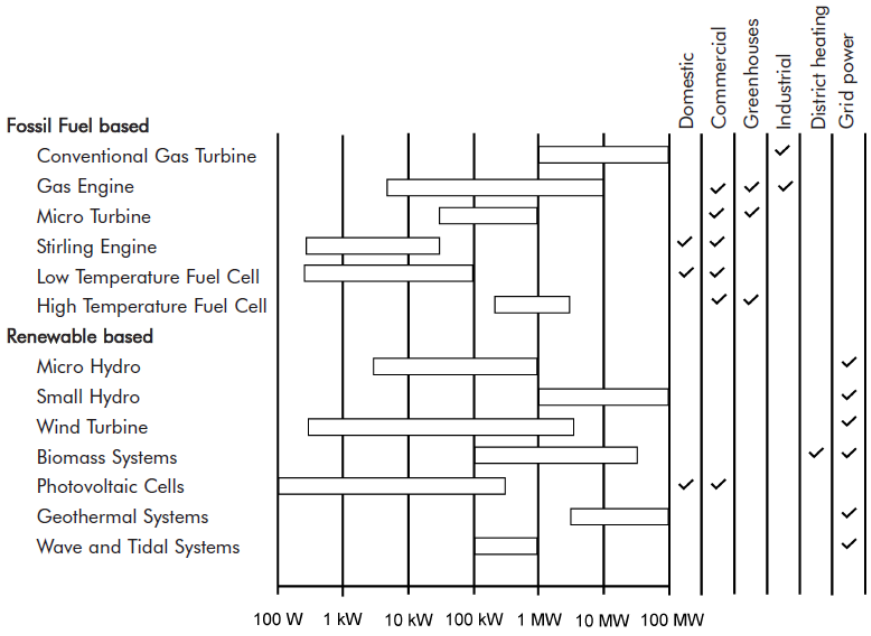


**Figure 3.1: Overview of fossil fuel- and renewable-based DER technologies. (Adapted from van Gerwen, 2006)**

The various elements making up this broad spectrum of DER technologies differ in characteristic behavior, scale (or size), typical applications, and the level of maturity of the technology, among other pertinent aspects. The intention of this chapter is no more than to provide a rough sketch of the various DER technologies as they relate to distributed power generation. Generally, the consideration of these technologies will be confined to a brief discussion of the principal of operation, and other aspects such as the characteristic behavior, level of maturity and typical applications.

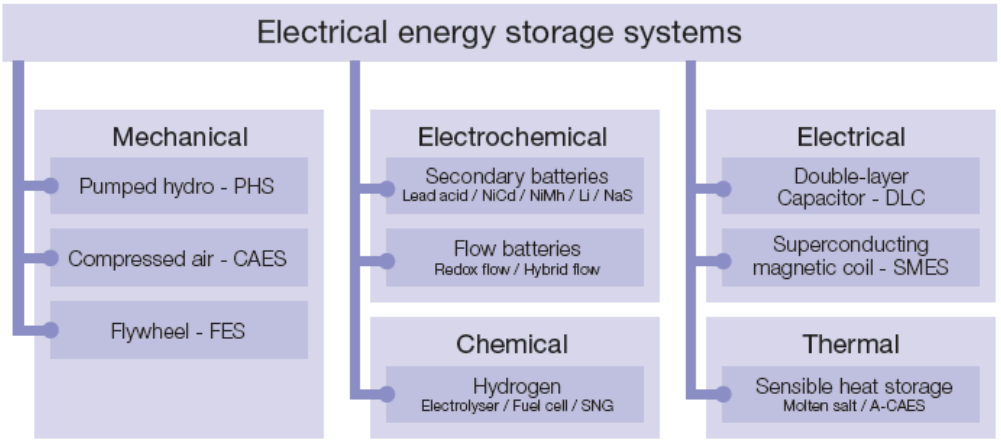


**Figure 3.2: Overview of electrical energy resource technologies. (Adapted from IEC, 2011)**

The discussion of the DER technologies begins with the fossil fuel-based ones in Section 3.2, followed by some renewable energy sources in Section 3.3, and is rounded up by the consideration of the energy storage technologies in Section 3.4.

Since it is typical to integrate a number of DER technologies into what are usually referred to as Hybrid Distributed Power Generation (HDPG) systems, some aspects of these hybrid systems are highlighted in Section 3.5. Section 3.6 concludes the chapter with a few main points about the information considered in the chapter.

## 3.2. Fossil fuel-based DER technologies

Fossil fuel-based DER technologies have been in use for a long time. They find a wide range of applications in residential, commercial and industrial sectors, which include (and by no means limited to) standby, back-up or base-load power, utility grid support, demand response peaking, Combined Heat and Power (CHP), customer peak shaving, and premium power supply (Goldstein *et al.*, 2003). Fossil fuel-based technologies are also quite mature. Some of the prominent ones that can be highlighted are *reciprocating engines, gas turbines, and combustion turbines*. *Fuel cells* are another DER technology of increasing importance in the DPG sector that is undergoing considerable development. They are classified as a non-renewable technology due to their extensive use of fossil fuels (IEA, 2002).

In the following subsections, some aspects of these fossil fuel-based technologies are considered. The consideration of these technologies for the various applications takes into account a variety of factors, such as the typical capacity, the capital and running costs, the required amount of maintenance, noise and emissions levels.

### 3.2.1. Reciprocating engines

Reciprocating engines are a widely used power generation technology, with the capacity ranging from a few kilowatts (small portable gensets) to larger industrial-scale multi-megawatt power generators. They use a variety of fuels, from natural gas, propane and gasoline (the spark ignition engines) to diesel or heavy oil (compression ignition engines) (Goldstein *et al.*, 2003).

The wide-spread use of reciprocating engines may be attributed to a number of their desirable characteristics, such as their low initial cost, fast start-up ability (desirable for standby and emergency power supply applications), good operating reliability (with proper maintenance), good load-following characteristics, and the wide size range, making their applicability versatile.

Reciprocating engines do have drawbacks as well, however, such as having relatively high noise levels, high emissions, and requiring quite costly regular maintenance (IEA, 2002: 27). Technological improvements for the reciprocating engines are mainly aimed at the enhancement of the combustion process by means of the suitable design and control of the engine system (Goldstein *et al.*, 2003).

### 3.2.2. Gas turbines

Gas turbines are a well-established power generation technology that was originally developed for jet engines. In terms of power generation for general applications, their size ranges from several hundred kilowatts up to around 50 megawatts.

Gas turbines use high-temperature, high-pressure gas as the fuel, part of the heat of which is converted directly to mechanical work to drive a turbine. A variety of petroleum fuels can also be used. High-temperature, high-pressure gas rushes out of the combustor and pushes against the turbine blades, causing them to rotate (CADER, 2012).

Gas turbines for power generation may be of the simple-cycle or combined-cycle type. The combined-cycle turbine improves the unit’s efficiency by making use of exhaust heat to drive a steam turbine that can generate electricity or drive a mechanical load. One important and desirable characteristic of the Gas turbines is the high-quality waste heat available in the high-temperature exhaust gas, which may effectively be used for generating high-pressure steam. Additionally, they incur very low maintenance costs, and technologies are available to minimize their emissions. These characteristics make them suitable for CHP applications, and they are in effect the preferred technology for large-scale industrial CHP applications (Goldstein *et al.*, 2003). They also find use in peaking power plants and emergency power applications (Resource Dynamics Corporation, 2005).

### 3.2.3. Microturbines

Microturbines are small combustion turbines, originally developed for transport applications (aircraft auxiliary power systems, diesel engine turbochargers, and automotive designs). Their capacity typically ranges from 30 kilowatts to around 300 kilowatts (Friedman, 2000).

In a typical Microturbine-based generation system, a high-speed turbine shaft (rotational speed of up to 120 000 rpm) drives a high-speed permanent-magnet generator, whose high-frequency output then has to be converted to the line-frequency level through the appropriate control of the Power Electronic interfaces (Goldstein *et al.*, 2003).

Microturbines have a number of desirable characteristics which have earned them significant interest for DPG applications. Among these are being of compact size and lightweight, allowing them to be used on-site close to the load, even in cases of space limitations; the opportunity to implement recuperation and cogeneration for improved efficiency; relatively low maintenance due to having only few moving parts (and thus also having relatively high reliability); relatively low emissions, also favouring their proximity to the load; and the opportunity they provide to use waste fuels such as landfill gas, (CADER, 2012; Resource Dynamics Corporation, 2005; El-Khattam & Salama, 2004; IEA, 2002).

Microturbines may be used in a broad range of applications, including base-load power, remote power supply, premium power, cogeneration, and peak shaving, among others. Technological developments are aimed at enhancing the efficiency, reliability, and commercial viability of the Microturbines (Friedman, 2000).

### 3.2.4. Fuel cells

Fuel cells generate direct current electricity by an electrochemical process that involves the oxidation of hydrogen in an electrolyte, accompanied by the production of heat and water as by-products. Having been invented in 1839, but found application only in niche areas due to cost and technology constraints, resurgence of interest in the fuel cell technology in recent decades has taken place in the wake of changing power supply requirements, supported by cost and efficiency improvements in the technology (Alternative Energy, 2014).

The hydrogen used in fuel cells is commonly (and most economically) derived from natural gas. Fuel cells may be distinguished by means of the (liquid or solid) electrolyte used, within which the chemical-to-electrical energy conversion process takes place. Some among these are Proton Exchange Membrane Fuel Cells (PEMFC), Phosphoric Acid Fuel Cells (PAFC), Molten Carbonate Fuel Cells (MCFC), and Sodium Oxide Fuel Cells (SOFC). These technologies differ both in characteristic performance and developmental stage (as regards commercial application).

The fuel cell technology is anticipated to play a significant role in the growing demand for high-quality, reliable power supply, as fuel cells are credited with the desirable characteristics of high efficiency and reliability, good maintainability, near-zero emission levels, and low noise, among others (Zuo & Zhang, 2012; IEA, 2002). Moreover, their modular nature makes them suitable for a wide range of applications of varying scale.

The fuel cell technology is at present a subject of extensive research and development, in view of the need to resolve the technological challenges that it presents, and especially to substantially reduce the current high capital costs required to implement the technology. The areas of application considered for the various technologies under research and development include stationary, portable, as well as transportation (IET, 2009).

## 3.3. Renewable-based DER technologies

The European directive on renewable energy-based electricity (2001) defines renewable sources as: "Renewable non-fossil energy sources (wind, solar, geothermal, wave, tidal, hydro-power, biomass, landfill gas, sewage treatment plant gas and biogases)". Globally, there is a drive to substantially increase the contribution of renewable sources to primary energy needs, as an attempt to minimize dependability on fossil fuels, which are considered to be both detrimental to the environment and unable to guarantee sustainable and secure energy supply.

In the following subsections, operational characteristics of some of the main renewable sources are briefly discussed.

### 3.3.1. Hydropower generation

Hydropower generation exploits the change in the potential energy of water falling through a certain height. It has been in use quite long, and can be classified as fairly mature technology (Jenkins *et al*., 2010). In the context of DER, small hydro is considered, taken to be the capacity of 10 MW or less (Peña & Medina, 2010). Small hydro systems employ simple and robust mechanisms, with compact, ready-to-install-and-operate electromechanical equipment based on simple hydraulic design and standard components, all in order to reduce costs and maintenance so as to assure profitability of investment (CIGRÉ, 2000). Small hydro generation compares very favorably with other renewable energy systems in terms of having high efficiency, predictability, capacity factor, and longevity of operation (Peña & Medina, 2010), but requires high capital costs and special geographical conditions. The quest to fully exploit it has increased nonetheless, in tandem with the growth in the distributed generation industry.

### 3.3.2. Wind Energy Conversion (WEC) systems

Wind Energy Conversion (WEC) systems capture some of the kinetic energy available in the intercepted wind, and convert it to electrical energy (CIGRE, 2000). The kinetic energy in an

airstream ( $E_w$ ) having an effective mass, $m_a$, and moving at a velocity, $v_w$, can be expressed by:

$$E_w = \frac{1}{2} m_a v_w^2 \tag{3.1}$$

The power in the airstream can be derived by considering the mass flow rate of the air ( $\dot{m}_a$ ) through a rotor disc having an area $A$ (Figure 3.3), as a function of the air density ( $\rho$ ) and the airstream velocity, which, according to fluid mechanical principles, is given by (Manuell *et al.*, 2002):

$$\dot{m}_a = \rho A v_w \tag{3.2}$$

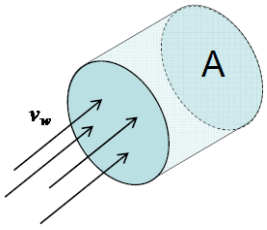


**Figure 3.3: Depiction of airstream flow (velocity $v_w$ ) across a rotor disc, area A. (Adapted from Kalmikov & Dykes, 2010)**

Substituting the airstream mass ( $m_a$ ) in Equation (3.1) by the mass flow rate expression given by Equation (3.2) provides the expression for the kinetic energy per-unit time, which is equivalent to the power in the airstream ( $P_w$ ), expressed by:

$$P_w = \frac{1}{2} \dot{m}_a v_w^2 = \frac{1}{2} \rho A v_w^3 \tag{3.3}$$

Equation (3.3) shows that the power available in the airstream (wind) is directly proportional to the air density, to the rotor swept area (or equivalently, to the square of the rotor blade diameter) and to the cube of the wind velocity. The main components of the WEC system are depicted in Figure (3.4), whose details are further discussed in Chapter 4, when the modeling of the system is considered.

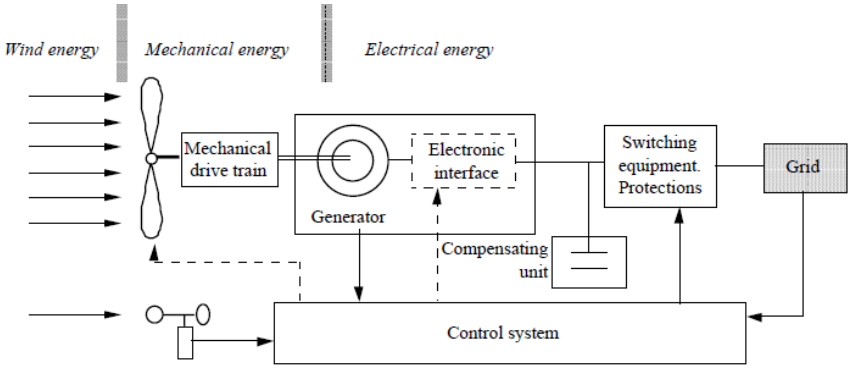


**Figure 3.4: Generic configuration of a Wind Energy Conversion system. (Adapted from CIGRE, 2000)**

Due to the abundance of the wind resource and the technological advances that have been made in wind energy systems in recent decades, wind energy today forms a very significant part of the alternative energy industry, and contributes considerably to new generation capacity. Its importance continues to grow, as utilities and national governments strive to diversify primary energy sources and reduce generation-related emissions, among other reasons (GWEC, 2012). Greatest growth has been experienced in utility-scale onshore systems, but even offshore and small wind turbine systems are enjoying considerable market growth.

Research and development efforts are aimed at decreasing the levelized cost of wind energy systems, encompassing all facets of wind energy systems such as wind turbine technology, advanced control and condition monitoring, grid integration, and operation and maintenance (IEA Wind, 2013).

### 3.3.3. Photovoltaic (PV) generation systems

Photovoltaic (PV) generation systems make use of semi-conductor (solar) cells to generate direct-current power by means of a phenomenon known as the *Photovoltaic Effect*, when the cell is exposed to light energy. The PV effect sets up an electric field across the solar cell's pn-junction, as the photon energy of the incident light is transferred to the junction's charge carriers, creating an electric potential that can drive a DC current in an external circuit connected to the junction terminals (Patel, 2006).

Having initially been developed for space station applications, PV technology had until recently not received much consideration for wide-spread application, chiefly due to cost and technology constraints. Today PV technology can be considered to be at the forefront of the emerging alternative energy sector, and this mainly owing to the favorable policy developments and technological advancements that have greatly contributed to performance improvements and dramatic system cost reductions, thus engendering investment and further development (Labouret & Villoz, 2010). Although the cost of PV energy systems remains comparatively higher, making them more suitable for remote stand-alone applications, there is significant growth in utility-scale grid-connected systems and other applications. Development efforts remain focused on energy conversion efficiency improvement as well as reduction of cost per installed capacity (mainly by research on and development of lower-cost modules), both of which highly affect the cost per kWh of PV energy.

### 3.3.4. Biomass

Biomass encompasses a variety of organic and plant matter whose stored energy (produced by means of photosynthesis) can be exploited. It has been used very long in its traditional form (burning of wood), and continues to be a significant energy source for heating and cooking, especially in developing countries. Prime sources of bio-energy are biomass residues,

dedicated energy crops, as well as organic municipal solid waste (CIGRÉ, 2000). A broad range of bio-energy technologies at different levels of maturity have been developed to exploit the various bio-energy sources for the production of electricity, heat, gaseous, liquid and solid fuels. Biomass is considered to form a significant part of the alternative energy sources mix, despite other issues associated with its exploitation, such as land use for energy crops against food production (Alternative energy, 2014).

### 3.3.5. Geothermal energy

Geothermal energy utilizes the accessible thermal energy from the earth's interior, which is usually drawn by means of wells in the form of steam or hot water, and can then be used to drive a turbine-generator system for electricity production, or for heat supply. Although not self-replenishing, and therefore not renewable in a full sense, geothermal energy is counted among renewable sources due to the fact that it is a natural energy flow (CIGRÉ, 2000). Its exploitation is limited to a few locations that have sufficient concentrations of geothermal energy, and geothermal power plants are usually large-capacity systems (Alternative energy, 2014).

### 3.3.6. Marine energy

Marine energy can be thermal or mechanical (tidal and wave energy), and both types can be used for electricity production, using various technologies that are presently at different levels of development. Marine energy systems tend to be large in size, limited to few locations that have sufficient resource for economical operation, and technical issues such as intermittence (for wave and tidal) as well as siting issues that take ecological impact considerations into account need to be considered (House of Commons, 2008).

## 3.4. Energy storage technologies

Electrical Energy Storage (EES) as a component of the electric power system has always played a vital role in electricity cost reduction, power supply reliability improvement as well as power quality enhancement (IEC, 2011; Price, 2000). With the expected growth of the share of grid-integrated renewable energy, utility-scale EES systems are anticipated to play an increasingly greater role in ensuring the reliable operation of the power system. Likewise for DPG systems, which usually incorporate a significant portion of intermittent renewable sources with generation profiles defined by weather fluctuations, EES is needed to augment the energy supply from these stochastic sources during low-generation periods, thus helping with generation profile smoothening, which improves both the quality and reliability of power supply.

There is quite a wide range of EES technologies, as has been depicted in Figure (3.2). In the following subsections, the main characteristics of the EES technologies as categorized in Figure (3.2) are briefly discussed.

### 3.4.1. Mechanical energy storage

Mechanical energy storage systems normally store energy by using off-peak power to store potential energy in a body of water at a higher reservoir (in the case of pumped hydro), pneumatic energy in Compressed-Air Energy Storage (CAES), and kinetic energy in a rotating mass (flywheel). These are usually large-scale storage systems, with applications ranging from power quality intervention for short durations (Flywheel) to bulk storage for time-shifting and supply reserve (CAES; pumped storage).

### 3.4.2. Electrochemical energy

Electrochemical energy storage systems are very widely used in a range of storage applications that encompass utility scale for power quality purposes as well as minute scale portable applications. Many technologies have also been developed over the years to cater for various applications, and battery storage technology is a highly researched field, with the research focus being on enhancing the many performance characteristics that improve the economy of electrical energy storage.

With their very favorable cost-to-performance ratio, *Lead-acid* batteries enjoy a considerably much wider application than any other battery technology in many areas of application, despite their low energy density and the hazardous nature of Lead. Relatively newer technologies such as *Lithium-ion* and Nickel-based (*Nickel Metal Hydride & Nickel Cadmium*) batteries are preferred in mobile applications however, which demand high energy-to-weight ratios, efficiencies and life cycles, among other factors. Lithium-ion batteries have especially become important in mobile applications on account of their high energy density, cell voltage, efficiency, and life cycles, and are highly considered for application in transportation (electric vehicles), and even large-scale energy management, despite their currently high cost (EPRI, 2010).

Other battery technologies of interest for power management, particularly in view of large-scale system development, are *Metal-air (Me-air), Sodium sulphur (NaS), Sodium Nickel Chloride (NaNiCl), and Flow batteries*.

### 3.4.3. Chemical energy storage

The chemical energy storage technologies considered for electricity generation are Hydrogen and Synthetic Natural Gas (SNG), produced by the electrical processes of electrolysis and methanation (the production of methane by the reaction of hydrogen and carbon dioxide) respectively. Despite having relatively low efficiencies, these storage technologies may be

favorable for providing practically unlimited storage for large amounts of off-peak grid electricity or generation from renewable sources when it cannot all be fed to the grid (IEC, 2011).

On-going research on the commercial application of chemical storage aims at improving the AC-AC efficiency so as to enhance their economic viability.

### 3.4.4. Electrical energy storage

Electrical energy storage technologies possess many desirable high-performance characteristics not inherent to the electrochemical ones. The *Double-Layer Capacitor super-capacitor (DLC)*, which falls somewhere between conventional capacitors and batteries, is a prime candidate for applications requiring very fast-response, high power density storage, with other features such as very long, robust operation in diverse environmental conditions, environmental friendliness, and high efficiency, plus requiring little to no maintenance. On the other hand, its low energy density and high self-discharge rate deters its use for long-term storage applications. *Superconducting Magnetic Energy Storage (SMES)* is also an electrical storage technology very suitable for power quality applications with its almost instantaneous response, being able to provide very high short-term power at high roundtrip efficiency. And with research enabling the production of higher-critical-temperature superconducting coils, SMES systems may see a wider range of applications in future energy storage requirements (Patel, 2006; DeWinkel & Lamopree, 1997). The main drawback of the SMES technology is the crucial dependence of the system's reliable operation on the cooling system.

With such a wide range of technologies with diverse characteristics, it is evident that the intended application heavily weighs on the selection of the appropriate technology. For DPG systems, which are the subject of this study, the objective of selecting the storage technology to be used is not made any easier by the requirement to achieve maximum possible reliable supply at minimum possible cost, two significantly conflicting objectives. Figure (3.6) roughly portrays the classification of the various energy storage technologies, considering typical sizes, applications as well as discharge rates (a measure of the specific energy capacity).

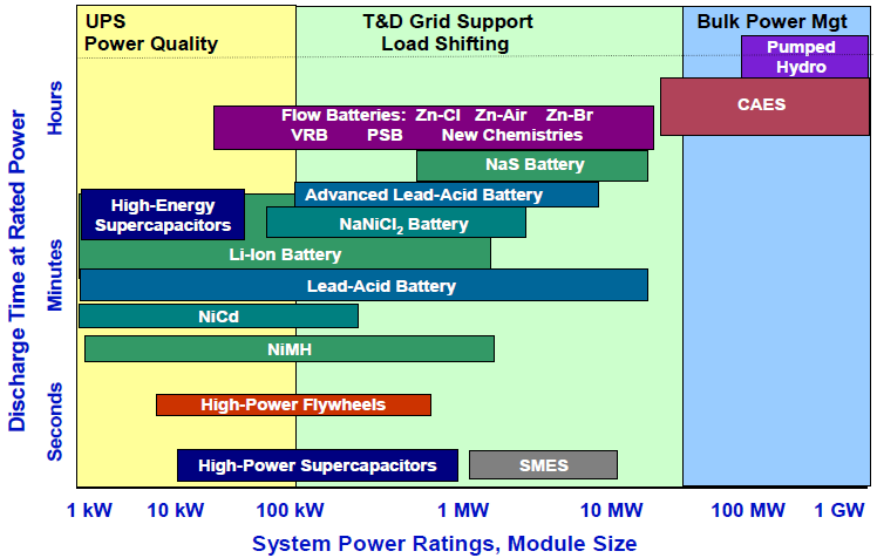


**Figure 3.5:** **Size and discharge characteristics of various EES technologies. (Adapted from EPRI, 2010)**

## 3.5. Hybrid Distributed Power Generation (HDPG) systems

Hybrid Distributed Power Generation (HDPG) systems are a subclass of Distributed Power Generation (DPG) systems that integrate one or more primary energy sources (often with energy storage) for electric power generation. They have always played a vital role in remote electric power supply, as stand-alone power systems in locations where grid power is unavailable for economic or other reasons, where they are usually comprised of an engine-based generator as the primary energy source, with the possibility of other sources and/or storage in parallel (Patel, 2006; Wichert, 1997).

With the current trend towards a greater share of renewable power generation, HDPG systems based on renewable resources are gaining greater importance as an effective vehicle for increased renewable energy harvesting, as they usually allow taking advantage of the complementary nature of the characteristics of many of the renewable sources to provide more reliable power supply than would be achieved from systems made up of the individual sources (Nehrir *et al.*, 2011; Omari *et al.*, 2007; Wang, 2006; Salameh & Davis, 2003). Over the decades since the interest in DPG experienced revival, a variety of HDPG systems with different combinations of primary energy sources and storage have been developed. Although the focus of many studies is often on stand-alone systems for remote area power supply (usually in rural areas), another emerging application for these systems is the grid-integration of the HDPG systems in urban areas, which may serve the purpose of power quality or power supply reliability improvement, or simply provide a platform for renewable energy harvesting. Some of the benefits of such systems applied to urban areas are (Servansing *et al.*, 2012; Salameh & Davis, 2003):

- their modularity and small-scale nature favors their application, in view of the high cost of land, and provides transmission and distribution reinforcement;

- close proximity to the load permits their participation in demand-side management and reduces power distribution losses, contributing to the carbon footprint reduction;
- they contribute to reduced dependence on fossil fuel-based power, which at times has to be transmitted over very long distances; and
- they represent a sustainable and ecologically friendly form of meeting the growing energy demand.

With the potential benefits of this subclass of DPG systems, there is certainly a significant need for more research into urban grid-interactive HDPG systems. Despite the many existing technical and economical hindrances to the widespread implementation of such systems, history has shown that the right human input, in the way of technological advancements, favorable policies and incentives, and social paradigm change, among other factors, can propel the development of these systems in the desired direction (Hirsh *et al.*, 2005).

In the following subsections, some aspects of the design and operation of HDPG systems, such as common configurations, connectivity to the electric grid, and the design and operational requirements, are briefly discussed.

### 3.5.1. Common configurations for HDPG systems

The composition of a HDPG system is usually determined by resource availability and load requirements. A lot of systems, especially those aimed at the exploitation of renewable resources in locations whose weather conditions are favorable, usually comprise of wind and/or Photovoltaic (PV) power generation in combination with a host of other primary energy sources, such as diesel generators, Fuel Cells, micro-hydro power, Microturbines, and a number of energy storage technologies (Wang, 2006).

Depending on how the various components of the HDPG system are integrated, it can be referred to as an *AC-coupled*, a *DC-coupled* or a *hybrid AC/DC-coupled* HDPG system (Servansing *et al.*, 2012; Wang *et al.*, 2010; Strauss & Engler, 2003). The choice of the configuration may take into account the available resources and the intended application, and certainly has a bearing on the operational strategy used for the system. The three typical configurations are depicted in Figures (3.6)-(3.8).

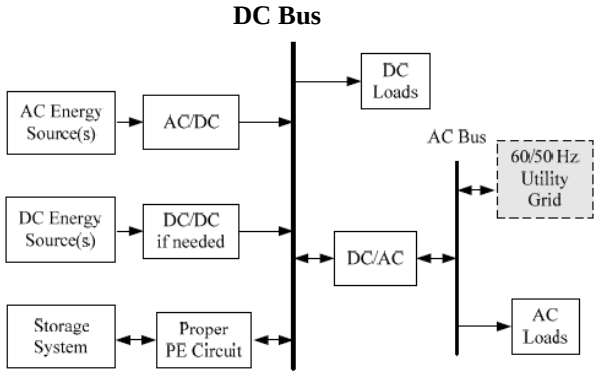


**Figure 3.6:** DC-coupled HDPG system block diagram. (Adapted from Wang, 2006)

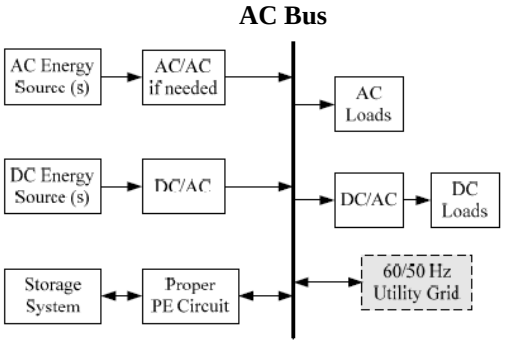


**Figure 3.7:** AC-coupled HDPG system block diagram. (Adapted from Wang, 2006)

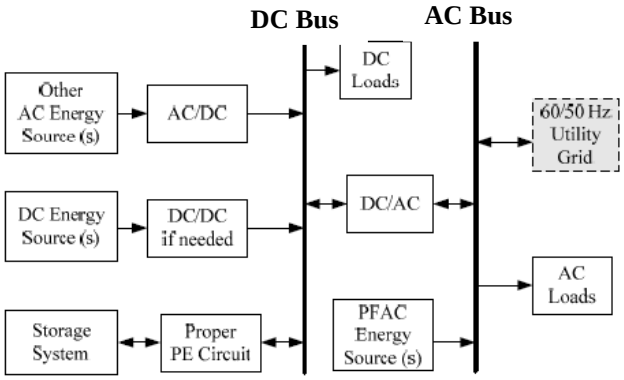


**Figure 3.8:** Hybrid DC/AC-coupled HDPG system block diagram. (Adapted from Wang, 2006)

Both technical as well as economic factors distinguish the three integration methods of HDPG systems. Some of the important characteristics taken into account are *modularity* (which influences *extensibility*), *component count*, *system reliability* (based on single point of failure), *voltage magnitude* and *frequency compatibility*, and the *complexity of coordinated control*. Since HDPG systems usually bring together units of varying characteristics, intermittent sources among them, achieving a properly integrated system that is able to provide reliable power to the load is always a complex, multi-objective optimization problem. The intended application weighs considerably on the optimization parameters that are prioritized, the chosen

topology, and the operational strategy. This notwithstanding, cost minimization and supply availability are integral components of all HDPG system optimization objective functions.

### 3.5.2. Connectivity of the HDPG system to the grid

A HDPG can operate autonomously or it can be grid-interactive. Connectivity to the electric grid is an important distinguishing factor for the HDPG systems because it affects both their design as well as operational philosophy to a significant degree.

An **autonomous HDPG system** operates in isolation (from the grid), and is thus required to regulate its own system voltage magnitude and frequency, which have to be kept within acceptable bands around the nominal values to assure proper operation of the system. Additionally, generation from the system's primary energy sources and/or storage has to exactly match the load demand, the failure of which leads to power imbalance in the system, with consequent power quality deterioration, and possibly even the failure of the HDPG system to successfully operate autonomously. In this configuration, the system is usually considered to be a micro-grid (*i.e.* a miniature electric grid), made up of generation, local loads and the energy storage that may aid the generation profile to meet the load profile (Mauri *et al.*, 2011; Lasseter, 2002). Autonomous HDPG systems normally serve as remote area power supply systems. In this role, it is desirable that they have minimal dependence on fossil fuels (for both cost and logistical reasons), be robust and require minimal specialized maintenance, and achieve a favorable Levelized system Cost Of Energy (LCOE). These are evidently conflicting objectives that are difficult to simultaneously satisfy, and tradeoffs are inevitable (Sharma & Agarwal, 2008; Ding & Buckeridge, 2000; Wichert, 1997).

A **grid-connected HDPG system**, in contrast with its autonomous counterpart, is supposed to be so operated that it follows the grid-imposed voltage magnitude and frequency. The focus for the HDPG system in this case shifts from self-sustenance to grid support with minimal adverse impact on grid operations, both in the steady-state and dynamic modes of grid operation. The operational and power quality requirements that have to be met by the grid-interactive HDPG systems makes their control and energy management significantly more complex than the autonomous systems (Servansing *et al.*, 2012).

### 3.5.3. Requirements for renewable source-based HDPG systems

#### 3.5.3.1. Design requirements

Design requirements for renewable-based HDPG systems are normally dictated by the need to realize the best available techno-economic balance for the intended application of the system. Since renewable generation is still relatively much costlier than conventional generation, optimal sizing of the generation and storage components constitutes a very important initial step in system design, and many methods exist for this system planning function, as reported

in literature (Luna-Rubio *et al.*, 2012). Optimal sizing invariably requires the availability of relevant data on load profile, geographic information for assessing the site's weather resource, and financial data, among others.

#### 3.5.3.2. Operational requirements

Operational requirements for HDPG systems, on the other hand, depend to a significant extent on whether the system is autonomous or grid-integrated, because the control and operational objectives are different for the system in the two configurations.

Grid-integrated HDPG systems are generally required to:

- operate in current-control mode, injecting low-distortion, high-quality current into the grid;
- follow grid voltage and maintain magnitude and frequency synchronicity while operating in grid-tie mode; and
- have fast control for disconnection from the grid upon loss of grid supply.

Autonomous HDPG systems must:

- be able to regulate the system voltage magnitude and frequency, to maintain it within the nominal values stipulated by power quality standards;
- achieve (ideally) exact generation-load demand balance and have energy storage sufficient for generation profile smoothening;
- have supervisory control to oversee system power flow and energy storage management, which is a very key component of stand-alone DPG systems; and
- have a proper load management strategy, with the possibility of load prioritization and non-critical load shedding, in cases of insufficient generation to meet the entire system load.

## 3.6. Conclusion

This chapter has discussed the various aspects related to Distributed Power Generation (DPG) systems, highlighting their growing share in meeting the present and future energy requirements, and then looking at the Distributed Energy Resource (DER) technologies commonly implemented in DPG systems.

HDPG systems, which represent an important subclass of DPG systems with a high potential for maximizing renewable energy harvesting, have also been discussed in terms of the commonly used topologies, integration configurations, as well as design and operational requirements.

Having covered an overview of the noteworthy DER technologies that form the basis for DPG in this chapter, attention in the following chapter is turned to the modeling of the distributed generation sources and the design of controllers to derive the maximum available power from them. Photovoltaic (PV) and Wind Energy Conversion (WEC) systems are the ones considered for this modeling and controller design analysis, as two of the most significant renewable energy sources.

# Chapter 4

# MODELING AND MAXIMUM POWER POINT TRACKING (MPPT) CONTROL OF PHOTOVOLTAIC AND WIND ENERGY CONVERSION SYSTEMS

## 4.1. Introduction

Mathematical models are often needed to facilitate the analysis of real dynamical systems, and are required to incorporate as much of the phenomena having a bearing upon the dynamical system's behavior as is reasonably possible (taking into account practical aspects and the level of complexity), and to an adequate degree of accuracy (Ogata, 2004). In the analysis of Distributed Power Generation (DPG) systems, models of the primary energy sources play a key role, both for the energy yield characterization and for the controller design to maximize the energy yield.

Thus in this chapter, the main characteristics of Photovoltaic (PV) and Wind Energy Conversion (WEC) systems are discussed, and their mathematical models suitable for use in computer simulations oriented towards energy yield analysis and controller design are developed. These models would then facilitate the study and analysis of the grid-integration of renewable-based DPG systems, as considered in this thesis.

The discussion begins with the consideration of the PV energy generation system in Section 4.2, where, after outlining the physical principles that form the basis for the PV energy conversion, the mathematical model of the PV generator is developed, followed by the consideration of the Maximum Power Point Tracking (MPPT) control of the PV energy generation system. The WEC system is discussed in Section 4.3, which also covers the main operational characteristics of wind power generation, the modeling of the WEC subsystems, as well as a simulation case study focused on the analysis of the maximum-power extraction operation of a small-scale wind power generation system. Section 4.4 concludes the chapter with a highlight of the main results from the chapter.

## 4.2. Photovoltaic energy conversion

Photovoltaic (PV) energy conversion is a practical application of the photo-electric effect discovered by the German Physicist Heinrich Rudolf Hertz in 1887, which essentially constitutes the release of electrically charged particles from a material following the absorption of electromagnetic radiation of sufficient frequency (Encyclopaedia Britannica Online, 2014; Di Piazza & Vitale, 2013). Typically, a solar cell, the basic building block of the PV energy generator, is a large-surface p-n junction-based device, which is formed from two oppositely doped semiconductor devices. As a photovoltaic device, the electrical behavior of the solar cell is explained in terms of its voltage and current characteristics when it is exposed

to radiant energy (particularly solar irradiance), and on the basis of semi-conductor theory as well as quantum physics (Hersch & Zweibel, 1982).

The microscopic-level processes occurring in the solar cell's p-n junction, which enable the conversion of the radiant energy falling on the solar cell into electrical energy, are theorized on the basis of quantum physics. These processes include (1) photon *absorption* from the incident light, (2) charge carrier *generation*, and then (3) *diffusion* and (4) *migration* under the influence of the p-n junction's built-in electric field (Green, 2002). These processes induce an electric potential across the cell, and enable it to drive a direct current through a closed circuit across its terminals. The processes are illustrated in Figure (4.1). According to Green (2002), there are effectively four prerequisites for the taking place of PV energy conversion: (1) the excitement of an electron from the valence band to the conduction band by a photon of sufficiently high frequency; (2) the replenishment, by some means, of the vacated electron in the valence band; (3) the transportation of the electron to the negative contact of the junction; and (4) the maintenance of the separation between the junction's negative and positive contacts. Solar cells are so designed as to enhance these microscopic processes with a view to maximizing the photo-generated current and the induced electrical potential, both of which determine the output power of the device.

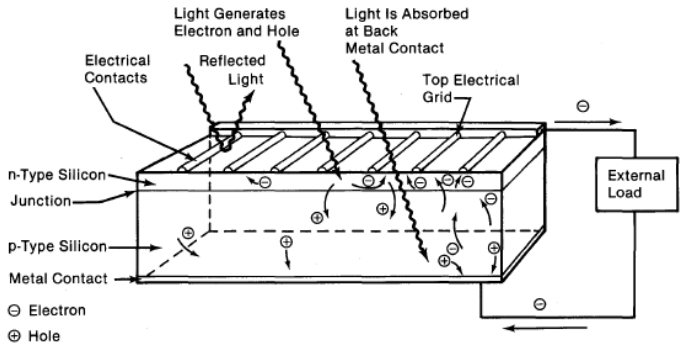


**Figure 4.1: Microscopic-level processes in a pn-junction solar cell exposed to radiant energy (Adapted from Hersch & Zweibel, 1982)**

As discussed in Section (4.2.1), the analysis of the PV energy generation system takes a macroscopic view of the energy conversion process (as opposed to the microscopic one, referred to above), and looks at the terminal characteristics of the cell (voltage, current and power) subject to given irradiance and temperature conditions. The solar cell's microscopic view and the quantum theory used to analyze it are nonetheless highlighted here because they form the basis for the PV model used in the macroscopic-level analysis and design (Di Piazza & Vitale, 2013).

It is also worth mentioning that PV energy conversion analysis is traditionally based on the crystalline silicon p-n junction (Hersch & Zweibel, 1982). This may partly be explained by the fact that crystalline silicon formed the basis for the initial practical realization of solar cells,

and it continues to be the leading PV raw material for commercial applications. Nonetheless, the quest to significantly decrease the cost of PV-based electricity has spurred intensive research in the field of photovoltaics, giving rise to new PV technologies such as thin-film (e.g. Amorphous Silicon, Copper Indium Diselenide and Cadmium Telluride), and dye-sensitized organic cells. Though at the expense of lower efficiency, these alternative solutions for PV raw material are less costly, and consequently they enhance the economic viability of PV-based electricity. Significant research also goes into multi-junction solar cells, which combine two or more single-junction cells of different band gaps into a single unit in order to exploit a greater energy spectrum of the incident radiation, thus considerably improving the device's efficiency (Hersch & Zweibel, 1982).

A solar cell typically produces a few watts of power at a terminal voltage of roughly 0.6 volt. For power generation applications, therefore, it is essential to have a series-parallel arrangement of cells into what is commonly referred to as a PV module, the number of cells and the configuration depending on the desired voltage, current and power ratings of the module. An array of series-parallel connected modules can in turn be put together to achieve the desired PV system output, as depicted in Figure (4.2).

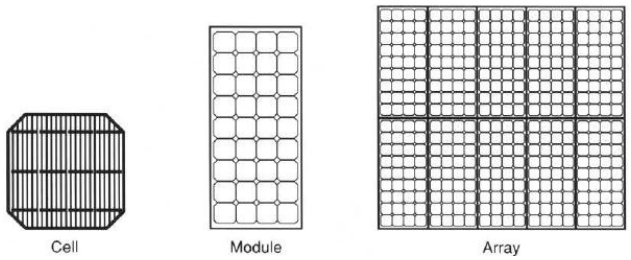


**Figure 4.2: A PV cell, module and array (Adapted from Hersch & Zweibel, 1982)**

### 4.2.1. PV system modeling

The mathematical model of the PV cell serves as the main component for the analysis and characterization of the PV energy conversion system in terms of current, voltage and power outputs, as well as the energy yield over a given period of time. The cell is most commonly modeled as an idealized irradiance-dependent current generator in parallel with diodes that represent the p-n junction nature of the device, together with parasitic resistances, as illustrated in Figure (4.3). According to Di Piazza and Vitale (2013), this double-diode model of the PV cell, with its representation of such microscopic-level processes as space-charge recombination by means of the second diode, is taken to be representative of the most accurate PV model, and is especially useful for cell manufacturing-oriented analyses. From the review of the literature available on PV modeling, however, there is generally good agreement that the single-diode model (Figure 4.4) suffices for representing the electrical characteristics of

the PV cell (Villalva *et al.*, 2009; Sera *et al.*, 2007; Xiao *et al.*, 2004; Walker, 2001; Lorenzo, 1994).

**Table 4.1: List of symbols used in the definition of the PV energy conversion system**

| Symbol[1] | Definition | Symbol | Definition |
|---|---|---|---|
| $I_{ph}$ (ref) [A] | Photo-generated current | G (ref) [W/m$^2$] | Solar irradiance |
| $I_{sc}$ (ref) | Short-circuit current | $T_a$ [$^o$C] | Ambient temperature |
| $I_o$ (ref) | Diode saturation current | $T_c$ (ref) | Cell temperature |
| $I_{D1,2}$ | Diode current | $\alpha_{SC}$ [A/$^o$C] | $I_{sc}$ temperature coefficient |
| $I_{mpp}$ (ref) | Cell current at MPP | $\beta_{OC}$ [V/$^o$C] | $V_{oc}$ temperature coefficient |
| $I_{pv}$ | Cell output current | q [C] | Electron charge |
| $V_{oc}$ (ref) [V] | Open-circuit voltage | k [J/$^o$K] | Boltzmann's constant |
| $V_{mpp}$ (ref) | Cell voltage at MPP | $n_{id}$ | Diode ideality factor |
| $V_{pv}$ | Cell output voltage | $R_s$ [Ω] | Cell series resistance |
| $V_t$ (ref) | Cell junction thermal voltage | $R_p$ | Cell parallel resistance |
| $P_{mpp}$ (ref) [W] | Cell output power at MPP | $N_s$ | Number of series-connected cells |
| $P_{pv}$ | Cell output power | $N_p$ | Number of parallel-connected cells |
| $I_P$ [A] | Shunt leakage current | | |

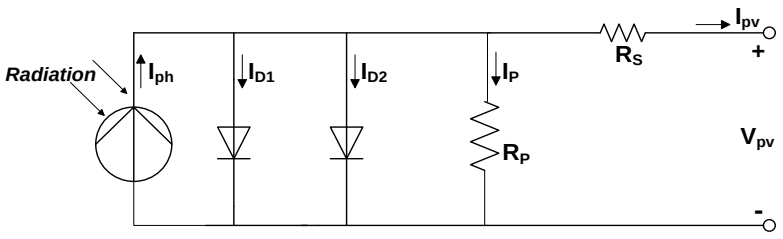


**Figure 4.3: PV cell double-diode model (Adapted from Gow & Manning, 1999)**

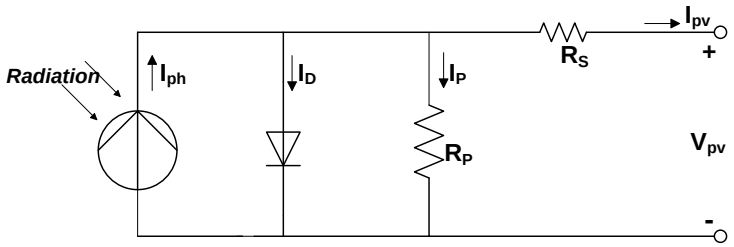


**Figure 4.4: PV cell single-diode, five-parameter model**

Based on the single-diode, five-parameter representation of the solar cell (Figure 4.4), and using the mathematical symbols listed in Table (4.1), the mathematical expressions of the PV cell can be derived as:

$$I_{pv} = I_{ph} - I_D - I_P \tag{4.1}$$

$$I_D = I_o \cdot (exp^{\frac{V_{pv}+I_{pv}R_s}{V_t}} - 1) \tag{4.2}$$

[1] Symbols listed with (*ref*) imply that values of the quantities at standard test conditions (STC) also apply.

$$I_p = \frac{V_{pv} + I_{pv}R_s}{R_p} \tag{4.3}$$

$$V_t = \frac{n_{id}kT}{q} \tag{4.4}$$

$$I_{pv} = I_{ph} - I_o \cdot (exp^{\frac{V_{pv}+I_{pv}R_s}{V_t}} - 1) - \frac{V_{pv} + I_{pv}R_s}{R_p} \tag{4.5}$$

Equation (4.1) expresses the PV cell's output current in terms of the photo-generated current ( $I_{ph}$), the diode current ($I_D$), and the shunt leakage current ($I_p$), represented by the path to ground through the cell's shunt resistance. The relation between the cell's output current and voltage can be deduced once the branch currents are replaced by their respective expressions given by Equations (4.2)-(4.4), which leads to Equation (4.5). The solution of Equation (4.5) requires the determination of a number of parameters, particularly the *photo-generated current (*$I_{ph}$*), diode saturation current* $I_o$*), diode ideality (*$n_{id}$) *factor*, and the *parasitic resistances* ( $R_s$, $R_p$). These parameters are normally not provided by PV module manufacturers, and therefore require determination by some means. Analytical, numerical as well as heuristic methods have been applied in PV model parameter determination, based on the literature reviewed on the topic. All these techniques employ measured experimental data and/or data provided by PV module manufacturers. There has been growing interest in improved numerical methods for PV model parameter estimation based entirely on the PV manufacturer data, as these often prove to be more convenient and cost-effective means for PV model development. However, it necessitates model simplifications that may cause significant deviation of the derived model from the real PV characteristics (Di Piazza & Vitale, 2013). A sufficiently accurate model may still be obtained by the incorporation of the temperature and irradiance dependencies of some of the parameters. In this thesis, the numerical method for PV model parameter estimation is used.

In the manner similar to that proposed by Sera *et al* (2007), PV model parameters may be determined using the PV cell characteristic's salient point data (short-circuit, open-circuit & Maximum Power Point (MPP)), which are available from PV module manufacturer datasheets. Equation (4.5) written at the salient points leads to the following three expressions (with the simplification for Equations (4.6)-(4.8) that the "-1" in the bracketed term of Equation (4.5) has been neglected due to its insignificance in comparison with the exponential term (Sera et al., 2007).

When the PV cell is short-circuited (hence $V_{pv} = 0$ & $I_{pv} = I_{sc}$), Equation (4.5) can be redefined as:

$$I_{sc} = I_{ph} - I_o \cdot exp^{\frac{I_{sc}R_s}{V_t}} - \frac{I_{sc}R_s}{R_p} \tag{4.6}$$

When the PV cell is open-circuited (hence $V_{pv} = V_{oc}$ & $I_{pv} = 0$), Equation (4.5) can again be redefined as:

$$I_{ph} = I_o \cdot exp^{\frac{V_{oc}}{V_t}} + \frac{V_{oc}}{R_p} \tag{4.7}$$

At the MPP (when $V_{pv} = V_{mpp}$ & $I_{pv} = I_{mpp}$), Equation (4.5) can be written as:

$$I_{mpp} = I_{ph} - I_o \cdot (exp^{\frac{V_{mpp}+I_{mpp}R_s}{V_t}} - 1) - \frac{V_{mpp} + I_{mpp}R_s}{R_p} \tag{4.8}$$

Combining Equations (4.6) and (4.7) and noting that ($exp^{V_{oc}/V_t} >> exp^{I_{sc}R_s/V_t}$), the expression for the short-circuit current is derived as:

$$\begin{aligned} I_{sc} &= I_o(exp^{\frac{V_{oc}}{V_t}} + exp^{\frac{I_{sc}R_s}{V_t}}) + \frac{V_{oc}}{R_p} - \frac{I_{sc}R_s}{R_p} \\ &\cong I_o\, exp^{\frac{V_{oc}}{V_t}} + \frac{V_{oc} - I_{sc}R_s}{R_p} \end{aligned} \tag{4.9}$$

From Equation (4.9), the expression for the saturation current ($I_o$) is obtained as:

$$I_o = (I_{sc} - \frac{V_{oc} - I_{sc}R_s}{R_p}) exp^{-\frac{V_{oc}}{V_t}} \tag{4.10}$$

When Equations (4.7) and (4.10) are substituted into Equation (4.8) and normalized, the expression for the PV module current at the Maximum-Power Point (MPP) is obtained:

$$I_{mpp} = I_{sc} - \frac{V_{mpp} + (I_{mpp} - I_{sc})R_s}{R_p} - (I_{sc} - \frac{V_{oc} - I_{sc}R_s}{R_p}) \cdot exp^{\frac{V_{mpp} - V_{oc} + I_{mpp}R_s}{V_t}} \tag{4.11}$$

Equation (4.11) has three (unknown) variables to be determined: the series and shunt resistances ($R_s$ ; $R_p$), and the diode ideality factor ($n_{id}$), which is part of the expression for the cell junction thermal voltage ($V_t$), according to Equation 4.4). One more expression can be derived by considering the conditions at the MPP on the PV cell's characteristic, at which point the derivative of the power with respect to the voltage is zero. By multiplying Equation (4.11) with the voltage value at the MPP, differentiating it with respect to the voltage and equating to zero, the following expression is derived (since the shunt resistance is normally much larger than the series resistance, without much loss of accuracy the simplifying assumption is made that: $R_p/(R_p + R_s) \approx 1$):

$$\frac{dP_{mpp}}{dV_{mpp}} = \frac{d}{dV_{mpp}}(V_{mpp}I_{mpp})$$

$$= \frac{d}{dV_{mpp}}[\frac{R_p}{R_p+R_s}(V_{mpp}I_{sc} - \frac{{V_{mpp}}^2 - V_{mpp}I_{sc}R_s}{R_p} - (I_{sc} - \frac{V_{oc}-I_{sc}R_s}{R_p}) \times V_{mpp} \cdot exp^{\frac{V_{mpp}-V_{oc}+I_{mpp}R_s}{V_t}}]$$

$$= I_{sc} - \frac{2V_{mpp}-I_{sc}R_s}{R_p} - (I_{sc} - \frac{V_{oc}-I_{sc}R_s}{R_p}) \cdot (1+\frac{V_{mpp}}{V_t}) \cdot exp^{\frac{V_{mpp}-V_{oc}+I_{mpp}R_s}{V_t}} \quad (4.12)$$

In Equations (4.11) and (4.12), only $R_s$, $R_p$ and $n_{id}$ (as part of $V_t$) are unknown. The diode ideality factor is an empirical curve-fitting parameter that is often used in the single-diode model to approximate the combined effect of the double-diode representation, with a value typically in the range between 1 and 2. A value of 1.3 is usually considered to be a good approximation for crystalline silicon cells (Castañer & Markvart, 2003; Lorenzo, 1994). Thus, the above two expressions can be solved numerically for the determination of $R_p$ and $R_s$. The Newton-Raphson method for the solution of nonlinear equations, formulated in Matlab, has been applied for this problem to estimate the values of the two parasitic resistances, and is made part of the initialization process for the PV module implemented in Simulink (Appendix C.1).

Because PV module data from manufacturers are obtained at standard test conditions, the irradiance and thermal dependencies of the model parameters also have to be incorporated into the final solution of the model. The most significant dependencies are those of the cell temperature on the ambient temperature, and the irradiance, as well as of the cell temperature and irradiance effect on the open-circuit voltage and short-circuit current. The following relations are commonly applied (Castañer & Markvart, 2003):

$$T_c = T_a + C_2 G \quad (4.13a)$$

$$C_2 = \frac{NCOT - 20}{800 Wm^{-2}} \quad (4.13b)$$

$$I_{sc} = I_{scref} \cdot (1+\alpha_{sc}\Delta T_c) \cdot \frac{G}{G_{ref}} \quad (4.14)$$

$$V_{oc} = V_{ocref} - \beta_{oc}\Delta T_c \quad (4.15)$$

Equation (4.13a) relates the cell operating temperature ($T_c$) to the ambient ($T_a$) temperature and the irradiance ($G$), with the factor $C_2$ being a function of the Nominal Cell Operating Temperature (NCOT, °C) according to Equation (4.13b), and assumes heat transfer from the cell to the ambient to be chiefly by means of conduction, thus neglecting wind velocity effects (Castañer & Markvart, 2003). $C_2$ can be approximated to be $0.03^{\circ}C/W/m^2$, where the nominal cell temperature is unknown (Lorenzo, 1994).The weather dependence that is commonly

considered to be of significance is that of the short-circuit current (Equation 4.14) and that of the open-circuit voltage (Equation 4.15). The temperature dependence of the diode saturation current has been considered to be incorporated into that of the open-circuit voltage and short-circuit current, of which it is a function (Equation 4.10).

With all the relevant model parameters estimated as outlined above, Equations (4.4-4.5), (4.7), (4.10), and (4.13-4.15) constitute the mathematical model for the electrical behavior of the PV energy conversion system. The PV module has been implemented in the Simulink® software environment (see Appendix C.1 for further details).

To verify the validity of the developed PV model, simulations have been carried out in Matlab/Simulink using the data for the BP MSX 120 PV module by BP Solar (Appendix C.1), listed in Table (4.2). Figures (4.5) and (4.6) show the current-voltage and power-voltage characteristics of the developed model, respectively, simulated at various levels of irradiance and standard cell temperature (25 °C). The simulation results show good agreement with the manufacturer data, as can be deduced from comparing the data from Table (4.2) to the readings on the plots. The incorporation of the temperature dependence of the PV module parameters in the model by means of Equations (4.13)-(4.15) has also led to results that compare very favorably with the manufacturer-provided characteristic curves (Figures 4.7 & 4.8) (Appendix C.1).

**Table 4.2: PV module data for BP MSX 120**

| | |
|---|---|
| Maximum power ($P_{mpp}$) | 120W |
| Voltage at MPP ($V_{mpp}$) | 33.7V |
| Current at MPP ($I_{mpp}$) | 3.56A |
| Short-circuit current ($I_{sc}$) | 3.87A |
| Open-circuit voltage ($V_{oc}$) | 42.1V |
| Temperature coefficient of $I_{sc}$ | (0.065±0.015)%/°C |
| Temperature coefficient of $V_{oc}$ | -(80±10)mV/°C |
| Nominal Cell Operating Temperature (NCOT) | 47±2°C |
| Number of series cells per module | 72 |

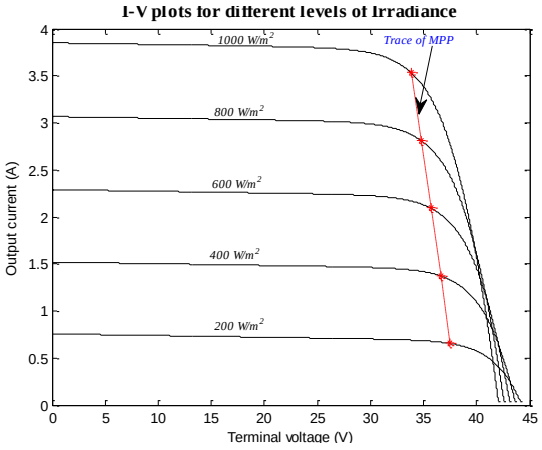


**Figure 4.5: PV module current-voltage characteristics for various irradiance values.**

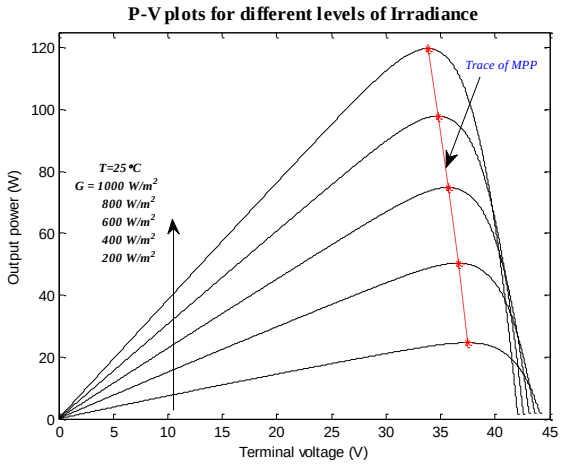


**Figure 4.6:** PV module's power-voltage characteritsics for various irradiance values.

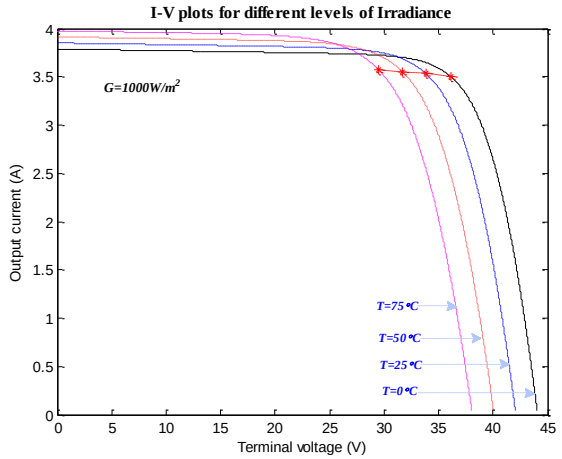


**Figure 4.7:** Temperature dependence of the PV module's current-voltage characteristic.

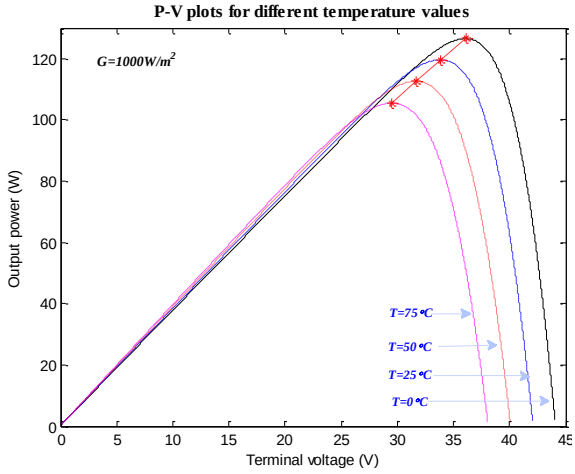


**Figure 4.8:** Temperature dependence of the PV module's power-voltage characteristic.

### 4.2.2. PV module Maximum Power Point Tracking (MPPT)

The output power of the PV module is mainly a function of the level of irradiance and temperature, as can be deduced from the power-voltage characteristic curves plotted for various irradiance and temperature levels (Figures 4.6 & 4.8 respectively). Moreover, at any given values of irradiance and temperature, the output power yield normally exhibits only one

maximum, which is also evident from the power-voltage characteristic curves. When either ambient conditions change or the load varies, the PV output power yield experiences a deviation from the optimal operating point. Maximum Power Point Tracking (MPPT) is a control technique that is used to automatically drive the PV module's operating point (i.e. output voltage & current) back towards the operating point of maximum power yield for the given irradiance and temperature conditions (Esram & Chapman, 2007). The MPPT controller fundamentally does this by adjusting the PV module's terminal voltage so as to maximize the power output, which is considered to be a form of load matching that is necessitated by the variations in the system operating conditions (Swiegers & Enslin, 1998).

A wide variety of MPPT methods for PV generation systems have been suggested in recent years, which vary in accuracy, complexity, efficiency and cost, among other performance characteristics. An overview of the various MPPT techniques that have been suggested in recent decades has been presented by Esram and Chapman (2007). A few of them are highlighted in the following paragraphs.

**Perturb and observe (P&O) technique:** arguably one of the most popular MPPT algorithms (Esram & Chapman, 2007), the P&O MPPT technique attempts to keep the PV module's operating point at the Maximum-Power Point (MPP) by continually adjusting (*i.e.* increasing or decreasing) the PV module's terminal voltage in a direction towards the MPP. One common way to implement the P&O technique is to periodically slightly adjust (or perturb) the duty ratio of the DC-DC converter that interfaces the PV module to the load, and then to observe the PV output voltage and power changes that accompany this duty ratio perturbation. If increasing the duty ratio increases the output power, the duty ratio is increased further, whereas if the duty ratio increase causes a decrease in the output power, then the duty ratio adjustment is reversed (*i.e.* made opposite to the previous one). Generally then, the direction of duty ratio perturbation is maintained if it leads to a positive PV output power change; otherwise, the direction of perturbation is reversed. The P&O MPPT technique thus uses the converter duty ratio perturbation to adjust the PV module's terminal voltage so as to operate the module at the MPP.

The main drawbacks with the P&O MPPT technique are that the PV module operating point often oscillates about the MPP, rather than settling at it, and that it performs especially poorly under rapidly changing atmospheric conditions. Many modifications to the standard P&O algorithm have been suggested in order to improve its performance under all operating conditions (Femia *et al*., 2005; Xiao & Dunford, 2004; Tafticht & Agbossou, 2004).

**Incremental Conductance technique:** the PV module power curve (Figure 4.6) has a positive slope on the left side of the MPP, a negative slope on the right side of the MPP, and a slope of zero at the MPP. This can be expressed mathematically as:

$$\left.\frac{dP_{pv}}{dV_{pv}}\right|_{V_{pv}<V_{mpp}} > 0 \tag{4.16}$$

$$\left.\frac{dP_{pv}}{dV_{pv}}\right|_{V_{pv}>V_{mpp}} < 0 \tag{4.17}$$

$$\left.\frac{dP_{pv}}{dV_{pv}}\right|_{V_{pv}=V_{mpp}} = 0 \tag{4.18}$$

where $V_{pv}$ and $P_{pv}$ are the PV output voltage and power respectively, and $V_{mpp}$ is the PV voltage at the MPP. This electrical characteristic of the PV module forms the operational basis for the incremental conductance MPPT technique. To formulate the incremental conductance MPPT technique, the PV's power derivative relative to the PV voltage is written as:

$$\frac{dP_{pv}}{dV_{pv}} = \frac{d(I_{pv}\cdot V_{pv})}{dV_{pv}} = I_{pv} + V_{pv}\cdot\frac{dI_{pv}}{dV_{pv}} \cong I_{pv} + V_{pv}\cdot\frac{\Delta I_{pv}}{\Delta V_{pv}}, \quad where \quad \frac{dI_{pv}}{dV_{pv}} \cong \frac{\Delta I_{pv}}{\Delta V_{pv}}$$

$$\therefore \frac{dP_{pv}}{dV_{pv}} \cong I_{pv} + V_{pv}\cdot\frac{\Delta I_{pv}}{\Delta V_{pv}} \tag{4.19}$$

Since the PV power curve has a slope of zero at the MPP, Equation (4.19) can be written at the MPP as:

$$\frac{I_{pv}}{V_{pv}} + \frac{\Delta I_{pv}}{\Delta V_{pv}} = 0 \tag{4.20}$$

The first term on the left-hand-side of Equation (4.20) is referred to as the instantaneous conductance, while the second term is known as the incremental conductance. The objective of the incremental conductance MPPT technique then is to drive the sum of the instantaneous conductance and the incremental conductance towards zero, and consequently bring the PV module operating point to the MPP. The common way to achieve this is to adjust the PV module terminal voltage in a direction toward to the MPP, as is also the case with the P&O technique. Figure (4.9) illustrates the flowchart that may be used to implement the incremental conductance MPPT technique (Esram & Chapman, 2007). The voltage and current variables in Figure (4.9) are those of the PV module, although the "pv" subscript has been omitted for ease of representation.

Incrementing/decrementing the PV converter duty ratio, depending on the prevailing PV module operating point, adjusts the PV terminal voltage, and thus drives its operating point towards the MPP. The duty ratio step size is a major design factor affecting the performance of the incremental conductance algorithm, along with the update rate of the MPPT algorithm. A tradeoff is often necessary between fast tracking (requiring a large duty ratio increment factor) and losses due to oscillations about the MPP when the increment factor is too large. A two-stage approach that makes use of a variable step size has been suggested by many authors

for improving the operation of the incremental conductance algorithm, such as for instance by Kobayashi *et al.* (2003).

**Fractional voltage/current-based MPPT techniques**: two MPPT techniques with relatively simpler structures work on the basis of the linear proportionality that has been empirically established between the voltage and current at the MPP ($V_{mpp}$ & $I_{mpp}$), and the open-circuit voltage and short-circuit current ($V_{oc}$ & $I_{sc}$) respectively.

It has been found that as the irradiance and temperature vary, the ratio of $V_{mpp}$ to $V_{oc}$ remains essentially constant, according to the relation (Swiegers & Enslin, 1998):

$$V_{mpp} = k_v V_{oc} \tag{4.21}$$

where $k_v$ is the constant of proportionality between $V_{mpp}$ and $V_{oc}$ which holds fairly well over a significant range of ambient condition variations. The constant of proportionality is normally determined experimentally, and varies from one PV module to another, but is always less than unity.

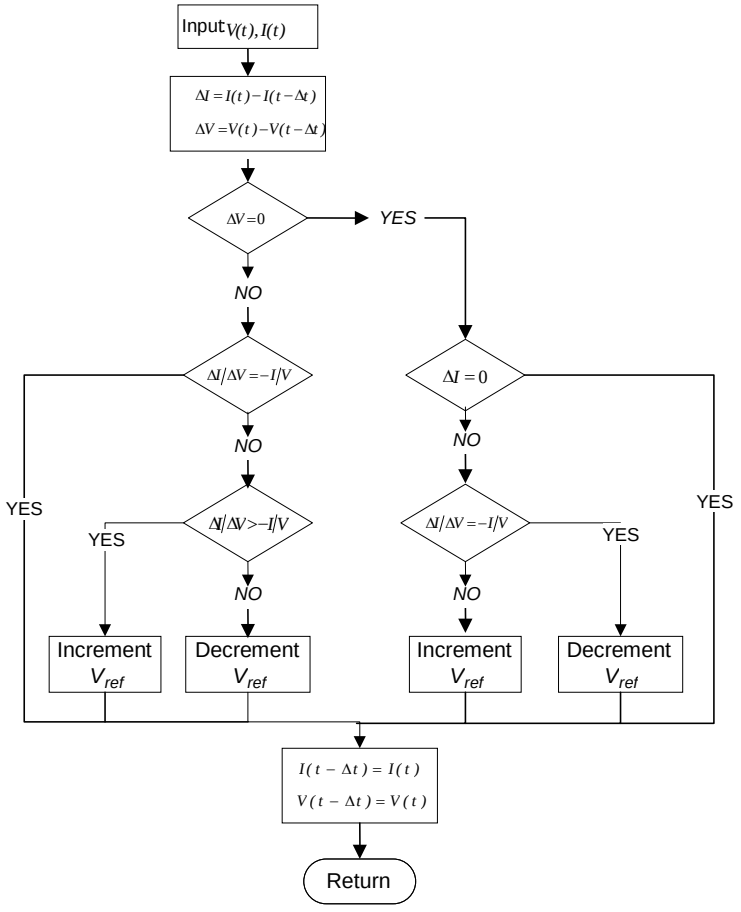


**Figure 4.9: Incremental Conductance algorithm flow chart.**
**(Adapted from Esram & Chapman, 2007)**

The MPPT technique developed on the basis of Equation (4.21) is referred to as the **fractional open-circuit voltage** MPPT technique. A relationship similar to Equation (4.21) can also be established between the MPP current ( $I_{mpp}$ ) and the short-circuit current ( $I_{sc}$ ), and forms the operational basis for the **fractional short-circuit current** MPPT technique.

Despite their advantage of being of a simpler structure, the fractional voltage/current-based MPPT techniques' main drawbacks are their considerably low tracking accuracy (due to their not being true MPPT techniques, but rather based on rough empirical approximations), the significant power losses associated with the low accuracy, as well as the difficulty associated with the sensing of the open-circuit voltage and short-circuit current. Their application is usually limited to cases where the low cost of MPPT implementation takes precedence over requirements for high tracking accuracy (Esram & Chapman, 2007).

**Knowledge-based MPPT techniques**: the two main knowledge-based MPPT techniques are the Fuzzy Logic Control- and Neural network-based MPPT algorithms. Both are well-suited to the non-linear nature of the PV output power control problem, and are especially suitable for implementation by means of micro-controllers.

**Fuzzy Logic Control** (FLC) especially has the advantage of not requiring a precise mathematical model of the plant (the PV generator in this case), relying only on the application of the linguistic control rules (devised by the control designer) to the system input variables recast into linguistic variables, for the synthesis of the control output (Salhi & El-Bachtri, 2011). Moreover, FLC has demonstrated good performance under varying atmospheric conditions.

**Neural networks** are based on pattern recognition through training (Esram & Chapman, 2007). The Neural network usually has three interconnected layers of neurons (*i.e.* input, hidden & output layers) between the input and the output, with weighted links interconnecting the nodes of the various layers. The training process consists in assigning the appropriate weights to the links, and occurs over some determined period of time, during which the PV module is tested in order to establish the input-output patterns for various operating conditions.

The effectiveness of the knowledge-based techniques is mainly influenced by the knowledge of the controller designer (FLC), the algorithms chosen for control output synthesis (FLC & Neural network), as well as the length of the training period (Neural network), among other factors. The main drawback of these methods is that once optimized for a specific application, they are usually not easily adaptable to another case using PV modules with different characteristics, making their implementation comparatively costly (Esram & Chapman, 2007).

In this thesis, the Incremental Conductance technique has been chosen for its satisfactory tracking ability, at medium computational and implementation cost.

### 4.2.3. Incremental Conductance MPPT technique implementation

As discussed in the preceding section, the incremental conductance method tracks the MPP by attempting to drive the sum of the instantaneous and incremental conductances to zero, according to Equation (4.20). At any PV operating point other than the MPP, the left-hand-side of Equation (4.20) evaluates to a nonzero value, and may be written as:

$$e_{pv} = \frac{I_{pv}}{V_{pv}} + \frac{\Delta I_{pv}}{\Delta V_{pv}} \tag{4.22}$$

where $e_{pv}$ is the error magnitude by which the PV operating point deviates from the desired (optimum) operating point. As discussed by Esram and Chapman (2007), the incremental conductance algorithm can be implemented by means of a Proportional-Integral (PI) regulator that drives $e_{pv}$ to zero on the basis of Equation (4.22). This method has been adopted for the MPPT algorithm implemented in this thesis. The algorithm has been implemented in the Matlab/Simulink simulation platform.

The circuit in Figure (4.10) has been used to test the performance of the MPPT algorithm. The PV module data used in the test is that of the BP MSX 120 PV module by BP Solar, presented in Section (4.2.1). As can be seen from the circuit in Figure (4.10), the PV module is connected to a resistive load via a boost converter. In the circuit, $L_{boost}$, $C_{in}$, $C_{out}$ and $R_L$ represent the boost inductor, the converter input capacitor, the converter output capacitor, and the load resistance respectively. D and Q are the diode and switch, respectively, which form part of the boost converter configuration. The MPPT block synthesizes the duty ratio (D) using the sensed terminal voltage and current inputs. The duty ratio is then fed into the PWM block, which generates the gate pulse signal required by the converter switch to regulate the PV module terminal voltage.

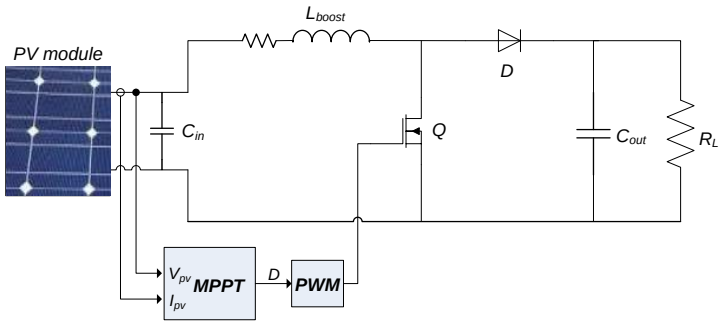


**Figure 4.10:** **MPPT control of a PV module connected to a load via a boost converter.**

The results of the simulations evaluating the performance of the incremental conductance MPPT technique are depicted in Figures (4.11) and (4.12).

Figure (4.11) shows the comparison of the PV power yield, when no MPPT controller has been implemented, with the maximum expected PV yield for various levels of irradiance. The simulation has been so performed as to examine the PV power yield for both instantaneous and gradual increase and decrease in the irradiance. When no MPPT controller has been implemented, the boost converter's duty ratio is normally fixed, and in this simulation case it has been set to 0.3. Figure (4.11) reveals that there is a significant power under-yield due to the absence of a means to adjust the converter duty ratio to the optimum value as the irradiance changes.

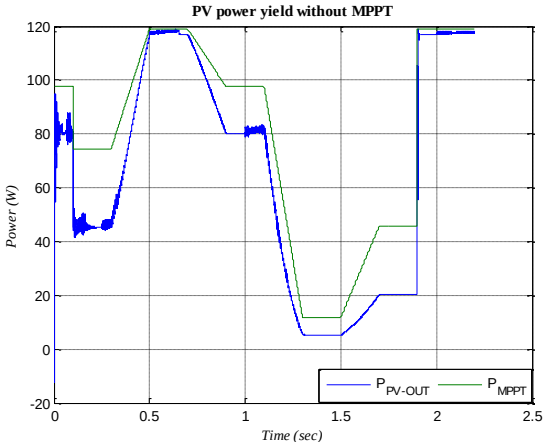


**Figure 4.11: PV module power yield without MPPT: comparison with the expected maximum ($P_{mpp}$).**

In Figure (4.12), the PV power yield with the incremental conductance MPPT controller having been implemented is compared with the maximum expected power output. The figure shows that the MPPT controller works fairly well in tracking the optimal operating point, and the disparity between the actual power yield and the expected maximum value is kept minimal, both for instantaneous and gradual irradiance variations. Due to the constraints in the maximum duty ratio perturbation and the frequency of execution of the MPPT algorithm, the actual power-yield curve tends to trail the expected maximum-yield curve, as Figure (4.12) reveals. The steady-state value, however, very closely approaches the expected maximum value.

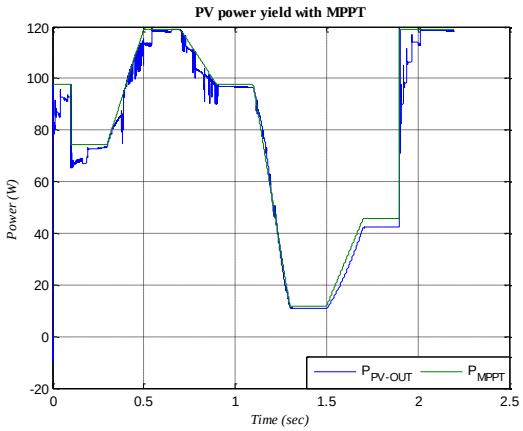


**Figure 4.12: PV module power yield with MPPT: comparison with the expected maximum ($P_{mpp}$).**

Comparison of Figures (4.11) and (4.12) demonstrates the significant improvement in the PV power yield that results from having an MPPT controller in the circuit of Figure (4.10). In the case considered here, the percentage increase in the power yield gets higher as the irradiance gets lower. This trend is clearly depicted in Table (4.3), in which the power yield, with and without the MPPT controller, is tabulated against the maximum expected power yield, for a range of irradiance values.

In Table (4.3), the open-loop duty ratio refers to the converter duty ratio for which the PV power yield is maximum for given load and ambient conditions, and was determined by varying the converter duty ratio during the simulation (keeping all other circuit conditions constant), then noting the value at which the PV power yield was maximum. As can be deduced from the table, the duty ratio has to correspondingly vary with PV circuit variations (in load or ambient conditions), in order for the PV operating point to be maintained at the MPPT. The last column of Table (4.3) indicates the change in the duty ratio enabled by the MPPT controller, thus keeping the PV module operating at the maximum-power point. The dynamically adjusted duty ratio is denoted as the closed-loop duty ratio in the table.

**Table 4.3: Percentage increase in PV power yield due to MPPT.**

| Irradiance ($W/m^2$) | $P_{OUT}$ (W) | | | $P_{OUT}$ increase due to MPPT (% ) | Open-loop duty ratio | Closed-loop duty ratio |
|---|---|---|---|---|---|---|
| | Expected maximum | Without MPPT | With MPPT | | | |
| 1000 | 119 | 118 | 118.9 | 0.76 | 0.26 | 0.26 |
| 800 | 97.5 | 81 | 97.2 | 16.67 | 0.213 | 0.16 |
| 600 | 74.5 | 45.3 | 73.2 | 38.11 | 0.13 | 0.15 |
| 400 | 45.6 | 20.21 | 42.23 | 52.14 | 0.023 | 0.02 |
| 200 | 11.8 | 5.2 | 10.81 | 51.9 | 0.015 | 0.02 |

The trend of the MPPT controller making a greater difference in the PV power yield at lower irradiance levels in the simulation case considered is well illustrated in Figure (4.13) as well, where the percentage increase in the power yield from the non-MPPT to the MPPT-case is plotted against the corresponding irradiance level. Such observations may be useful in

ascertaining when the operation of the MPPT controller is most profitable, and in which site (weather) conditions its implementation may be deemed optional.

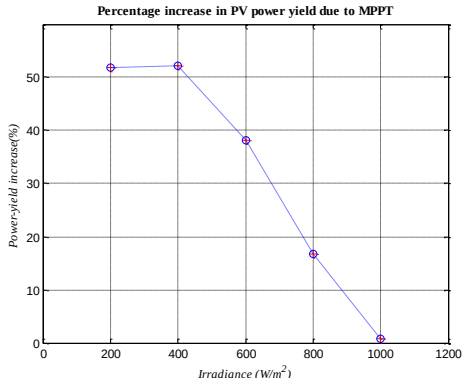


**Figure 4.13:** **PV power-yield percentage increase due to MPPT as related to the irradiance level.**

## 4.3. Wind Energy Conversion (WEC) system

The Wind Energy Conversion (WEC) system was introduced in Section 3.3.2, where it was established that it harnesses a fraction of the power available in the wind and converts it to electrical energy. One significant classification of WEC systems is on the basis of the rotor axis orientation, under which two main topologies can be considered. These are: the Horizontal Axis Wind turbine (HAWT) and the Vertical Axis Wind Turbine (VAWT). Figure (4.14) portrays typical designs for each of these wind turbine types. In the HAWT, the turbine rotor's axis of rotation is horizontal (or parallel to the ground), and is also parallel to the free stream wind direction (Teachergeek, 2006). The opposite applies in the case of the VAWT, in which the axis of rotation is vertical (*i.e.* perpendicular to the ground).

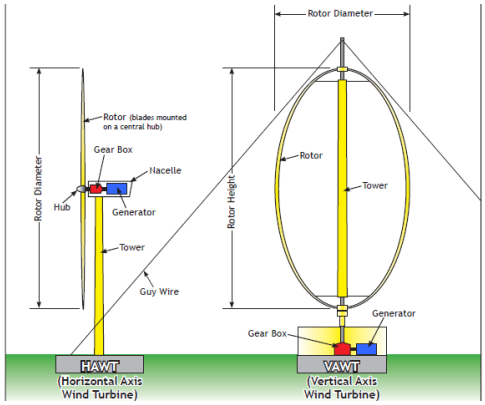


**Figure 4.14:** **Illustration of the Horizontal-Axis and Vertical-Axis Wind Turbines. (Adapted from Teachergeek.org, 2006)**

Most of the modern WEC systems are of the HAWT type. As discussed by Manwell *et al* (2002), the main reasons for this trend are the superior aerodynamic characteristics as well as the better economy of the HAWT topology relative to the VAWT type. The discussion of the

WEC system in this section is thus focused on the HAWT type, as also mentioned in Section 2.4.2.2.

The consideration of the characteristics and the modeling of WEC systems begins with the definition of a few terms in Section 4.3.1, which should aid the explanation of the WEC system-related concepts that follow. In Section 4.3.2, the four main subsystems of the WEC system are discussed in terms of their main characteristics and functionalities. The mathematical modeling of these subsystems is then considered in Section 4.3.3, followed by the presentation of the WEC system model implementation and simulation analysis in the Matlab/Simulink software development environment in Section 4.3.4.

### 4.3.1. Definitions related to WEC systems

**Relative wind speed** in HAWTs is the effective component of the free stream wind velocity responsible for setting up the lift and drag forces (defined below) on the rotor blade; it's magnitude is the vector sum of the wind velocity at the rotor blades and the wind velocity due to blade rotation.

**Airfoil** is defined as "any surface producing more lift than drag force when passing through the air at a suitable angle" (FAA, 2012). Modern HAWTs are lift-based machines (*i.e.* they are designed to be driven by the lifting effect of the wind force), and so the cross-section of their rotor blades is airfoil-shaped, optimized to have a high lift-to-drag coefficient ratio.

**Lift and Drag forces** are the two component forces into which the effective force on the rotor blade due to the power in the relative wind are normally resolved. The lift force results from the airflow over the airfoil setting up a positive upward pressure on the airfoil, which produces a lift effect on the rotor blade. It acts perpendicular to the direction of the relative wind. The drag force is mainly caused by the viscous friction between the airflow and the airfoil surface; it acts parallel to the direction of the relative wind.

**Angle of attack** is defined as the angle between the relative wind and the straight line connecting the airfoil's leading edge (or foremost point) and trailing edge (or rearmost point), also referred to as the *chord line*; its magnitude determines the proportion of the lift coefficient to the drag coefficient of the relative wind force.

**Blade pitch**, for pitchable-blade wind turbines, is the turning of the rotor blade about its longitudinal axis, which changes the angle between its chord line and the plane containing the rotor hub, the *blade pitch angle*. The blade pitch angle is an important characteristic in wind power generation control; its effect is to adjust the angle of attack, which in turn changes the magnitudes of the lift and drag forces on the rotor blade.

**Blade stall** occurs when, due to the angle of attack being very large, airflow separates from the airfoil, taking on a turbulent pattern that leads to the airfoil being subjected to a greater

drag force than the lift force, such that the effective wind force produces no rotating effect on the rotor blade (FAA, 2012).

**Yaw system**, required in HAWTs, is the mechanism used to orient the rotor shaft relative to the wind stream direction, mainly for optimal energy capture. Upwind turbine systems tend to employ an active yaw drive to keep the rotor shaft properly aligned with the wind stream, whereas downwind turbine configurations normally use self-alignment to achieve the same objective (referred to as free yaw systems).

**Tip-speed ratio** (**TSR**) is defined as the ratio of the linear speed of the tip of the rotor blade to the free stream wind speed. For a wind turbine rotor blade of radius $R$ having a rotational speed $\omega_T$ and subjected to the free wind speed $v_w$, the tip-speed ratio $\lambda$ is given by:

$$\lambda = \frac{\omega_T R}{v_w} \tag{4.23}$$

**Aerodynamic efficiency (Power coefficient)** is the parameter that represents the fraction of the power in the wind that is successfully extracted by the turbine rotor (*i.e.* the ratio of the rotor power to the total wind power), and is commonly used to characterize the aerodynamic performance of the wind turbine. If the power available in the wind is given by $P_w$ and the rotor power is considered to be $P_T$, then the power coefficient $C_P$ can be expressed as:

$$C_P = \frac{P_T}{P_w} \tag{4.24}$$

For HAWTs, the power coefficient is mainly a function of the tip-speed ratio and the blade pitch angle.

Many of the terms defined above can be seen in the depiction of an airfoil in Figure (4.15). In the following section, a brief discussion of the main components making up the WEC system based on the HAWT topology is presented. Reference is made to Figure (4.16) in the discussion.

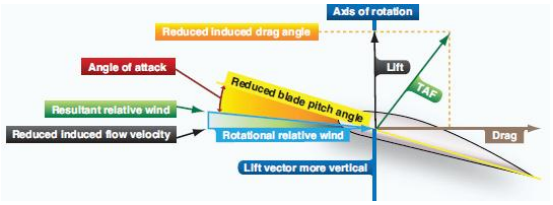


**Figure 4.15: Illustration of an airfoil, showing the component forces, relative wind and angle of attack.**
**(Adapted from FAA, 2012)**

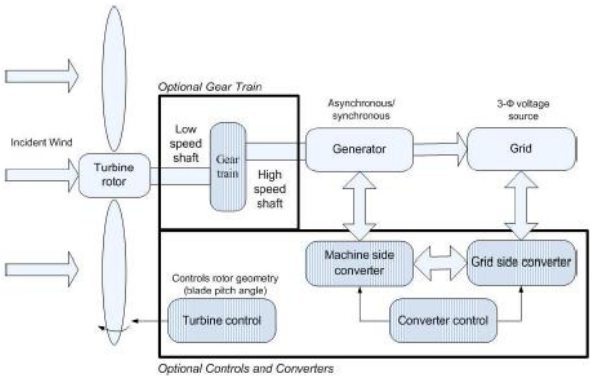


**Figure 4.16: The main components of the (HAWT) WEC system. (Adapted from Singh & Santoso, 2011)**

### 4.3.2. Components of the Wind Energy Conversion (WEC) system

An examination of Figure (4.16) reveals that the energy conversion part of the WEC system comprises mainly of the aerodynamic, mechanical and electrical subsystems that have to operate harmoniously in order to derive the useful energy from that which is available in the wind. This is to a large extent made possible by a comprehensive control system, which ensures the effective control of the power extraction and conversion process, from the motive energy in the wind to the electrical energy fed into the electric grid. These four subsystems are accordingly briefly discussed in the following subsections in terms of the main characteristics and functionalities.

#### 4.3.2.1. Aerodynamic subsystem

The most significant components of the aerodynamic subsystem of the WEC system are the *rotor blades* and the *rotor hub*, which together form the primary means of capturing the power available in the wind and converting it into rotary motion.

Rotor blades are a vitally important component of the WEC system in two fundamental ways: firstly, their aerodynamic design largely determines the power extraction efficiency of the wind turbine; and secondly, their structural design significantly influences the structural soundness of the entire WEC system assembly (Manwell *et al.*, 2002).

As pointed out in Section 4.3.1, HAWTs are lift-based machines. That is, the force in the wind creates a lifting effect on the rotor blades as the wind interacts with the wind turbine, producing the rotary motion of the blades. In order to achieve this lifting effect, the blade is so designed that its cross section resembles an airfoil (Figure 4.15), with a slightly more elongated upper-side surface than the bottom surface (Patel, 2006). Airflow over the airfoil creates a pressure gradient across it, resulting in the generation of two forces: the lift force (responsible for exerting the useful (lifting) torque on the rotor blade), and the drag force (which exerts a retarding torque on the blade).

Thus the principal aim of the aerodynamic blade design for HAWTs is to achieve an optimal lift-to-drag coefficient ratio across the blade span, from the root to the tip of the blade, and thus optimize the power extraction capability of the wind turbine. Because the lift force is the one that produces the useful torque of the wind turbine, whereas the drag force negates the magnitude of the useful torque, the airfoils for wind turbine blades are designed to have the highest possible lift-to-drag coefficient ratio (Patel, 2006).

The aerodynamic performance (or power coefficient) of the wind turbine is mainly a function of the Tip-Speed Ratio (TSR) and, therefore, the design TSR is another important parameter to consider in the aerodynamic design of the rotor blades. Both for economical and power efficiency reasons, high TSRs are generally preferred in modern large wind turbines. The high rotor blade rotational speed associated with the high-TSR blade design, however, necessitates careful design to take into account the various aspects of the wind turbine operation affected by the choice of the TSR. Some of these aspects are listed in Table (4.4), showing how they relate to the magnitude of TSR, whether low or high.

**Table 4.4: Influence of choice of tip-speed ratio on other WTS parameters. (Adapted from Schubel & Crossley, 2012)**

| | **Low TSR** | **High TSR** |
|---|---|---|
| Drive train torque | High | Low |
| Stress (aerodynamic and centrifugal) | Low | High |
| Noise | Low | High |
| Aerodynamic efficiency | Low (for very low TSR) | Higher (up to a certain value) |
| Rotor area solidity | High | Low |
| Aerodynamic design (airfoil shape) | Simple (thick airfoil, long chord length) | Complex (thinner airfoil, short chord length) |
| Cut-in speed | Low | Moderately high |

It can be observed from Table (4.4) that, generally, high-TSR designs usually imply more sophisticated aerodynamic (airfoil) design. The rotor blade flexibility and low torque required for high rotational speeds entail fewer and thinner rotor blades, and this in turn calls for a more complex airfoil shape design, and greater strength and stiffness of the blade material. Some of the desirable properties of the blade material are a high strength-to-weight ratio, long fatigue life, greater strength and stiffness, and greater ease of airfoil fabrication (Óskardottir, 2014). Today, composites (glass fibers, carbon fibers and wood-epoxy laminates) are extensively used in rotor blade fabrication for their good tensile strength and stiffness properties (Manwell *et al.*, 2002).

The Rotor hub is the point of attachment of the blades to the rest of the wind turbine drive train. As the transmitter of the loads generated in the rotor blades to the drive train, the rotor hub must be designed to bear these aerodynamic and dynamically induced loads in a way that

insures reliable system operation. Two main types of rotor hub are commonly employed in HAWTs (Manwell *et al.*, 2002): one is referred to as the *rigid hub*; the other one is the *teetering hub*.

The rigid hub fixes the position of the blades relative to the main shaft, so that as the rotor rotates, there is no relative motion between the blades and the main shaft. The blade positions may be adjusted about their longitudinal axes (for pitchable-blade machines), but may not move relative to the main shaft. The hub itself has to be so attached to the main shaft that it neither slips nor spins on the shaft. This rotor hub design is employed in nearly all multiple-blade (*i.e.* blade count greater than two) wind turbine systems.

The teetering hubs, in contrast with the rigid hub, do provide for blade motion relative to the main shaft, and are commonly used for one- or two-bladed wind turbine systems. This is because one- and two-bladed wind turbines are susceptible to unbalanced loads due to aerodynamic imbalances and the dynamic effects of rotor rotation or yaw operation, and the teetering hub design is well-suited to reducing these load imbalances. The teetering hub has a more complex design than the rigid hub, however, especially if blade pitching capability is desired as well.

#### 4.3.2.2. Mechanical (drive train) subsystem

The wind turbine's mechanical subsystem essentially corresponds to the drive train, which is the rotary part of the wind turbine, typically consisting of such components as the rotor blades, low-speed (main) shaft, gearbox, high-speed (generator) shaft, bearings, couplings, and a mechanical braking system. (Patel, 2006) These components (except for the rotor blades) are normally housed in the nacelle, a compartment which provides protection for the drive train components from harsh environmental conditions. Inside the nacelle, the drive train components are attached to the main frame, a steel structure that serves to align them properly, and to provide rigidity to the drive train assembly. An example of the drive train components for a large wind turbine housed in the nacelle is illustrated in Figure (4.17) (Ragheb, 2014).

Besides providing the necessary mechanical support to the rotating rotor blades, the drive train's other main function is the transmission of the torque generated by the blades' rotary motion, through the shaft assembly to the electrical generator, which is then driven to generate electrical power. Most wind turbine generators are four-pole machines, thus having a synchronous speed of 1500 rpm (50 Hz system) or 1800 rpm (60 Hz system) (Manwell *et al.*, 2002). The wind turbine rotor, on the other hand, rotates at a significantly lower speed. Thus the gearbox is incorporated into the drive train (between the main shaft and the generator shaft) for the purpose of converting the wind turbine's low rotational speed to the higher speed required for the electrical power generation.

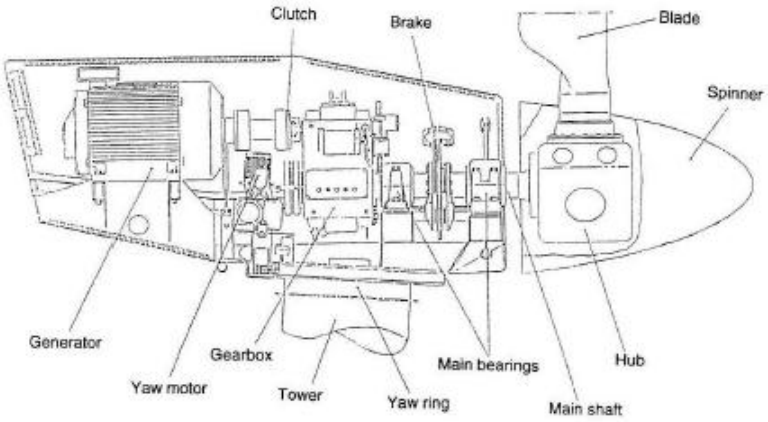


**Figure 4.17: Drive train components of a large wind turbine, housed in a nacelle. (Adapted from Ragheb, 2014)**

The auxiliary components in the drive train (*i.e.* besides the shafts, the gearbox, and the generator) serve a number of important functions as well. The bearings, for instance, attach the rotary components (*e.g.* the shafts) to the main frame, and transfer the reaction loads of the rotary components to the wind turbine structure. They are thus required to be able to bear the axial and thrust reaction loads (Manwell *et al.*, 2002).

The mechanical brakes prevent rotor motion when the turbine is not generating power, and may also be used to halt the rotor under certain operating conditions. They have to be designed for the maximum torque that they are required to apply in stopping the rotor, for the amount of kinetic energy they have to absorb from the decelerating rotor, and for the rate at which they have to apply the retarding torque.

HAWTs may be classified as either upwind or downwind (of the turbine tower) machines. This classification affects the yawing mechanism used, which is considered part of the mechanical components of the WEC system, and has been defined in Section 4.3.1. The upwind machines employ an actively controlled yawing mechanism, which may comprise a tail vane, small yaw rotors and fantails, or a servo mechanism to keep the turbine blades oriented towards the wind as the wind direction changes (Ragheb, 2014). The downwind machines, on the other hand, make use of a free (*i.e.* not actively controlled) yawing mechanism, which often simply requires a yaw bearing and some yaw dampers for slowing the yaw rate.

The drive train components must be designed for a long fatigue life, low maintenance, and high efficiency, being costly as they are (especially the gearbox), and considering that they are critical (or key) components for the reliable operation of the wind turbine (Manwell *et al.*, 2002).

#### 4.3.2.3. Electrical subsystem

The electrical subsystem of the WEC system constitutes the part responsible for the conversion of the (drive train's) mechanical power into electrical power (the electrical generator), and the interface to the electric grid (either direct generator connection or coupling via a power converter). Based on the configuration of the electrical subsystem, generally two main classes of the WEC system can be identified: the fixed-speed WEC system and the variable-speed WEC system (Carrasco *et al.*, 2006).

The fixed-speed WEC system makes use of a Squirrel-Cage Induction Generator (SCIG). As depicted in Figure (4.18), this WEC system configuration is normally connected directly to the electric grid. This direct connection to the grid is possible because the fixed-speed operation of the wind turbine rotor means that the frequency of the induction generator's terminal voltage is fairly constant, having only about 1-2% variation (Blaabjerg *et al.*, 2004), thus requiring no frequency conversion. The drive train must incorporate a gearbox of suitable gear ratio, in order to step up the generator shaft rotational speed to the level required for electric power generation by the induction generator. Additionally, reactive power compensation (in the form of a capacitor bank) is required to be connected to the generator terminals in order to supply some of the reactive power consumed by the machine in its running, as is depicted in Figure (4.18).

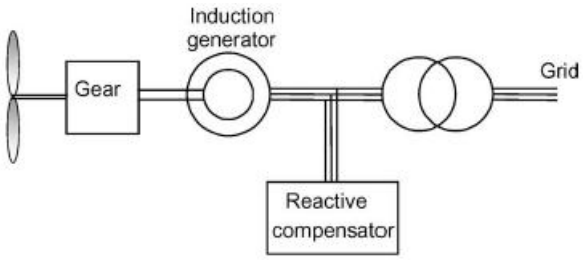


**Figure 4.18: Fixed-speed, induction generator-based WEC system, directly coupled to the grid. (Adapted from Blaabjerg *et al.*, 2004)**

The fixed-speed, SCIG-based WEC system was popular in the initial developmental stage of wind energy generation. It has a number of advantages, such as simple, low-cost design, high reliability, low-maintenance requirements, and relatively simpler controller structure. Modern WEC systems are designed for optimal aerodynamic performance, effective mechanical load regulation and (especially in the context of grid code requirements for grid-integrated systems) fault ride-through and reactive power support. The simple structure of the fixed-speed, SCIG-based WEC system falls far short in satisfying these desired requirements, and so the implementation of this concept has shown considerable decline in recent times (Perdana, 2008).

The variable-speed WEC system configuration makes use of either a wound-rotor induction generator or a synchronous generator, and power electronic converters for power control and frequency conversion.

In the first variable-speed WEC system configuration considered (referred to as the limited variable-speed concept), the variable-speed operation of the wind turbine is accomplished by incorporating variable resistance into the wound-rotor induction generator's rotor circuit, which is then controlled through a power converter to allow about 2-4% speed variation in the wind turbine rotor. This configuration is depicted in Figure (4.19), and it can be seen that in this case also the generator is directly connected to the electric grid. According to Carrasco *et al* (2006), the commercial version of this WEC system configuration is offered by the Danish company Vestas under the trade name *OptiSlip*, and its market share is significantly less than that of the other configurations.

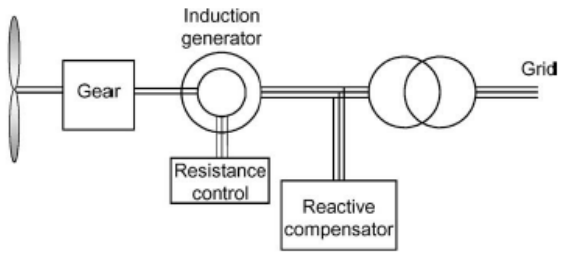


**Figure 4.19: Limited-variable-speed wound-rotor induction generator-based WEC system. (Adapted from Blaabjerg *et al.*, 2004)**

The second variable-speed concept also makes use of a wound-rotor induction generator, in a configuration commonly referred to as the Doubly-Fed Induction Generator (DFIG)-based variable-speed wind turbine system. In this case the variable-speed operation of the wind turbine rotor is accomplished by incorporating a power converter into the rotor circuit of the generator, which controls the rotor currents and provides the necessary decoupling between the grid electrical frequency and the turbine mechanical frequency (Carrasco *et al.*, 2006; Blaabjerg *et al.*, 2004). This configuration is depicted in Figure (4.20).

From Figure (4.20), it is observed that the generator's stator circuit is directly connected to the electric grid, whereas the rotor circuit is interfaced to the electric grid via a back-to-back power converter. Thus power may be transferred from the WEC system to the grid partly through the stator circuit and partly through the rotor circuit, such that it is also referred to as the partial-power-converter variable-speed wind turbine concept (Perdana, 2008).

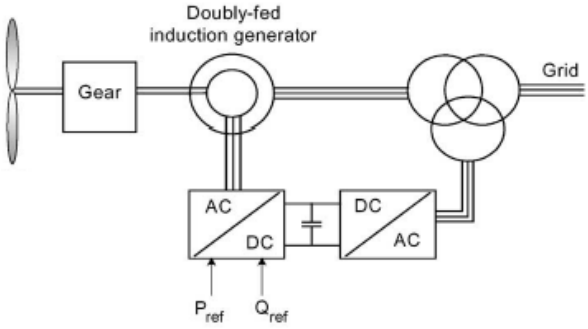


**Figure 4.20:** **Doubly-Fed Induction Generator (DFIG) -based WEC system. (Adapted from Blaabjerg *et al.*, 2004)**

The third variable-speed WEC system is referred to as the full-power-converter variable-speed concept. It may be based either on a high-speed wound-rotor induction generator or a multi-pole, low-speed Permanent-Magnet Synchronous Generator (PMSG) or a field-excited synchronous generator (Fox *et al.*, 2007). The full-power-converter variable-speed WEC system is depicted in Figure (4.21).

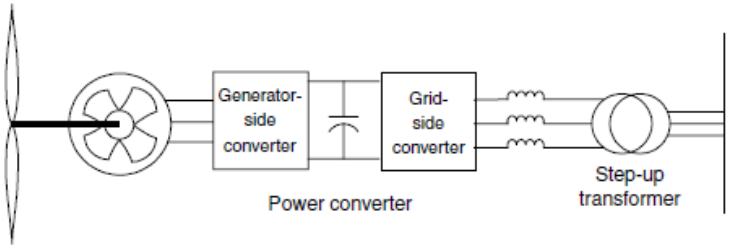


**Figure 4.21:** **Full-power-converter synchronous/asynchronous generator-based WEC system. (Adapted from Fox *et al.*, 2007)**

There are relative benefits associated with the use of each of the WEC system concepts presented above. Many factors have to be taken into account in the choice of the configuration to be used. As mentioned earlier, the low capital and maintenance costs associated with the fixed-speed SCIG-based concept, coupled with its simple structure and high reliability, make it suitable for small-scale wind energy generation (including remote power supply) applications.

The variable-speed WEC system, on the other hand, provides for easier compliance with the grid-code requirements, and so is the preferred choice for grid-interactive WEC systems. In terms of the relative merits of the various variable-speed WEC system concepts, the main advantage of the partial-power converter DFIG-based WEC configuration over the full-power-converter configuration is its use of a lower-rated power converter, which implies lower power converter-related costs and power losses. The full-power-converter configuration, on the other hand, exhibits better technical performance (in terms of power controllability), and when a multi-pole synchronous generator is used, the resultant WEC system may have lower cost,

lower losses, and improved reliability, mainly due to the absence of the costly gearbox (Carrasco *et al.*, 2006; Blaabjerg *et al.*, 2004).

The control requirements of the various configurations also exhibit some differences, as briefly discussed in the following subsection.

#### 4.3.2.4. Control system

The common role and objectives of the control system in the various WEC system configurations are fairly well-defined, despite the differences in the means to accomplish them that may exist. As elaborately discussed by Leithead *et al* (1991), common to the 'good control' of any WEC system are the aims to *maximize the wind turbine's energy yield*, to *regulate and smoothen the generated power*, to *reduce the transient loads* experienced by the wind turbine and the associated structure, and to *ensure the stability of the control system, with well-shaped dynamic response and steady-state behavior*. To what extent these control objectives may be realized (and their significance to the desired operation of the WEC system) is largely a function of the concept used for the WEC system, as well as the scale of the WEC system (in the sense that small- and large-scale WEC systems invariably have different mechanical load regulation requirements). Put another way, the control goals and strategies for a WEC system are mainly a function of the wind turbine configuration (Pao & Johnson, 2009; Leithead *et al.*, 1991), as has also been highlighted in the preceding sections. For the fairly generic discussion of control systems for WEC systems that is intended here, only the general aspects can be highlighted (most of which in practice apply mainly to the large-scale end of the wind turbine size spectrum).

The choice of either upwind or downwind configuration of the wind turbine affects the choice of the yaw control system. As mentioned in Section 4.3.1, the upwind configuration normally makes use of an active yaw control system (whose task is to keep the rotor blades oriented towards the wind), whereas a free yawing system suffices for the downwind configuration of the wind turbine.

The difference in the wind turbine's aerodynamic design (in terms of being either variable-pitch or fixed-pitch) affects the control of the turbine's mechanical loads in the operating region beyond the rated machine output. Blade pitch control (the turning of the rotor blades about their longitudinal axis) is used to limit the power developed by the (variable-pitch) wind turbine, when the turbine rated power output is exceeded. The fixed-pitch wind turbine is aerodynamically designed such that the rotor blades stall (*i.e.* the blades do not rotate, due to the lift component of the force induced by the wind turbulence being insufficient) when the wind speed exceeds the maximum rated value for the turbine (Patel, 2006). Thus the power-limitation function of the wind turbine control system is realized by different means in the fixed- and variable-pitch wind turbines. Both mechanisms have relative merits that have to be

taken into account relative to the size and configuration of the wind turbine (Leithead *et al.*, 1991).

There is also a significant difference in the control strategies for the fixed-speed and variable-speed WEC systems. As discussed in the preceding section on the *electrical subsystem*, the fixed-speed WEC system has a simple control structure, and has the electric generator directly connected to the electric grid. The disadvantage of this configuration from the control perspective is that little can be accomplished in terms of optimizing the energy yield over a wide range of wind speed variations, and the implementation of fault-ride-through (as specified by some grid codes) is difficult, because it cannot supply much reactive power when required to. The variable-speed WEC system, on the other hand, allows the adjustment of the turbine rotor speed in response to wind speed variations (for the optimal energy yield operation of the WEC system over a wide wind speed range), and by means of the suitable control of the power electronic interfaces, reactive power support can be provided when required by the grid (Carrasco *et al.*, 2006).

Figure (4.22) depicts a typical torque-speed characteristic of a wind turbine that is normally used for control purposes, showing the various operating regions of the turbine, with different control goals and control strategies (Fox *et al.*, 2007).

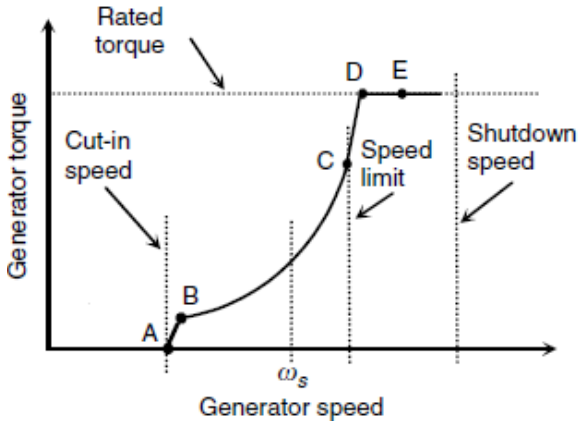


**Figure 4.22: Torque-generator speed characteristic of a wind turbine. (Adapted from Fox *et al.*, 2007)**

The variable-speed wind turbine (such as the one based on the DFIG) would allow the variation of the turbine rotor speed so as to optimize the turbine's energy yield in the B-C region of the characteristic curve, which is below the rated output of the turbine. Constant-speed operation is normally employed for the A-B and C-D regions, and constant torque-operation for the D-E region, so as to limit the electrical and mechanical loads on the turbine. The power limitation, as mentioned earlier, may be by means of pitch regulation (for a variable-pitch wind turbine) or stall regulation (for the fixed-pitch wind turbine). The wind turbine is halted when the shut-down wind speed limit is exceeded (Fox *et al.*, 2007).

In the following section, the mathematical modeling of the WEC system is discussed, the components of which correspond to the subsystems of the wind power generation system presented in the preceding sections.

### 4.3.3. Model of the WEC system

Modeling of the WEC system consists in the establishment of the mathematical expressions to represent the aerodynamic, mechanical, and electrical characteristics of the wind energy generation, as the main subsystems which determine its dynamic behavior (and have been discussed generically in Section 4.3.2). The main components making up the WEC system to be modelled are depicted in Figure (4.26) (Boukhezzar & Siguerdidjane, 2005). Among the model components is also a block representing the wind speed model, which has a significant influence on the dynamic response of the WEC system.

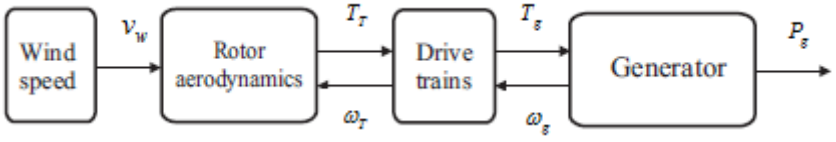


**Figure 4.23: Generic block diagram of the WEC system model. (Adapted from Boukhezzar & Siguerdidjane, 2005)**

#### 4.3.3.1. Wind speed model

The model of the wind speed signal that is commonly used in WEC system analyses is a combination of four components: a mean value; a ramp component representative of a steady increment in the mean value of the wind speed; a wind gust; and a component representative of turbulence in the wind (Slootweg *et al.*, 2003).

The wind speed ramp component is modeled as having some amplitude ( $A_r$ ), and occurring within some start- and end-time ( $t_{sr}(\sec)$ ; $t_{er}(\sec)$ ). In like manner, the wind gust is modeled as being of some amplitude ( $A_g$ ), with start-time ( $t_{sg}(\sec)$ ) and end-time ( $t_{eg}(\sec)$ ). The following expression may be used for the wind gust (Anderson & Bose, 1983):

$$\begin{aligned} t < t_{sg} \quad &: \quad v_{wg} = 0 \\ t_{sg} \le t \le t_{eg} &: \quad v_{wg} = A_g[1 - \cos(2\pi(t - t_{sg})/D_g)] \\ t_{eg} < t \quad &: \quad v_{wg} = 0 \end{aligned} \tag{4.25}$$

where $v_{wg}$ represents the wind gust signal, and $D_g(\sec)$ represents the duration of the gust (i.e. difference between $t_{eg}(sec)$ & $t_{sg}(sec)$). The turbulence in the wind may be represented as a spectral density function ( $S(f)$) for a stationary process, given by (Slootweg *et al.*, 2003):

$$S(f)=\frac{\frac{1}{\ln(h/z_o)^2}\cdot l\cdot v_w}{(1+\frac{3f\cdot l}{2v_w})^{5/3}} \tag{4.26}$$

where $h\ (m)$ represents the height above ground of the wind speed signal, $z_o$ is a measure of the landscape's roughness length, $l\ (m)$ is the turbulence length scale, and $f\ (Hz)$ represents the system fundamental frequency.

The wind speed model that incorporates the four components as presented above approaches in representation that of the wind regime in which the wind turbine is likely to operate, and is especially useful for dynamic response analyses of wind power generation. It has thus been presented here for the sake of completeness, although it is not the one implemented in the simulation case study to be considered later.

#### 4.3.3.2. Rotor aerodynamics model

The power $P_w$ available in the wind stream flowing at velocity $v_w$ has been established by means of Equation (3.3) in Section 3.3.2, which is restated below for ease of reference as:

$$P_w=\frac{1}{2}\dot{m}_a v_w^{\ 2}=\frac{1}{2}\rho A v_w^{\ 3} \tag{4.27}$$

where $\dot{m}_a$ is the air-mass flow rate ($kg/m^2$) expressed by Equation (3.2), $\rho$ is the air density ($kg/m^3$), and $A$ is the rotor swept area ($m^2$).

The wind turbine is able to extract only a fraction of the power available in the wind, and so it is necessary in the study of wind energy generation systems to establish the relation between the power available in the wind and that developed by the wind turbine through interaction with the wind (Fox *et al.*, 2007). Two parameters are defined in this regard, referred to as the power coefficient (or aerodynamic efficiency) and the tip-speed ratio. The mathematical expressions of the power coefficient (as it is related to the power developed in the turbine and that available in the wind) and the tip-speed ratio have been defined in Section 4.3.2, and are also restated here for convenience as:

$$\lambda=\frac{\omega_T R}{v_w} \tag{4.28}$$

$$C_p=\frac{P_T}{P_w} \tag{4.29}$$

where $\lambda$ represents the tip-speed ratio, $\omega_T$ represents the wind turbine rotor angular velocity, $R$ is the turbine rotor blade radius, $C_p$ denotes the power coefficient, and $P_T$ denotes the power developed in the wind turbine through interaction with the wind. Both $C_p$ and $\lambda$ are

dimensionless quantities, making them convenient for the performance characterization of wind turbines (Fox *et al.*, 2007).

The power coefficient essentially defines the power-yield performance of a given wind turbine, and is a function of a given machine's aerodynamic design. In terms of fluid mechanical physics, however, its maximum value, irrespective of the wind turbine type, is set by the Betz limit, given as 59.3%; this implies that a wind turbine can extract no more than about 59% of the power available in the wind stream (Manwel *et al.*, 2002).

The relationship between the mechanical power developed by the turbine ($P_T$) and the available wind power ($P_w$) is highly nonlinear, and this is also reflected in the model of the aerodynamic efficiency ($C_p$). The commonly used methods for characterizing the turbine's aerodynamic efficiency are based on either blade element theory or numerical approximations from analytical calculations. Because of the computational complexity associated with the blade element theory-based aerodynamic efficiency characterization, the use of nonlinear numerical approximations is more popular (Perdana, 2008; Slootweg *et al.*, 2003). One such expression that is frequently employed is given by (Cultura & Salameh, 2011):

$$C_p(\lambda,\beta) = c_1\left(\frac{c_2}{\lambda_i} - c_3\beta - c_4\right)e^{-c_5/\lambda_i} + c_6\lambda$$

$$where \quad \frac{1}{\lambda_i} = \frac{1}{\lambda + 0.08\beta} - \frac{0.035}{\beta^2 + 1} \qquad (4.30)$$

$$and \quad c_1 = 0.5176;\ c_2 = 116;\ c_3 = 0.4;\ c_4 = 5;\ c_5 = 21;\ c_6 = 0.0068;$$

The power coefficient characterization of the wind turbine based on Equation (4.30) is a nonlinear function of the tip-speed ratio ($\lambda$) and the blade pitch angle ($\beta$). Its relation to the tip-speed ratio for various values of the blade pitch angle (implemented in Matlab according to the program listing in Appendix C.2) is depicted in Figure (4.24). The figure shows that the power coefficient based on Equation (4.30) attains a maximum value of 0.48 (or 48%), which is associated with a *tip-speed ratio* of 8.1 and a *blade pitch angle* of 0°.

The output of the rotor aerodynamic model is actually the aerodynamic torque ($T_T$), which is related to the turbine mechanical power by (Boukhezzar & Siguerdidjane, 2005):

$$T_T = \frac{P_T}{\omega_T} \qquad (4.31)$$

Consideration of Equations (4.27) and (4.28) in Equation (4.31) leads to the following expression for the aerodynamic torque:

$$T_T = \frac{1}{2}\rho\pi R^3 C_T(\lambda,\beta)v_w^2 \qquad (4.32)$$

where $C_T(\lambda,\beta)$ is the torque coefficient, related to the power coefficient by the expression:

$$C_T(\lambda,\beta)=\frac{C_p(\lambda,\beta)}{\lambda} \tag{4.33}$$

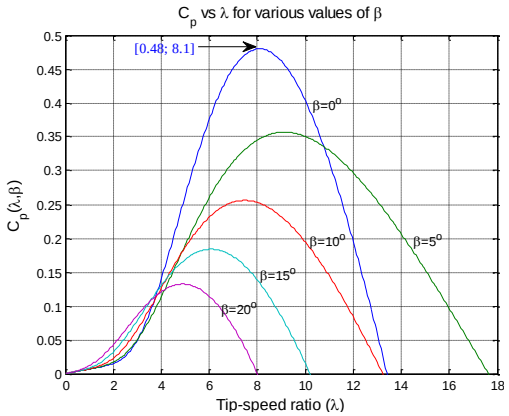


**Figure 4.24:** **Power coefficient as a function of tip-speed ration and pitch angle.**

#### 4.3.3.3. Drive train model

The dynamics of the wind turbine's drive train have a significant influence on the overall electrical and structural dynamics of the wind turbine generator, and many studies have been conducted with the goal of establishing a valid mathematical representation of these drive train dynamics (Novak *et al.*, 1994). The most common representation of the drive train dynamics is as a multi-mass system with a number of inertial masses and some spring and damper combinations (Perdana, 2008).

A rather detailed model of the drive train considers three inertial masses, these being the generator rotor, the turbine hub, and the rotor blades respectively, such as presented by Wasynczuk *et al* (1981). This, however, leads to quite a complex model, and thus the two-mass model is more commonly used, in which the drive train model is reduced to the consideration of the turbine and generator inertias, and a number of damping coefficients and stiffness constants, such as expressed by (Perdana, 2008):

$$\begin{aligned}
2H_T\frac{d\omega_T}{dt} &= T_T - K_s(\theta_g-\theta_T) - D_m(\omega_g-\omega_T)\\
2H_g\frac{d\omega_g}{dt} &= T_g + K_s(\theta_g-\theta_T) + D_m(\omega_g-\omega_T)\\
\frac{d\theta_T}{dt} &= \omega_T\\
\frac{d\theta_g}{dt} &= \omega_g
\end{aligned} \tag{4.34}$$

where $H_T$ and $H_g$ represent the turbine and generator inertia constants respectively, $K_s$ and $D_m$ represent the shaft stiffness and mutual damping coefficient respectively, $T_g$ represents

the electromagnetic torque, $\omega_g$ represents the generator rotor angular speed, and $\theta_T$ and $\theta_g$ represent the turbine and generator rotor angular positions respectively. A one-mass model can also be derived from the two-mass model represented above, by neglecting the mutual damping and the shaft stiffness, and considering the turbine and generator inertial masses as one lumped mass, which leads to the following simplified model of the drive train, adequate for steady-state dynamic analysis (Perdana, 2008):

$$2(H_T + H_g)\frac{d\omega_g}{dt} = T_T - T_g \tag{4.35}$$

#### 4.3.3.4. Electrical model

The electrical generator for the WEC system may be any one of the (squirrel-cage or wound-rotor) asynchronous, or (permanent-magnet or field-excited) synchronous types, as discussed in Section 4.3.2. The Permanent-Magnet Synchronous Generator (PMSG) has lately gained popularity both in small- and large-scale WEC system applications (Gonzalez *et al.*, 2009; Carrasco *et al.*, 2006; Cultura & Salameh, 2005), and is used here as the basis for the consideration of the electrical model.

An example of the treatment of the PMSG modeling for WEC systems application can be found in the work of Gupta and Kumar (2012). According to the authors, in the derivation of the electrical model of the PMSG, the stator flux set up by the generator's permanent magnets is normally considered to be sinusoidal, with the result that the machine internal electromotive force (emf) can be taken to be sinusoidal as well. The model equations are usually expressed in the synchronous (dq) reference frame, and basically comprise three expressions: the dynamic equations of the stator q-axis and d-axis currents, and the equation of the electromagnetic torque, represented as (Gupta & Kumar, 2012):

$$\begin{aligned}
\frac{di_{sd}}{dt} &= \frac{1}{L_{sd}}v_{sd} - \frac{R_s}{L_{sd}}i_{sd} + \frac{L_{sq}}{L_{sd}}p\omega_g i_{sq} \\
\frac{di_{sq}}{dt} &= \frac{1}{L_{sq}}v_{sq} - \frac{R_s}{L_{sq}}i_{sq} + \frac{L_{sd}}{L_{sq}}p\omega_g i_{sd} - \frac{\psi p\omega_g}{L_{sq}} \\
T_g &= \frac{3}{2}p[\psi i_{sq} + (L_{sd} - L_{sq})i_{sd}i_{sq}]
\end{aligned} \tag{4.36}$$

where $i_{sd}$, $i_{sq}$, $v_{sd}$ and $v_{sq}$ represent the d- and q-axis components of the stator current and voltage, respectively; $L_{sd}$ and $L_{sq}$ are the d- and q-axis stator inductances; $R_s$ is the stator winding resistance; $p$ is the number of magnetic poles of the machine; $\omega_g$ is the generator rotor angular velocity; $\psi$ is the permanent magnet-induced stator winding flux; and $T_g$ represents the electromagnetic torque of the generator.

In the section that follows, the implementation of a small-scale WEC system based on the Permanent-Magnet Synchronous Generator (PMSG) in the Matlab/Simulink software development environment is presented. By comparing the mathematical models presented above with the generic block diagram in Figure (4.23), it can be observed that each of the blocks has been covered, from the wind speed model in Section 4.3.3.1 through to the generator model in Section 4.3.3.4. The WEC system implementation in the following section considers adaptations of the models presented above (and the details of implementation are discussed further in the same section), except for the generator model, which is present in the simulation environment.

### 4.3.4. Matlab/Simulink implementation of the WEC system model

The SimPowerSystems Blockset in the Simulink simulation software development environment provides models for many of the components of the WEC system to be simulated, such as the PMSG, power electronic devices, and loads. Thus only the models of the wind speed and the aerodynamic subsystems (with the drive-train dynamics implicitly incorporated) have had to be devised in SimPowerSystems in order to have the complete simulation model of the WEC system.

To implement the aerodynamic subsystem model, the aerodynamic characteristics of the Gaia-11kW wind turbine (Huskey *et al.*, 2009) have been used. This is a two-bladed, fixed-pitch (thus stall-regulated), narrow-range variable-speed wind turbine that is optimized for power generation in low-to-medium wind speed regimes. The performance coefficient, power yield, and turbine rotor speed of the Gaia-11kW wind turbine have been plotted in Figure (4.25), and the related turbine data can be found in Appendix C.2.

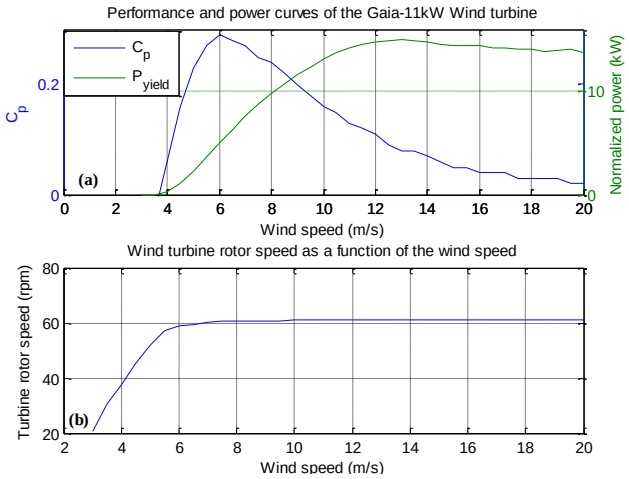


**Figure 4.25: Performance characteristics of the Gaia-11 kW wind turbine. (a) aerodynamic performance and power yield over the operating range; (b) corresponding turbine rotor speed.**

From Figure (4.25), it can be observed that the turbine is designed to operate at optimal aerodynamic efficiency in the low-wind speed range, such that the power coefficient curve

increases monotonically from cut-in speed (about 3 m/s) up to about 6 m/s, when it starts decreasing, an indication of the reduction in the turbine's aerodynamic performance. The turbine has a rated wind speed of 9.5 m/s, and may be operated at variable rotor speed so as to maintain optimal aerodynamic performance, up to the rated wind speed. Beyond the rated wind speed, the rotor speed is kept constant (Figure 4.25b) in order to diminish the aerodynamic performance, and thus limit the power developed by the turbine. The turbine has a cut-out speed of 25 m/s (not depicted in the figure), beyond which the turbine is stalled into standstill, because the loads due to the excessively high wind speed exceed the design loads of the machine.

In the simulation model of the WEC system, a wind speed signal that incorporates the mean and ramp components of the wind speed model discussed in Section 4.3.3.1 has been used, to facilitate the steady-state performance evaluation of the system. Together with the measured generator rotor speed, they constitute the input data for the aerodynamic subsystem model, whose output is the aerodynamic torque (scaled by the speed conversion ratio) that is applied to the PMSG for electric power generation.

In implementing the aerodynamic subsystem model, a one-dimensional look-up table has been used to derive the optimal power coefficient characteristic, $C_p$, which employs the wind speed signal input and the turbine characteristic data relating the power coefficient to the wind speed (as depicted in Figure 4.25a). The derived value for power coefficient is used in Equation (4.29) to obtain the mechanical power developed by the turbine ($P_T$), the power available in the wind ($P_w$) being obtained by means of Equation (4.27). The aerodynamic torque is then obtained using Equation (4.31), which is scaled by the speed ratio of the drive train to finally provide the (generator) torque that is applied to the PMSG so as to generate the electric power.

Figure (4.26) depicts the simulation model for the WEC system that has been implemented in Simulink. A simple simulation case has been set up, in which the PMSG-based WEC system supplies a stand-alone DC load to which it is interfaced by means of a diode rectifier. The intention has been to study the response of this system when so operated as to follow the optimal-aerodynamic-performance characteristic, as discussed above.

The response of the system depicted in Figure (4.26) is summarized in Figures (4.27) and (4.28). Figure (4.27a) depicts the wind speed signal that has been used to test the system response, which comprises mean as well as ramp components, as mentioned earlier. Based on this wind speed signal, the look-up table used to implement the power coefficient function (in this case as a function of the wind speed, that is $C_p(P_w)$) outputs the optimal characteristic curve depicted in Figure (4.27b).

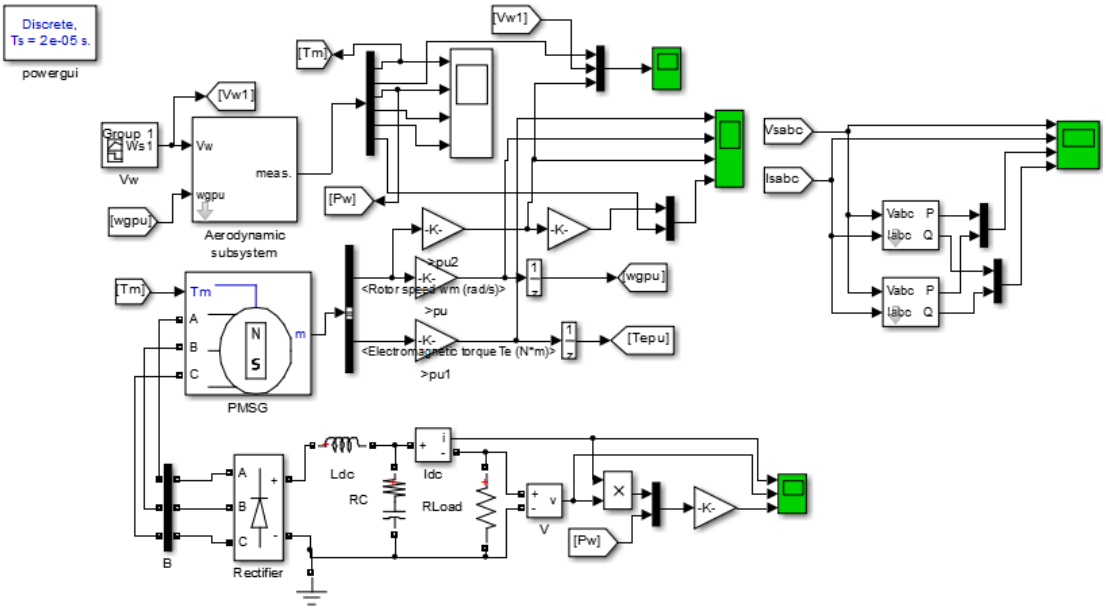


**Figure 4.26:** Simulation diagram for the WEC system in Simulink.

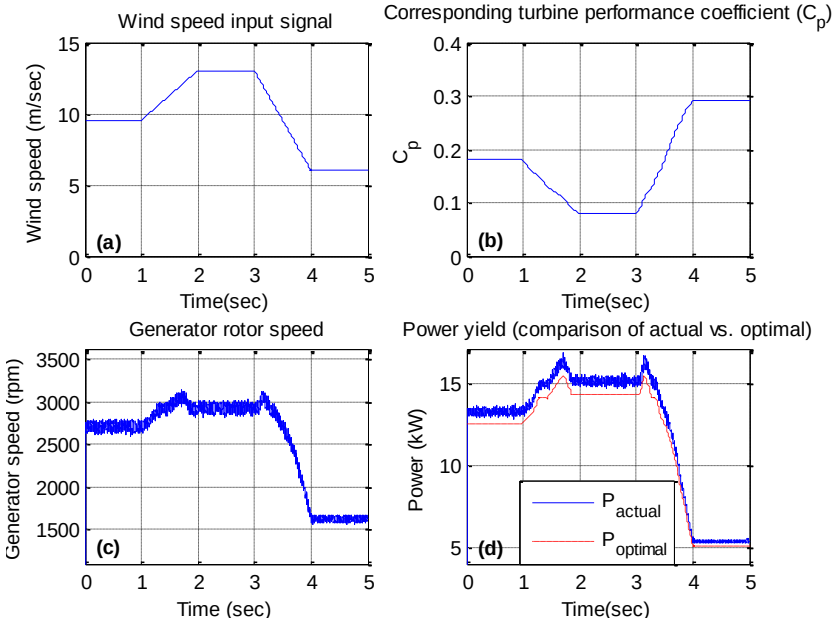


**Figure 4.27:** Performance response of the WEC system. (a) wind speed input signal; (b) optimal power coefficient characteristic; (c) generator rotor speed; (d) generator power yield compared with the optimal yield.

It can be observed from Figure (4.27b) that in the time interval [1 sec-2 sec], the power coefficient decreases, because during this interval the wind speed is on a steady increase, and also lies above the turbine rated wind speed. The power coefficient then increases in the time interval [3 sec-4 sec] as the wind speed decreases, indicating an increase in the turbine aerodynamic efficiency. The turbine has a maximum aerodynamic efficiency of about 29% (well below the Betz limit of 59.3%), which coincides with the wind speed and generated power of 6 m/s and 3.88 kW respectively (and thus does not actually occur at the maximum power yield-point of the turbine.

The generator speed depicted in Figure (4.27c) shows that it varies in proportion with the wind speed variations, which is necessary to maintain the optimal tip-speed ratio, as can be deduced from Equation (4.28).

The comparison of the actual power yield of the turbine with the expected optimal yield (based on the turbine characteristic) demonstrates that the system is operating to yield the maximum possible power within the confines of its design specifications. Thus without implementing any complex control system, the maximum-power extraction operation of the WEC system is realized in this simulation case simply by driving the generator with the optimal torque characteristic over the operating range of the system. Of course this is enabled by the precise knowledge of the system characteristics. Where such precise knowledge is not available (as often is the case in practice), the design of an effective control system, based on the known dynamics of the plant, becomes critical to the optimal operation of the system.

The generator terminal voltage and current supplied to the load are depicted in Figure (4.28). It is evident from the distortion observable in both the voltage and current that a simple simulation case such as considered in this section would fall far short of meeting the requirements for a practical system, and would require additional components for waveform shaping, among other functions.

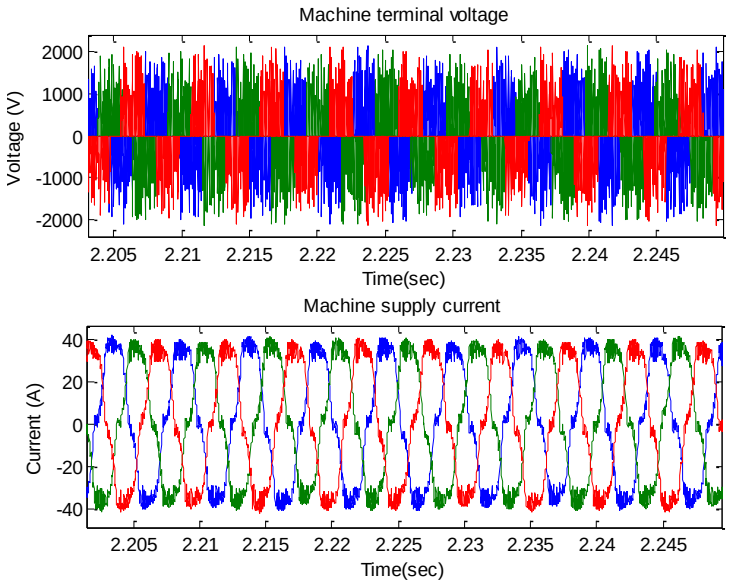


**Figure 4.28: Terminal voltage and generated current of the PMSG-based WEC system.**

## 4.4. Conclusion

The main focus in this chapter has been to establish valid mathematical models for the analysis and controller design of Photovoltaic (PV) and Wind Energy Conversion (WEC) systems as the two key renewable energy sources. The models developed incorporate the necessary dynamics to facilitate the study of the operational and control characteristics of

these systems, which is applicable to both grid-integrated and stand-alone renewable power generation systems.

It has been observed that although the PV and WEC systems are both intermittent renewable energy sources, their modeling and operational characteristics are markedly different. The PV generator on the one hand is a static energy conversion system that generates DC power, and is mainly based on solid-state electronics. The wind power generator, on the other hand, is a multi-subsystem energy conversion system that generates AC power, and usually incorporates both rotational subsystems as well as solid-state electronic systems. These considerations are vital, especially when the intention is to design the Hybrid Distributed Power Generation (HDPG) system that has been briefly discussed in Chapter 3. The approach taken in this chapter has been to move from the general (in terms of discussing the generic characteristics of each of the considered systems) to the particular (looking at the model implementation of a sample case study). The developed models have been validated by computer simulations, and comparison of the simulation results with the previous work of other authors.

The intention for developing the models for the renewable energy generation systems (as dealt with in this chapter) is to study their integration into the electric grid (at least in the context of this thesis). Power electronic converter interfaces (particularly the inverter) play a key role in the grid integration, and the following chapter thus looks at the modelling of the inverter as a power conditioning and control device for the grid-integrated Distributed Power Generation (DPG) system.

# CHAPTER 5

# INVERTER MODEL FOR CURRENT-MODE CONTROL DESIGN

## 5.1 Introduction

An inverter plays a very significant role as the interface between a Distributed Power Generation (DPG) system and the utility grid or an autonomous load. This applies especially to Distributed Energy Resources (DER) that generate DC power, such as Photovoltaic (PV) and Fuel Cell power systems, which requires the transformation of the DC power to AC power at the frequency and magnitude suitable for grid integration (Liserre *et al.*, 2010). Even the DPG systems that generate AC power, but at frequencies not directly compatible with the grid, such as Microturbines and variable-speed Wind Energy Conversion (WEC) systems, do require the use of an inverter as a power conditioning and interface unit.

In acting as the interface for the DPG system to the grid, the inverter has as its main task the control of the power transfer from the DC bus to the AC bus. A control strategy to realize this power transfer is developed on the basis of the model of the inverter and its associated filter interface (Teodorescu *et al.*, 2011; Wang, 2006). Thus, as a preliminary step to the inverter controller design task dealt with in the subsequent two chapters, a model that is suitable for controller design is discussed and presented in this chapter.

With the ever-increasing scope of power inverter applications in electrical power processing, inverter design has continued to attract a lot of research interest for some decades now (Yazdani & Iravani, 2010). This is typically reflected in the wide variety of inverter designs and topologies that are available, some commercially, others under research and development. A generic (and certainly not comprehensive) classification of common inverter types is illustrated in Figure (5.1). The inverter considered in this study is the two-level, three-phase Voltage-Source Inverter (VSI), which is generally the preferred choice for the coupling of DPG systems to the grid or to a load at medium to high power levels (Mohan *et al.*, 2003). For medium to high power levels, three-phase two-level inverters give satisfactory performance in terms of power quality and power handling capability relative to cost and component count, among other desirable characteristics (Evyu, 2006).

The material discussed in this chapter is mainly focused on the highlighted part of Figure (5.2) (*i.e.* the inverter & the filter interface). Figure (5.2) depicts a generic representation of the DPG interfaced to an arbitrary load by means of the inverter-filter interface combination. The inverter uses fast-switching Power Electronic switches to modulate its output voltage, thereby converting the DC voltage at its input terminals to an equivalent AC output voltage (Mohan *et al.*, 2003). The filter interface attenuates the high-frequency harmonics, generated by the high-frequency switching action of the inverter, from the inverter output voltage. This is necessary for the inverter output power to satisfy the power quality requirements stipulated in the grid

codes. The main task of the grid-inverter control system (discussed in the following chapter) is to regulate the inverter's DC input voltage and AC output current, both of which require suitable plant models for the controller design task.

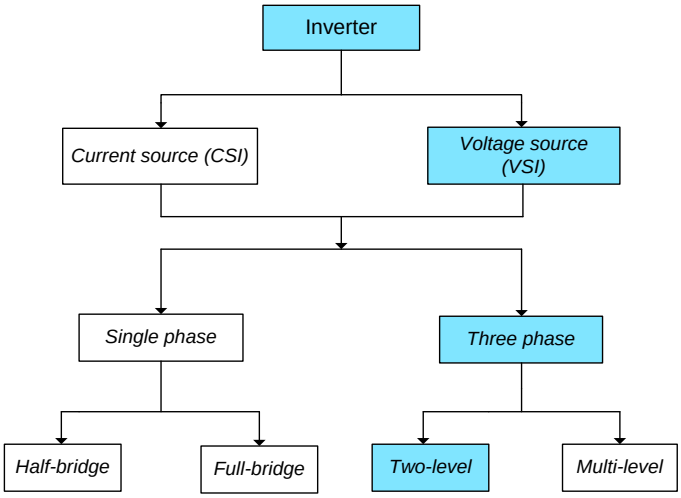


**Figure 5.1:** **Inverter generic classification**

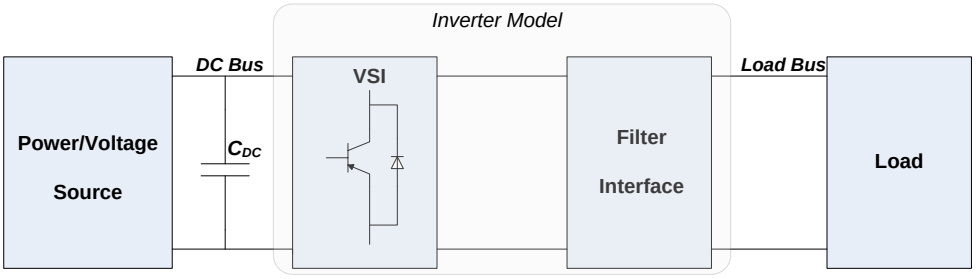


**Figure 5.2:** **Generic block diagram for the Distributed Power Generation system interfaced to a load.**

As Figure (5.2) well illustrates, the filter is the actual interface of the DPG to the load. The topology chosen for it highly influences the dynamics of the inverter current control system, and as a consequence of this, it merits detailed consideration in the development of the inverter model for current controller design (Teodorescu *et al.*, 2011). In developing the inverter model for the controller design, the work presented in this chapter is outlined as follows.

In Section 5.2, passive filter topologies that are commonly employed in low- to medium-power converter interfaces are briefly discussed, from which the topology to be implemented in this thesis is chosen. A mathematical model of the chosen filter topology is then presented in Section 5.3, as it forms the basis for the derivation of the plant model for the inverter output current control system. Subsequent to that, the inverter model is developed in Section 5.4, taking into account an averaged equivalent model of the inverter switched output voltage and the filter mathematical model presented in Section 5.3. The plant model for the inverter (DC) input voltage regulation is addressed next, in Section 5.5. Then in Section 5.6, parameters for

the filter interface are determined, which are useful in the inverter controller design task. Section 5.7 concludes the chapter with a highlight of the main results of the work discussed in the chapter.

As is discussed further in subsequent sections, the main control objective of the system in Figure (5.2) is to regulate the current output (for the grid-connected system) or the terminal voltage (for the stand-alone system) of the filter, which requires deriving a control transfer function between the relevant output and input parameters of the filter interface.

## 5.2. Common filter topologies

Three of the commonly used filter configurations for interfacing the inverter to the utility grid or to a load are depicted in Figures (5.3)-(5.5).

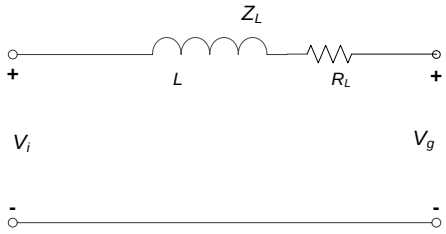


**Figure 5.3:** L filter

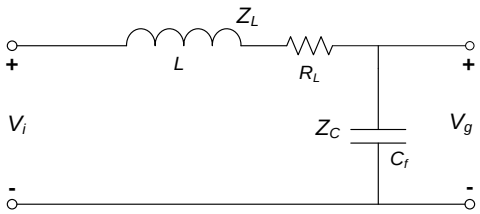


**Figure 5.4:** LC filter

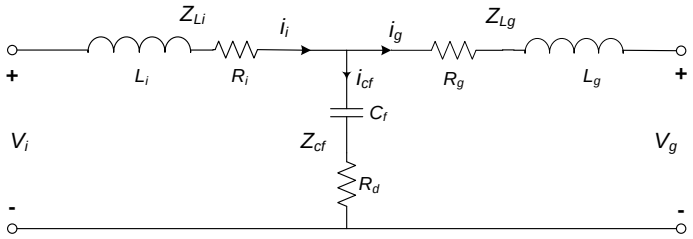


**Figure 5.5:** LCL filter.

The symbols in Figures (5.3)-(5.5) are defined as follows: $V_i$ = inverter output (filter input) voltage; $V_g$ = grid voltage; $L$ = filter inductor; $R_L$ = inductor parasitic resistance; $Z_L$ = (L & LC) filter inductive impedance; $C_f$ = filter capacitance; $Z_C$ = LC filter capacitive impedance; $L_i$ = LCL filter inverter-side inductance; $R_i$ = LCL-filter inverter-side inductor parasitic resistance; $Z_{Li}$ = LCL-filter inverter-side inductive impedance; $L_g$ = LCL filter grid-side inductor; $R_g$ = LCL-filter grid-side inductor parasitic resistance; $Z_{Lg}$ = LCL-filter grid-side

inductive impedance; $R_d$ = LCL filter damping resistor; $Z_{cf}$ = LCL filter shunt impedance; $i_i$ = inverter output (filter input) current; $i_{cf}$ = LCL filter shunt branch current; and $i_g$ = grid current. A short description of these three filter configurations is presented below.

### 5.2.1. L filter

The L filter (Figure 5.3) constitutes the simplest configuration for a current-harmonic-attenuation filter. It has a first-order (20dB/dec) attenuation characteristic, is simple to design, and exhibits no stability issues in terms of the dynamic response. As a first-order filter, however, it provides comparatively low attenuation, and may need to be very large in size in order to guarantee sufficient harmonic attenuation, which may be undesirable from the losses and physical design point of view. It may be suitable for use in high switching-frequency applications, where switching harmonics are relatively easier to handle, especially with its positive aspect of not being prone to the resonance problems faced in higher-order filters (Lettl *et al.*, 2011).

### 5.2.2. LC filter

Adding a shunt capacitor to the L-filter output terminals leads to an LC filter (Figure 5.4), with a second-order attenuation characteristic, and consequently improved harmonic attenuation. The LC filter is characterized by peak gain at resonance frequency, having zero gain below it, and a 40dB/dec roll-off beyond the resonance frequency. One drawback of the LC filter is that it exhibits variable resonance frequency when connected to a stiff grid whose impedance may be subject to variations, which may in turn make the stable control of the system problematic. In the LCL filter configuration, discussed next, this problem is less pronounced.

### 5.2.3. LCL filter

The LCL filter is depicted in Figure (5.5) (with the passive damping resistor in series with the filter capacitor). It adds a series inductor to the LC filter output terminals, and this enables the design of the filter parameters in a way that largely decouples the filter dynamics from the grid impedance variations. The LCL filter is a third-order filter, providing an attenuation of 60dB/dec for frequencies beyond its resonance frequency. It thus provides comparatively superior harmonic attenuation for a given switching frequency. Other desirable characteristics of the LCL filter are (Ahmed *et al*., 2007):

- the possibility to use a lower switching frequency for a given harmonic attenuation requirement;
- lower output current distortion due to lower reactive energy storage;
- good current ripple attenuation for lower filter component values, thus higher efficiency at lower cost; and
- lower current ripple across the grid inductor.

Despite having many desirable characteristics, one major limitation of the LCL filter is the requirement for very precise parameter design to ensure satisfactory steady-state and dynamic performance. Being a third-order filter, it introduces resonance issues that necessitate both proper damping and more complex controller design. This is mainly a result of the filter's additional poles and zeros which, if not properly compensated for, may cause poor harmonic attenuation, even unstable behavior (in the form of oscillations). Properly designed though, the LCL filter may be the best alternative for satisfying power quality requirements for grid inverters (Teodorescu *et al*., 2011).

The LCL filter has been chosen for implementation in this study, due to the advantages highlighted above. Design guidelines that minimize the filter's adverse characteristics have been suggested in the reviewed literature, and are consulted in carrying out this task.
The mathematical model of the LCL filter is thus considered in greater detail in the next section, as a preliminary step in the development of the inverter model for controller design.

## 5.3. Mathematical model of the LCL filter

The LCL filter's electrical equivalent circuit in Figure (5.6) allows the application of Kirchhoff's current and voltage laws to derive the relevant input-output voltage and current relations, which in turn form the basis for the inverter model for controller design. For the current-mode controller design (adopted for the grid-connected inverter), for instance, the control plant considered is the inverter current-inverter voltage transfer function (Teodorescu *et al*., 2011), while current harmonic analysis requires the grid current-inverter current transfer function, and both these transfer functions are obtainable from the filter voltage-current expressions.

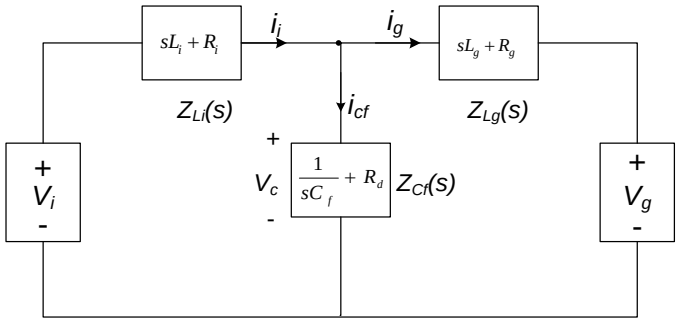


**Figure 5.6: LCL filter electrical equivalent model.**

The relevant transfer functions required for the LCL filter dynamic analysis can also be directly derived from Figure (5.6) using the filter component impedances depicted in the circuit diagram, as presented later. The circuit variables appearing in Figure (5.6) are defined in Table (5.1).

**Table 5.1: Definition of symbols for Figure 5.6**

| Symbol | DEFINITION |
|---|---|
| $V_i$ | Filter input (inverter output) voltage |
| $V_g$ | Filter output voltage |
| $V_c$ | Filter capacitor voltage |
| $i_i$ | Filter input (inverter output) current |
| $i_{cf}$ | LCL-filter shunt branch current |
| $i_g$ | Grid current |
| $Z_{Cf}$ | Filter capacitor impedance |
| $Z_{Li}$ | Inverter-side filter inductor impedance |
| $Z_{Lg}$ | Grid-side filter inductor impedance (encompasses transformer, line and grid source impedances) |

Based on Figure (5.6), expressions relating circuit voltages and currents (considering a symmetrical three-phase system) can be derived as follows.

For the filter input loop:

$$v_{iabc} - L_i \frac{d}{dt}(i_{iabc}) - R_i i_{iabc} - R_d(i_{iabc} - i_{gabc}) - v_{cabc} = 0 \tag{5.1}$$

For the filter output loop:

$$v_{cabc} + R_d(i_{iabc} - i_{gabc}) - R_g i_{gabc} - L_g \frac{d}{dt}(i_{gabc}) - v_{gabc} = 0 \tag{5.2}$$

And for the node at the shunt branch:

$$i_{cabc} = i_{iabc} - i_{gabc} = C_f \frac{d}{dt}(v_{cabc}) \tag{5.3}$$

where $v_{iabc}$, $v_{gabc}$, $v_{cabc}$, $i_{iabc}$, $i_{gabc}$ and $i_{cabc}$ represent the three-phase signals of the inverter output (filter input) voltage, filter capacitor voltage, filter output voltage, filter capacitor voltage, inverter output (filter input) current, filter output current, and filter capacitor current, respectively.

Using the state vector:

$$\boldsymbol{x} = [i_{iabc} \quad i_{gabc} \quad v_{cabc}]^T \tag{5.4}$$

And the input vector:

$$\boldsymbol{u} = [v_{iabc} \quad v_{gabc}]^T \tag{5.5}$$

Equations (5.1)-(5.3) can be represented in state space form as:

$$\dot{\boldsymbol{x}} = \boldsymbol{A}\boldsymbol{x} + \boldsymbol{B}\boldsymbol{u} \tag{5.6}$$

That is:

$$\frac{d}{dt}\begin{bmatrix} i_{iabc} \\ i_{gabc} \\ v_{cabc} \end{bmatrix} = \begin{bmatrix} -\frac{R_i + R_d}{L_i} & \frac{R_d}{L_i} & -\frac{1}{L_i} \\ \frac{R_d}{L_g} & -\frac{R_g + R_d}{L_g} & \frac{1}{L_g} \\ \frac{1}{C_f} & -\frac{1}{C_f} & 0 \end{bmatrix} \cdot \begin{bmatrix} i_{iabc} \\ i_{gabc} \\ v_{cabc} \end{bmatrix} + \begin{bmatrix} \frac{1}{L_i} & 0 \\ 0 & -\frac{1}{L_g} \\ 0 & 0 \end{bmatrix} \cdot \begin{bmatrix} v_{iabc} \\ v_{gabc} \end{bmatrix} \tag{5.7}$$

The system in Equation (5.7) represents a mutual-coupling-free, symmetrical three-phase system that is in essence comprised of nine first-order differential equations (Yazdani & Iravani, 2010). When transformed into an equivalent two-phase system (useful in reducing the order of the system to simplify analysis and control design), the system order reduces to six differential equations, and in the synchronous (dq0) reference frame, the system is as expressed by Equation (5.8):

$$\frac{d}{dt}\begin{bmatrix} i_{id} \\ i_{iq} \\ i_{gd} \\ i_{gq} \\ v_{cd} \\ v_{cq} \end{bmatrix} = \begin{bmatrix} -\frac{R_i + R_d}{L_i} & \omega & \frac{R_d}{L_i} & 0 & -\frac{1}{L_i} & 0 \\ -\omega & -\frac{R_i + R_d}{L_i} & 0 & \frac{R_d}{L_i} & 0 & -\frac{1}{L_i} \\ \frac{R_d}{L_g} & 0 & -\frac{R_g + R_d}{L_g} & \omega & \frac{1}{L_g} & 0 \\ 0 & \frac{R_d}{L_g} & -\omega & -\frac{R_g + R_d}{L_g} & 0 & \frac{1}{L_g} \\ \frac{1}{C_f} & 0 & -\frac{1}{C_f} & 0 & 0 & \omega \\ 0 & \frac{1}{C_f} & 0 & -\frac{1}{C_f} & -\omega & 0 \end{bmatrix} \begin{bmatrix} i_{id} \\ i_{iq} \\ i_{gd} \\ i_{gq} \\ v_{cd} \\ v_{cq} \end{bmatrix} + \begin{bmatrix} \frac{1}{L_i} & 0 & 0 & 0 \\ 0 & \frac{1}{L_i} & 0 & 0 \\ 0 & 0 & -\frac{1}{L_g} & 0 \\ 0 & 0 & 0 & -\frac{1}{L_g} \\ 0 & 0 & 0 & 0 \\ 0 & 0 & 0 & 0 \end{bmatrix} \begin{bmatrix} v_{id} \\ v_{iq} \\ v_{gd} \\ v_{gq} \end{bmatrix} \tag{5.8}$$

The significance of Equation (5.8) is that it also depicts the cross-coupling that exists between the d- and q-axis quantities as a result of the transformation from the natural (abc) to the synchronously rotating (dq0) reference frame, and it is important to take this cross-coupling into account in the dq0-based inverter current controller design.

For the purpose of analyzing the dynamic performance of the filter, some transfer functions relating the filter output and input voltages and currents can be derived on the basis of applying Kirchhoff's laws to Figure (5.6), and omitting inductor resistors (Teodorescu *et al*., 2011; Ahmed *et al*., 2007).

The filter input current-input voltage transfer function is defined as (Evyu, 2006):

$$G_{i_i v_i}(s) = \frac{i_i(s)}{v_i(s)} = \frac{Z_{Lg}(s) + Z_{Cf}(s)}{Z_{Cf}(s) \cdot (Z_{Li}(s) + Z_{Lg}(s)) + Z_{Li}(s) \cdot Z_{Lg}(s)} \tag{5.9}$$

The filter input current-grid voltage transfer function is defined as:

$$G_{i_i v_g}(s) = \frac{i_i(s)}{v_g(s)} = \frac{Z_{Cf}(s)}{Z_{Cf}(s)\cdot(Z_{Li}(s)+Z_{Lg}(s))+Z_{Li}(s)\cdot Z_{Lg}(s)} \tag{5.10}$$

The grid current-filter input voltage transfer function is also given by Equation (5.10). That is:

$$G_{i_g v_i}(s) = \frac{i_g(s)}{v_i(s)} = \frac{Z_{Cf}(s)}{Z_{Cf}(s)\cdot(Z_{Li}(s)+Z_{Lg}(s))+Z_{Li}(s)\cdot Z_{Lg}(s)} \tag{5.11}$$

The grid current-grid voltage transfer function is defined as:

$$G_{i_g v_g}(s) = \frac{i_g(s)}{v_g(s)} = \frac{Z_{Li}(s)+Z_{Cf}(s)}{Z_{Cf}(s)\cdot(Z_{Li}(s)+Z_{Lg}(s))+Z_{Li}(s)\cdot Z_{Lg}(s)} \tag{5.12}$$

The grid current-filter input current transfer function is defined as:

$$G_{i_g i_i}(s) = \frac{i_g(s)}{i_i(s)} = \frac{Z_{Cf}(s)}{Z_{Lg}(s)+Z_{Cf}(s)} \tag{5.13}$$

And the filter capacitor voltage-filter input voltage transfer function is defined as:

$$G_{v_c v_i}(s) = \frac{v_c(s)}{v_i(s)} = \frac{Z_{Cf}(s)\cdot Z_{Lg}(s)}{Z_{Cf}(s)\cdot(Z_{Li}(s)+Z_{Lg}(s))+Z_{Li}(s)\cdot Z_{Lg}(s)} \tag{5.14}$$

The transfer functions above are presented on account of their usefulness, both for the inverter controller design as well as the filter dynamic response analysis, and are valid for both the undamped and passively damped LCL filters. The impedances are as they appear in Figure (5.6).

Equation (5.9) expresses the dynamics of the inverter output (filter input) current as a function of the inverter output (filter input) voltage, and forms the basis for the inverter current-mode controller design (Teodorescu *et al*., 2011). Equation (5.13) expresses the dynamics of the grid current as a function of the inverter output current, and is later used in the LCL filter parameter design for analyzing and specifying the ripple attenuation factor of the filter.

The model for the inverter current-mode controller design is presented in the following two sections.

## 5.4. Averaged inverter model for the current loop controller design

Due to the high-frequency Pulse-Width Modulation (PWM), the inverter output voltage is a switched signal that contains a fundamental component as well as high-frequency components around the switching frequency. Filtering normally takes care of the harmonic components, and if designed correctly, these harmonics can be neglected in the steady-state analysis, such that an averaged value of the inverter output voltage is considered. The averaged inverter output voltage, as a function of the DC-link voltage ($V_{DC}$) and the averaged switching function for the inverter switches ($\overline{m}_{abc}$), can be expressed as (Yazdani & Iravani, 2010):

$$\bar{v}_{iabc} = \bar{m}_{abc} \cdot \frac{1}{2} V_{DC} \tag{5.15}$$

It is worth keeping in mind that the inverter voltage that appears in the inverter model is taken to be that expressed by Equation (5.15). This equation also shows that the inverter basically regulates the terminal voltage in relation to the DC-link voltage by means of switch modulation, represented by the switching function. Since in grid-connected mode it is the current rather than the voltage that the inverter may regulate, as per grid code specifications (IEEE-1547, 2003), the purpose of the controller design for the grid-connected inverter is to regulate the inverter output current as a function of the inverter terminal voltage. Thus, the model for the grid-inverter controller design is the *inverter-output-current-to-inverter-output-voltage* transfer function, derived from the filter model.

Equation (5.8) represents the LCL filter model in the dq0 reference frame, and the desired inverter model is derived from it, because the dynamics of the inverter current control are mainly determined by the filter interface. The first two rows of Equation (5.8) provide the relation between the inverter output current and the inverter output voltage in the dq0 reference frame, which can be written as:

$$L_i \frac{di_{id}}{dt} = v_{id} - R_i i_{id} + \underline{\omega L_i i_{iq} - v_{cd}} + \underline{\underline{R_d (i_{gd} - i_{id})}} \tag{5.16a}$$

$$L_i \frac{di_{iq}}{dt} = v_{iq} - R_i i_{iq} - \underline{\omega L_i i_{id} - v_{cq}} + \underline{\underline{R_d \left(i_{gq} - i_{iq}\right)}} \tag{5.17a}$$

Equations (5.16a) and (5.17a) constitute the inverter current control plant model, in which the controlled state variables can be taken to be the d-axis and q-axis components of the inverter current ( $i_{id}$ & $i_{iq}$ ), the d-axis and q-axis components of the inverter voltage ( $v_{id}$ & $v_{iq}$ ) being the control inputs, and the underlined terms considered to be disturbances to the control system (Evyu, 2007).

The terms with double underscores are due to the shunt branch of the filter. For steady-state analysis and controller design, the influence of the shunt branch of the filter can be assumed to be negligible within the control bandwidth of interest, provided that the filter capacitor has a small value, since its main role in the system is to provide a low impedance path to ground for the switching-frequency harmonics, so that they are not injected into the grid (Wang, 2006). Thus the terms with the double underscore may be omitted from Equations (5.16a) and (5.17a) without much loss of accuracy, leading to the expressions:

$$L_i \frac{di_{id}}{dt} = v_{id} - R_i i_{id} + \underline{\omega L_i i_{iq} - v_{cd}} \tag{5.16b}$$

$$L_i \frac{di_{iq}}{dt} = v_{iq} - R_i i_{iq} - \underline{\omega L_i i_{id} - v_{cq}} \tag{5.17b}$$

The terms with the single underscores in Equations (5.16b) and (5.17b) are each made up of a cross-coupling component ( $\omega L_i i_{iq}$ , $\omega L_i i_{id}$ ) due to the axis transformation and a component that can be considered to be a disturbance ( $v_{cd}$ , $v_{cq}$ ) to the control system. It is desirable to achieve the independent control of the d-axis and q-axis inverter current control loops, and this is conventionally attained by means of decoupling and feed-forward compensation (Milosevic, 2003), as elaborated on further in Chapter 6. Two new variables, $v'_{id}$ and $v'_{iq}$, can be introduced that represent the effect of implementing the decoupling and feed-forward compensation, expressed by:

$$v'_{id} = -\omega L_i i_{iq} + v_{cd} \tag{5.18}$$

$$v'_{iq} = \omega L_i i_{id} + v_{cq} \tag{5.19}$$

If Equations (5.18) and (5.19) are added to Equations (5.16b) and (5.17b) respectively, with some rearrangements, the following expressions are obtained:

$$L_i \frac{di_{id}}{dt} + R_i i_{id} = v_{id} \tag{5.20a}$$

$$L_i \frac{di_{iq}}{dt} + R_i i_{iq} = v_{iq} \tag{5.21a}$$

In keeping with Equations (5.16a) and (5.17a), Equations (5.20a) and (5.21a) represent the dynamic model of the inverter current control system, in which $i_{id}$ and $i_{iq}$ are the controlled state variables, subject to the control input variables $v_{id}$ and $v_{iq}$.

In arriving at the dynamic model of the inverter current control system represented by Equations (5.20a) and (5.21a), the shunt branch of the LCL filter interface (Figure 5.5) has been neglected, for the reason mentioned earlier. Thus looking at the LCL filter circuit representation in Figure (5.5), the neglect of the shunt branch implies that the effective inductance, $L_{eff}$ , and parasitic resistance, $R_{eff}$ , of the filter interface are obtained from the addition of the corresponding inverter-side and grid-side inductance ( $L_i$ , $L_g$ ) and resistance ( $R_i$ , $R_g$ ) values. That is:

$$L_{eff} = L_i + L_g \tag{5.20b}$$

$$R_{eff} = R_i + R_g \tag{5.21b}$$

The $L_{eff}$ and $R_{eff}$ given by Equations (5.20b) and (5.21b) can thus replace the $L_i$ and $R_i$ in Equations (5.20a) and (5.21a) respectively. Taking this into account, Equations (5.20a) and (5.21a) can be expressed in the Laplace domain as:

$$\frac{i_{id}(s)}{v_{id}(s)} = \frac{1}{sL_{eff} + R_{eff}} \tag{5.20c}$$

$$\frac{i_{iq}(s)}{v_{iq}(s)} = \frac{1}{sL_{eff} + R_{eff}} \tag{5.21c}$$

It can be noticed from Equations (5.20c) and (5.21c) that the transfer functions of the d-axis and q-axis inverter current control loops are identical, which is made possible by the decoupling and feed-forward compensation technique used in implementing this control strategy. This is one of the positive aspects of the decoupled dq-framed-based inverter current control strategy. Not only does it enable the independent control of the d-axis and q-axis loops, the controller design task is further simplified by the fact it is only necessary to design one controller, which is equally applicable to both loops because of their being structurally identical.

Thus in the place of Equations (5.20c) and (5.21c), a single transfer function that is representative of both control loops, or equivalently, representative of the plant model for the inverter current controller design, can be written as:

$$\frac{i_i(s)}{v_i(s)} = \frac{1}{sL_{eff} + R_{eff}} \tag{5.22}$$

where $i_i(s)$ is the inverter output current, $v_i(s)$ is the inverter output voltage, $L_{eff}$ and $R_{eff}$ are the effective inductance and resistance of the filter interface.

Another one of the positive aspects of the decoupled dq-frame-based inverter current controller design is apparent from the plant model (Equation 5.22), which is effectively a first-order transfer function, and thus permits the use of less complex compensators than might be required if control were designed in the natural reference frame.

It may perhaps just be mentioned that the current controller plant model expressed by Equation (5.22) could also be obtained directly (and perhaps more straight-forwardly) from Equation (5.9) by making the same assumptions made in the above analysis, and making the relevant substitutions. The added benefit of the derivation based on Equation (5.8) is that it depicts the decoupling and feed-forward compensation that has to be implemented in the overall control system.

## 5.5. Model for DC-link voltage regulation

The grid inverter is controlled to transfer power from the DC link to the grid. In the event that the DC link is supplied by a variable power source, as would be the case with renewable-based DPG, the inverter also has to regulate the DC link voltage, which would be subject to variations in proportion to the generated power variations. In this section, the dynamic model

that forms the basis for the DC-link voltage regulation is developed, considering DC type variations, based on the work of Yazdani and Iravani (2010).

**Dynamic model of the DC link**

The approach commonly used in analyzing DC link dynamics is to consider the power balance between the power source (DPG in this case) and the grid. Figure (5.7) depicts the DPG interfaced to the grid through a three-phase inverter. From this circuit, a power balance expression for the DC link, assuming the inverter to be ideal, can be formulated as (Yazdani & Iravani, 2010):

$$\frac{d}{dt}\left(\frac{1}{2}CV_{DC}{}^{2}\right) = P_{DPG} - P_{loss} - P_i \tag{5.23}$$

where $P_{DPG}$, $P_{loss}$ and $P_i$ represent the power supplied to the DC link, the power loss at the DC link, and the power on the AC side of the inverter, respectively. $V_{DC}$ is the voltage across the DC link, whereas $C$ is the capacitance of the DC-link capacitor.

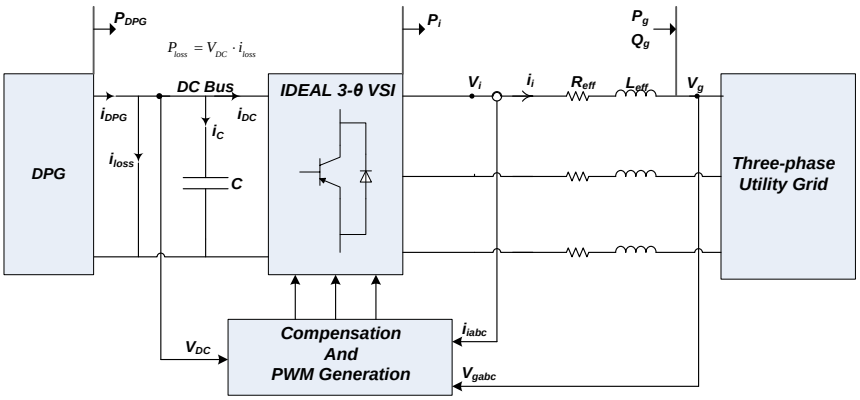


**Figure 5.7: Schematic diagram of the grid-integrated inverter-based DPG system.**

According to Equation (5.23), $V_{DC}{}^{2}$ can be considered to be the controlled variable, $P_i$ the control input (determining the power injected into the grid, less the losses incurred in the grid coupling inductor), $P_{DPG}$ and $P_{loss}$ disturbances to the DC link voltage control loop (as the inverter cannot directly control these signals). The DC link voltage is thus related to the grid injected power ($P_g$) through the AC-side inverter power ($P_i$). Development of the dynamic model of the DC link can consequently be accomplished on the basis of relating $P_i$ to $P_g$. This relation can be derived by considering the expression for the inverter AC-side dynamics which, for a balanced three-phase system, and neglecting the impact of the inductor parasitic resistance, is given by (Yazdani & Iravani, 2010):

$$L_{eff}\frac{d}{dt}i_{iabc} = v_{iabc} - v_{gabc} \tag{5.24}$$

where $i_{iabc}$, $v_{iabc}$ and $v_{gabc}$ are the three-phase AC-side line (inverter output) current, inverter output voltage and the grid voltage respectively, and $L_{eff}$ is the effective interface inductance between the inverter and the grid. This equation can be conveniently written in the space-phasor form, with the space-phasor representation, $\vec{X}$, of an arbitrary three-phase signal, $x_{abc}$, having an amplitude $X_m$ and a phase angle $\theta$, is defined by:

$$\vec{X} = X_m e^{j(\omega t+\theta)} \tag{5.25}$$

where $\omega$ is the angular frequency of the signal. Equation (5.24) rewritten in terms of the space-phasor thus becomes:

$$L_{eff}\frac{d}{dt}(\vec{i}) = \vec{v}_i - \vec{v}_g \tag{5.26}$$

By scaling Equation (5.26) by the term $\frac{3}{2}\vec{i}^{*}$ (in order to get the AC-side power relations), the following expressions are obtained:

$$\frac{3}{2}L_{eff}\frac{d}{dt}(\vec{i}_i\vec{i}_i^{*}) = \frac{3}{2}\vec{v}_i\vec{i}_i^{*} - \frac{3}{2}\vec{v}_g\vec{i}^{*} \tag{5.27}$$

$$\frac{3}{2}L_{eff}\cdot R_e\{\frac{d}{dt}(\vec{i}_i\vec{i}_i^{*})\} = \frac{3}{2}R_e\{\vec{v}_i\vec{i}_i^{*}\} - \frac{3}{2}R_e\{\vec{v}_g\vec{i}_i^{*}\} \tag{5.28}$$

where $R_e\{\bullet\}$ is the real-component operator (*i.e.* it extracts the real part of a complex signal; this is done in order to obtain the expression for the active power transfer from the DC side to the AC side of the inverter). The left-hand-side of Equation (5.28) represents the interface inductor's instantaneous power absorption, in which the DC link dynamics due to power transfer variations are embedded, whereas the first term of the right-hand-side is the inverter output power, $P_i$, and the second term is the power transferred to the grid, $P_g$. That is:

$$\frac{3}{2}L_{eff}\cdot R_e\{\frac{d}{dt}(\vec{i}_i\vec{i}_i^{*})\} = P_i - P_g \tag{5.29}$$

It has further been shown by Yazdani and Iravani (2010) that the left-hand-side of Equation (5.29) develops into:

$$\frac{3}{2}L_{eff}\cdot R_e\{\frac{d}{dt}(\vec{i}_i\vec{i}_i^{*})\} = \frac{L_{eff}}{3V_{sm}^{\ 2}}\cdot\frac{d}{dt}(P_g^{\ 2}) + \frac{L_{eff}}{3V_{sm}^{\ 2}}\cdot\frac{d}{dt}(Q_g^{\ 2}) \tag{5.30}$$

where $V_{sm}$, $P_g$, and $Q_g$ are the grid peak phase-to-neutral voltage, transferred real power and transferred reactive power respectively. Equations (5.30) and (5.29) allow the desired expression of $P_i$ in terms of $P_g$ to be obtained, which is:

$$P_i = P_g + \frac{2L_{eff}}{3V_{sm}{}^2} \cdot P_g \frac{d}{dt}(P_g) + \frac{2L_{eff}}{3V_{sm}{}^2} \cdot Q_g \frac{d}{dt}(Q_g) \tag{5.31}$$

Using the expression for the inverter output power in terms of the power transferred to the grid (expressed by Equation 5.31), the DC-link voltage variations may then be expressed in terms of the grid power variations, and this is possible by means of combining Equations (5.31) and (5.23), thus obtaining:

$$\frac{d}{dt}(V_{DC}{}^2) = \frac{2}{C}P_{DPG} - \frac{2}{C}P_{loss} - \frac{2}{C}(P_g + \frac{2L_{eff}P_g}{3V_{sm}{}^2} \cdot \frac{d}{dt}(P_g)) + \frac{2}{C}(\frac{2L_{eff}Q_g}{3V_{sm}{}^2} \cdot \frac{d}{dt}(Q_g)) \tag{5.32}$$

In the comprehensive expression of the DC-link dynamics in Equation (5.32), $V_{DC}{}^2$ can be taken as the controlled variable, $P_g$ being the control input, whereas $P_{DPG}$, $P_{loss}$ and $Q_g$ are disturbances to the DC-link voltage regulation system. Regulation of $V_{DC}{}^2$ according to Equation (5.32) constitutes the outer control loop that sets the reference for the real power control (and hence for the inner current control loop of the inverter). It is common to regulate $Q_g$ at zero, in order to operate the inverter at unity power factor, as stipulated by grid code requirements (IEEE 1547-2003).

Equation (5.32) is nonlinear because it contains the product of the control input and its time derivative. To obtain the *injected real power-DC-link voltage* transfer function, $G_{pv}(s)$, Equation (5.32) is perturbed and linearized at an arbitrary equilibrium point. It has been shown that the perturbation and linearization of Equation (5.32) provides the desired transfer function, $G_{pv}(s)$, relating the DC-link voltage to the real power exchanged between the DC link and the grid through the inverter, given by (Yazdani and Iravani, 2010):

$$G_{pv}(s) = \frac{\tilde{v}_{DC}^2}{\tilde{p}_g} = -\frac{2}{C} \cdot \frac{\tau_{dc} + 1}{s} \tag{5.33}$$

Where $\tau_{dc}$ is the operating point-dependent time constant of the system dynamics, given by:

$$\tau_{dc} = \frac{2L_{eff}P_{go}}{3V_{sm}{}^2} \tag{5.34}$$

and $P_{go}$ is the injected real power at the chosen point of equilibrium for the process of linearization. Equation (5.33) shows that the plant for the DC-link voltage regulation comprises of an integrator as well as a transfer function zero, which might lie on the right-half-plane of the real-imaginary (s-plane) axis under certain operating conditions, and this characteristic can have a significant influence on the DC-link voltage regulation dynamic response.

If the effects of the AC-side interface inductor's instantaneous power absorption (expressed by Equation (5.29) on the DC-link dynamics are ignored (that is, the inductance is regarded to be zero for the analysis, making the expression for the time-constant Equation (5.34) to evaluate to zero), then the DC-link voltage dynamics are described simply by an integrator, the gain of which is determined by the value of the capacitor, $C$ (Yazdani & Iravani, 2010).

Equations (5.22) and (5.33) form the basis for the inverter current-mode controller design with DC-link voltage regulation. This is a dual-loop control strategy, in which the outer loop (based on Equation 5.33) is designed to regulate the DC-link voltage in relation to the power transferred to the grid, and the inner loop (based on Equation 5.22) is designed to regulate the current injected into the grid by the inverter.

The actual interface of the DPG to the grid is the filter, and its parameter design tends to precede the design of the controller, because the parameters of the inverter model in effect correspond to those of the filter. The design of the LCL filter used in this study is discussed.

## 5.6. LCL filter design

The design of the parameters for an LCL filter is largely an iterative process, because it requires the simultaneous satisfaction of a number of conflicting objectives, and thus some tradeoffs are often necessary in order to address all the design requirements. As mentioned earlier, the superior harmonic attenuation characteristic of the LCL filter (relative to the other passive filter topologies) comes at the cost of the need to fine-tune its component parameters and to design a controller that assures the robustness of the inverter control system to the effects of resonance damping and grid impedance variations (Ahmed *et al.*, 2007).

A number of strategies have been suggested in the technical literature with regard to the design of the LCL filter, out of which the common design objectives can be ascertained (Lettl *et al*., 2011; Ahmed *et al*., 2007; Araújo *et al*., 2007; Liserre *et al*., 2005) as being the:

1. reduction of the inverter current ripple below a specified maximum;
2. minimization of the reactive energy storage in the filter components so as to avoid current distortion, power factor displacement, as well as inverter overrating;
3. attenuation of the switching harmonics in the current injected into the grid to levels stipulated by grid codes;
4. limitation of the filter inductive reactance in relation to the base impedance, so as to limit filter voltage drop, and thus avoid using very high dc-link voltage;
5. confinement of the filter resonance frequency within a specified bandwidth to avoid resonance issues at lower and higher frequency bands; and
6. sufficient damping of the filter resonance to ensure an acceptable dynamic and steady-state performance of the filter

Meeting the above-stated objectives does suggest a systematic (and iterative) procedure that seeks to harmonize the objectives in an effort to come up with a design that satisfies each of the requirements to a sufficient degree. Liserre *et al.* (2005) provided one such systematic procedure in their design of an LCL filter for an active rectifier, an approach that has more or less been employed by quite a number of other authors prior to and subsequent to their work (Lettl *et al.*, 2011; Araújo *et al.*, 2007; Prodanovic & Green, 2003). A similar procedure has been employed in this thesis as well, and can be concisely outlined (with the corresponding objective to be achieved indicated) as the:

- determination of the inverter-side inductance value that reduces inverter current ripple to a specified percentage of the rated inverter current (*corresponding to objective 1*); this in turn permits working out the grid-side inductance value as a percentage of the inverter-side inductance;
- computation of the filter capacitance value based on the permissible reactive energy storage, specified as a fraction of the base capacitance at the nominal system frequency (*corresponding to objective 2*);
- calculation of the grid-side inductance value, based on the desired inverter-current-to-grid-current harmonic ripple attenuation, and in relation to the inverter-side inductance (*corresponding to objective 3*);
- calculation of the per-unit total filter inductive reactance, to ensure it does not exceed the specified maximum value (*corresponding to objective 4*); adjustments may be made to already computed inductance/s and/or capacitance if need be;
- determination of the filter resonance frequency to ascertain that it falls within the stipulated bandwidth (*corresponding to objective 5*); adjustments may be made to the already computed inductance/s and/or capacitance if need be, while ensuring that the other objectives are still met; and
- determination of the passive damping resistor value, which adds some impedance to the filter at resonance, in order to avoid the oscillatory behavior of the filter (*corresponding to objective 6*).

In the following paragraphs, the procedure outlined above is applied to the design of the LCL filter for interfacing the inverter both to the grid and to the load in the autonomous operational mode. The relevant data required for the filter design, as applicable to this study, are as listed in Table (5.2). As may be inferred from the procedure above, some steps may have to be reiterated, should certain pertinent requirements not be satisfied.

**Table 5.2:** **Data required for the design of the LCL filter**

| PARAMETER | VALUE |
|---|---|
| Inverter rating ($P_n$) | 15 (kW) |
| System type | Three-phase |
| Operational power factor (pf) | 1 |
| Nominal DC-link voltage ($V_{DC}$) | 720 (V) |
| Line voltage ($V_{LLrms}$) | 400 (V) |
| Nominal line current ($I_{nrms}$) | 21.65 (A) |
| Nominal line frequency ($f_n$) | 50 (Hz) |
| Switching frequency ($f_{sw}$) | 20 (kHz) |
| Inverter modulation range ($m_a$) | $0 \leq m_a \leq 1$ |

Some values derived from the nominal data provided in Table (5.2) are used in the calculations to follow. These are the base impedance and base capacitance, given by:

$$Z_b = \frac{V_{LLrms}^{\ 2}}{P_n} = \frac{400^2}{15\times10^3} = 10.667\Omega \tag{5.35}$$

$$C_b = \frac{1}{Z_b\omega_n} = \frac{1}{10.667\cdot100\pi} = 298\,\mu F \tag{5.36}$$

### 5.6.1. Parameter design

#### 1. Inverter-side inductance ( $L_i$ : objective 1):

The primary function of the inverter-side inductor is to reduce the inverter output current ripple to an acceptable level. A current ripple value of 10% or 20% of the nominal inverter current is usually recommended. Although a large inverter-side inductor would minimize the current ripple even further, its size is limited by the need to minimize core and coil losses to enhance the filter efficiency, and to limit the total inductive reactance below 10% of the base impedance to avoid an over-sized inverter and/or too high a DC-link voltage value (Liserre *et al.*, 2005).

These requirements may be more easily met if a high switching frequency is used, but that is also limited by the permissible inverter switching losses, which increase proportionately with the switching frequency. For this work, a switching frequency of 20 kHz has been chosen as a compromise between a limit on the switching losses and the provision to use smaller filter components to achieve lower harmonic content, as well as to obtain higher controller bandwidth.

If it is taken that the current ripple is required not to exceed 10% of the nominal value, setting the inverter-side per-unit inductive reactance, $X_{Lipu}$, to 6.2% of the base impedance enables the meeting of this requirement. That is:

$$X_{Lipu} = \frac{\omega_n L_i}{Z_b} \qquad \therefore L_i = \frac{X_{Lipu} \cdot Z_b}{\omega_n} = \frac{0.062 \times 10.667}{100\pi} = 2.11 mH$$

With this value of inductance for the inverter-side inductor, the current ripple, $\Delta I_{L\,max}$, is found to be (Ahmed *et al.*, 2007):

$$\Delta I_{L\,max} = \frac{V_{DC}}{8 \cdot L_i \cdot f_{sw}} = \frac{720}{8 \times 2.11 \times 10^{-3} \times 20 \times 10^3} = 2.133 A \ (= 0.0985 I_{nrms})$$

where $f_{sw}$ is the PWM switching frequency; so the inverter-side inductor alone should confine the current ripple below 10% according to the calculation done above. The idea is to decrease the ripple even further (ideally 2%) by the addition of the grid-side inductor, as is determined later.

**2. Filter capacitor ($C_f$ : objective 2):**

The role of the filter capacitance is to act as a sink for high-frequency harmonics by providing a low impedance path to ground for them. The determination of its size is dictated by the permissible reactive energy storage of the filter, and the value is computed as a percentage of the base capacitance (commonly set to 5%). A larger capacitance value is desirable to allow the use of a smaller inductance, but that also increases current distortion.

Choosing the initial capacitance value to be 3% of the base capacitance (may be adjusted if need be) results in:

$$C_f = 0.03 \cdot C_b = 0.03 \times 298 \times 10^{-6} = 8.95 \mu F$$

**3. Grid-side inductor ($L_g$ : objective 3):**

The grid-side inductor value is set in accordance with the required current harmonic attenuation from the inverter current to the grid current, and is usually set as a fraction of the inverter-side inductor according to the relation:

$$L_g = r \cdot L_i \tag{5.37}$$

The objective of grid-side inductor calculation thus translates into the determination of the value of $r$ that provides the required ripple attenuation. Equation (5.13), evaluated at the switching frequency (at which maximum ripple attenuation is desired), represents the ripple attenuation factor from the inverter current to the grid current. If the damping resistor and the filter resistive losses are ignored, the expression for the ripple attenuation factor is found from Equation (5.13) to be:

$$G_{i_g i_i}(s) = \left| \frac{i_g(s)}{i_i(s)} \right| = \left| \frac{Z_{Cf}}{Z_{Lg} + Z_{Cf}} \right| = \left| \frac{1/sC_f}{sL_g + 1/sC_f} \right| = \frac{1}{\left| 1 + s^2 L_g C_f \right|} \tag{5.38}$$

Evaluated at the switching frequency, Equation (5.38) becomes:

$$\left|\frac{i_g(j\omega_{sw})}{i_i(j\omega_{sw})}\right| = \frac{1}{\left|1 + L_g \cdot C_f \cdot (j\omega_{sw})^2\right|} = \frac{1}{\left|1 - L_g \cdot C_f \cdot \omega_{sw}{}^2\right|} \tag{5.39}$$

Substituting Equation (5.37) into Equation (5.39) leads to the expression:

$$\left|\frac{i_g(j\omega_{sw})}{i_i(j\omega_{sw})}\right| = \frac{1}{\left|1 - r \cdot L_i \cdot C_f \cdot \omega_{sw}{}^2\right|} \tag{5.40}$$

Equation (5.40) expresses the current ripple attenuation as a function of the ratio of the grid-side inductor to the inverter-side inductor (the other parameters being fixed, although the capacitance may be adjusted if certain objectives are not met), and thus allows setting $r$ to the value that provides the desired attenuation. Figure (5.8) depicts a plot of the current ripple attenuation as a function of $r$ based on Equation (5.40) (implemented in Matlab according to the program listing in Appendix D). The plot shows that a value of $r$ as low as $0.2$ per-unit allows obtaining current ripple attenuation below $2\%$, and this may be attributed to the high switching frequency used in this work, which is the positive aspect of using a high switching frequency. With the selected value of $r$, the grid-side inductor value is set to:

$$L_g = 0.2 \times 2.11 \times 10^{-3} = 0.42\,mH$$

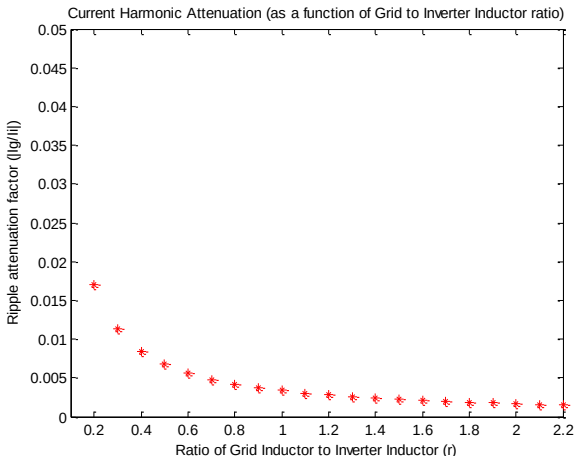


**Figure 5.8:** **Plot of the inverter-side current ripple attenuation as a function of the ratio of the grid-side- to the inverter-side inductance, $r$ .**

It is necessary to check that the combined inductance of the inverter-side and the grid-side inductors satisfies the requirement of *objective 4*. If not, then another ripple attenuation factor may be selected, or the ratio of the filter capacitance to the base capacitance may be adjusted. The grid-side inductance calculated above adds only $1.2\%$ to the total inductive reactance, bringing the total per-unit inductive reactance to $0.074$ per-unit., and thus confirming that *objective 4* has been satisfied with the initially calculated values. Assuming a further contribution to the effective interface inductive reactance of $1.6\%$ from the grid side (*i.e.* the interface transformer, line reactance and grid source impedance), the per-unit inductive

reactance comes to 0.09 per-unit (still within the specified limit), and the corresponding total (effective) inductance, $L_{eff}$ , is found to be:

$$L_{eff} = \frac{X_{Lpu} \cdot Z_b}{\omega_n} = \frac{0.09 \times 10.667}{100\pi} = 3.06\,mH$$

$$\therefore \quad L_i = 2.11mH$$

$$and \quad L_g = 0.95\,mH$$

**4. Resonance frequency ( $f_{res}$ : objective 5):**

The filter resonance frequency is given by:

$$f_{res} = \frac{1}{2\pi} \cdot \sqrt{\frac{L_{eff}}{L_i \cdot L_g \cdot C_f}} = \frac{1}{2\pi} \cdot \sqrt{\frac{3.06 \times 10^{-3}}{2.11 \times 10^{-3} \times 0.95 \times 10^{-3} \times 8.95 \times 10^{-6}}} = 2079Hz$$

The desired minimum value of the resonance frequency is ten times the nominal line frequency, and should ideally be limited to half the switching frequency or less. This is in order to avoid resonance issues in the lower and upper parts of the harmonic spectrum (Teodorescu *et al.*, 2011). The filter resonance frequency calculated above is only about 10% of the switching frequency, and exceeds the nominal frequency by a factor greater than 40, and thus satisfies the relevant requirement (*objective 5*).

**5. Passive damping resistor ( $R_d$ : objective 6):**

The LCL filter has an impedance value of zero at the resonance frequency. Because of its third-order attenuation characteristic, damping the infinite gain that occurs at the point of resonance is necessary to avoid oscillatory or even unstable behavior of the inverter control system. Passive damping by means of a resistor connected in series with the shunt filter capacitor may be used to provide this damping. The passive damping resistor adds a fraction of the impedance of the capacitor at the resonance frequency (Evyu, 2007).

A large passive resistor provides a greater damping effect, but the size is limited by filter efficiency considerations (due to ohmic losses in the resistor) and the impact on the filter's harmonic attenuation capability. A factor of one-third of the capacitive reactance at the resonance frequency (*i.e.* $1/3C_f(\omega_{res})$) is commonly used (Ahmed *et al.*, 2007), but losses due to the resistor at the switching frequency and the sidebands have to be evaluated and adjustments made as appropriate.

Following the guideline given above and setting the passive damping resistance, $R_d$ , to a third of the filter capacitive reactance at the resonance frequency, the damping resistor value is computed as follows:

$$R_d = \frac{1}{3 \cdot \omega_{res} \cdot C_f} = \frac{1}{3 \times 2\pi \times 2079 \times 8.95 \times 10^{-6}} = 2.85\Omega$$

The designed parameters for the LCL filter used in this thesis, as calculated above, are listed in Table (5.3). These parameters are used later in the inverter control system design.

**Table 5.3: Designed LCL filter parameter values**

| PARAMETER | VALUE |
|---|---|
| Inverter-side inductance ($L_i$) | 2.11 (mH) |
| Grid-side inductance ($L_g$) | 0.95 (mH) |
| (Approximated) total inductor parasitic resistance ($R_L$) | 0.1 (Ω) |
| Filter capacitance ($C_f$) | 8.95 ($\mu$F) |
| Passive damping resistance ($R_d$) | 2.85 (Ω) |
| Resonance frequency ($\omega_{res}$) | 13063 (rad/sec) |

### 5.6.2. Dynamic analysis of the designed filter

It is useful to analyze the designed filter's stability and dynamic response, especially with regard to resonance damping, so that adjustments in the design may be made if necessary. For this analysis task, the inverter-current-to-inverter-voltage transfer function (Equation 5.9) is considered. The transfer function for the damped filter derived on the basis of Equation (5.9) and Figure (5.6) is as stated in Equation (5.41) below. The transfer function for the undamped system may be obtained from Equation (5.41) by setting the passive resistance ( $R_d$ ) to zero.

$$\left.\frac{i_i(s)}{v_i(s)}\right|_{damped} = \frac{s^2 L_g C_f + sR_d C_f + 1}{s^3 L_i L_g C_f + s^2 R_d C_f (L_i + L_g) + s(L_i + L_g)} \tag{5.41}$$

It is desired to examine both the open-loop frequency (*i.e.* magnitude and phase) and closed-loop time (step response and pole-zero location) characteristics, to ascertain the steady-state and dynamic behavior of the designed filter, especially giving attention to the resonance behavior and the effectiveness of the resonance damping method implemented in the design.

For the closed-loop response analysis, the system is assumed to be compensated by a proportional-integral (PI) compensator ( $G_{ci}(s)$ ) with the transfer function given by Equation (5.42). Detailed information on the compensator design is to be found in the following chapter (Chapter 6). Stability analysis of the closed-loop system has been done by considering pole-zero locations of the closed-loop system in the complex plane, discretized at a sampling frequency of 5 kHz (Liserre *et al.*, 2005).

$$G_c(s) = \frac{1.53 \cdot s + 50}{s} \tag{5.42}$$

Figure (5.9) depicts the open-loop magnitude-phase response of the filter subject to a range of passive damping resistance values (the Matlab program lsiting for the following analyses can be found in Appendix D). From the plots it can be seen that the undamped system response exhibits quite a sharp increase in the loop gain at the filter resonance frequency. If not compensated for by means proper damping, the resonance could cause very unsatisfactory behavior of the inverter control system. As damping resistance values are step-wise incremented, the gain at resonance can be observed to proportionately decrease, showing that the main effect of the passive damping resistor is to smoothen the response of the system around the resonance frequency, which enhances both the steady-state and dynamic responses of the closed-loop system.

Figure (5.10) portrays a comparison of the open-loop magnitude-phase responses of the L-filter (Equation 5.22) and the LCL-filter (Equation 5.41). The responses show that the two filter models exhibit a similar response characteristic in the low-frequency range, up to the LCL-filter resonance frequency. This is the characteristic that is usually used to support the simplifying approximation of the LCL-filter model by an equivalent L-filter model for control design purposes (Teodorescu *et al*., 2011).

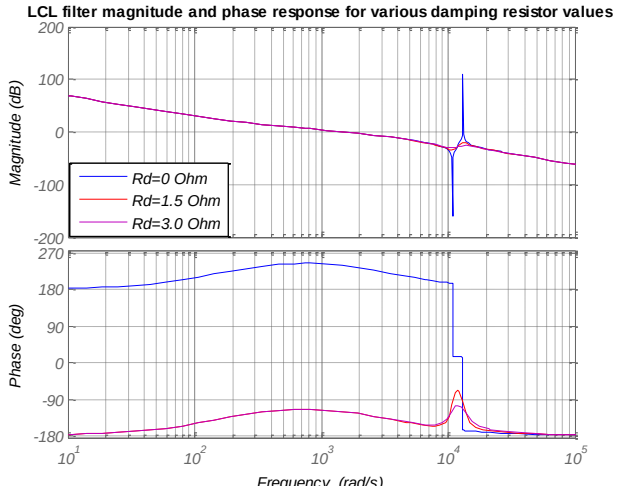


**Figure 5.9: Open-loop bode plot of the LCL filter showing the effect of (passive) resonance damping**

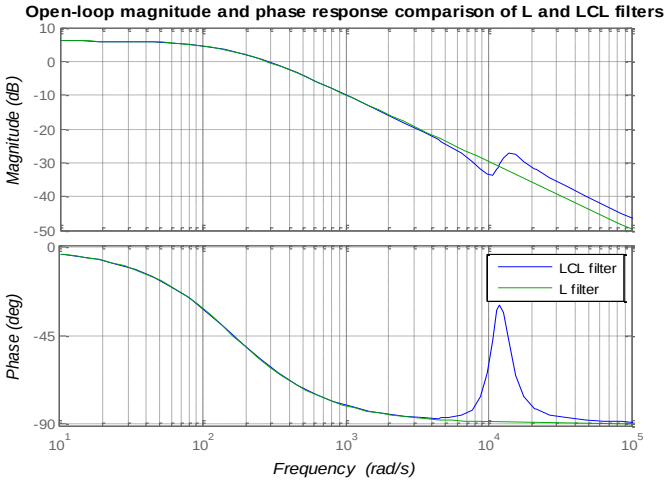


**Figure 5.10:** Open-loop magnitude and phase response comparison of the L- and LCL-filters

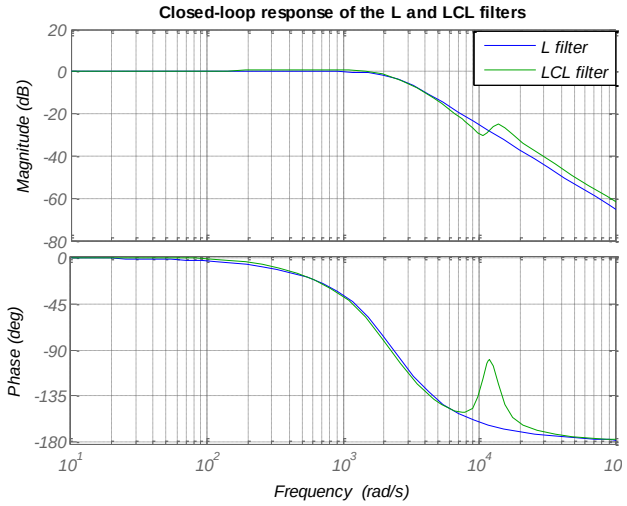


**Figure 5.11:** Closed-loop magnitude and phase response comparison of the L- and LCL-filters

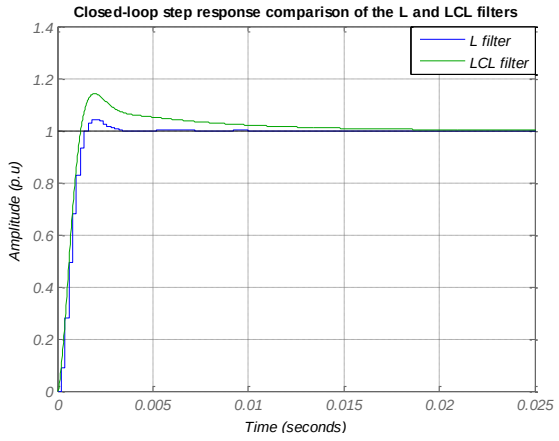


**Figure 5.12:** Closed-loop step response comparison of the L- and LCL-filters.

Comparison of the closed-loop magnitude-phase and step responses of the L- and LCL-filters is depicted in Figures (5.11) and (5.12) respectively. The closed-loop bode plot can be used to investigate the closed-loop system bandwidth, whereas the step response highlights the effect of the extra poles and zeros of the LCL-filter on the closed-loop system time response. A

slight slowing down of the response and increased overshoot can be noticed in Figure (5.12), which may be mitigated by the tuning of the compensator gain parameters.

Finally, the closed-loop pole and zero locations of the system in the z-plane are examined for the undamped filter as well as for the damped filter for various values of the damping resistance, as depicted in Figure (5.13). The plots show that the undamped system is marginally stable, as there are system poles that lie on the radius of the unit circle. As the damping resistance is step-wise incremented, the unstable poles are shifted into the stable region of the z-pane.

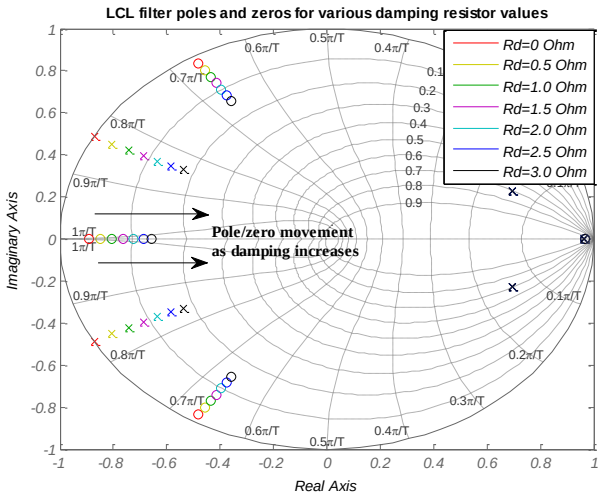


**Figure 5.13: LCL filter closed-loop pole-zero location trajectory as a function of the resonance damping resistance magnitude**

## 5.7. Conclusion

As a vital component in the system for the transfer of high-quality power from a Distributed Power Generation (DPG) system to the grid (isolated load), the inverter requires a well-designed control strategy to insure the desirable steady-state and dynamic operation of the overall system. The design of such a controller in turn requires the availability of a model that adequately represents the dynamics of the controllable part of the inverter. This chapter has addressed the need for such an inverter model, as well as the design of the interface filter to ensure the high quality of the inverter output power.

The control of the inverter must take into account both the AC-side dynamics (characterized by the inverter output current as a function of the inverter output voltage) and the DC-side dynamics (characterized by the DC-link voltage variations as a function of the active power transferred from the DC link to the grid). Both these dynamic characteristics have been discussed, and appropriate models have been presented that are later used in the controller design.

The DC-side dynamics are largely a function of the energy storage variations in the inductive interface between the inverter and the grid, and the power variations in the power source input

to the inverter, and these considerations have formed the basis for the development of the DC-link voltage dynamic model. The AC-side dynamics are highly influenced by the filter topology chosen for interfacing the inverter to the grid. In this regard, the passive filter topologies that are commonly used in grid-interactive inverter interfaces have been briefly discussed, these being the $L$-, $LC$- and $LCL$- filter topologies. More detailed discussion and parameter design for the $LCL$- filter, which is chosen for implementation in this work, has then been presented.

The dynamic performance of the $LCL$-filter, using the designed filter parameters, has also been carried out. The results from this analysis align well with the results obtained by other authors (Ahmed *et al*., 2007; Liserre *et al*., 2005), and thus provides a measure of confidence that the designed filter may enable the meeting of the grid-code power quality requirements by the inverter-based DPG system being studied.

The main focus of the following chapter is the design of the current-mode controller for the grid-mode operation of the inverter, in which the models developed in this chapter are used.

# Chapter 6

# INVERTER CONTROLLER DESIGN FOR GRID-CONNECTED MODE OPERATION

## 6.1. Introduction

With the sustained global expansion of the Distributed Power Generation (DPG) sector, the inverter as an integral part of the DPG system is correspondingly growing in importance, increasingly being required to carry out more and more functions. Moreover, the new and stricter standards for grid interconnection that are deemed necessary to preserve the integrity of the power system in the face of an ever-increasing penetration of the DPG systems are also placing special demands on the inverter control and operation (Blaabjerg *et al*., 2006).

Many factors need to be taken into account in the process of designing a control strategy for the grid inverter. Ultimately, the inverter should ideally be controlled to seamlessly interface the DPG to the utility grid, being able to inject low-distortion current into the grid and to keep its terminal values within the stipulated nominal ranges, so that it remains synchronized with the grid under normal operating conditions.

The main purpose of this chapter is to develop a current-mode control strategy for the grid-mode operation of the inverter that interfaces the DPG to the utility grid (hereafter referred to simply as the *grid-inverter*). An outline of the work covered in the various sections of the chapter follows.

In Section 6.2, the functionalities that are most commonly associated with the grid-inverter are highlighted, as an aid to contextualizing the work covered in this and the other chapters directly related to the grid-inverter control. Also, since the grid-inverter must remain properly synchronized with the grid during normal operation, common methods for the synchronization of the inverter to the grid are addressed in Section 6.3. The technique used for the synthesis (or modulation) of the switched output signals of the inverter has a bearing on the inverter control system. Thus in Section 6.4, common inverter modulation techniques are briefly considered. This is followed by a discussion of some of the methods employed for the control of the inverter in Section 6.5, and then the controller design for the grid-mode operation of the grid-inverter is presented in Section 6.6. The performance of the designed control strategy is analyzed in Section 6.7, before concluding the chapter with an outline of the main results of the chapter in Section 6.8.

## 6.2. Functions performed by the inverter

The main function of an inverter can be concisely stated as being to condition the power at its input so that the voltage and current at its output match the requirements of the load in terms of magnitude, phase, frequency, power quality, and other important characteristics (Liserre *et al*., 2010). The inverter has to satisfy these power conditioning objectives for a wide range of

Distributed Energy Resources (DER), both DC and AC, as depicted in Figure (6.1), which shows some of the widely studied DERs. The functionalities associated with the control of the grid-inverter are quite similar, irrespective of the DER used, as outlined below.

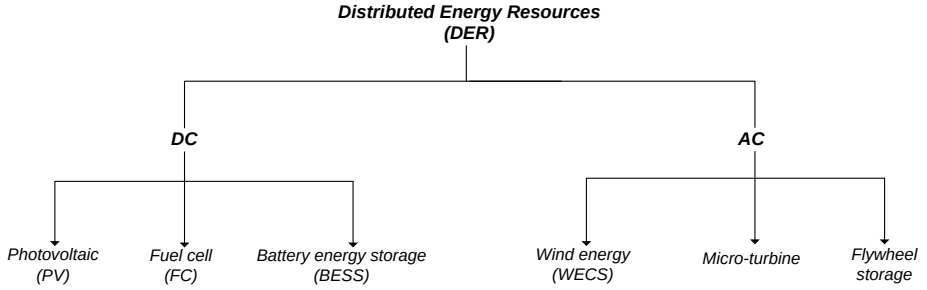


**Figure 6.1: Main categories of distributed energy sources. (Adapted from Teodorescu *et al.*, 2011)**

The main functionalities that are commonly associated with the operation and control of the grid-inverter can be outlined as (Teodorescu *et al.*, 2011):

- Grid synchronization:
  - maintaining the inverter terminal parameters within nominal values under normal operating conditions
- Grid current control:
  - current injection at the power factor stipulated by the grid code (normally unity)
  - maintaining stable control in the presence of grid disturbances
- Grid voltage control:
  - regulating the DC-link voltage in response to power transfer fluctuations
- Grid and plant monitoring to ensure:
  - synchronized terminal parameter values
  - fast detection of abnormal voltage/frequency deviations to prevent unintentional islanded operation
- Grid support (with certain restrictions in most currently applicable grid codes):
  - Point-of-Common-Coupling (PCC) voltage control
  - reactive power compensation
  - harmonic compensation
  - fault ride through capability

In the context of the work covered in this thesis, all the functionalities listed above, with the exception of the grid support services (which lie beyond the scope of work covered in the thesis), are addressed to some degree. Specifically, both grid synchronization and grid (AC current & DC voltage) control are covered in this chapter. Grid and plant monitoring to ensure the fast detection of abnormal grid conditions and the prompt instigation of preventive

measures is addressed in the following chapter, which deals with the autonomous-mode operation of the inverter-based DPG system.

In the following section, methods for the synchronization of the inverter to the grid are discussed.

## 6.3. Inverter grid synchronization

### 6.3.1. Grid synchronization techniques

Synchronism between the grid-inverter terminal voltage and the grid voltage is a very pertinent requirement included in the grid code. It essentially implies the requirement to monitor the instantaneous values of grid parameters, and subsequently to harmonize the inverter terminal parameters with those of the grid at the PCC (Teodorescu *et al.*, 2011). This ensures, among other things, that the inverter injects low-distortion current into the grid. Moreover, proper control of the grid-inverter current relies on the accurate sensing of the grid voltage phase angle, so that the inverter current is modulated to be in phase with the grid voltage, as required by grid codes (IEEE-1547, 2003). Several methods, differing in accuracy and complexity, have been suggested in the reviewed literature concerned with the synchronization of grid inverters (Teja, 2013; Teodorescu *et al*., 2011; Timbus *et al*., 2005; Chung, 2000).

**Zero-crossing detection** is one simple method that may be used for grid voltage frequency tracking. It permits the extraction of the frequency and phase information from the grid voltage signal simply by detecting and registering the zero-crossing instances of the voltage signal and the application of op-amps as comparators. The technique is thus simple to implement, but its sensitivity to signal noise and other non-ideal grid conditions significantly degrades its performance (Teja, 2013).

**Grid voltage axis transformation**, from the three-phase natural (abc) reference frame to either the two-phase stationary (αβ) or the two-phase synchronously rotating (dq) reference frames, in conjunction **with filtering**, has also been employed in the grid voltage frequency and phase angle determination. The arctangent function is applied to the orthogonal components of the transformed voltage signal, to compute the desired phase angle. The main drawback of the *filtering method* is its questionable performance in the presence of grid anomalies such as notches, harmonics and grid faults, especially on account of the time delay introduced into the technique by the filtering process. Timbus *et al.* (2005) stressed the importance of the proper filter type selection and tuning for the acceptable performance of the *grid-synchronization-by-filtering* method, and even then, significant distortion gets embedded into the synchronization algorithm in the presence of grid frequency variations.

The **Phase-Lock Loop** (PLL) technique employs an internal oscillator and negative feedback to synchronize its periodic input signal’s frequency and phase angle with that of the signal at

its output. This feature of the PLL circuit is exploited in the grid-inverter system to extract the frequency and phase angle information from the grid voltage signal, which plays a pivotal role in the proper control of the inverter. The most widely implemented phase-lock technique in grid-connected converter applications is the Synchronous Reference Frame Phase-Lock Loop (SRF-PLL) (Timbus *et al.*, 2005), which involves the transformation of the three-phase signals to the synchronous (dq) reference frame.

The PLL technique is the method of choice in most cases, as it can be designed to deal with most of the factors that make grid frequency tracking difficult. It is thus the technique that has been adopted for implementation in this study as well, particularly the SRF-PLL.

In its elementary form, the PLL circuit is comprised of a *phase detector*, a *loop filter* and a *Voltage-Controlled Oscillator* (VCO), as depicted in Figure (6.2) (Evyu, 2007).

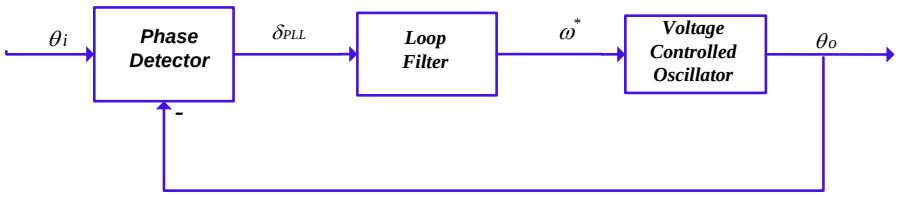


**Figure 6.2: Elementary block diagram of the Phase-Lock Loop circuit. (Adapted from Evyu, 2006)**

The *phase detector* acts as the comparator of the phase angles of the PLL input signal ($\theta_i$) and the signal at the output of the VCO ($\theta_o$). The result of the comparison provides a measure of the phase deviation ($\delta_{PLL}$) between the two compared signals (Gardner, 1967). The phase deviation ($\delta_{PLL}$) is fed into the loop filter as a next stage of the phase-locking technique.

The *loop filter* acts on the phase deviation output of the phase detector, and attempts to minimize the phase error to the value necessary to sustain the control signal of the VCO. It thus performs the important task of regulating the signal that is responsible for controlling the frequency of the oscillator, and its effectiveness is critical to the dynamic and steady-state performance of the PLL (Timbus *et al.*, 2005).

Driven by the control output of the loop filter, the *Voltage-Controlled Oscillator* adjusts its oscillation frequency in a way that minimizes the phase deviation between the tracked signal and the VCO output signal. When in lock, the output of the VCO represents nearly the phase angle of the input signal to the PLL. A minimal phase deviation is necessary because the operating principle of the PLL requires a non-zero input to the loop filter, to sustain the control voltage input to the VCO. This implies a steady-state phase difference between the input and VCO signals, but this is normally small in a well-designed PLL circuit (Gardner, 1967).

A PLL circuit can be designed with a very narrow bandwidth and automatic frequency tracking with good noise rejection, and thus when applied to grid voltage phase tracking, it exhibits improved grid disturbance rejection characteristics in comparison with such methods as *zero-crossing detection* or *grid voltage filtering* discussed earlier. This may, however, necessitate the design of higher-order filters and more complex circuit configurations for dealing with the grid distortion that may appear in the form of phase imbalance due to asymmetrical faults, harmonics, and voltage offset resulting from other grid anomalies (Chung, 2000).

### 6.3.2. SRF-PLL design

For the loop filter design task, the linearized model of the PLL circuit in Figure (6.2), expressed in the Laplace domain as illustrated in Figure (6.3), can be considered.

Two important transfer functions for the PLL loop filter design are the *output phase-input phase* ($H_c(s)$) as well as the *phase error-input phase* ($H_e(s)$) transfer functions which, considering Figure (6.3) can be formulated as (Chung, 2000):

$$H_c(s) = \frac{\theta_o(s)}{\theta_i(s)} = \frac{G_f(s)}{s + G_f(s)} \tag{6.1}$$

$$H_e(s) = \frac{\delta_{PLL}(s)}{\theta_i(s)} = \frac{s}{s + G_f(s)} \tag{6.2}$$

where $\theta_i(s)$, $\theta_o(s)$ and $\delta_{PLL}(s)$ denote the Laplace transforms of the input signal phase angle, the output signal phase angle, and the phase deviation between the input and output signals respectively, and $G_f(s)$ represents the transfer function of the loop filter in the Laplace domain.

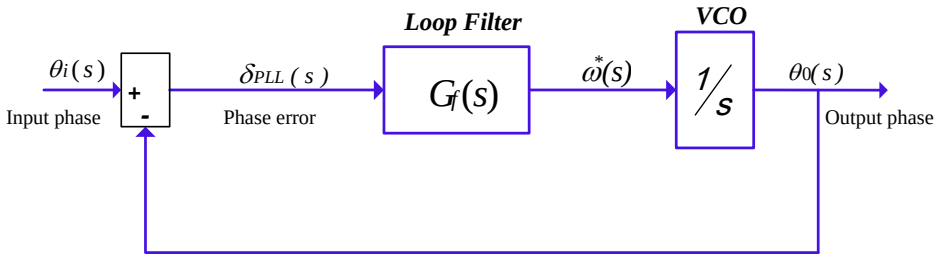


**Figure 6.3: Linearized model of the PLL circuit in the Laplace domain. (Adapted from Chung, 2000)**

Loop filter design for the PLL circuit is inherently an optimization task. As discussed by Gardner (1967), there is a requirement to simultaneously satisfy two conflicting objectives. The PLL must be designed for as narrow a bandwidth as possible on the one hand (to ensure fast dynamic response), whereas a wider bandwidth is desirable for improved error tracking on the other hand. A design tradeoff that takes into account both the input signal type and the

most critical performance criteria to be met thus becomes inevitable. While a higher-order PLL may perform better under occasional grid abnormal conditions, a simpler PLL control structure, with its characteristic of being easier to tune, may lead to better overall dynamic response control (Chung, 2000).

With these design considerations in mind, a loop filter that leads to a second-order closed loop PLL circuit is often chosen as a good tradeoff between filter performance and system stability enhancement (Chung, 2000; Gardner, 1967). Thus if a proportional-integral (PI) compensator expressed by Equation (6.3) is implemented in order to realize a second-order closed-loop characteristic for the PLL circuit, the *output phase angle* ($H_c(s)$) and *phase-error* ($H_e(s)$) transfer functions given by Equations (6.1) and (6.2) can be rewritten as in Equations (6.4) and (6.5), with the natural frequency of oscillation, $\omega_{nPLL}$, and the damping ratio, $\xi$, expressed by Equations (6.6) and (6.7) respectively (Chung, 2000):

$$G_f(s) = K_p \cdot \frac{1 + s\tau_{iPLL}}{s\tau_{iPLL}} \tag{6.3}$$

$$H_c(s) = \frac{2\xi\omega_{nPLL}s + \omega_{nPLL}{}^2}{s^2 + 2\xi\omega_{nPLL}s + \omega_{nPLL}{}^2} \tag{6.4}$$

$$H_e(s) = \frac{s^2}{s^2 + 2\xi\omega_{nPLL}s + \omega_{nPLL}{}^2} \tag{6.5}$$

$$\omega_{nPLL} = \sqrt{\frac{K_p}{\tau_{iPLL}}} \tag{6.6}$$

$$\xi = \sqrt{\frac{K_p \cdot \tau_{iPLL}}{2}} \tag{6.7}$$

where $K_p$ and $\tau_{iPLL}$ denote the loop filter (PI compensator) proportional gain and integrator time constant respectively.

The design task is thus reduced to the determination of the damping ratio and the PLL circuit's natural frequency of oscillation that provide fast tracking, while ensuring good filtering and minimal tracking error. According to Gardner (1967) and later Chung (2000), the Wiener optimization method is one of the most widely used techniques for problems of this nature. It allows the determination of the PLL circuit's natural frequency of oscillation by considering the stochastic information of the input signal and the associated noise. The expression for the optimal natural frequency based on the Wiener method is given by (Chung, 2000):

$$\omega_{nPLL} = \Delta\omega_{PLL} \cdot \lambda_{PLL} \cdot \sqrt{\frac{2P_{iPLL}}{W_{iPLL}}} \tag{6.8}$$

The PLL parameters in Equation (6.8) represent:

- $\omega_{nPLL}$ : PLL circuit closed-loop bandwidth
- $\Delta\omega_{PLL}$ : frequency deviation between PLL circuit input and output signals
- $P_{iPLL}$ : PLL circuit input signal active power
- $W_{iPLL}$ : PLL circuit input signal's noise spectral density
- $\lambda_{PLL}$ : A Lagrangian multiplier for the solution of the Wiener optimization problem

The difficulty in ascertaining the stochastic information of the input signal noise, as stated by Chung (2000), necessitates the empirical choice of the bandwidth that minimizes the steady-state phase error caused by a varying frequency of the input signal. For the PI-based second-order loop filter considered, this phase error is inversely proportional to the square of the natural frequency (Gardner, 1967). The choice of a high natural frequency would thus lead to a smaller steady-state error caused by input signal frequency variations, but may degrade the PLL performance under distorted grid conditions. An angular natural frequency of oscillation that is twice the input signal angular frequency, $\omega_o$ (where $\omega_o = 2\pi f_o \ rad/sec$, with $f_o = 50Hz$), has been found to provide acceptable performance in terms of phase tracking and speed of response (Evyu, 2007; Chung, 2000).

Therefore, choosing the natural frequency of oscillation, $\omega_{nPLL}$, and damping ratio, $\xi$, for the closed-loop PLL circuit as follows:

$$\omega_{nPLL} = 2\omega_o = 2\times 100\pi = 628319 \ rad/sec$$

$$\xi = \frac{1}{\sqrt{2}}$$

the gain values for the PI compensator can be determined using Equations (6.6) and (6.7) as:

$$K_p = 2\xi\omega_{nPLL} = \sqrt{2}\times 200\pi = 888.58$$

$$\tau_{iPLL} = \frac{K_p}{\omega_{nPLL}^{\ 2}} = \frac{888.58}{(200\pi)^2} = 2.251\times 10^{-3} \ sec$$

$$K_i = \frac{K_p}{\tau_{iPLL}} = \omega_{nPLL}^{\ 2} = (200\pi)^2 = 39478418$$

where $K_i$ is the loop filter integral gain. The response of the designed PLL can be seen in Figures (6.4)-(6.7). Figure (6.4) shows the plot of the output-input-phase closed-loop magnitude and phase response. It has a closed-loop bandwidth of about 885 rad/sec, and exhibits a -20dB/decade magnitude attenuation characteristic beyond the cut-off frequency.

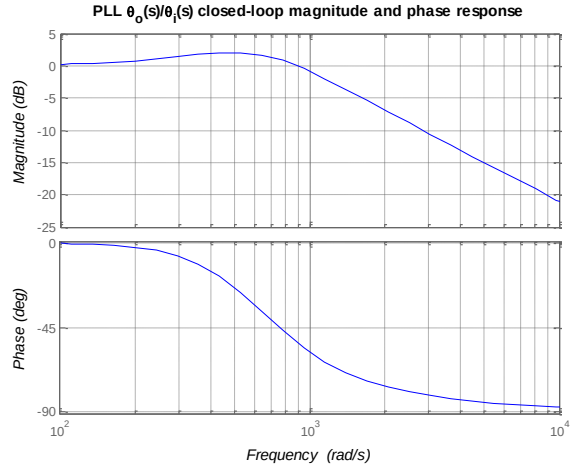


**Figure 6.4:** Magnitude-phase plot of the PLL circuit output/input closed-loop phase transfer function

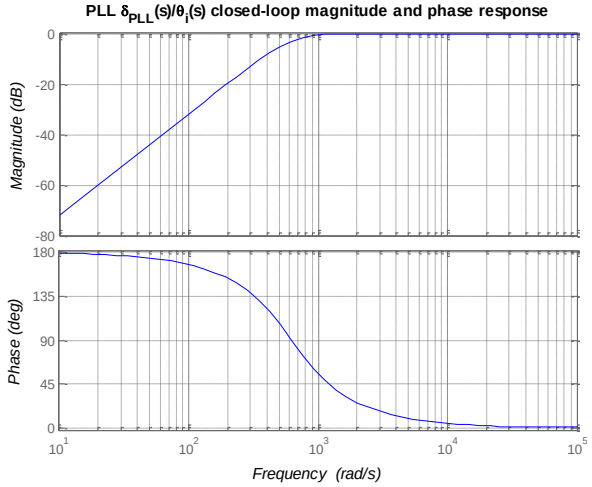


**Figure 6.5:** Bode plot of the phase-error/input-phase closed-loop transfer function of the PLL circuit.

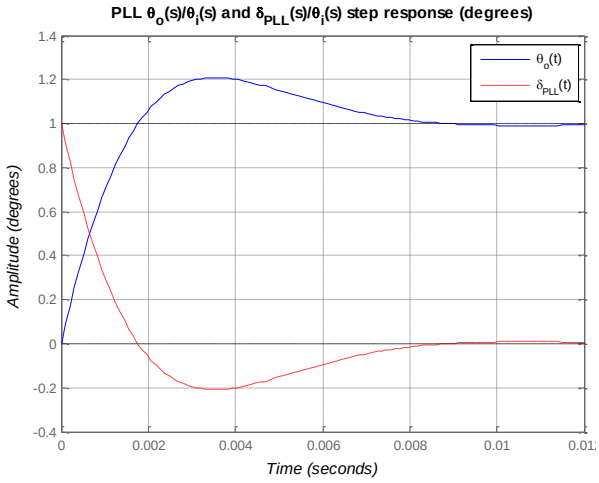


**Figure 6.6:** Step responses of the output/input-phase and phase-error/input-phase closed-loop transfer functions of the PLL circuit.

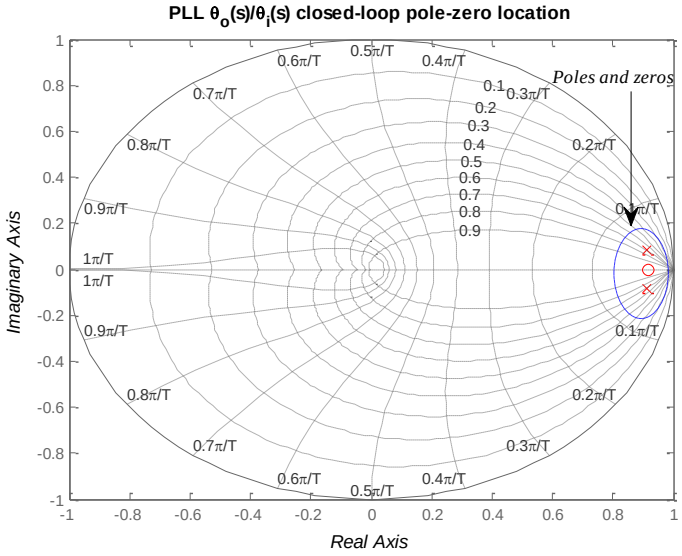


**Figure 6.7: Location of the closed-loop poles and zeros of the PLL circuit on the complex plane.**

The closed-loop Bode plot of the *phase-error-input-phase* response is shown in Figure (6.5), with a characteristic positive 40dB/decade gain slope. The closed-loop step responses of both the *output phase* and the *phase error* are plotted in Figure (6.6). The plot shows that the designed PLL circuit has a fairly good transient and steady-state response, settling within 10 milliseconds with a 20% overshoot. The error is also regulated to zero within the settling time as expected of a step disturbance to the PI-based second-order PLL circuit. Figure (6.7) confirms the stability of the circuit by showing both poles and the zero of the discretized system (discretized at 10 kHz sampling frequency, using zero-order hold) within the unit circle of the z-plane.

### 6.3.3. Implementation of the designed SRF-PLL

One way of implementing the phase detector in the SRF-PLL is as illustrated in Figure (6.8) (Mathworks, 2013). The *abc-dq0* axis transformation is so performed that the rotating frame is aligned to be orthogonal to the phase-A signal, lagging it by 90° at time 0 sec (Mathworks, 2013). With this transformation, a three-phase input signal with null phase angle produces a zero-amplitude *q-axis signal*, while the d-axis signal equals the three-phase signal in amplitude.

The PLL circuit implemented in Matlab/Simulink is depicted in Figure (6.9), based on the circuit in Figure (6.8) A three-phase programmable generator that permits the programming of the source frequency and phase angle variations (available in the SimPowerSystems model library) was used as the input to the PLL circuit, for further performance analysis of the designed circuit.

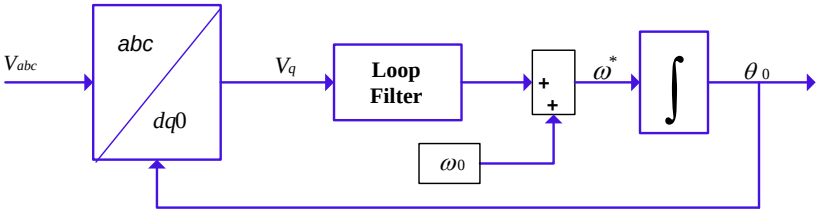


**Figure 6.8:** PLL circuit implementation in the synchronous reference frame (SRF-PLL). (Adapted from Mathworks, 2013)

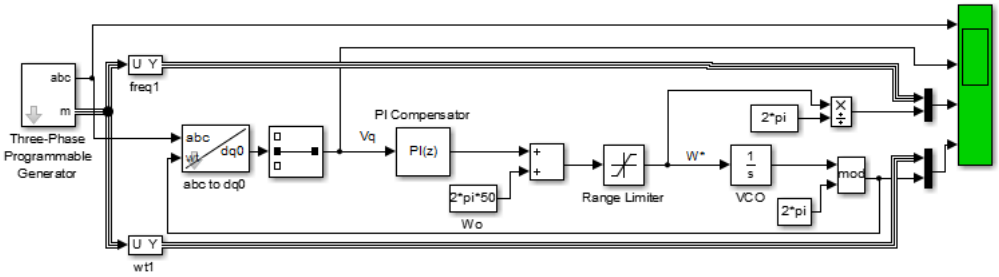


**Figure 6.9:** Simulink implementation of the SRF-PLL circuit.

Figures (6.10) and (6.11) show the plots of the PLL's *phase error*, *output phase angle* and *frequency*, respectively, to an input signal in which no disturbance is programmed. The responses depict how the PLL circuit would track the frequency and phase angle of a non-distorted grid voltage signal, and show good steady-state and dynamic behavior.

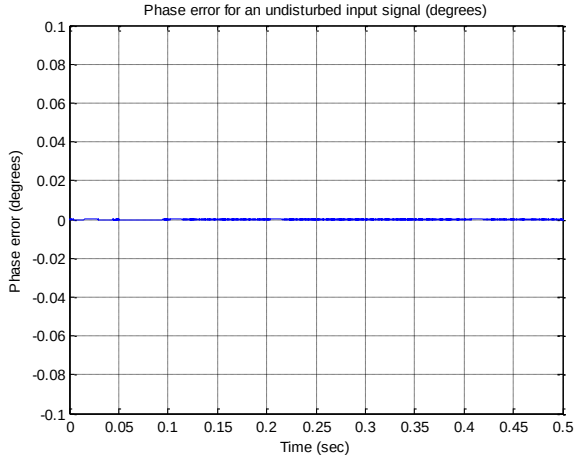


**Figure 6.10:** Phase error regulation of the PLL circuit for an undisturbed input signal.

For a step change in the phase angle of the input signal, the PLL circuit is expected to quickly bring the error to zero, and this is depicted in Figures (6.12) and (6.13) for a 3-degree phase step change introduced at 0.15 seconds and withdrawn at 0.35 seconds. The same response would be exhibited for a phase ramp disturbance.

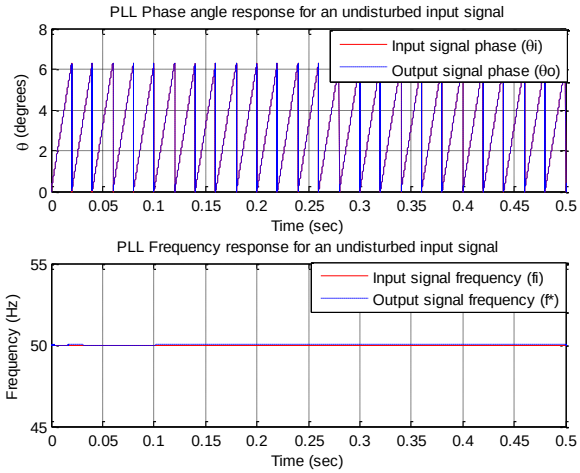


**Figure 6.11:** Phase and frequency responses of the PLL circuit for an undisturbed input signal.

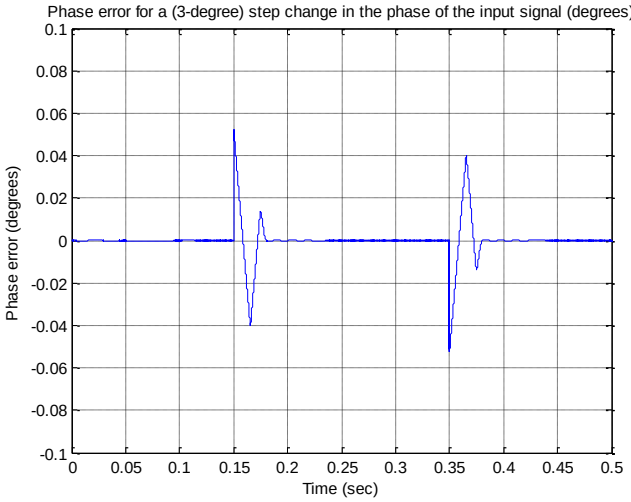


**Figure 6.12:** Phase error response for a step change in the phase of the PLL circuit input signal.

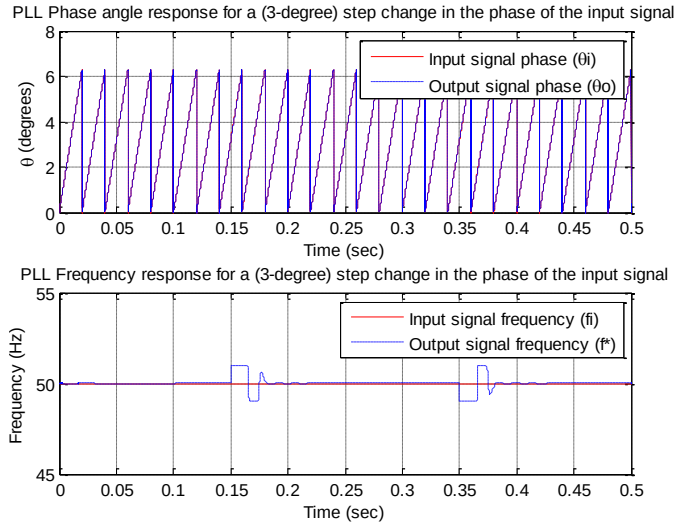


**Figure 6.13:** Phase and frequency responses for a step change in the phase of the PLL circuit input signal

However, when there is frequency variation in the input signal, this second-order PLL circuit is found to perform unsatisfactorily. This is confirmed by observing the PLL circuit's response to a 10 Hz/second ramp change in the input frequency, programmed into the input signal between 0.15 seconds and 0.35 seconds of the simulation time. The results of the simulation are shown in Figures (6.14) and (6.15), which clearly demonstrates this PLL circuit's inability to deal well with such grid anomalies as frequency variations. The circuit's behavior thus suggests that a higher-order PLL circuit would be required where the grid voltage is expected to exhibit a lot of anomalies, as discussed also by Chung (2000).

The performance of the designed PLL circuit suffices for the application considered in this study, being limited as it is to consideration of only idealized grid conditions. The PLL circuit is implemented in the inverter current controller system (Section 6.6) for synchronizing the inverter current phase angle with the grid voltage phase angle, in order to achieve unity-power-factor inverter current injection into the grid.

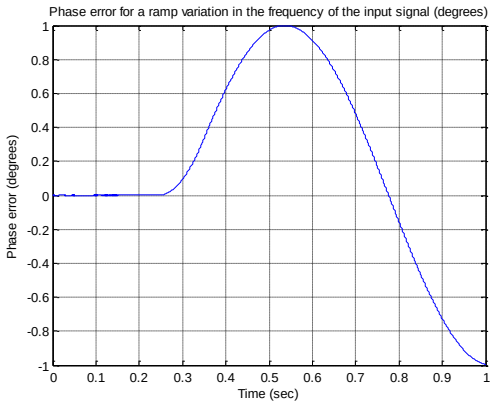


**Figure 6.14:** **Phase error response of the PLL circuit for a ramp change in the frequency of the input signal.**

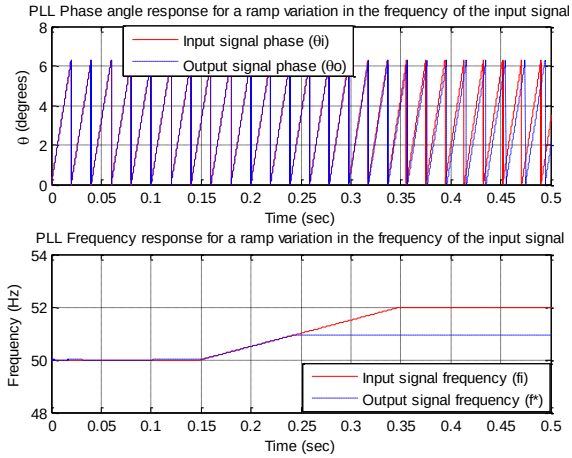


**Figure 6.15:** **Phase and frequency responses for a ramp change in the frequency of the PLL circuit input signal.**

## 6.4. Grid-connected inverter system

### 6.4.1. Topology

The grid-connected inverter system considered in this study is very similar to that suggested by Kramer *et al* (2008), as illustrated in Figure (6.16). The system in Figure (6.16) is a generic topology that may act as a grid interface for a variety of Distributed Energy Resources (DER), and highlights the main components that are typically present in a Power Electronic converter interface for a DER.

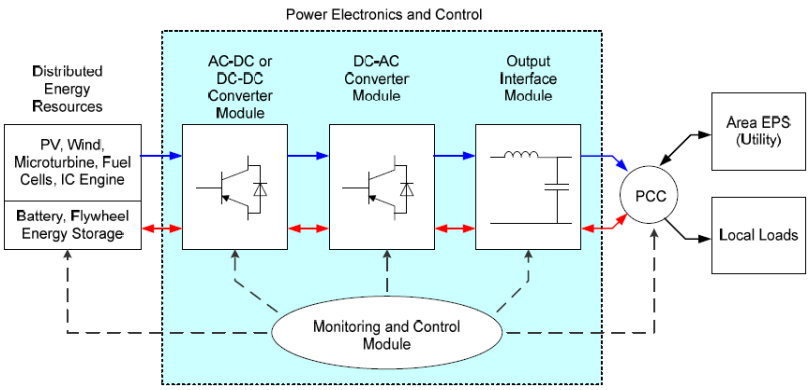


**Figure 6.16: Generic block diagram of a Power Electronic converter interfacing a DER to the grid.**
**(Adapted from Kramer *et al.*, 2008)**

These main components (besides the inverter) are:

- Primary energy source
- Generator-side power converter
- Filter interface
- Monitoring and control system

Chapter 4 dealt with the DER (*i.e.* PV & WEC systems) modeling and the generator-side power converter control; the filter interface is discussed in Chapter 5; and in this chapter, the inverter control and monitoring system is addressed.

The intention of the work in this thesis is to develop a monitoring and control system for operating the inverter system both in grid-connected and stand-alone modes of operation. This chapter focuses on the control strategy for the grid-connected operational mode, while the stand-alone operation is dealt with in the following chapter.

Inverter modulation is an important design choice that has to be made as part of the control system design, since the controller output signals are fed to the modulator for the synthesis of the switch gating signals (Holtz, 1992). So the next sub-section briefly discusses common inverter modulation techniques, prior to presenting the controller design procedure.

### 6.4.2. Inverter modulation

In an inverter circuit, it is desired to derive a sinusoidal voltage signal waveform having a specified magnitude and frequency from a DC voltage that acts as the input to the inverter. The inverter uses the on-off action of fast power switches to realize this DC-AC signal transformation, and the means by which these switches are controlled is referred to as *modulation* (Yazdani & Iravani, 2010).

A common way to implement inverter switch modulation is Pulse Width Modulation (PWM). The idea behind PWM switch control is to vary the switch on-time relative to a fixed switching period (constant-frequency PWM), thus controlling the magnitude of the output signal as a function of the DC input and the modulation ratio (Mohan *et al*., 2003). The switching signals are produced by comparing a modulating (or control) signal with a triangular repetitive signal, as illustrated in Figure (6.17). To produce three-phase sinusoidal waveforms, a set of three-phase (uniformly spaced) sinusoidal modulating signals at a desired magnitude and fundamental frequency is compared to a triangular carrier signal (referred to as Carrier-Based Sinusoidal Pulse-Width-Modulation, or CB-SPWM) (Teodorescu *et al*., 2011), as can be deduced from Figure (6.17). The frequency of the carrier signal sets the switching frequency of the inverter, and the resultant pulse signal then acts as the gate-drive signal for the inverter switches.

In sinusoidal CB-SPWM, the magnitude of the fundamental output voltage waveform varies linearly with the modulation ratio for a modulation ratio not exceeding 1.0 per-unit. This significantly limits the magnitude of the fundamental AC-side voltage of the inverter.

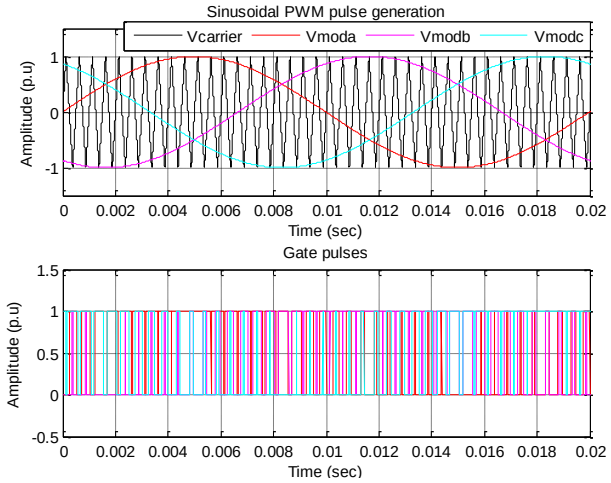


**Figure 6.17: Generation of switch gate pulses by Carrier-Based Sinusoidal Pulse Width Modulation (CB-SPWM).**

Modulating ratio in excess of 1.0 per-unit allows increasing the magnitude of the fundamental AC-side voltage, but this leads to over-modulation, which may be undesirable where a pre-defined harmonic spectral characteristic is required (Mohan *et al*., 2003).

One approach used to slightly extend the range of the modulating ratio is what is referred to as third-harmonic injection, otherwise known as zero-sequence injection, because in a symmetrical three-phase system, triple-n harmonics have zero length, and consequently do not produce harmonic currents (Yazdani & Iravani, 2003; Holtz, 1992). The amplitudes of the inverter AC-side fundamental waveform for the CB-SPWM and CB-SPWM with third-harmonic injection are given by Equations (6.9) and (6.10) respectively (Mohan *et al*., 2003).

$$V_{LLrms\_SPWM} = \frac{\sqrt{3}}{2\sqrt{2}} \cdot V_{DC} = 0.612 V_{DC} \tag{6.9}$$

$$V_{LLrms\_SPWM+3rd\_Harm} = \frac{1}{\sqrt{2}} \cdot V_{DC} = 0.707 V_{DC} \tag{6.10}$$

where $V_{LLrms\_SPWM}$ is the amplitude of the inverter AC-side fundamental waveform for the CB-SPWM, $V_{LLrms\_SPWM+3rd\_Harm}$ is the amplitude of the inverter AC-side fundamental waveform for the CB-SPWM with third-harmonic injection , and $V_{DC}$ is the input DC voltage of the inverter.

Another commonly used form of inverter modulation is Space-Vector modulation-based Pulse Width Modulation (SVPWM). It is based on the mathematical representation of a three-phase signal as a space vector in the complex plane.

The space vector normally follows a circular locus, and can only assume discrete positions. The objective of the SVPWM technique is to optimally determine the space vector's position by means of averaging three adjacent state vectors (two active, one zero) over a switching period. The switching pattern is determined so as to minimize harmonic distortion and the count of inverter commutations; the switching vectors are so determined as to obtain an averaged voltage vector equal to the sampled reference vector at a constant sampling interval (Holtz, 1992). Figure (6.18) (Neacsu, 2001) illustrates the switching state vectors for the two-level, three-phase SVPWM, showing six active and two zero state vectors, as well as the average voltage vector.

In Figure (6.18), $V_s$ and $\alpha$ are the magnitude and phase angle, respectively, of the voltage space vector $\underline{V_s}$, and $\underline{\mathbf{V_i}}$, $\mathbf{i} = \overline{\mathbf{0}\ldots\mathbf{7}}$ are the eight different space vector positions that can be assumed by the voltage space vector on the circular locus defined by the vector's amplitude.

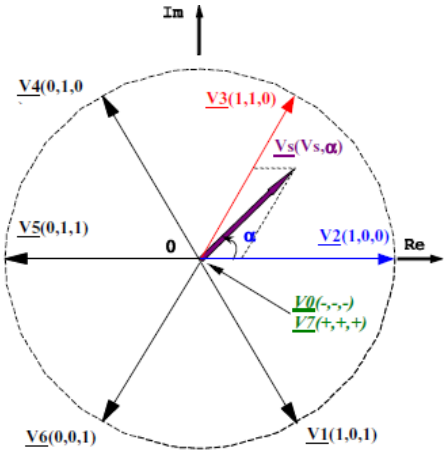


**Figure 6.18:** **Voltage space vector generation by space vector modulation (Adapted from Neacsu, 2001).**

The switching reference function, defined in analogy to the CB-SPWM for relative ease of implementation represents the normalized (relative to the sampling period) conduction time of each inverter leg. It varies between 0.0 and 1.0, and is centered at about 0.5. The presence of a third-harmonic component in the switching function (although not in the output voltages) can be used to either maximize the amplitude of the fundamental output voltage (similar to the case of CB-PWM with third-harmonic injection) or to minimize the harmonic current factor, depending on the zero-state-vector placement. The magnitude of the inverter AC-side fundamental waveform for the SVPWM is given by Equation (6.11) (Neacsu, 2001). Because of the mathematical approach of the space vector modulation technique, it lends itself to digital implementation on a microprocessor.

$$V_{LLrms\_SVPWM} = \frac{1}{\sqrt{2}} \cdot V_{DC} = 0.707 V_{DC} \tag{6.11}$$

where $V_{LLrms\_SVPWM}$ represents the amplitude of the inverter AC-side fundamental waveform for the space vector modulation.

Random PWM (or Frequency Modulation) may be used where it is desired to achieve a more even harmonic distribution than that which is obtained in constant-frequency SPWM, which normally has very pronounced harmonic components at side-bands centered on the switching frequency and its multiples. This is especially the case in AC motor drives, where the acute side-band harmonics often cause acoustic noise in the machine (Holtz, 1992). Moreover, this technique also allows the reduction of conducted and radiated *Electromagnetic Magnetic Interference* (EMI) with less filtering and shielding efforts (Evju, 2007).

## 6.5. Inverter common control strategies

### 6.5.1. Modes of control

An inverter is generally controlled to transfer power from the DC bus to the AC-side bus. Two main approaches of power transfer control are *voltage-mode* and *current-mode control* (Yazdani & Iravani, 2010).

In the *voltage-mode* control approach, the power delivered by the inverter is regulated by controlling the amplitude and phase angle of the inverter terminal voltage. Based on power flow theory, the strategy aims to achieve decoupled control of the active and reactive components of the inverter output power by the appropriate control of the phase angle and amplitude of the inverter voltage, respectively, relative to the corresponding quantities of the bus to which the inverter feeds the power.

Assuming that the inverter, with terminal voltage amplitude $V_i$ and phase angle $\delta$, supplies active power $P_i$ and reactive power $Q_i$ to the grid bus of voltage amplitude $V_g$, the expressions for the power transfer from the inverter to the grid can be written as (Ängquist & Lindgren, 1991):

$$P_i = \frac{V_i \cdot V_g}{X_L} \cdot sin(\delta) \tag{6.12}$$

$$Q_i = \frac{V_i \cdot (V_i cos(\delta) - V_g)}{X_L} \tag{6.13}$$

where $X_L$ is the effective inductive reactance between the inverter and the grid (neglecting the resistive component of the interface impedance). The voltage-mode inverter output power control technique is devised on the basis of Equations (6.12) and (6.13).

Inverter output power control can also be implemented by a *current-mode* control strategy, in which the amplitude and phase of the inverter current are used to control the active and reactive power outputs of the inverter. There are many strategies used to realize current-mode control of the inverter. These are discussed in Section (6.5.2).

As respects performance characteristics, current-controlled techniques are considered to yield superior results to voltage-mode control strategies in terms of, among other aspects, accurate control of the instantaneous current waveform with inherent current limiting, very good controller dynamics with good disturbance rejection and grid parameter independence, as well as ability to compensate for DC-link and AC-side voltage changes (Kazmierkowski & Malesani, 1998). Moreover, for the grid-connected inverter, the grid is stiff and sets the voltage magnitude and frequency; consequently, inverter terminal voltage regulation may not be allowed, such that current-control is usually the technique that allows meeting power quality requirements of grid-integrated inverter systems. On the other hand, when the inverter

supplies a load autonomously, voltage-mode control becomes the preferred method, since the inverter should then regulate the terminal voltage at a desired magnitude and nominal frequency.

A number of researchers have presented an overview of commonly used linear and no-linear PWM voltage-source inverter current-control techniques (e.g. Teodorescu *et al*., 2011; Monreal *et al*., 2009; Timbus *et al*., 2009; Kazmierkowski & Malesani, 1998). A few of them are briefly discussed in the following sub-section, the discussion being limited to the linear methods. The generic unity-feedback system of Figure (6.19) is considered for the discussed control techniques.

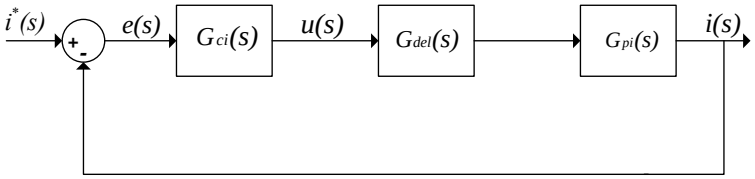


**Figure 6.19: Generic inverter current controller block diagram (Adapted from Teodorescu *et al*., 2011).**

In Figure (6.19) $G_{ci}(s)$, $G_{pi}(s)$ and $G_{del}(s)$ are the transfer functions of the controller, the plant model, and the computational delay respectively, while $i^*(s)$, $i(s)$ and $u(s)$ are the reference current, output current and the control output signals in the Laplace domain respectively. $e(s)$ represents the error between the reference and output current signals, which the current controller has to minimize.

As discussed by Teodorescu *et al*. (2011: 317), the delay term included in the controller block diagram is necessitated by the fact that both signal measurement (involving sampling and filtering) as well as gate pulse synthesis (by the PWM) introduce a delay into the control system that needs to be taken into account in the controller design. The computational time delay is approximated as one-and-half of the sampling period (*i.e.* $1.5T_s$, where $T_s$ is the sampling period) (Teodorescu *et al*., 2011).

### 6.5.2. Linear current-control techniques

The inverter system is inherently non-linear; however, a linearized model of the inverter is normally considered for controller design purposes, as discussed in Section (5.4). This permits design of the inverter current controller based on linear control theory (Teodorescu *et al*., 2011).

A salient feature of linear current control is the clear demarcation of the current error compensation and inverter modulation parts. Thanks to this separation, such desirable characteristics of open-loop modulators as constant switching frequency, a well-defined

harmonic spectrum, and enhanced dc-link utilization can be exploited when linear control is used (Kazmierkowski & Malesani, 1998).

#### 6.5.2.1. Proportional-Integral (PI) regulator

A PI regulator has the general form:

$$G_{cPI}(s) = K_p + \frac{K_i}{s} \tag{6.14}$$

$G_{cPI}(s)$, $K_p$ and $K_i$ represent the transfer function, the proportional gain, and the integral gain of the regulator, respectively.

The regulator applies purely proportional and integral gain factors to the error signal (that is, the difference between the reference and the system output signals), and outputs the actuating signal that is applied to the controlled plant in an effort to bring the control error to zero.

With their simple structure, PI regulators are an attractive choice whenever their application can provide acceptable steady-state and dynamic response. It is possible to implement them both in the natural (abc) and equivalent two-axis (αβ- or dq-) reference frames. However, PI regulation in abc- and αβ-frames exhibits steady-state magnitude and phase error response, due to the sinusoidal reference tracking nature of the problem in these reference frames, and a PI regulator cannot track a varying reference signal with zero steady-state error (Yazdani & Iravani, 2010).

A common strategy is to transform the controlled signals from the natural reference frame to the rotating (dq) reference frame whose frequency of rotation is matched to that of the grid voltage. In this way, the controlled signals become time-invariant, consequently allowing implementation of the simple PI regulation to achieve the control objectives. Three-phase-to-synchronous-dq transformation has the added advantage of enabling independent control of the inverter active and reactive power by two separate PI compensators. Satisfactory performance of this method, however, normally requires decoupling and feed-forward compensation, and may necessitate further enhancements to the control structure, especially under unbalanced grid conditions (Yuan *et al*., 2002; Milosevic, 2003).

#### 6.5.2.2. Proportional-Resonant (PR) regulator

The synchronous-reference-frame PI control scheme performs quite satisfactorily, but actual implementation may be computation-intensive on account of the necessary enhancements mentioned in the previous paragraph.

The PR (also called stationary-frame generalized integrator) regulator provides another linear solution to the inverter current control problem. It is designed to be able to track sinusoidal reference signals with zero steady-state error, based on the *internal model control* (IMC)

principle, which states that good reference tracking and disturbance rejection can be realized by including models of the reference and disturbance in the compensator. For the PR current regulator, this is done by devising a compensator that places a pair of poles on the imaginary axis at the frequency of the reference signal (Teodorescu *et al.*, 2011). The PR regulator is generally formulated as:

$$G_{cPR}(s) = K_p + K_i \cdot \frac{s}{s^2 + \omega_o^{\,2}} \tag{6.15}$$

where $G_{cPR}(s)$, $K_p$ and $K_i$ represent the transfer function, the proportional gain, and the integral gain of the PR regulator respectively, and $\omega_o$ is the frequency of the fundamental signal to be regulated.

The PR regulator succeeds in achieving zero-steady-state-error sinusoidal reference tracking because it exhibits infinite gain at the frequency of the signal to be compensated for, and is characterized by negligible frequency response at all other frequencies. This permits its use for selective harmonic filtering for any harmonics of choice using the expression (considering harmonic compensation of the $3^{rd}$, $5^{th}$ and $7^{th}$ harmonics, which are the dominant grid harmonics):

$$G_{cPR\_harm}(s) = \sum_{h=3,5,7} K_{ih} \cdot \frac{s}{s^2 + (h\omega_o)^2} \cdot \tag{6.16}$$

where $G_{cPR\_harm}(s)$ is the harmonic compensator for the $h^{th}$ harmonic (in addition to the fundamental-frequency compensator, given by Equation 6.15), and is usually comprised of only the integral gain $K_{ih}$, having no proportional gain factor (Evyu, 2006).

According to Teodorescu *et al*. (2011), the αβ-frame PR-based control scheme exhibits a frequency response similar to that obtained in the case of the dq-frame PI-based control strategy. In fact, it has been demonstrated that the PR regulator is obtainable from the dq-frame PI regulator by a dq-to-αβ transformation operation. The attractiveness of the PR-based control scheme is the avoidance of the rotating-frame transformation and the associated decoupling and feed-forward compensation.

#### 6.5.2.3. Deadbeat control

Deadbeat control is a discrete-time predictive control technique which uses a simplified model of the plant to predict the likely trajectories of the controlled variable (the current in this case), and then computes a switching state vector that drives the control error to zero within a specified number of sampling periods (Monreal *et al*., 2009; Holtz, 1992). The current is thus controlled to follow a predictive model-based reference with minimum error.

The main objective of the control action is to achieve a closed-loop response where the actual current equals the reference value within a finite number of sampling periods, which may be a design parameter (Timbus *et al*., 2009; Hetthéssy *et al*., 2004). That is, the closed-loop response should obey the control law (n representing the number of samples):

$$\frac{i(z)}{i^*(z)} = G_{DBCL}(z) = z^{-(n+1)} \tag{6.17}$$

where $i^*(z)$, $i(z)$ and $G_{DBCL}(z)$ are the z-domain representations of the reference current, the system output current and the closed-loop transfer function respectively, and $z$ is the time-delay operator (Blaabjerg *et al*., 2006).

Considering a discretized form of the generic current control block diagram (Figure 6.19), and representing the transfer functions of the controller and the plant model (which also incorporates the system delay transfer function) by $G_{cDB}(z)$ and $G_{pi}(z)$ respectively, the closed-loop control system transfer function can be derived as (Teodorescu *et al*., 2011):

$$G_{DBCL}(z) = \frac{G_{cDB}(z) \cdot G_{pi}(z)}{1 + G_{cDB}(z) \cdot G_{pi}(z)} \tag{6.18}$$

Expressed in terms of $G_{cDB}(z)$, equation (6.18) becomes:

$$G_{cDB}(z) = \frac{1}{G_{pi}(z)} \cdot \frac{G_{DBCL}(z)}{1 - G_{DBCL}(z)} \tag{6.19}$$

Equations (6.17) and (6.19) can be combined to obtain the expression for the deadbeat controller:

$$G_{cDB}(z) = \frac{1}{G_{pi}(z)} \cdot \frac{z^{-(n+1)}}{1 - z^{-(n+1)}} \tag{6.20}$$

One feature of the deadbeat control technique is that it theoretically has a very high closed-loop bandwidth due to the (n+1) poles located at the origin in the closed-loop response (Equation 6.17). It thus exhibits a very fast dynamic response and good reference tracking ability, and is considered to be among the fastest current controllers, able to null the control error in a minimum number of sampling periods.

The drawback of the deadbeat control technique is its sensitivity to system delays, parameter variations and model uncertainties (being a model-based control technique). These factors affect the reference-tracking characteristic as well as the stability of the technique. Use of observers to estimate unavailable parameters and including them in the control structure may improve the control action. Moreover, combination of the deadbeat technique with other controllers is often considered as a means to compensate for the deadbeat controller's

sensitivity to parameter variations and un-modeled dynamics (Teodorescu *et al*., 2011; Monreal *et al*., 2009; Dell'Aquila *et al*., 2003).

#### 6.5.2.4. State feedback control

State feedback control design involves the determination of the feedback gain matrix that places the closed-loop poles of the controlled system at desired locations (pole-placement method), to guarantee sufficient damping, and thus provide a good steady-state and dynamic response of the system (Kazmierkowski & Malesani, 1998).

The system to be controlled is expressed in state space form, which is a convenient way of representing an arbitrary-order multivariable system in the time domain, and thereby enables observation and control of the process variable(s) of interest in the system. This is unlike systems that are expressed in the frequency (Laplace) domain, which are mostly suited to single-variable control.

A system may be formulated in a state-space form as:

$$\begin{aligned} \dot{\boldsymbol{x}}(t) &= \boldsymbol{A}\boldsymbol{x}(t) + \boldsymbol{B}\boldsymbol{u}(t) \\ \boldsymbol{y}(t) &= \boldsymbol{C}\boldsymbol{x}(t) + \boldsymbol{D}\boldsymbol{u}(t) \end{aligned} \tag{6.21}$$

where $\boldsymbol{x}(t)$ is an n-element vector of system state variables ($R^{1\times n}$), $\boldsymbol{u}(t)$ is an m-vector of system inputs ($R^{1\times m}$), and $\boldsymbol{y}(t)$ is an l-element vector of output signals ($R^{1\times l}$). $\boldsymbol{A}$, $\boldsymbol{B}$, $\boldsymbol{C}$ and $\boldsymbol{D}$ are the system matrices containing the state, input, output and feed-forward coefficients (and belonging to the vector spaces $R^{n\times n}$, $R^{n\times m}$, $R^{l\times n}$ and $R^{l\times m}$) respectively. State feedback control may be implemented either in the stationary reference frame or the synchronous reference frame. Its performance is significantly superior to that of the classical PI controller, especially in its inherent ability to properly decouple state disturbances, and is thus popular in AC motor control for its effectiveness in providing system damping and guaranteeing dynamic compensation of the machine back emf.

Lorenz and Lawson (1987) provided a good pedagogical explanation of why state feedback control is more suitable for induction machine current control than PI control. Although synchronous-reference-frame PI current control does better than the stationary-frame counterpart, it is not only more complex to practically implement (especially in digital form), its effective disturbance rejection is hampered by the inherent system parameter sensitivity of the means by which the disturbance rejection is achieved, which is system pole cancellation by the transfer function zero provided by the PI controller. Gain tuning amid varying armature time-constant thus proves to be less than straightforward. This is not the case with the state feedback control, for which the choice of the feedback gain matrix to (for instance)

compensate for the grid voltage disturbance does not exhibit such parameter sensitivity, and thus enables easier, individual tuning of the feedback gains.

## 6.6. Controller design for the grid-connected inverter

An inverter connecting a distributed generation system to the utility grid is normally operated in current-mode control. This enables taking advantage of the various positive attributes of the current-mode control, such as inherent current limiting, fast dynamic response, higher control precision and greater immunity to grid parameter variations (Kazmierkowski & Malesani, 1998). This in turn makes it more probable for the inverter terminal characteristics to satisfy the power quality requirements of the interconnection standards (Yazdani & Iravani, 2010).

Some of the most vital considerations for the grid inverter current control are to ensure that the injected current has sufficiently low harmonic content (that is, it satisfies total harmonic distortion requirements), that the inverter remains properly synchronized with the grid under normal operating conditions, and that it correctly responds to abnormal grid conditions (anti-islanding).

The interface filter to enable the inverter output voltage and current to satisfy power quality requirements for this study has been developed in Section (5.6). Grid synchronization is discussed in Section 6.3, along with the design of a PLL circuit, which is used for obtaining the grid voltage phase angle, for use in the inverter current controller adopted in this thesis. Anti-islanding is dealt with in the following chapter, which deals with the distributed generation system's operation in autonomous mode.

### 6.6.1. Control approach

Common control strategies for the inverter were briefly discussed in Section 6.5.2, with the scope limited to the linear methods. Properly designed linear current control techniques generally have comparable performance attributes when such indices as transient response (closed-loop bandwidth, settling time, overshoot damping), steady-state response (error-tracking), stability and harmonic distortion are taken into account (Monreal *et al*., 2009; Timbus *et al*., 2009).

In this study, the synchronous-reference-frame proportional-integral (PI) control approach has been adopted (Rocabert *et al*., 2012).

Some of the positive aspects of the synchronous-reference frame PI control approach are: Decoupled control of active and reactive power outputs of the inverter;

- Unity-power-factor control of the inverter current by aligning the d-axis inverter voltage component with the grid voltage;
- Easier synchronization of the inverter with the grid by the regulation of the q-axis voltage component to zero (discussed in Section 6.3.3); and

- Regulation of DC (rather than AC) signals, thus allowing use of simpler-structure (PI) regulators, which is desirable from the system complexity and parameter tuning point of view.

The synchronous reference frame-PI-based inverter current control technique does require some control structure enhancements in order to insure acceptable performance under distorted grid conditions (Marwali & Keyhani, 2004). The scope of this study is limited to the consideration of nominal, undistorted grid conditions, however. So controllers are developed on the assumption that the grid operates under normal conditions. Implementation of control strategies for general grid conditions is considered for future work.

The grid inverter controller is developed on the basis of Figure (6.20). In this dual-loop scheme, $G_{cv}(s)$ is the outer-loop controller transfer function, which regulates the DC-link voltage, $V_{DC}$, based on the power transferred to the grid, $P_i$, and sets the reference current, $i_i^*$, for the inner loop; $G_{ci}(s)$ is the inner-loop controller transfer function, which regulates the inverter output current. The magnitude and phase angle of the grid voltage, represented by $V_g$ and $\theta$ respectively, are also required to be sensed for use in the current control scheme (Liserre *et al*., 2010). The phase angle of the grid voltage is provided by a PLL circuit, represented in the figure by the PLL block.

The approach usually employed in designing such a dual-loop control scheme is to design the inner (current) control loop such that it has a high closed-loop bandwidth. This ensures that it exhibits fast dynamic response, and that it can track command changes with minimal error. In this way, the performance of the current controller has a considerable bearing on the inverter's ability to satisfy power quality requirements. The outer (DC-link voltage) control loop is in turn designed to have a relatively lower bandwidth, its main objective being to regulate the DC-link voltage as a function of the variations in the power flow from the DC link to the grid, and to ensure overall stability of control (Liserre *et al.*, 2010).

That the bandwidths of the inner and outer control loops are designed to be considerably disparate implies that the two loops' responses are also fairly decoupled, and this permits designing them independently (Yazdani & Iravani, 2010). The design of the current controller is considered first, before designing the DC-link regulator.

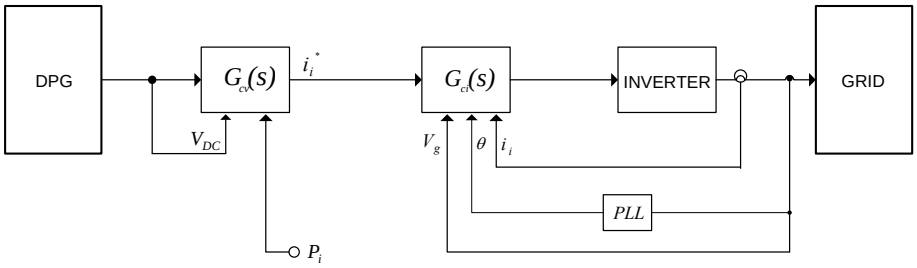


**Figure 6.20:** **Dual-loop controller for the grid-connected inverter system (Adapted from Liserre *et al.*, 2005)**

### 6.6.2. Controller structure

As already mentioned, the inverter output current is controlled on the basis of the decoupled dq-frame PI control technique. The plant model for the controller design is therefore also derived in the dq reference frame, on the basis of the dq-frame electrical model of the LCL filter (the filter interface used in this thesis). This plant model derivation was presented in Chapter 5 (Section 5.4), and some relevant results from there are restated here as an aid to the devising of the controller structure.

The inverter current control plant model derived in Section 5.4 from the dq-frame electrical model of the LCL filter is given by Equations (5.16b) and (5.17b), restated here as:

$$L_i \frac{di_{id}}{dt} = v_{id} - R_i i_{id} + \underline{\omega L_i i_{iq} - v_{cd}} \tag{6.21a}$$

$$L_i \frac{di_{iq}}{dt} = v_{iq} - R_i i_{iq} - \underline{\omega L_i i_{id} - v_{cq}} \tag{6.22a}$$

where $i_{id}$ and $i_{iq}$ are the dq-axis inverter output current components, $v_{id}$ and $v_{iq}$ are the dq-axis inverter output voltage components, $v_{cd}$ and $v_{cq}$ are the dq-axis shunt capacitor voltage components, $L_i$ and $R_i$ are the inductance and parasitic resistance of the LCL-filter's inverter-side inductor, respectively, and $\omega$ is the line angular frequency.

As discussed in Section 5.4, in the dynamic inverter current control model expressed by Equations (6.21a) and (6.22a), the inverter current components ($i_{id}$ & $i_{iq}$) are the controlled state variables, whereas the inverter voltage components ($v_{id}$ & $v_{iq}$) represent the control inputs. This is a two-channel control scheme, made up of the d-axis current control and the q-axis current control. Some pertinent aspects pertaining to the inverter current control based on the model given by Equations (6.21a) and (6.22a) are worth pointing out as a first step to presenting the controller structure.

The first aspect that may be noted about the system of equations (6.21a) and (6.22a) is that there is cross-coupling between the d-axis and the q-axis control loops, due to the presence of

a component of q-axis current (*i.e.* $\omega L_i i_{iq}$) in the expression for the d-axis current (Equation 6.21a), and likewise the presence of a component of the d-axis current ($\omega L_i i_{id}$) in the expression for the q-axis current (Equation 6.22a). This cross-coupling is a result of the (three-phase-to-dq) axis transformation. The second aspect to note is that each of the two channels has a component of the shunt filter capacitor voltage ($v_{cd}$, $v_{cq}$), which may be considered to be a disturbance in the control loop. These cross-coupling and disturbance components are the underlined terms in Equations (6.21a) and (6.22a).

Independent control of the d-axis and q-axis current channels is commonly realized by means of decoupling and feed-forward compensation; the decoupling is implemented in a way that eliminates the mutual influence of the two control channels on each other, and the feed-forward compensation is meant to eliminate the adverse effect of the capacitor voltage on the control loops. Capacitor voltage is usually not available as a sensed parameter, however. Thus, in many cases the grid voltage is used for implementing the feed-forward compensation in the place of the capacitor voltage, based on the assumption that the difference between the capacitor and grid voltages is small enough to be compensated for by the well-designed current controller (Evyu, 2007).

A third point to take note of is that in arriving at the set of Equations (6.21a) and (6.22a), the shunt branch of the LCL filter, consisting of the filter capacitor and the damping resistor (Figure 5.5, Chapter 5), has been neglected, having been assumed to have negligible influence on the control dynamics of the fundamental-frequency line current (Teodorescu *et al.*, 2011). With this simplification, the inverter-side and grid-side inductances and parasitic resistances can be combined to represent the effective inductance of the interface filter, as expressed by Equations (5.20b) and (5.21b) in Section 5.4, and restated here for ease of reference:

$$L_{eff} = L_i + L_g \tag{6.21b}$$

$$R_{eff} = R_i + R_g \tag{6.22b}$$

Thus in Equations (6.21a) and (6.22a), $L_i$ can be replaced by $L_{eff}$, and $R_i$ by $R_{eff}$. Also, for the reason stated above, the shunt capacitor voltage components ($v_{cd}$, $v_{cq}$) can be replaced by the corresponding grid voltage components ($v_{gd}$, $v_{gq}$) for the purpose of implementing the feed-forward compensation. Taking these adjustments into account, Equations (6.21a) and (6.22a) can be rewritten as:

$$L_{eff}\frac{di_{id}}{dt} = v_{id} - R_{eff} i_{id} + \underline{\omega L_{eff} i_{iq} - v_{gd}} \tag{6.21c}$$

$$L_{eff}\frac{di_{iq}}{dt} = v_{iq} - R_{eff} i_{iq} - \underline{\omega L_{eff} i_{id} - v_{gq}} \tag{6.22c}$$

Then two terms were introduced in Section 5.4 that represent the effect of implementing the decoupling and feed-forward compensation on the system of Equations (6.21c) and (6.22c), given by Equations (5.18) and (5.19) and restated here ($v_{gd}$, $v_{gq}$, & $L_{eff}$ replacing $v_{cd}$, $v_{cq}$ & $L_i$ respectively) as:

$$v'_{id} = -\underline{\omega L_{eff} i_{iq} + v_{gd}} \tag{6.21d}$$

$$v'_{iq} = \underline{\omega L_{eff} i_{id} + v_{gq}} \tag{6.22d}$$

Adding Equations (6.21d) and (6.22d) to Equations (6.21c) and (6.22c) respectively and rearranging the expressions, the resultant expressions are given by:

$$L_{eff}\frac{di_{id}}{dt} + R_{eff} i_{id} = v_{id} \tag{6.21e}$$

$$L_{eff}\frac{di_{iq}}{dt} + R_{eff} i_{iq} = v_{iq} \tag{6.22e}$$

Then taking the Laplace transform of Equations (6.21e) and (6.22e), the following transfer functions for the d-axis and q-axis control loops are obtained:

$$\frac{i_{id}(s)}{v_{id}(s)} = G_{pid}(s) = \frac{1}{sL_{eff} + R_{eff}} \tag{6.23a}$$

$$\frac{i_{iq}(s)}{v_{iq}(s)} = G_{piq}(s) = \frac{1}{sL_{eff} + R_{eff}} \tag{6.23b}$$

As can be seen from Equations (6.23a) and (6.23b), and as has already been established in Section 5.4, the two control loops are structurally identical. This implies that it is sufficient to consider only one of the loops (d-axis or q-axis) in the design of the controller, and to apply the thus obtained controller to the other loop (Yazdani & Iravani, 2010). The plant model for the inverter current control can also be considered, which makes no distinction between the d-axis and q-axis control loops, $G_{pi}(s)$, given by:

$$\frac{i_i(s)}{v_i(s)} = G_{pi}(s) = \frac{1}{sL_{eff} + R_{eff}} \tag{6.23b}$$

Thus following from the discussion and analysis presented above, the controller for the inverter current control can be formulated as follows:

The error signal ($e(s)$) between the reference ($i_i^*(s)$) and the actual output ($i_i(s)$) of the inverter current is fed into the controller ($G_{ci}(s)$, to be designed), providing the controlled output signal ($u(s)$), which can be written as:

$$e_{id}(s) = i_{id}^{*}(s) - i_{id}(s) \tag{6.24a}$$

$$e_{iq}(s) = i_{iq}^{*}(s) - i_{iq}(s) \tag{6.25a}$$

$$u_{id}(s) = e_{id}(s) \cdot G_{cid}(s) \tag{6.24b}$$

$$u_{iq}(s) = e_{iq}(s) \cdot G_{ciq}(s) \tag{6.25b}$$

The decoupling and feed-forward compensation terms (Equations 6.21d and 6.22d) are then added to the controlled output signals, to obtain the inverter output voltages, which can be expressed as:

$$v_{id}(s) = u_{id}(s) + v_{id}^{'}(s) \tag{6.24c}$$

$$v_{iq}(s) = u_{iq}(s) + v_{iq}^{'}(s) \tag{6.25c}$$

The modulation of the inverter output voltage, given Equations (6.24b) and (6.25b), then allows the achieving of the desired inverter current control (this amounts to the indirect control of the inverter output current by means of the inverter output voltage, since the inverter allows the synthesis of its output voltage, but not its output current (Yazdani & Iravani, 2010)).

One more thing that is left to establish in the controller structure is the determination of the reference values for each of the two control loops. These are derived on the basis of the magnitudes of the active power, $P_i$, and reactive power, $Q_i$, to be transferred from the DPG to the grid, because the control of the inverter output current is essentially aimed at controlling the power transfer through the inverter (Wang, 2006). The expressions for the inverter active and reactive power output magnitudes ($P_{idq}, Q_{idq}$) in the dq reference frame can be written as (see Appendix A.2):

$$P_{idq} = \frac{3}{2}(v_{id} i_{id} + v_{iq} i_{iq}) \tag{6.24d}$$

$$Q_{idq} = \frac{3}{2}(-v_{id} i_{iq} + v_{iq} i_{id}) \tag{6.25d}$$

In the control strategy used here for the inverter current control, the d-axis component of the inverter output voltage is aligned with the magnitude of the grid voltage, whereas the q-axis component is regulated to zero. This is a strategy commonly employed to achieve the unity-power-factor grid-mode operation of the inverter, as stipulated in most cases by grid-code requirements (IEEE 1547-2003). Thus with a null value for the q-axis inverter voltage ($v_{iq}$), the expressions for the current reference values ($i_{id}^{*}$, $i_{iq}^{*}$) can be derived from Equations (6.24c) and (6.25c) as:

$$i_{id}^{*} = \frac{2}{3} \cdot \frac{P_{idq}}{v_{id}} \tag{6.24e}$$

$$i_{iq}^{*} = -\frac{2}{3} \cdot \frac{Q_{idq}}{v_{id}} \tag{6.25e}$$

Thus combining Equations (6.21d), (6.22d), (6.23a), (6.23b), (6.24a)-(6.24c), (6.25a)-(6.25c), (6.24e) and (6.25e), the inverter current controller structure is arrived at, as depicted in Figure (6.21).

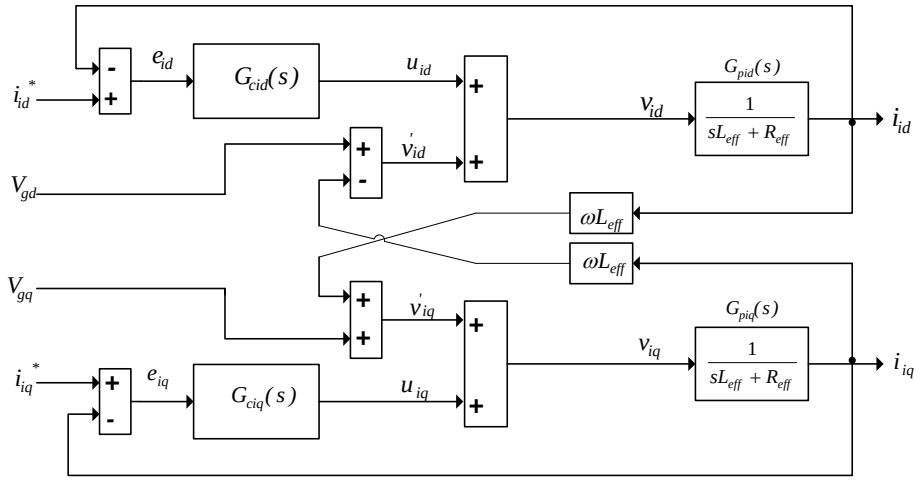


**Figure 6.21:** **Control scheme for the decoupled dq-reference frame PI inverter current-mode control**

In the following two sub-sections, the controller design task is addressed, starting with the design of the inner-loop current controller (based on the control scheme depicted in Figure 6.21), followed by the outer-voltage loop regulator design (based on the model presented in Section 5.5, in conjunction with the result of the inner-current loop controller design). The controllers are designed on the basis of the inverter rating specifications listed in Table (5.2) and the filter parameters listed in Table (5.3), which are both reproduced below for ease of reference. The d-axis loop is considered for the current controller design, and the resulting controller is also valid for the q-axis loop, as explained earlier.

**Table 6.1:** **Parameters considered for the inverter control system design**

| PARAMETER | VALUE |
|---|---|
| Inverter rating ($P_n$) | 15 (kW) |
| System type | Three-phase |
| Operational power factor (pf) | 1 |
| Nominal DC-link voltage ($V_{DC}$) | 720 (V) |
| Line voltage ($V_{LLrms}$) | 400 (V) |
| Nominal line current ($I_{nrms}$) | 21.65 (A) |
| Nominal line frequency ($f_n$) | 50 (Hz) |
| Switching frequency ($f_{sw}$) | 20 (kHz) |
| Inverter modulation range ($m_a$) | $0 \leq m_a \leq 1$ |

**Table 6.2:** LCL filter parameter values for the designed inverter control system

| PARAMETER | VALUE |
|---|---|
| Inverter-side inductance ($L_i$) | 2.11 (mH) |
| Grid-side inductance ($L_g$) | 0.95 (mH) |
| (Approximated) total inductor parasitic resistance ($R_L$) | 0.1 (Ω) |
| Filter capacitance ($C_f$) | 8.95 ($\mu$F) |
| Passive damping resistance ($R_d$) | 2.85 (Ω) |
| Resonance frequency ($\omega_{res}$) | 13063 (rad/sec) |

### 6.6.3. Current controller design

Once the decoupling and feed-forward compensation have been implemented as shown in Figure (6.21), a simplified block diagram, such as that depicted in Figure (6.22), corresponding to Figure (6.19), can be considered for the controller design. In Figure (6.22), $G_{cid}(s)$ represents the transfer function of the controller to be designed, $G_{pid}(s)$ is the transfer function of the plant model for the current controller design, and $G_{del}(s)$ represents the computation-related delay of the control loop (explained in Section 6.5.1).

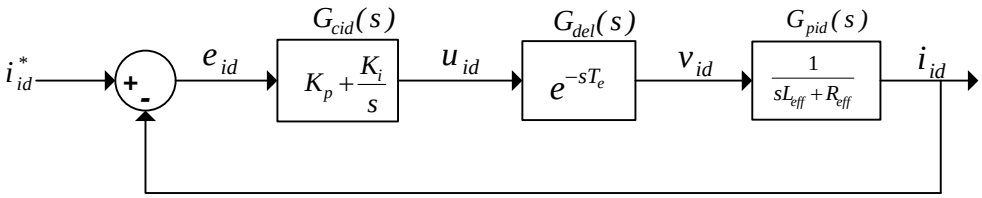


**Figure 6.22:** Current control scheme block diagram.

It is useful to look at the characteristics of the plant model alone, before designing the controller to improve the system response. Considering Equations (6.23a), (6.21b) and (6.22b) in conjunction with the parameters listed in Table (6.2), the transfer function of the plant model can be derived as:

$$L_{eff} = L_i + L_g = 2.11\times10^{-3} = 3.06\times10^{-3}\ H$$

$$R_{eff} = R_i + R_g = 0.1\Omega$$

$$G_{pid}(s) = \frac{1}{sL_{eff} + R_{eff}} = \frac{1}{3.06\times10^{-3}\cdot s + 0.1} = \frac{326.8}{s + 32.68} \qquad (6.26)$$

The plant model for the inverter current controller, as given by Equation (6.26), is essentially a first-order filter. Figure (6.23) depicts the (open-loop) root-locus plot of this plant model alone, and Figure (6.24) depicts the plant model's (closed-loop) response to a unit step input change. Figure (6.23) reveals that the transfer function pole of the plant model is located quite close to the origin (at 32.7 rad/sec in the left-half plane).

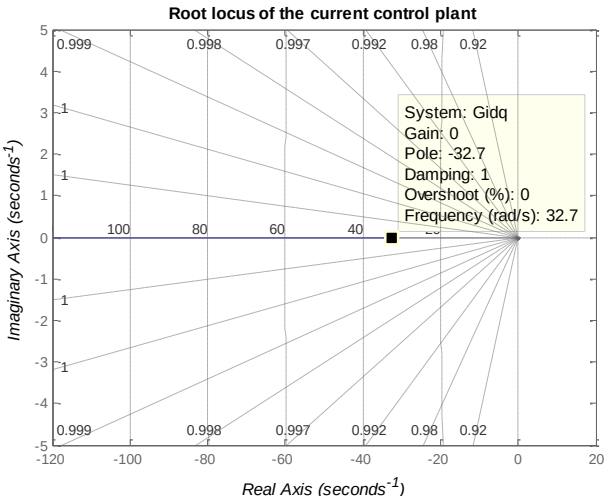


**Figure 6.23:** **Root locus plot of the unregulated current control plant**

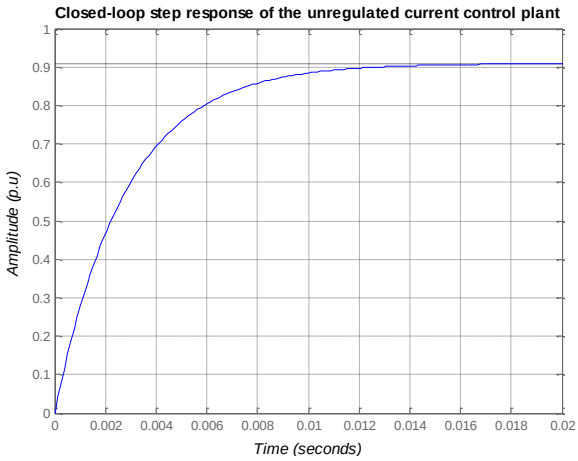


**Figure 6.24:** **Closed-loop step response of the unregulated current control plant**

The known effect of this characteristic of the plant model is that it induces some phase lag into the current control loop (Yazdani & Iravani, 2010), which affects both the transient and steady-state behavior of the control loop, as the step response in Figure (6.24) shows (exhibiting both slowed response and a steady-state error).

One approach employed to regulate the current control plant is to cancel the effect of the pole of the plant by means of a transfer function zero provided by the PI compensator (pole cancellation permissible in this case because the pole is always on the left-half plane of the complex plane, which means that it is a stable pole). This pole cancellation implies that the time-constant of the integral term of the PI compensator is set to match the plant model's time constant (Yadzani & Iravani, 2010).

The current control block diagram, as represented in Figure (6.22), can be considered as being comprised of two time constants: the one dominant and given by the control plant, $G_{pid}(s)$, the other minor and given by the system delay, $G_{del}(s)$ (the controller yet to be considered) (Bajracharya *et al*., 2008). Taking the system delay into account in the controller design

allows achieving an improved control system performance, as opposed to the direct implementation of the pole-cancellation technique (Teodorescu *et al*., 2010). A common controller design approach for a system such as the current control loop represented in Figure (6.22) is referred to as Modulus Optimum (Evyu, 2007), the approach used in this current controller design task, as discussed next.

**Modulus optimum (MO) control design method**

The MO method (also known as the absolute-value optimum criterion) is a frequency response-based technique whose aim is to bring the modulus (*i.e.*, the absolute value) of the control loop's frequency characteristic as close to the value of 1 as possible, and doing so over as wide a frequency range as possible (Evyu, 2007). This method is suitable for the current control loop (Figure 6.22), which exhibits a large time constant in the form of the plant model transfer function, and a small time constant due to the system delay transfer function. For such a system, the MO design criterion is achieved by the cancellation of the large time constant by means of a suitably selected regulator, which simultaneously ensures a higher-than-unity closed-loop gain over as wide a frequency range as possible (Bajracharya *et al*., 2008). The method is characterized by a simple structure that nonetheless provides fast response, and is thus widely used for current control, for which fast response is a desirable characteristic (Bajracharya *et al*., 2008).

For a system that can be represented by one large time constant and one small time constant, the MO design criterion can be realized by means of a PI regulator, and leads to a critically damped closed-loop response, with an overshoot of only about 5% (Teodorescu *et al.*, 2011).

Considering the current control block diagram in Figure (6.22), the transfer functions of the compensator and the system delay are given by:

$$G_{cid}(s) = \frac{K_p s + K_i}{s} \tag{6.27}$$

$$G_{del}(s) = \frac{1}{1 + sT_e} \tag{6.28}$$

where the system delay transfer function in Figure (6.22) is represented by Pade's first-order approximation, and $T_e$ represents the effective control loop delay. From Equations (6.23a), (6.27) and (6.28), the system open-loop transfer function, $G_{col}(s)$, is given by:

$$G_{col}(s) = G_{cid}(s) \cdot G_{del}(s) \cdot G_{pid}(s) = \frac{K_p s + K_i}{s} \cdot \frac{1}{1 + sT_e} \cdot \frac{1/L_{eff}}{s + R_{eff}/L_{eff}}$$
$$= \frac{K_p}{L_{eff}} \cdot \frac{s + K_i/K_p}{s} \cdot \frac{1}{1 + sT_e} \cdot \frac{1}{s + R_{eff}/L_{eff}} \quad (6.29a)$$

In order to cancel the large time constant (due to the plant pole: $s = -R_{eff}/L_{eff}$), the PI regulator gains are selected such that:

$$K_i/K_p = R_{eff}/L_{eff} \quad (6.29b)$$

The following is obtained when Equation (6.29b) is substituted into Equation (6.29a):

$$\frac{K_p}{L_{eff}} \cdot \frac{s + R_{eff}/L_{eff}}{s} \cdot \frac{1}{1 + sT_e} \cdot \frac{1}{s + R_{eff}/L_{eff}} = \frac{K_p}{L_{eff}} \cdot \frac{1}{s} \cdot \frac{1}{1 + sT_e} = \frac{K_p/L_{eff}}{s + s^2 T_e} \quad (6.29c)$$

If, for ease of analysis, the following temporary change of variable is made:

$$k = K_p/L_{eff} \quad (6.29d)$$

The transfer function of the closed-loop control system (considering Equations 6.29b to 6.29d) becomes:

$$G_{ccl}(s) = \frac{G_{col}(s)}{1 + G_{col}(s)} = \frac{\frac{k}{s + s^2 T_e}}{1 + \frac{k}{s + s^2 T_e}} = \frac{k/T_e}{s^2 + 1/T_e \cdot s + k/T_e} \quad (6.30)$$

The closed-loop transfer function given by Equation (6.30) is a second-order system, which can be represented in the form:

$$G_{ccl}(s) = \frac{\omega_n^2}{s^2 + 2\varsigma\omega_n \cdot s + \omega_n^2} \quad (6.31)$$

where $\omega_n$ and $\varsigma$ represent the closed-loop control system's natural frequency of oscillation and the damping factor respectively. Relating Equation (6.31) to Equation (6.30) leads to the following expressions:

$$\omega_n^2 = \frac{k}{T_e} \quad (6.32a)$$

$$2\varsigma\omega_n = \frac{1}{T_e} \qquad \therefore \ \omega_n = \frac{1}{2\varsigma T_e} \quad (6.32b)$$

The natural frequency of oscillation may be eliminated from the above expressions (to decrease the number of unknown parameters) by combining Equations (6.32a) and (6.32b), leading to:

$$\frac{1}{2\varsigma T_e} = \sqrt{\frac{k}{T_e}} \tag{6.32c}$$

The value of the parameter $k$ is not known in Equation (6.32c). Another unknown parameter is the damping factor, $\varsigma$, but its value can be determined on the basis of the specifications for the desired behavior of the closed-loop system. In order to achieve a critically damped closed-loop control response, the damping factor is set to $1/\sqrt{2}$. Substituting this value of the damping factor into Equation (6.32c) and squaring both sides of the equation leads to:

$$\left(\frac{1}{2\cdot \frac{1}{\sqrt{2}}\cdot T_e}\right)^2 = \left(\sqrt{\frac{k}{T_e}}\right)^2 \quad \therefore \quad \frac{1}{2T_e^2} = \frac{k}{T_e} \quad \therefore \quad k = \frac{T_e}{2T_e^2} = \frac{1}{2T_e} \tag{6.32d}$$

Substituting Equation (6.29d) into Equation (6.32d) then allows expressing the PI regulator proportional gain in terms of the inductance value of the plant model, $L_{eff}$, and the effective control loop delay, $T_e$, given by:

$$k = \frac{K_p}{L_{eff}} = \frac{1}{2T_e} \quad \therefore \quad K_p = \frac{L_{eff}}{2T_e} \tag{6.32e}$$

From equations (6.29b) and (6.32e), the gain parameters of the PI compensator may be calculated, assuming an effective system delay (due to the computation, sampling and filtering) of one millisecond (*i.e.* $T_e = 1\,msec$) (Reznik, 2013; Evyu, 2007) as:

$$K_p = \frac{L_{eff}}{2T_e} = \frac{3.06\times10^{-3}}{2\times1\times10^{-3}} = 1.53$$

From Equation (6.29b):

$$K_i = \frac{K_p \cdot R_{eff}}{L_{eff}} = \frac{1.53\times0.1}{3.06\times10^{-3}} = 50$$

Figures (6.25) and (6.26) show the closed-loop magnitude-phase and step responses, respectively, of the designed current controller, using the PI compensator gain parameters computed above. The responses have been generated in Matlab on the basis of the current control block diagram represented by Figure (6.22), with the transfer functions in Figure (6.22) given by Equations (6.26)-(6.28), in conjunction with the controller gain and system time delay parameters derived above.

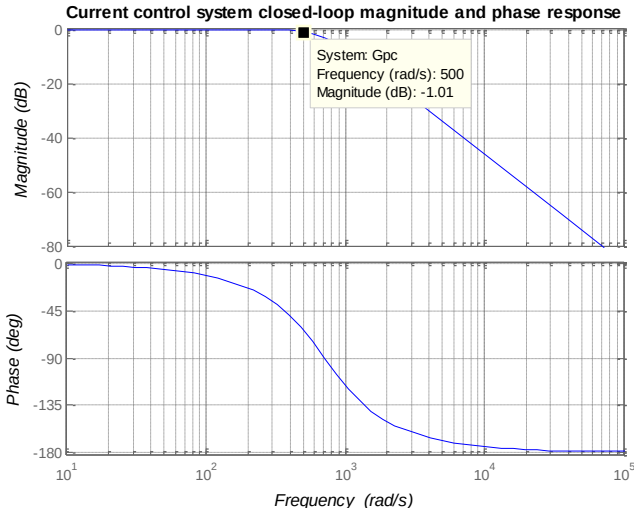


**Figure 6.25:** **Closed-loop magnitude-phase response of the current control system**

From the magnitude-phase response, the closed-loop bandwidth of the current controller is about 500 rad/sec, corresponding to a time constant of 2 milliseconds. The step response exhibits a critically damped characteristic, with zero steady-state error and an overshoot of only about 4%, as can be deduced from Figure (6.26). When compared to Figure (6.24), improvement in both the dynamic and steady-state responses can be observed in the regulated system.

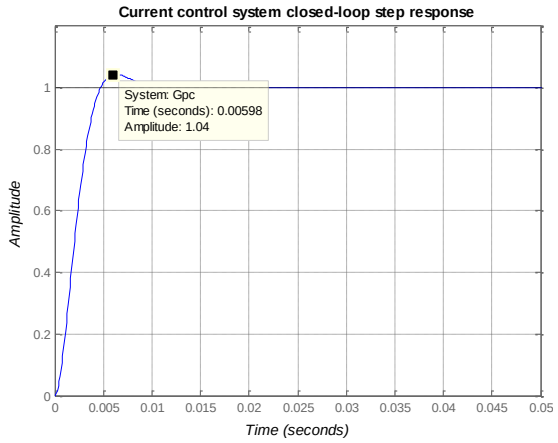


**Figure 6.26:** **Closed-loop step response of the current control system**

### 6.6.4. DC-link voltage regulator

As has been discussed in Section (6.6.1), the inverter current controller has a dual-loop control structure, according to Figure (6.20), in which the outer control loop regulates the DC-link voltage, while the inner current-control loop is regulated according to the power to be transferred to the grid.

The DC-link voltage regulation is here performed in the manner suggested by Yazdani and Iravani (2010), according to the control loop block diagram depicted in Figure (6.27), and the plant model presented in Section (5.5). In the control loop block diagram (Figure 6.27), $G_{cv}(s)$, $G_{pv}(s)$ and $G_i(s)$ represent, respectively, the DC-link voltage controller transfer

function, a transfer function of the linearized DC-link voltage dynamics (i.e. the plant model for the DC-link voltage regulation), and the inner current control closed-loop transfer function (equivalently representing the inverter active power output control).

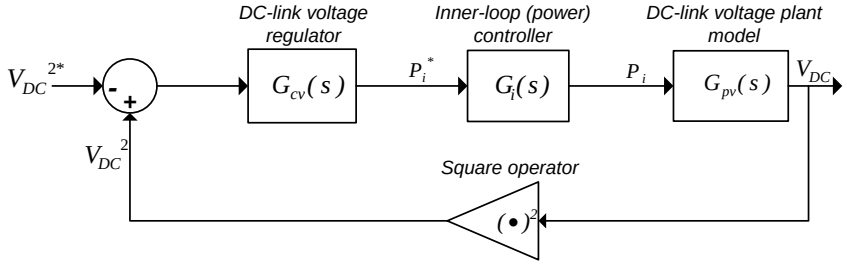


**Figure 6.27: DC-link voltage regulator block diagram (Adapted from Yazdani & Iravani, 2010)**

Variations in the active power transferred from the inverter DC side to the inverter AC side may cause the DC-link voltage to vary, especially where the inverter is supplied by a variable power source (Teodorescu *et al.*, 2011), and the main task of the DC-link voltage regulator is to compensate for these voltage variations, in order to keep the DC voltage input to the inverter within the range required for correct inverter operation. Accordingly then, Figure (6.27) shows the input to the outer-loop regulator to be the DC-link voltage error (actually, the error of the squares of the voltages, on account of the way the outer-loop plant model has been formulated). The regulated output of the outer loop sets the reference for the inner loop, which is responsible for regulating the inverter output current (or power). The DC-link voltage dynamics model, $G_{pv}(s)$, as developed in Section (5.5) is given by Equations (5.33) and (5.34), restated here as:

$$G_{pv}(s) = \frac{\tilde{v}_{DC}^2(s)}{\tilde{p}_g(s)} = -\frac{2}{C} \cdot \frac{\tau_{dc} + 1}{s} \tag{6.33}$$

$$\tau_{dc} = \frac{2L_{eff} P_{go}}{3V_{sm}^2} \tag{6.34}$$

where $\tilde{v}_{DC}^2(s)$ is the square of the small DC-link voltage perturbation, $\tilde{p}_g(s)$ is the small perturbation of the inverter active power injected into the grid, $C$ is the DC-link capacitance, $\tau_{dc}$ is the operating point-dependent time constant of the system dynamics, $L_{eff}$ is the effective inductance of the filter interface (to the grid), $V_{sm}$ is the inverter peak phase-neutral voltage, and $P_{go}$ is the inverter injected active power at the chosen equilibrium point for the linearization process (Yazdani & Iravani, 2010).

The negative set-point in the DC-link voltage regulation block diagram (Figure 6.27) can be explained by the negative sign on the plant model transfer function (Equation 6.33), which

implies the negative regulation of the DC-link voltage. As explained in the RSCAD user's manual (RTDS Technologies, 2006), the negative regulation of the DC-link voltage is necessitated by the fact that power transfer from the DC-link to the inverter AC-side requires the flow of power into the DC bus (from the power source supplying the inverter).

According to Equation (6.33), the plant model for the DC-link voltage regulation contains a zero ( $s = -1/\tau_{dc}$ ) whose location is a function of the inverter active power injected into the grid ( $P_g$ ), and may have a significant influence on the stable regulation of the DC-link voltage, depending on the magnitude and direction of the active power transfer through the inverter. If the inverter active power is assumed to be constrained to non-negative values (which is the case when only DC-to-AC power transfer is assumed), it is shown by Yazdani and Iravani (2010) that stable control of the DC-link voltage may be assured by designing the regulator for a null-inverter-power-transfer operating point (*i.e.* $P_g = 0\,W$ ). At this condition, the time constant (Equation 6.34) evaluates to zero; Equation (6.33) is then given by:

$$G_{pv}(s) = -\frac{2}{C} \cdot \frac{0 \cdot s + 1}{s} = -\frac{2}{C} \cdot \frac{1}{s} \tag{6.35}$$

Choosing the DC-link capacitance (arbitrarily) to be $1000\ \mu$F (see for instance Xue *et al*., 2004), the plant model (omitting the negative sign, which is encompassed in the control scheme of Figure 6.27) is given by:

$$G_{pv}(s) = \frac{2}{1000 \times 10^{-6}} \cdot \frac{1}{s} = \frac{2000}{s} \tag{6.36}$$

To design the DC-link voltage regulator, it is necessary to derive an effective representation for the inner control loop, which represents the inner-loop's influence on the outer-loop controller operation. The assumption usually taken in the design of the dual-loop current control scheme is that the inner loop is designed for a closed-loop bandwidth that is much higher than that of the outer loop, and thus leads to a largely decoupled operation of the two loops (Teodorescu *et al*., 2011; Yazdani & Iravani, 2010; Liserre *et al*., 2010; Evyu, 2006). Under this assumption, the inner loop may be approximated by an equivalent first-order transfer function for the purpose of outer loop controller design, representing the delaying effect of the inner loop on the outer loop controller (Evyu, 2006). Yazdani and Iravani (2010) suggest that the time constant of this *first-order approximation* of the inner loop may be taken to be the inverse of the inner loop's closed-loop bandwidth, which is why it is common to design the inner loop controller prior to designing the outer loop controller (Liserre *et al*., 2010; Yazdani & Iravani, 2010).

The closed-loop bandwidth of the current controller designed in Section 6.6.3 is about 500 rad/sec, as depicted in Figure (6.25); thus the time constant, $\tau_i$ , of the inner-loop's first-order

approximate representation is equal to (as a reciprocal of current controller closed-loop bandwidth) 2 milliseconds. The inner current closed-loop transfer function, $G_i(s)$ in Figure (6.27), is thus given by:

$$G_i(s) = \frac{1}{s \cdot \tau_i + 1} = \frac{1}{2 \times 10^{-3} s + 1} = \frac{500}{s + 500} \tag{6.37}$$

Given Equations (6.36) and (6.37), the voltage regulator open-loop transfer function, $G_{vol}(s)$, is expressed as:

$$\begin{aligned} G_{vol}(s) &= G_{cv}(s) \cdot G_i(s) \cdot G_{pv}(s) = G_{cv}(s) \cdot \frac{500}{s + 500} \cdot \frac{2000}{s} \\ &= G_{cv}(s) \cdot \frac{10 \times 10^5}{s^2 + 500s} \end{aligned} \tag{6.38}$$

A procedure similar to that used by Yazdani and Iravani (2010: 238) is adopted here for the design of the DC-link voltage regulator. This is an iterative procedure, based on the derivation of the open-loop transfer function of the system, then using it to investigate the system's magnitude and phase behavior. The design process is so carried out that the closed-loop magnitude and phase response of the final design satisfies the design requirements. Iterative improvements of the phase and magnitude response of the system are realized through progressive adjustments being made to the compensator under design (*i.e.* loop-shaping). The procedure can be outlined as follows:

1. Set the voltage-loop crossover frequency to a value that is a fraction of the current-control closed-loop bandwidth (usually about one-fifth to one-tenth)
2. As an initial step, set the voltage regulator to be a pure integral term (this integral term is necessary to eliminate the control system steady-state error because of the presence of a pole at the origin in the plant model); additional terms are subsequently added to this initial integral term as necessary to meet design requirements
3. Analyze the open-loop magnitude and phase response of the system having the integral term from step 2, noting the characteristics of the response at the desired crossover frequency (determined in step 1)
4. Determine the required phase lead to achieve the desired crossover frequency, and design an appropriate lead compensator, $G_{lead}(s)$
5. A combination of steps 2 and 4 provides the required voltage-loop regulator

Following the procedure outlined above, the voltage-loop crossover frequency is set to 100 rad/sec (*i.e.* one-fifth of the current-loop bandwidth, obtained from Figure 6.25). Then the voltage regulator, $G_{cv}(s)$, can initially be set as follows (the lead term included because ultimately it has to be designed):

$$G_{cv}(s) = \frac{1}{s} \cdot G_{lead}(s) \tag{6.39}$$

Substituting Equation (6.39) into Equation (6.38), the following expression is obtained for the system open-loop transfer function, $G_{vol}(s)$:

$$G_{vol}(s) = \left[\frac{1}{s} \cdot \frac{10 \times 10^5}{s^2 + 500s}\right] \cdot G_{lead}(s) = \left[\frac{10 \times 10^5}{s^3 + 500s^2}\right] \cdot G_{lead}(s) \tag{6.40}$$

The magnitude-phase response of the bracketed term of Equation (6.40) is shown in Figure (6.28). It can be deduced from the figure that the phase at the crossover frequency (44.6 rad/sec) is less that -180° (*i.e.* -185°). At 100 rad/sec (the desired crossover frequency), the open-loop response has a phase of -191°.

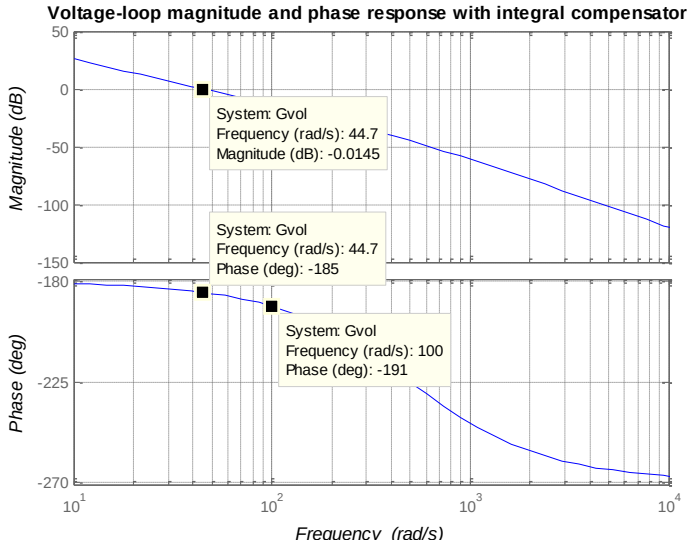


**Figure 6.28: Voltage-loop magnitude and phase response for an integral compensator**

According to linear control theory, the stability of a control system requires that the system's open-loop phase exceed -180° by some phase magnitude at the gain crossover frequency (commonly referred to as the phase margin) (Nise, 2004). A phase margin of about 45° or higher is normally taken to provide sufficient stability margin (Mohan, 2003).

Following the design strategy implemented by Yazdani and Iravani (2010), the phase margin at the gain crossover frequency is desired to be 53°, which, according to the authors, provides sufficient margin for the stability of the closed-loop control system, even with the anticipated phase-lag induced by the inner-current loop at higher frequencies (Yazdani & Iravani, 2010). In line with step 4 of the design procedure outlined above, therefore, a lead compensator, $G_{lead}(s)$, is to be designed that provides a phase lead of 64° at the desired crossover frequency (*i.e.* at 100 rad/sec), in order to obtain the specified phase margin of 53°.

The lead compensator, $G_{lead}(s)$, is generally comprised of a zero ($s=-z$) and a pole ($s=-p$), with the zero being located at a lower frequency than the pole, and can be expressed as (Ogata, 2001):

$$G_{lead}(s)=\frac{s+z}{s+p} \tag{6.41}$$

$$z=\frac{p}{a}, \qquad a>1 \tag{6.42}$$

where $z$ and $p$ are the frequencies of the locations of the zero and the pole respectively, and $a$ is a constant ratio of the pole location to the zero location, which is greater than 1 for the lead compensator (Ogata, 2001).

The lead compensator (Equation 6.41) exhibits a maximum phase, $\theta_m$, at the geometric mean frequency, $\omega_m$, of the zero ($s=-z$) and the pole($s=-p$). The expressions for the maximum phase and the geometric mean frequency are given by Equations (6.43) and (6.44) respectively (Erickson, 2001).

$$\theta_m=sin^{-1}\left(\frac{a-1}{a+1}\right) \tag{6.43}$$

$$\omega_m=\frac{p}{\sqrt{a}} \tag{6.44}$$

From Equation (6.43), and using the desired maximum phase of $64°$, the constant ratio $a$ is calculated to be:

$$a=\frac{1+sin(\theta_m)}{1-sin(\theta_m)}=\frac{1+sin(64°)}{1-sin(64°)}=18.762$$

And from Equation (6.44), the pole location is calculated to be:

$$p=\omega_m\cdot\sqrt{a}=100\sqrt{18.762}=433.15\,rad/sec$$

The zero location, from Equation (6.42) is computed as:

$$z=\frac{p}{a}=\frac{433.15}{18.762}=23.1\,rad/sec$$

By substituting Equation (6.41) into Equation (6.40), with the lead compensator values computed above, the magnitude and phase responses are obtained as depicted by the (blue) dashed sketch of Figure (6.29) below. The sketch shows that due to insufficient loop gain, it has a crossover frequency of only 10.8 rad/sec, whereas the desired crossover frequency is 100 rad/sec. This can be corrected for by adding a gain value of 26.9 dB to the system open-loop

gain. The required gain magnitude is obtained by applying the formula relating the gain in decibels to the absolute gain as follows:

$$Gain(dB) = 20\log_{10}\left(\left|G_{vol}(j\omega)\right|\right)$$

$$\therefore \left|G_{vol}(j\omega)\right| = 10^{gain(dB)/20} = 10^{26.9/20} = 22.13$$

where $\left|G_{vol}(j\omega)\right|$ is the absolute gain magnitude of the system open-loop gain. Following the augmentation of the system open-loop gain by the value computed above together with the designed lead compensator, the adjusted gain response obtained is as depicted by the solid (red) sketch in Figure (6.29).

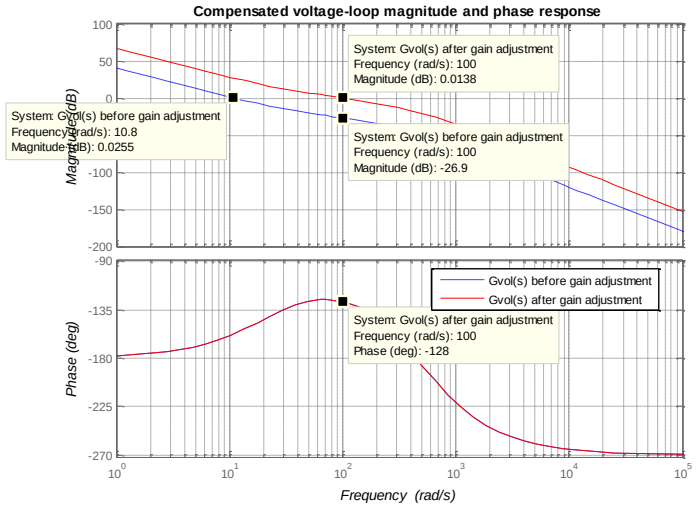


**Figure 6.29: Compensated voltage-loop magnitude and phase response**

The adjusted system exhibits the desired crossover frequency (100 rad/sec) as well as phase margin (52°). Thus the final DC-link voltage regulator is given by:

$$G_{cv}(s) = \left|G_{vol}(j\omega)\right| \cdot \frac{1}{s} \cdot G_{lead}(s) = 22.13 \cdot \frac{s + 23.1}{s^2 + 433.15s} \qquad (6.45)$$

The closed-loop magnitude-phase as well as closed-loop step responses of the DC-link voltage loop with the regulator given by Equation (6.45) are depicted in Figures (6.30) and (6.31) respectively. Despite the significant phase lag at high frequencies, mainly caused by the inner current loop (as anticipated), Figure (6.30) shows that the compensator provides sufficient phase boost within the frequency band of interest for the DC-link voltage regulation. As expected of a system having an integral term in the plant model (Teodorescu *et al.*, 2011), the step response depicted in Figure (6.31) exhibits a substantial overshoot (about 22%), and the (deliberately designed) relatively slow response of the voltage-loop control is also apparent from the step response, especially when compared with the corresponding response of the closed-loop current control system (Figure 6.26).

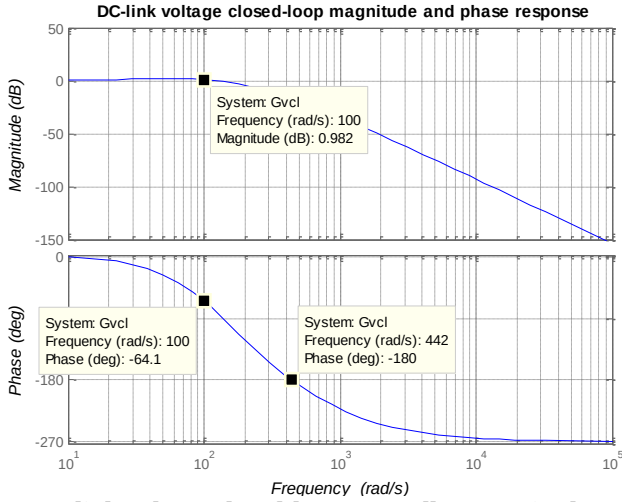


**Figure 6.30:** DC-link voltage closed-loop controller magnitude and response

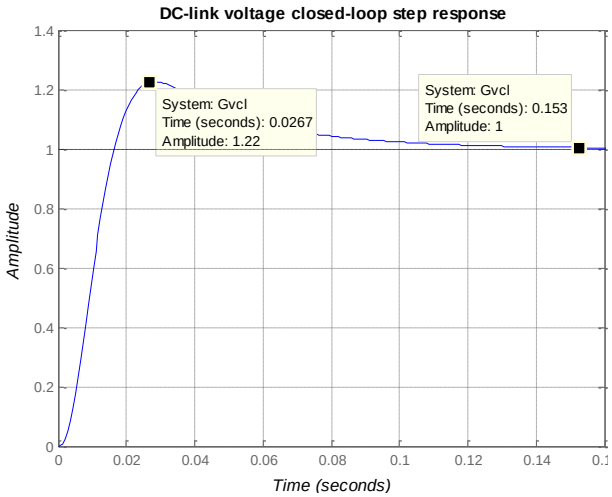


**Figure 6.31:** DC-liink voltage closed-loop controller step response

## 6.7. Analysis of controller performance

The control system designed in Section (6.6) has been implemented in *SimPowerSystems™*. This is a block-set that provides a platform for the physical modeling of electrical and control systems in the *Simulink* environment, and is a product of *Hydro-Québec* and *The MathWorks, Inc*. *SimPowerSystems™* is a very useful design tool for the rapid building and simulation of models for power systems, both large and small. Moreover, it provides a wide range of tools for electrical analysis, as well as interaction with the *Matlab engine*, so that algorithms developed in *Matlab* may be easily incorporated into the power system model by means of models and interfaces available in the comprehensive model library (MathWorks, 2010).

The system represented in Figure (6.32) below is considered for simulating the inverter control system designed for grid-connected operation. The interface to the grid is essentially comprised of an inverter and an LCL filter (although not depicted in Figure 6.32), whose specifications are as listed in Tables (6.1) and (6.2) respectively. The utility side is considered to be an ideal AC infinite bus, the data of which is listed in Table (6.3), adapted from Ye *et al*.

(2004). Figure (6.33) depicts the main simulation block diagram of the grid-connected inverter system as has been implemented in Simulink.

As can be seen from the simulation block diagram, an ideal voltage source has been taken as the input to the grid-connected inverter, which is a common approach for the analysis of inverter-interfaced Distributed Energy Systems when the focus is on the inverter current controller performance analysis (Teodorescu *et al.*, 2011; Esvyu, 2007). The DC-link voltage regulator that has been designed in Section 6.6.4 is also implemented and the control reference set to 1.0 per-unit (DC voltage), although its real influence on the system response is more noticeable when the inverter is supplied by a variable power source (Yazdani & Iravani, 2010).

It may be noted here that when the reference of the inner current control loop is exclusively set by the outer DC-link voltage control loop, then the current controller reference cannot really be arbitrarily set. So where the current controller reference is to be set arbitrarily, the outer-loop controller output is augmented to the current controller reference, rather than exclusively setting the reference (Teodorescu *et al.*, 2011).

The following scenarios are considered for testing the grid-mode operation of the grid-inverter using the designed controllers:

- Response of the system to step changes in the current controller references
- Response of the system to step (local) load adjustments
- Unity- and non-unity-power-factor operation of the inverter system (*i.e.* non-unity power factor when reactive power supply to the grid is considered)

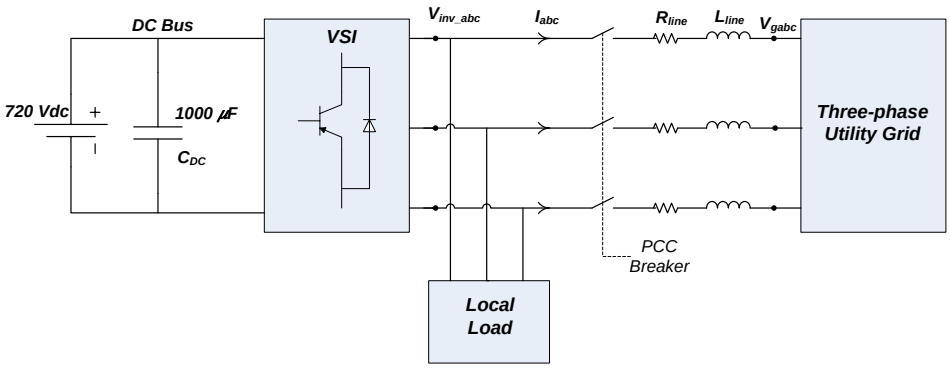


**Figure 6.32:** **Grid-connected inverter system.**

**Table 6.3:** Grid-side data for the grid-connected inverter system

| PARAMETER | VALUE | COMMENT |
|---|---|---|
| $f_o$ | 50 Hz | Nominal grid frequency |
| $V_{LLrms}$ | 400 V | RMS Line-line voltage |
| $L_s$ | $1.02\times10^{-3}$ | Grid inductance, 3% of inverter impedance |
| $R_s$ | 0.03 Ω | Grid source resistance, $X/R=10$ |
| $L_{line}$ | $6.791\times10^{-4}\ H$ | Combined line and interface transformer inductance $X/R=10$ |
| $R_{line}$ | 0.03 Ω | Combined line and interface transformer resistance $X/R=7$ |

### 6.7.1. Controller performance for nominal system conditions

At the beginning of simulation, the point-of-common-coupling (PCC) breaker is open, up until 0.1 second. This provides a time window in which the PLL circuit in the simulation can track the grid voltage phase angle that is necessary to properly synchronize the inverter terminal voltage to the grid voltage, and consequently ensure that the commencement of the inverter grid operation is not accompanied by undesirable transients (Osorio, 2011).

During the initial 0.1 second period of simulation, the q- and d-axis current reference commands are set to 0.0 per-unit and 1.0 per-unit respectively, the local load being purely resistive, and set to the inverter rated output. In the various simulation cases considered, the reference value for the DC-link voltage regulator remains set at 1.0 per-unit. To observe the response of the system to the current controller set-point changes, the following step changes in the d-axis current reference are made:

- From 1.0 per-unit to 0.4 per-unit at 0.15 seconds
- From 0.4 per-unit to 0.8 per-unit at 0.25 seconds

Figure (6.34) shows subplots of the system response following the reference command adjustments outlined above. Figure (6.34a) shows the current reference commands and their corresponding output signals. Both the d- and q-axis components exhibit well-damped responses with nearly zero steady-state error ( $e_{id}$ , $e_{iq}$ ), as Figure (6.34b) also illustrates.

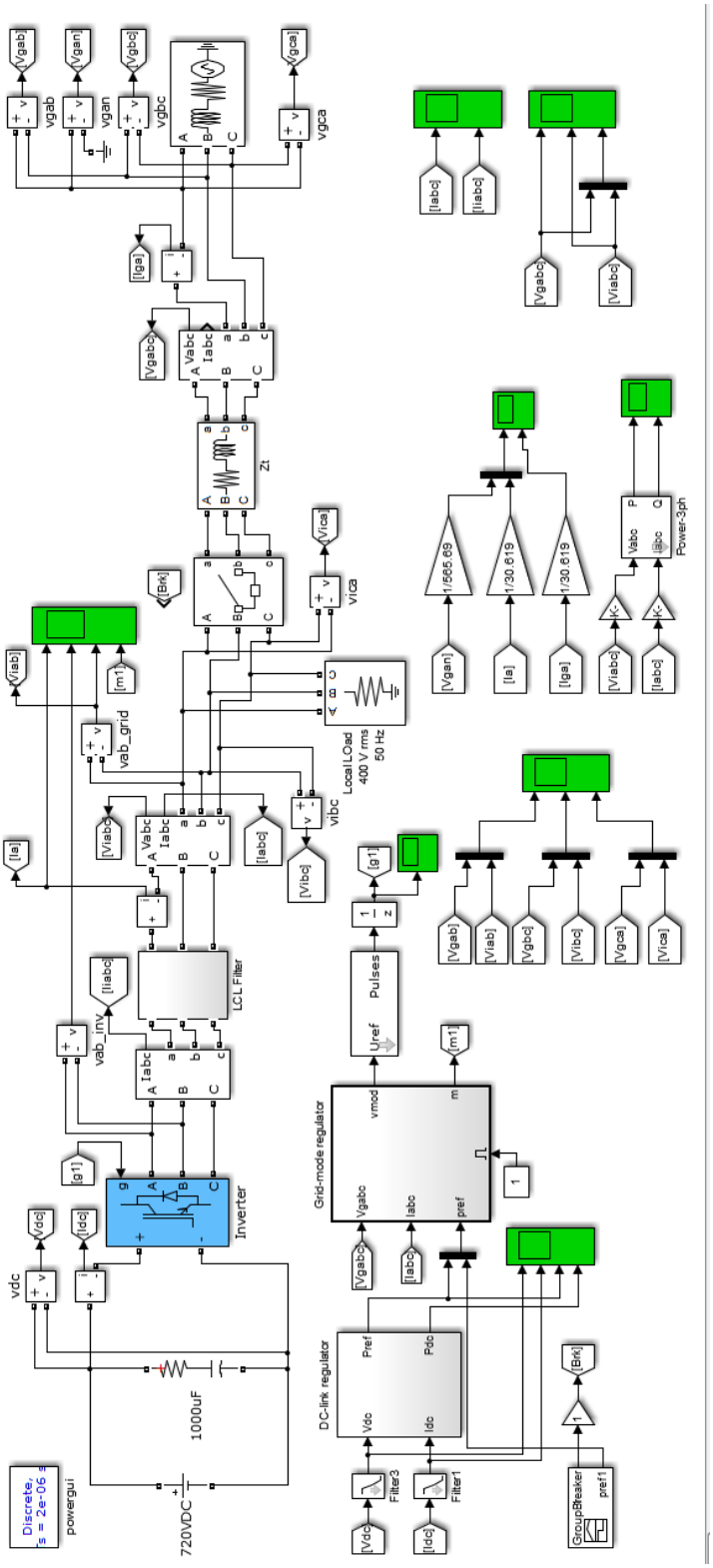


**Figure 6.33:** **Simulink block diagram of the designed grid-connected inverter system**

The voltages at the inverter output are also well regulated. In line with the voltage-oriented control (VOC) strategy employed in the current-mode controller, the d-axis inverter voltage is aligned with the grid voltage, while the q-axis inverter voltage is regulated at zero by the PLL circuit. The plot of the d- and q-axis components of the inverter output voltage in Figure (6.34c) shows that the inverter voltage is properly regulated. Figure (6.34d) depicts the q- and

d-axis components of the modulating signals ($V_{md}$ , $V_{mq}$) that are sent to the Pulse-Width Modulator (PWM). $V_{md}$ and $V_{mq}$ are essentially the actuating (and control output) signals, which are used to synthesize the gate-pulse signals that then drive the inverter switches, to achieve the required inverter output current control.

The active and reactive powers delivered by the inverter are shown in Figure (6.35a), where their relationship with the d- and q-axis current components becomes apparent when Figures (6.34a) and (6.35a) are compared. Figure (6.35b) compares the inverter output voltage ($V_{iab}$) with the grid voltage ($V_{gab}$), showing the effectiveness of the PLL circuit in establishing the phase angle for properly synchronizing the inverter output terminals to the grid. Figure (6.35c) shows the phase-A current injected into the grid ($i_{ia}$)together with the phase-A-to-neutral grid voltage ($V_{gan}$), demonstrating that the inverter is operating at unity power factor, which is normally the requirement for grid-connected inverter systems (IEEE 1547-2003).

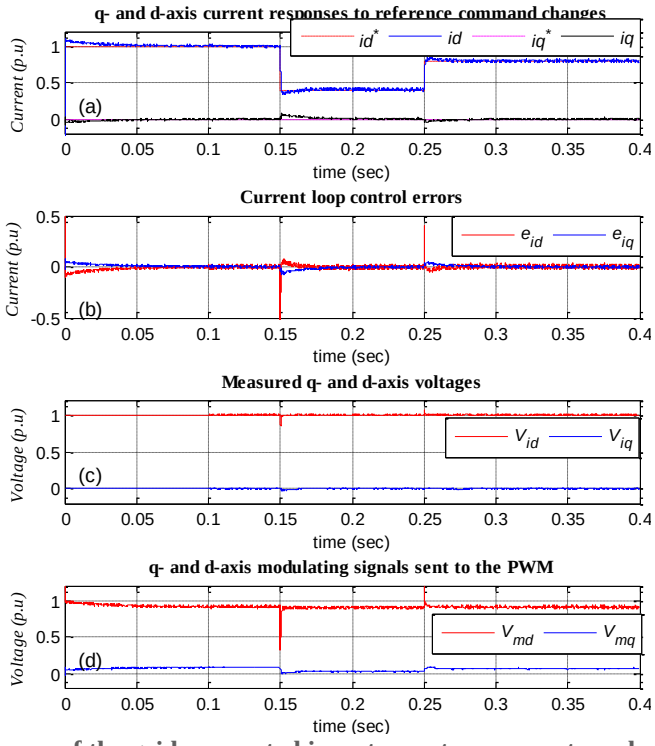


**Figure 6.34:** **Response of the grid-connected inverter system currents and voltages following active current reference adjustments.**

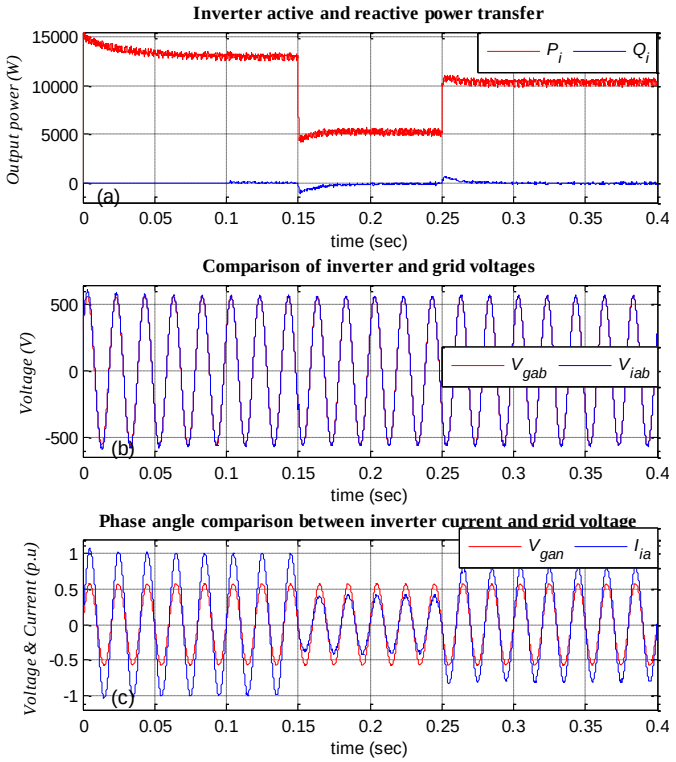


**Figure 6.35: Power, voltage and current outputs of the grid-connected inverter system following current controller reference adjustments.**

The inverter performs the DC-AC power conversion by means of pulse-width modulation, at frequencies much higher than the fundamental frequency of the modulated signals. The voltage and current at the terminals of the inverter (*i.e.* the pre-filter parameters) are thus markedly different from the corresponding grid parameters, containing harmonic components across a spectrum determined by the switching frequency, and these harmonics should be removed from the inverter output signals before the current can be injected into the grid (Mohan *et al*., 2003). It is thus necessary to analyze the harmonic content of the inverter signals, to determine if that satisfies the power quality requirements. This analysis is done on the inverter system as simulated above, with the current controller references staying the same (as depicted in Figure 6.34a).

Figure (6.36) shows the phase-phase (A-B) switched inverter voltage that is at the output terminals of the inverter ($V_{iab}$; blue trace in the top subplot of Figure 6.36), plotted together with the corresponding grid-side voltage ($V_{gab}$; red trace in the top subplot), the inverter output current (second subplot), the current through the filter capacitor ($i_{cf}$ ; third subplot), and the phase-A filter output current (*i.e.* the grid injected current, $i_{ga}$; bottom subplot). The significance of the filter is apparent from the plots of Figure (6.36), when the quantities at the filter input are compared with those at the output. Ripple attenuation from the inverter current is paramount to satisfying power quality requirements of interconnection standards. That is why the LCL filter is the one mostly considered for grid-connected inverters (Ahmed *et al.*,

2007). In Figure (6.36) it can be seen that most of the harmonic components present in the inverter output current are shunted to ground by the filter capacitor, thus preventing excessive harmonic injection into the grid, and it can be seen that the injected current (subplot 4) has significantly lower harmonic content than the inverter output current (subplot 2). The reduction in the inverter current seen in subplots two and four is due to changes in the active current controller reference that are induced at 0.15 seconds and 0.25 seconds during the simulation.

To examine the harmonic spectrum of the (filtered) inverter output current more closely, Fast-Fourier Transform (FFT) analysis is performed using the Powergui tool available in SimPowerSystems™. It is necessary to ascertain both the Total Harmonic Distortion (THD) and the individual harmonic components across the harmonic spectrum, both for which there are specified magnitude limits (IEEE 1547-2003). Interconnection requirements are presented in Appendix B, including power quality requirements. Harmonic limits for the inverter current injected into the grid are listed in Table B.3 (in Appendix B).

The harmonic spectrum obtained by performing an FFT analysis on the inverter current is displayed in Figure (6.37). The total harmonic distortion is found to be 1.05%, which is well below the THD limit of 5% (IEEE 1547-2003). Figure (6.37) displays the harmonic spectrum up to the $50^{th}$ harmonic component of the current. Limits for individual harmonic components are to be found in Table B.3 as well, and the strictest limit is in regard to the amplitude of the $35^{th}$ harmonic component and higher, which must not exceed 0.3% of the fundamental current component. Figure (6.37) shows that this requirement is satisfied as well.

What is noteworthy about the harmonic spectrum in Figure (6.37) are the relatively higher low-frequency harmonic component amplitudes for the switching frequency used (20 kHz). It is noted by Evyu (2007) that the timer resolution for the gate pulse signal generation does affect both the amplitude and spread of the harmonics over the frequency spectrum of interest. This is probably a phenomenon that varies with simulation platforms.

By increasing the frequency window for the FFT analysis, an overall picture of the harmonic spread can be observed, and this is depicted in Figure (6.38) for a frequency window up to 50 kHz. It is observed that significant high-frequency harmonic components occur around multiples of the switching frequency, although their amplitudes do not violate harmonic limit specifications.

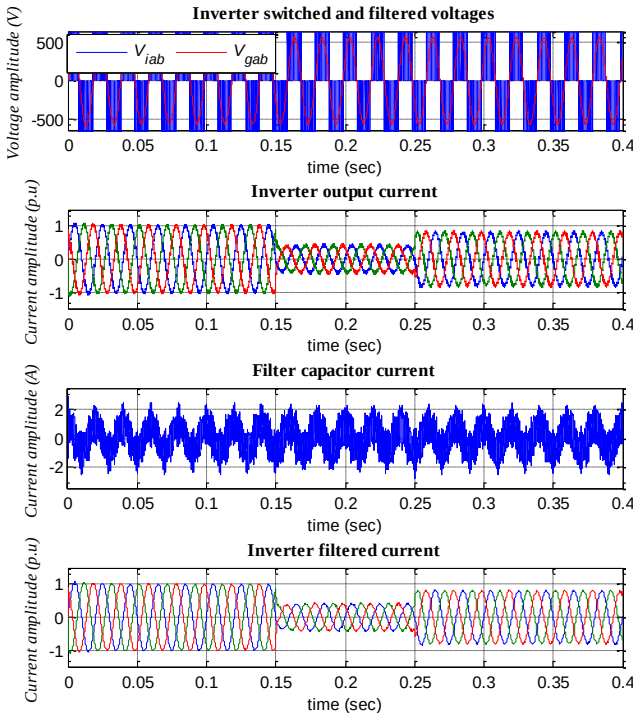


**Figure 6.36:** Comparison of the inverter output voltage and current before and after filtering

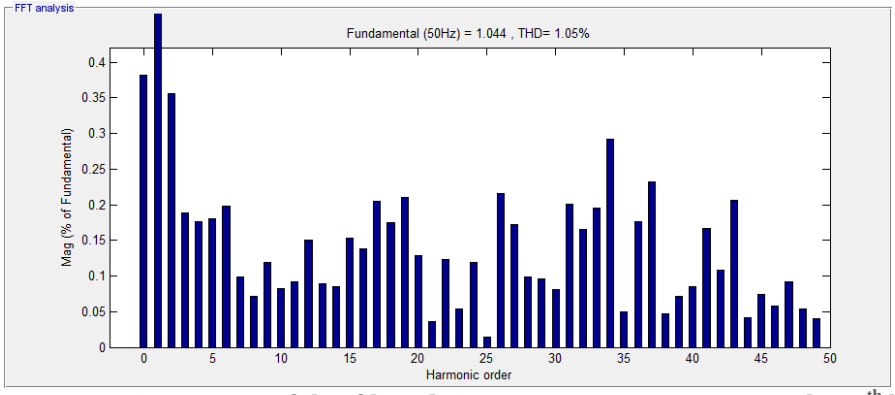


**Figure 6.37:** Harmonic spectrum of the (filtered) inverter output current, up to the 50$^{th}$ harmonic component

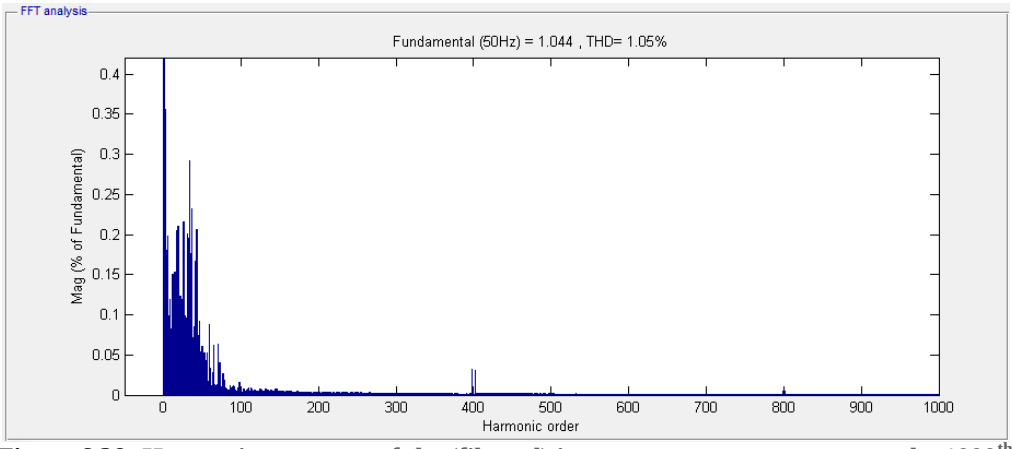


**Figure 6.38:** Harmonic spectrum of the (filtered) inverter output current, up to the 1000$^{th}$ harmonic component

### 6.7.2. Current controller performance for other system conditions

Controller performance was also analyzed for other system operating conditions, such as load step changes and non-unity-power-factor operation of the inverter, in order to examine the response of the system voltages and currents.

Initially, the grid circuit breaker is in an off position, such that the inverter operates independently for a short while following the start of simulation, and supplies a purely resistive load sized at 0.2 per-unit (of the inverter rating). Thus the inverter current controller references are initially set to 0.2 per-unit and 0.0 per-unit for the active and reactive components of the current (*i.e.* $i_{id}^{*}$ ; $i_{iq}^{*}$ ) respectively. Then the following sequence of events is initiated into the system:

- 0.05 sec: grid breaker closed
- 0.10 sec: connection of a (0.6 +j0.4) *per-unit* local load to the system
- 0.12 sec: $i_{id}^{*}$ step change (0.2-0.8) *per-unit* and $i_{iq}^{*}$ step change (0.0-0.4) *per-unit*
- 0.20 sec: $i_{iq}^{*}$ step change (0.4-0.0) *per-unit*
- 0.30 sec: local load step change (0.8+j0.4) *per-unit* to 0.5 *per-unit*
- 0.35 sec: $i_{id}^{*}$ step change (0.8-0.5) *per-unit*
- 0.40 sec: simulation ends

Figures (6.39) and (6.40) display the plots of the currents and voltages of the inverter in response to the sequence of events outlined above. From Figure (6.39), it is observed that closing of the grid breaker at 0.05 seconds induces noticeable transients into the system, as can be inferred from the markedly distorted currents and voltages after breaker closure, when compared to the simulation output in the interval prior to the grid connection. After performing a number of simulations with different values of the inverter system local load (with the inverter current reference set accordingly), it was observed that the inverter system draws considerably distorted current from the grid at light (local) loads, which could possibly be a consequence of some sort of generation-load imbalance. The distortion observed in the inverter current following the grid breaker closure is also noticeable in the current supplied by the grid to the inverter system (Figure 6.40b). This distortion was not observed when the (inverter system) local load was set to be higher, say half of the inverter rated output or higher.

To confirm the probable origin of the observed distortion as stated above, a simulation case similar to the one performed above, but one in which the local load is initially set to 0.5 per-unit purely resistive, is considered (the d-axis current controller reference is correspondingly set to 0.5 per-unit and the q-axis component to zero).

Since the main objective of the modified simulation case is simply to observe the influence of the initial local load magnitude on system transients following grid closure, the sequence of

events is essentially maintained as in the previous simulation case, except for the modified initial conditions, and the correspondingly modified controller reference and load adjustments in the course of the simulation. In particular, the local load adjustment made at 0.1 second is the connection of an additional (0.3+j0.4) per-unit to the system, and that made at 0.3 seconds is a reduction of the local load to 0.667 per-unit purely resistive. The d-axis reference current is increased to 0.8 per-unit at 0.12 seconds, and then decreased to 0.667 per-unit at 0.35 seconds. The q-axis reference current adjustment remains the same as in the previous simulation.

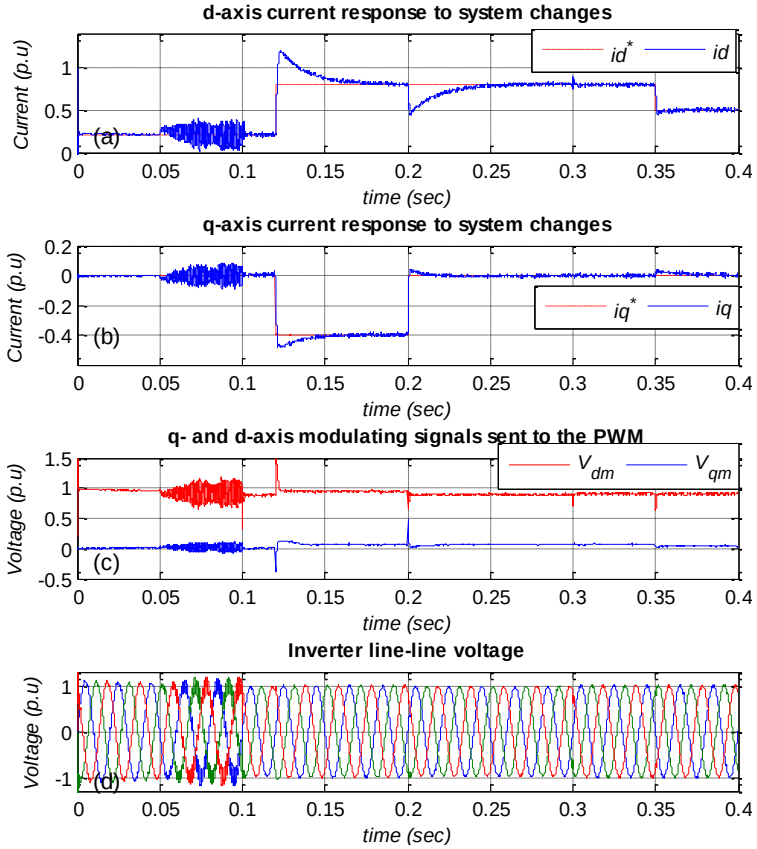


**Figure 6.39:** **Grid-connected inverter system response to load and current reference adjustments (light local load initially)**

The results of this simulation case can be observed in Figure (6.41), showing the plots similar to those generated for the previous simulation case. Comparison of the sub-plots in Figure (6.41) with the corresponding ones in Figure (6.39) reveals a clear distinction in the transient response of the system following grid closure at 0.05 seconds. Since the differentiating factor in the two simulation cases is the initial local load magnitude, the simulation results support the observation made earlier about the probable origin of the undesirable transients in the simulation case whose results are plotted in Figures (6.39) and (6.40).

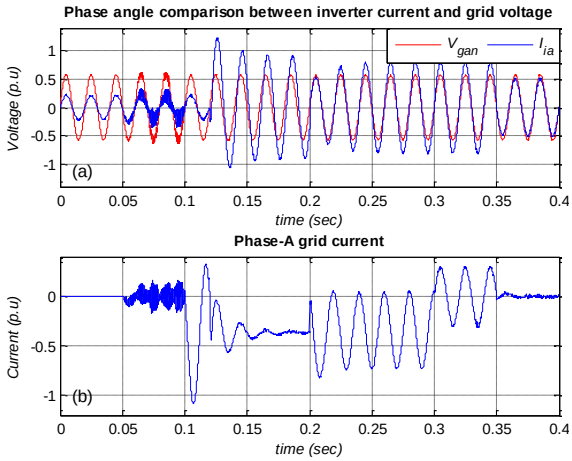


**Figure 6.40:** **Grid current and voltage responses to inverter system load magnitude and controller reference adjustments (light local load initially)**

With reference to Figure (6.39), when the local load is increased by active and lagging reactive power demands of 0.6 per-unit and 0.4 per-unit respectively at 0.1 second, the transients induced into the system at 0.05 seconds are observed to die out of both voltages and currents. Since the inverter current references remain set at 0.2 per-unit and 0.0 per-unit for the d- and q-axes respectively, the current drawn from the grid increases following the step increase in the local load. The grid current plot in Figure (6.40) exhibits a sharp increase at the instant of load adjustment, and this is evidently caused by the reactive power demand of the newly connected load.

The grid current surge decreases when the inverter reference currents are changed to 0.8 per-unit and 0.4 per-unit for the d- and q-axes respectively at 0.12 seconds. A phase displacement between the inverter current and the grid voltage is noticeable following the positive change in the q-axis inverter current reference, since the inverter now supplies both the active and reactive current components.

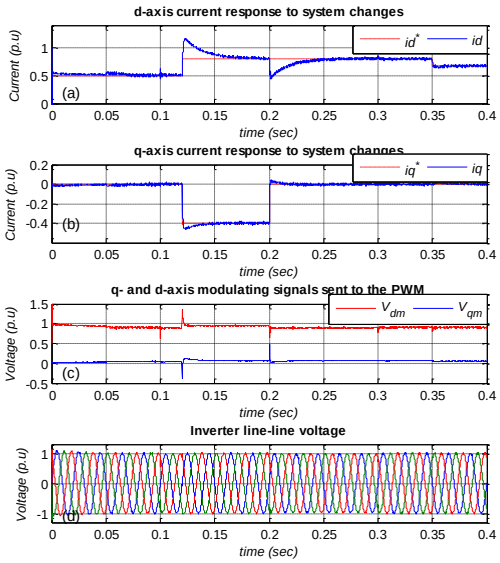


**Figure 6.41:** **Grid-connected inverter system response to load and current reference adjustments (adjusted initial local load)**

When the q-axis inverter reference current is decreased to 0.0 per-unit at 0.2 seconds, the grid must again supply the reactive power demand of the grid-connected inverter system's local load, and the current drawn from the grid exhibits a very asymmetrical characteristic following this reactive power demand. From 0.2 seconds to 0.3 seconds, the grid supplies a 0.8 per-unit. peak to peak current which has a significant DC offset, as can be seen in Figure (6.40b).

At 0.3 seconds, the local load is reduced, so that only an active power demand of 0.5 per-unit remains in the system. Because the inverter d-axis reference current is still set to 0.8 per-unit, grid current from 0.3 seconds is observed to have a value of 0.3 per-unit, which is the difference between the local load demand (0.5 per-unit) and the inverter current supply (0.8 per-unit), and is injected into the grid.

At 0.35 seconds, the inverter d-axis reference current is adjusted to 0.5 per-unit. (Figure 6.39a), and since this exactly matches the local load demand, the grid current is observed to decrease to zero at 0.35 seconds (Figure 6.40b).

What is also apparent from the responses of the currents and voltages plotted in Figures (6.39) and (6.40) is that inverter currents exhibit considerable overshoot following reference command adjustments, more so for the d-axis component, as can be observed from Figures (6.39a) and (6.39b). This may be explained by the fact that although the control scheme employed for inverter current control is the decoupled synchronous-reference-frame technique as discussed in Section (6.6), the two control channels are in actual fact not entirely decoupled. In particular, the scaled d-axis component that has to be added to the q-channel (according to Figure 6.21 and Equation 6.27) was in fact removed from the scheme of Figure (6.21) after analyzing a number of simulations. The reason for this is that the term ( $\omega L_{eff} i_{id}$ ) gave rise to very undesirable system transients, evidently because it increases the control effort to regulate the q-axis voltage component of the modulating signal to zero. Following the initial overshoots, nonetheless, the closed-loop system exhibits a well-damped response with a zero steady-state error. The modulating voltage commands also experience some spikes at instants where current overshoots are quite high, but they also quickly revert to normal values (Figure 6.39c).

These transients are only noticeable when the inverter operates at non-unity power factor (*i.e.* when it supplies reactive power in addition to the active power). In the grid-connected mode, however, the inverter considered in this study is required to operate at unity power factor. The analyses performed are nonetheless useful not only for completeness, but also for revealing some aspects of the system performance that may merit further analytical study.

Finally, an FFT analysis of the inverter phase-A current ( $i_{ia}$ ) for the scenario simulated above has been performed. The harmonic spectrum is depicted in Figures (6.42) and (6.43) (up to the

$50^{th}$ and $200^{th}$ components respectively), and as would have been expected, the total harmonic distortion has increased (1.53%), and the low-frequency harmonic component amplitudes are also larger. Power quality requirements (Table B.3, Appendix B) are nonetheless satisfied in this case as well, both for the total harmonic distortion and the individual harmonic component amplitudes.

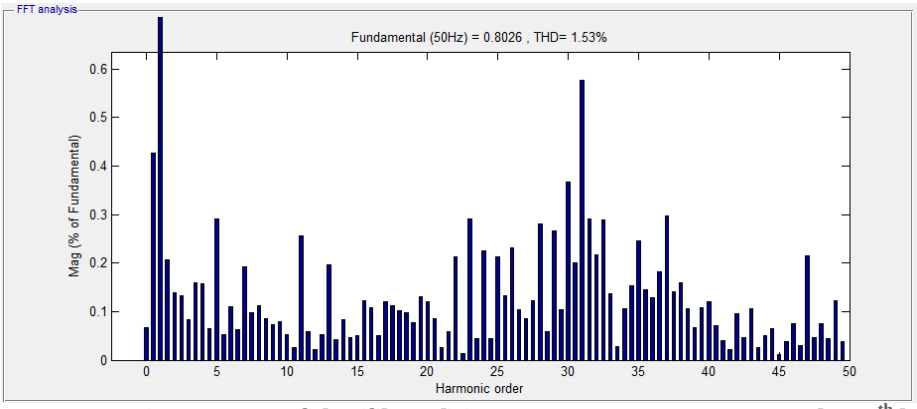


**Figure 6.42: Harmonic spectrum of the (filtered) inverter output current, up to the $50^{th}$ harmonic component, simulated with step reference command and load changes**

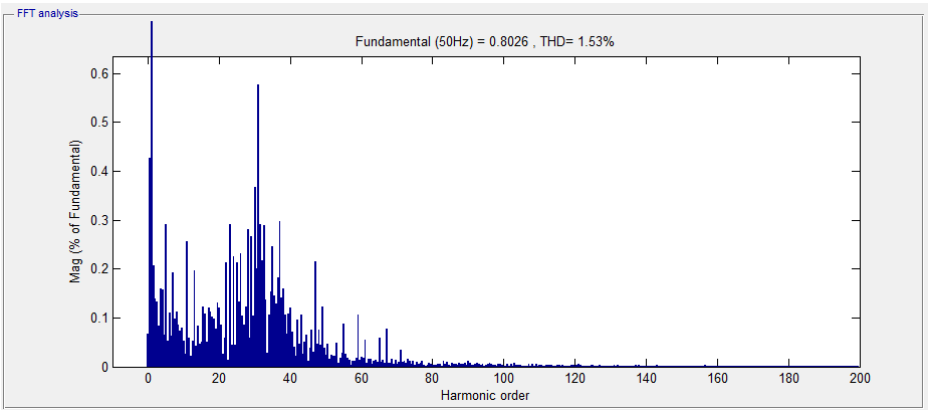


**Figure 6.43: Harmonic spectrum of the (filtered) inverter output current, up to the $200^{th}$ harmonic component, simulated with step reference command and load changes**

## 6.8. Conclusion

The minimum requirements (stipulated by the grid codes) for a grid-interactive inverter are that it remains properly synchronized with the grid under normal operating conditions (meaning that its terminal voltage magnitude and frequency match the corresponding grid voltage quantities), and that it injects high-quality, low-harmonic-distortion current into the grid. This ensures that the grid-connected operation of the inverter does not adversely interfere with the normal operation of the grid. The control of the grid-mode operation of the inverter to meet these requirements was the main focus of this chapter.

Thus, a Phase-Lock Loop (PLL) circuit was designed for the synchronization of the inverter terminal quantities with those of the grid, and a dual-loop current-mode controller was

developed for the control of the inverter to ensure that its output power satisfies the grid-code power quality requirements.

The performance of the designed control and synchronization scheme was analyzed by means of the computer simulation of a number of scenarios for the grid-mode operation of the inverter, with the focus being on the nominal, steady-state operating conditions (*i.e.* the grid operating conditions assumed to be devoid of any anomalies). Both the unity- and non-unity power factor operation cases were investigated.

Two cases were considered for the controller performance analysis: one in which the inverter injects unity-power-factor current into the grid (*i.e.* purely active power), and another in which the inverter operates at non-unity power factor. The responses of the system voltages and currents in both cases considered confirm that the developed controllers satisfy the objectives underlying their design. Both the steady-state and transient responses of the controllers for some load demand adjustments exhibit satisfactory behavior. The amount of harmonic distortion in the injected current has also been analyzed, and been found to satisfy the grid-code power quality specifications.

In the following chapter, attention is turned to the autonomous operation of the DPG-inverter. The autonomous-mode inverter controller is designed, and other vital aspects of the dual-mode inverter operation, such as island detection, and smooth operational mode transition, are also addressed.

# Chapter 7

# CONTROLLER DESIGN FOR THE AUTONOMOUS-MODE INVERTER OPERATION

## 7.1. Introduction

Among the many desirable characteristics of Distributed Power Generation (DPG) systems that are usually brought to the fore, one that is often highlighted is their high potential for making a significant contribution to power supply reliability. The prevalence of Uninterruptible Power Supply (UPS) systems in many industrial and commercial applications is sure evidence of the need for alternative means to realize the higher power supply reliability required by certain mission-critical loads than can be guaranteed by the grid supply.

Traditionally, UPS systems, the application regardless, have mostly made use of fossil-fueled auxiliary power generation systems. They cater to the needs of electrical loads for which even momenrary power supply interruptions are ideally to be avoided, and in this role, they are usually configured as online auxiliary power generation systems, able to quickly and seamlessly assume the role of powering critical loads in case of grid supply interruption for any reason. With the emergence and growing popularity of alternative (especially renewable) power generation systems, the scope of application of these systems is on the rise too, and they are earmarked to play a key role in auxiliary power supply systems for power supply reliability enhancement.

An inverter-based DPG system with the capability to operate both in grid-connected and autonomous modes would approach the characteristics of an online UPS system in its manner of operation, and where this is merited (that is, where the local load is critical and requires uninterrupted power supply), it can provide a cost-attractive alternative to the commonly used fossil fuel-based solutions for power supply reliability enhancement for sensitive loads. In this study, such a dual-mode DPG system is considered. The operation of such a system would imply an intentional island system, an operating condition which is still largely restricted by current grid interconnection standards (IEEE 1547-2003). Research on the implementation of such systems, however, is supported by the fact that such intentional islanded operation is envisaged in future electrical distribution networks with a sufficiently high contribution of generation from DPG systems, especially in view of the ever-growing share of distributed generation in distribution networks (Kroposki *et al.*, 2006).

Chapter 6 was focused on the operation of the DPG-inverter in the grid-connected mode, and a control system was designed for the grid-mode control of the inverter. In this chapter, attention is turned to the stand-alone operational mode. The distinctive system characteristics associated with the stand-alone operation of the inverter-based DPG system necessitate the adoption of a control strategy that is also distinct from that used in the grid-mode operation of the system.

The development of this control strategy and other aspects that have to be considered in the dual-mode operation of the inverter-based DPG are all dealt with in this Chapter. The various sections of the chapter address these aspects as follows.

All grid-interactive DPG systems are required to have a means to quickly detect abnormal grid conditions and to promptly implement corrective action so that the DPG does not interfere with the integrity of the grid operation. Accordingly, then, methods for the implementation of this function (known as anti-islanding detection and prevention) are discussed in Section 7.2. Additionally, the anti-islanding detection method implemented in this work is presented in this section as well. In Section 7.3, the control strategy used for the autonomous-mode operation of the DPG-inverter is discussed, and the control system design presented for implementation in the system considered in this thesis. Then in Section 7.4, a procedure for realizing the seamless transition of the inverter's mode of operation (between grid-mode and autonomous mode) is developed. Computer simulations are presented in Section 7.5 to analyze the performance of the designed system, in terms of satisfying the design requirements. Section 7.6 concludes the chapter with an outline of the main results of the chapter.

The next section discusses the common methods used in the implementation of islanding detection and prevention.

## 7.2. Islanding detection and prevention

According to the IEEE 1547-2003 international standard for the grid-integration of DPG, an island is formed when a portion of the utility grid is energized solely by a grid-integrated DPG system, while that portion is electrically separated from the rest of the grid supply system. For safety and operational concerns, discussed for instance in Ye *et al*. (2004), such an operating condition is not permitted, and grid-interactive DPGs are required to implement a means to prevent (unintentional) islanded operation, by disconnecting from the grid when the operating conditions become abnormal within the reaction times specified by the standard. The primary system parameters to be monitored that would indicate grid anomalies, thus necessitating the disconnection from the grid, are voltage magnitude and frequency, the ranges of which are specified by Tables (B.1) and (B.2) in Appendix B respectively (IEEE1547-2003).

Islanding prevention has become an active field of research, hand in hand with the increasing importance of DPG systems, and this has resulted in a variety of techniques that have been suggested for the implementation of anti-islanding protection. Research efforts are principally aimed at improving the effectiveness of the detection method (by reducing the Non-Detection Zone (NDZ)) and minimizing the techniques' adverse impact on power quality, while keeping implementation costs from becoming prohibitive, especially in the case of small-scale systems (Ye *et al.*, 2004). Most suggested algorithms may fall under the categories of either (i) ***remote/communication-based*** or (ii) ***locally-based*** anti-islanding techniques. Locally-based

techniques may in turn be classified as *passive*, *active* or *hybrid* (partly passive, partly active) algorithms (Mahat *et al.*, 2008). The main features of these techniques are outlined in the following sub-sections.

### 7.2.1. Remote anti-islanding techniques

When the decision of whether to keep the DPG connected to the grid or to initiate its disconnection from the grid is made on the basis of monitoring the distribution network's switchgear, the technique is remote-based, and relies on reliable communication between the distribution network operator's Supervisory Control And Data Acquisition system (SCADA), and the DG control and monitoring system.

One such common remote-based method is the *transfer trip* technique, which essentially requires that any distribution switchgear trip signal whose operation would lead to an island phenomenon be sent to the DPG's protection system, to ensure simultaneous disconnection of the DPG unit when operation of such switchgear is triggered. The transfer trip technique is simple in principle, and provides a reliable means to ensure that unintentional islanding is prevented. The main drawback presented by the scheme is the network topology-dependent complexity and the extensive communication required to implement it. It thus tends to be cost-prohibitive, except in the case of large DPG units (MW range), where the implementation cost and complexity may be justifiable.

Another method makes use of the *power line*, where a signal generator on the secondary side of the distribution system continually broadcasts a signal, using the power line as the signal carrier, which may be received by any DPG unit connected to the network and equipped with a signal detector. Because the signal is broadcast continually, it provides a continuity-check function, such that non-reception of the signal by the receiver installed at the DPG unit indicates an island condition, which should trigger the disconnection of the DPG unit. The power line signaling technique also provides a principally simple and reliable means to implement island detection and prevention, especially in the presence of many grid-integrated DPG units, since it only requires the use of one signal transmitter. As in the case of the transfer trip scheme, however, implementation costs may be an issue unless the number and sizes of connected DPG units warrants the cost associated with the installation of the (quite expensive) signal transmitter. Moreover, the scheme should ideally have minimal impact on other power line communication applications (Xu *et al*., 2004).

### 7.2.2. Passive anti-islanding techniques

As locally based methods, passive techniques work on the basis of the monitored local current and voltage magnitude and frequency to determine whether an island condition exists or not. Various methods based on these quantities have been suggested and are implemented, some working on the basis of *magnitude change* (voltage; frequency), others on the *time rate of*

*change* or *relative change of the quantities* (voltage; frequency; power; impedance, power factor), and even on the *change in harmonic distortion* (voltage) (Mahat *et al*., 2008).

Passive anti-islanding techniques are characterized by simplicity of implementation, short detection times, negligible impact on system power quality and stability, and satisfactory performance in cases of large power (generation-demand) mismatches in the ensuing island. Their main shortcomings though are their inability to guarantee reliable island detection (on account of the ever-present Non-Detection Zone (NDZ), an operational condition where the island phenomenon, though present, cannot be detected due to the monitored signals being much lower than the pre-determined thresholds), as well as their susceptibility to frequent mal-operation, which may stem from mild grid disturbances for which they should normally remain stable, or very narrow operational thresholds meant to decrease the NDZ.

Despite their limitations, passive techniques are widely implemented for their positive attributes pointed out above, albeit with certain constraints that act as a means to keep the NDZ to a minimum, and to lessen the risk of mal-operation. Limitations on the minimum load or minimum reverse power may be specified, for instance (Ye *et al*., 2004).

### 7.2.3. Active anti-islanding techniques

Active islanding detection methods also operate on the basis of local measurements, but in these techniques, perturbations are purposely introduced into the system and the decision made based on the system's response to the disturbances. The perturbations are generally small, and are such that their effect on the system parameters is negligible under normal operating conditions, only becoming influential under islanded conditions, which permits the detection of the grid anomaly leading up to islanding.

Perturbations in system frequency (***frequency shift***), phase angle (***phase shift***), current phase angle (***frequency drift***), terminal reactive power (***reactive power export error***) and injection of a high-frequency current signal (***impedance measurement***) are some of the many active islanding detection techniques (Kim & Hwang, 2000; Ropp *et al.*, 2000; O'Kane & Fox, 1997).

The main principle of operation of active islanding detection methods is attempting to destabilize the system by means of the small injected perturbations, which if successful, signifies the presence of the island phenomenon. Therefore, unlike passive methods, their effectiveness is decoupled from the magnitude of the power mismatch in an eventual island, making them have a comparatively lower NDZ. This, however, comes at the cost of their power quality deterioration and potential system destabilization effect, especially in the case of multiple DPG units all using active detection methods (Ye *et al.*, 2004). They also exhibit slightly slower response, since they should first perturb the system, monitor the system response, and only then ascertain the system condition.

Combinations of the methods discussed above (*i.e.* hybrid techniques) have also been tried, which can lead to simultaneous reduction in the large NDZ of the passive methods on the one hand, and the power quality deterioration effect of the active methods on the other (Mahat *et al.*, 2008).

### 7.2.4. Implemented islanding detection method

The islanding detection technique chosen for implementation in this thesis is the active method based on the perturbation of the reference of the inner current loop control, which is briefly explained below, as presented by Ye *et al*. (2004).

The active anti-islanding detection techniques presented by Ye *et al*. (2004) are based on the positive feedback phenomenon implemented in the synchronous reference (dq0) frame. The suggested techniques ensure a minimal NDZ without significantly compromising the system power quality. The main idea behind positive feedback techniques is to attempt to drive the system voltage and/or frequency away from nominal the ranges, which is meant to take place only when the system happens to be in an islanded state, and thus allows the detection of the island.

The positive *voltage magnitude feedback* scheme works on the basis of the direct proportionality between the inverter active power and the square of the inverter voltage (*i.e.* $P_i \propto V_i^2$). In the islanded mode of operation, positive perturbation of voltage has a destabilizing effect, since it increases the inverter active power output, which reinforces the voltage change due to perturbation, forcing it out of the nominal operating range. This is applicable in both cases of the voltage initially increasing or decreasing (in which case the voltage progressively decreases, until it violates the lower limit). Positive *frequency magnitude feedback* is another such scheme, and works on the basis of the direct proportionality between the reactive power and the frequency, similarly attempting to destabilize the system frequency by perturbing the reactive power consumption of the islanded system.

The voltage-based positive feedback scheme for islanding detection may be conveniently implemented in the decoupled synchronous reference frame (current-mode control) by exploiting the fact that the active power is directly controlled by the d-axis current component. So perturbing the d-axis reference current signal translates into perturbing the active power, and this has a destabilizing effect on the voltage, if islanding has occurred.

As Figure (7.1) (Ye *et al.*, 2004) shows, one way to implement the voltage-based positive feedback islanding detection scheme is to add a scaled d-axis voltage signal to the d-axis reference current signal (known as the $V_d - to - I_{dref}$ scheme). The scaled d-axis voltage component essentially represents a current perturbation, whose value is so tuned as to have

negligible influence on the operation of the system under normal conditions, and to cause voltage instability in the event of an island phenomenon occurring (Ye *et al.*, 2004).

The positive feedback scheme for islanding detection is comprised mainly of (Figure 7.1):

- signal filter;
- signal gain; and
- signal limits (saturation function)

Filtering of the perturbation component is necessary so as to block both low- and high-frequency harmonics from being added to the reference signal, and thus minimize the adverse power quality impact of the method. The gain value is carefully chosen to ensure stable operation of the system under normal grid conditions, while guaranteeing instability of the voltage upon loss of grid supply, to facilitate island detection. The limits on the perturbation signal are applied in view of the need to prevent inverter overloading, in case of large excursions in the grid voltage due to grid transients.

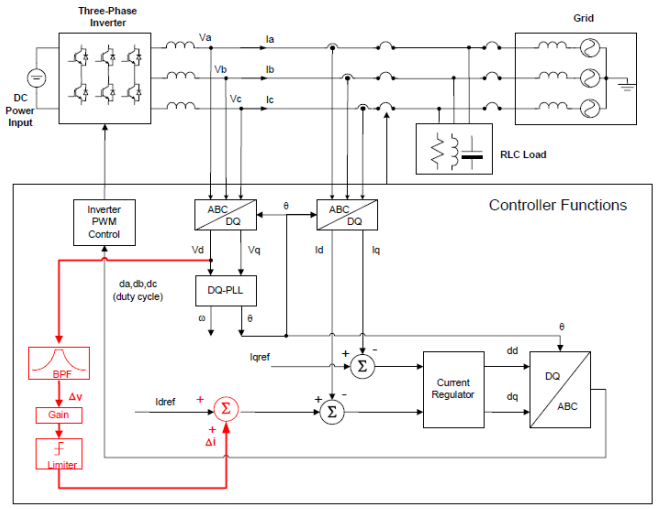


**Figure 7.1: Voltage-based ($V_d - I_{dref}$) positive-feedback islanding detection scheme (Adapted from Ye *et al.*, 2004)**

For this study a band-pass filter made up of a high-pass filter with a corner frequency of 0.2 Hz and a low-pass filter with a corner frequency of 10 Hz has been considered. The gain for the positive feedback signal compensator is set at 0.318, which ensures system voltage instability even under zero-power mismatch, while not excessively impacting the steady-state current controller set-point. The current controller set-point is limited to the inverter rated output in order to prevent inverter over-loading. The island detection scheme is made part of the grid-mode current controller implementation (added to the current controller set-point, similar to the depiction in Figure 7.1).

## 7.3. Control strategy for inverter autonomous-mode operation

The grid-connected inverter considered in Chapter 6 was operated in current-mode control, and this was a fitting control strategy because the terminal characteristics of the inverter in grid-connected mode are such that it is not able to significantly influence the system voltage magnitude and frequency (under the assumption that the inverter, with a relatively small rating, is connected to a stiff grid), and may thus only be able to control the real and reactive power injection into the grid, which is realized by means of the inverter current control. So the inverter terminal voltage magnitude and frequency are imposed by the grid, and the inverter is normally not permitted to perform voltage regulation.

In the autonomous operational mode, however, the inverter has to set up and maintain the terminal voltage according to load requirements. In this role the inverter is referred to as a grid-forming inverter, and the control strategy used is voltage-mode control, as opposed to the current-mode control implemented in the grid-mode operation (Rocabert *et al.*, 2012).

Ensuring voltage-loop control stability and minimal voltage steady-state error are the key objectives of inverter control in the stand-alone mode. Additionally, inverter peak current limiting is necessary to maintain system stability in the presence of load transients (Chen, 2011). These two control objectives may be satisfied by means of a dual-loop control strategy, such as that depicted in Figure (7.2).

Similar to the dual-loop current-mode control strategy discussed in the previous chapter, the dual-loop voltage-mode control scheme also comprises of an inner current control loop and an outer voltage loop. The significant difference is that the stand-alone inverter system is controlled in a way that makes it behave as an ideal voltage source, able to impose a specified voltage magnitude ($\hat{V}_i$) and frequency ($\omega$) across the load terminals.

In the scheme illustrated in Figure (7.2), $v_i^*$, $v_i$, $i_i^*$ and $i_i$, represent the signals of the outer voltage loop reference, the actual output voltage, inner current loop reference, and the actual current output, respectively. $G_{cv}(s)$, $G_{ci}(s)$, $G_{pi}(s)$ and $G_{pv}(s)$ are the Laplace-domain transfer functions of the outer-loop voltage regulator, the inner-loop current regulator, the inner-loop plant model and the outer-loop plant model, respectively. The outer voltage loop is designed with the primary objectives of minimizing the steady-state error in the terminal voltage and ensuring the stability of the overall control system, whereas the inner current loop enables the implementation of the inverter output current limiting. The scheme shows that the outer voltage loop also sets the reference for the inner current loop. Thus by means of this scheme, the inverter may be stably controlled to maintain the voltage across the load terminals within its nominal range while supplying the load power demand up to its rated capacity in the autonomous operational mode.

Based on the averaged model of the inverter as discussed in chapter 5, the dual-loop voltage-mode control system as represented in Figure (7.2) may be realized by means of any of the linear control techniques discussed in Section 6.5.2, Chapter 6. Here, two possible realizations are considered, which are (i) *synchronous-reference-frame Proportional-Integral* (dq-frame PI, similar to that implemented in the grid-mode system), and (ii) *stationary-reference-frame Proportional-Resonant* (αβ-frame PR) control techniques. Both techniques are developed for the considered system, and a comparative performance analysis of them is made.

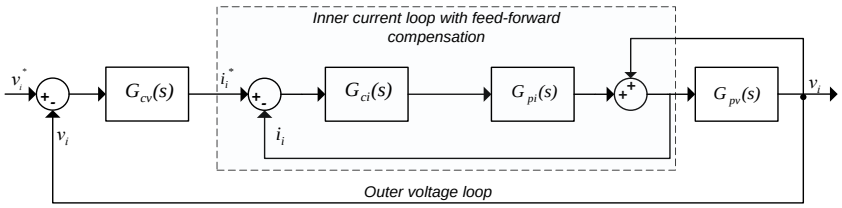


**Figure 7.2: Dual-loop control scheme for stand-alone mode inverter control (Adapted from Chen *et al.*, 2008)**

### 7.3.1. Voltage-mode synchronous reference (dq) frame PI control

With respect to the autonomous DPG-inverter, interfaced to a load by an LCL filter, as depicted by the simplified representation in Figure (7.3), the dynamic model representing the terminal voltage and current signals may be expressed in the space-phasor form by (Yazdani & Iravani, 2010):

$$L_i \cdot \frac{d\vec{i}_i}{dt} = -R_i \cdot \vec{i}_i + \vec{v}_i - \vec{v}_c \tag{7.1}$$

$$C_f \cdot \frac{d\vec{v}_c}{dt} = \vec{i}_i - \vec{i}_L \tag{7.2}$$

where $\vec{v}_i$, $\vec{v}_c$, $\vec{i}_i$ and $\vec{i}_L$ are the space-phasor representations of the inverter terminal voltage ($v_{iabc}$), filter capacitor voltage ($v_{cabc}$), inverter output current ($i_{iabc}$), and the load current ($i_{Labc}$), respectively. $L_i$, $R_i$ and $C_f$ represent LCL-filter's inverter-side inductor, its associated parasitic resistance, and the shunt filter capacitance, respectively. In the dynamic system represented by Equations (7.1) and (7.2), the inverter current ($\vec{i}_i$) can be considered to be the controlled (state) variable, the inverter voltage ($\vec{v}_i$) considered to be the control input, and the filter capacitor voltage ($\vec{v}_c$) considered to be a disturbance to the control system, similar to the current-mode control system considered in Chapter 6. Equation (7.2) represents the inverter terminal voltage dynamics, and shows that the terminal voltage is influenced by the load dynamics (Yazdani & Iravani, 2010).

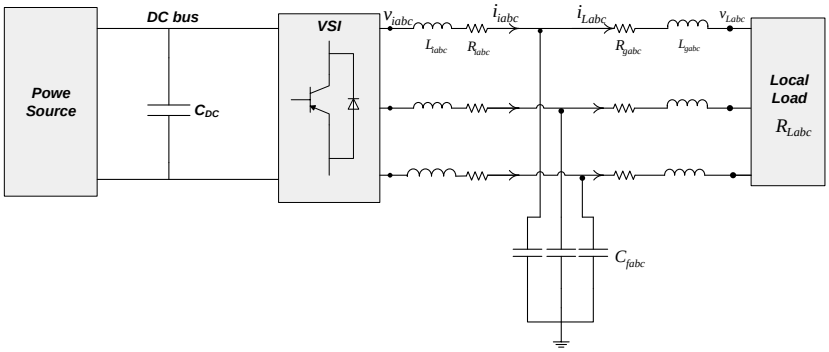


**Figure 7.3:** **Stand-alone operation of the inverter-interfaced DPG system.**

As discussed in Chapter 6, the abc-dq reference frame transformation introduces cross-coupling in the d-axis and q-axis loops due to the presence of derivative terms, and in the case of voltage-mode control, additionally requires feed-forward compensation of the capacitor voltage and load dynamics in the outer voltage loop in order to ensure effective voltage control (Chen, 2011).

### 7.3.1.1. Inner-loop current control

The decoupling and feed-forward compensation performed according to Figure (6.21) in Chapter 6, shown here in Figure (7.4), is valid also for the inner current loop of voltage-mode control. Since the grid voltage is not available for sensing in the autonomous mode of operation, the load voltage components ($V_{Ld}$ ,$V_{Lq}$) replace the grid voltage components ($V_{gd}$, $V_{gq}$) for the purpose of feed-forward compensation in Figure (7.4) (the inductance and resistance represent the effective values, as determined by Equations 6.21b and 6.22b).

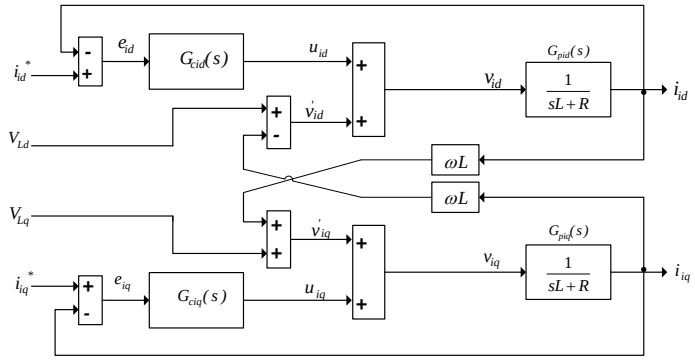


**Figure 7.4:** **Inner current loop decoupling and feed-forward compensation for the voltage-mode controller; the various parameters have been defined in Section 6.6.2.**

The plant model for the current controller design is considered to be a simple low-pass filter (Chen, 2011), which primarily has the effect of decreasing the closed-loop control bandwidth and causing a steady-state reference tracking error.

As discussed in Section 6.6.2 the decoupling and feed-forward compensation implemented according to Figure (7.4) reduces the inner current loop control problem to the regulation of two loops that are structurally identical, which permits the consideration of only one of the

loops for the controller design, with the resultant controller being valid for the other loop as well. So looking at the inner current loop in Figure (7.2) in conjunction with Figure (7.4), and considering the d-axis loop, the open-loop transfer function for the inner current loop regulated by a PI regulator can be written as:

$$G_{col}(s) = G_{cPI}(s) \cdot G_{pid}(s) = \frac{K_p}{L} \cdot \frac{s + K_i/K_p}{s} \cdot \frac{1}{s + R/L} \tag{7.3}$$

As in the grid-mode current controller design case, the PI regulator is used here with the pole cancellation technique to eliminate the effects of the large time-constant (due to the plant pole). This may be realized by setting the proportional and integral gain values of the PI regulator such that:

$$K_i/K_p = R/L \tag{7.4}$$

If Equation (7.4) is substituted into Equation (7.3), the following expression is obtained for the inner current open-loop transfer function:

$$G_{col}(s) = \frac{K_p}{sL} \tag{7.5}$$

The current controller time constant, $\tau_i$, can then be defined such that:

$$K_p/L = 1/\tau_i \tag{7.6}$$

If Equation (7.6) is in turn substituted into Equation (7.5), the (unity-feedback) closed-loop transfer function, $G_{ccl}(s)$, of the inner current loop is worked out, using the resultant expression, to be:

$$G_{col}(s) = \frac{1}{s\tau_i}$$

$$G_{ccl}(s) = \frac{G_{col}(s)}{1 + G_{col}(s)} = \frac{1/s\tau_i}{1 + 1/s\tau_i} = \frac{1}{1 + s\tau_i} \tag{7.7}$$

If the closed-loop control system is designed to achieve a time constant, $\tau_i$, of 1 millisecond (Yazdani & Iravani, 2010), using the inductance and resistance parameters for the LCL filter provided in Table (6.2) together with Equations (7.4) and (7.6) leads to the following PI regulator gain parameters for the inner current loop regulation:

$$K_p = \frac{L}{\tau_i} = \frac{3.06 \times 10^{-3}}{1.0 \times 10^{-3}} = 3.06$$

$$K_i = \frac{K_p \cdot R}{L} = \frac{3.06 \times 0.1}{3.06 \times 10^{-3}} = 100$$

Comparison between the uncompensated and compensated closed-loop system response is made in Figure (7.5).

As anticipated, the compensated system's closed-loop bandwidth is about 1000 rad/sec (that of the uncompensated system is only 290 rad/sec), as depicted in Figure (7.5a). A sufficiently high bandwidth for the inner loop is desirable, since although model simplification is performed for the purpose of controller synthesis, the actual plant (LCL filter) model has additional resonant poles, which must be damped to ensure system stability (Teodorescu *et al.*, 2011). The step response shows that the error-tracking performance is also significantly enhanced, being theoretically (although not practically) perfect.

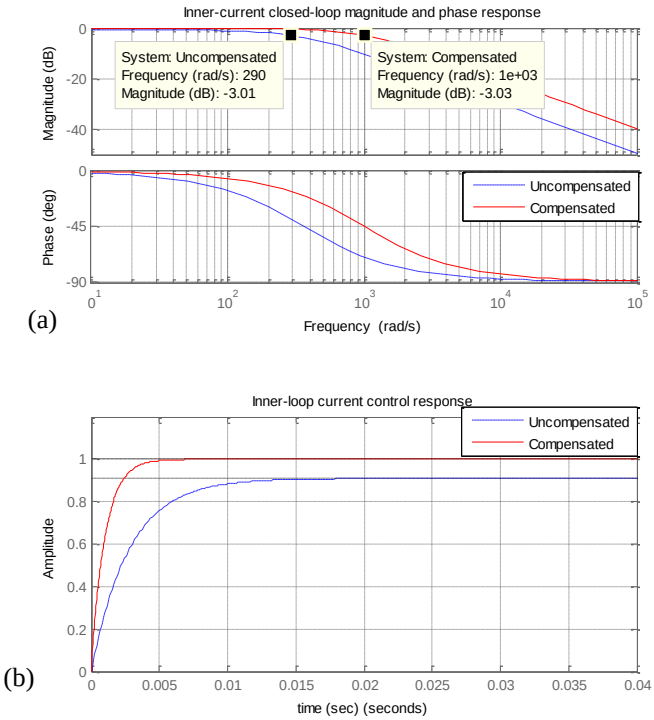


**Figure 7.5: Comparison of the compensated and uncompensated closed-loop (a) magnitude-phase and (b) step responses of the inner current control loop.**

### 7.3.1.2. Outer-loop voltage control

The output impedance seen by the inverter at its terminals in the autonomous operational mode constitutes the outer-loop voltage control plant transfer function, $G_{pv}(s)$, which, considering a resistive load, $R_L$, is given by (Maknouninejad *et al.*, 2011):

$$G_{pv}(s) = \frac{R_L}{1 + R_L C_f s} \tag{7.8}$$

where $C_f$ is the shunt filter capacitance. The outer voltage open-loop transfer function, $G_{vol}(s)$, may be obtained by considering Equations (7.7) and (7.8) in conjunction with Figure

(7.2), where the inner current closed loop transfer function is represented by Equation (7.7), and using the value of the time constant established above ( $\tau_i = 1ms$ ), is given by:

$$G_{ccl}(s) = \frac{1}{1+s\tau_i} = \frac{1}{1+1.0\times10^{-3}s} = \frac{1000}{s+1000} \tag{7.9}$$

Thus with the output impedance computed at the inverter rated output (Table 6.1), and the filter capacitance value obtained from Table (6.2) the expression for the outer voltage open-loop transfer function is obtained using Equations (7.8) and (7.9) as follows:

$$\begin{aligned} G_{vol}(s) &= G_{cv}(s)G_{ccl}(s)G_{pv}(s) = G_{cv}(s)\cdot\frac{1000}{s+1000}\cdot\frac{10.67}{9.55\times10^{-5}s+1} \\ &= G_{cv}(s)\cdot\frac{10.67\times10^{3}}{(s+1000)\cdot(9.55\times10^{-5}s+1)} \end{aligned} \tag{7.10}$$

From Equation (7.10) it can be seen that the plant model for the outer voltage loop control, $G_{pv}(s)$, given by Equation (7.8), is a high-frequency pole with a high gain. Its step response, without any compensation (and not taking the inner current loop into account), is depicted in Figure (7.6) (the solid sketch), and exhibits a short time constant. When the influence of the inner current loop is considered, the second sketch in Figure (7.6) is obtained, showing that the inner loop's main effect is to slow down the outer loop's response, with minimal effect on the steady-state response.

To improve the steady-state response (which is an important design requirement for the outer loop), a PI compensator is used, which allows to cancel the adverse effect of the inner current loop's large-time constant (*i.e.* the pole of $G_{ccl}(s)$) on the voltage loop, and to improve the steady-state response by the integrator it adds to the loop transfer function. The outer-loop (PI) regulator can thus be considered together with the inner current closed-loop transfer function (*i.e.* the open-loop transfer function, excluding $G_{pv}(s)$) as follows:

$$\frac{K_p s + K_i}{s}\cdot\frac{1000}{s+1000} = K_p\cdot\frac{s+K_i/K_p}{s}\cdot\frac{1000}{s+1000} \tag{7.11a}$$

The pole of $G_{ccl}(s)$ can then be cancelled by setting the PI regulator gain parameters such that:

$$\frac{K_i}{K_p} = 1000 \tag{7.11b}$$

In the case considered here, the proportional gain, $K_p$, has been arbitrarily set to the value of $0.5$, thus giving the integral gain, $K_i$, the value of $500$, according to Equation (7.11b). Substituting these gain parameters into Equation (7.11a) leads to the following:

$$\frac{K_p s + K_i}{s}\cdot\frac{1000}{s+1000} = \frac{500}{s} \tag{7.11c}$$

Then Equation (7.11c) can be substituted into Equation (7.10) to obtain the expression for the PI-regulated outer-voltage open-loop transfer function as:

$$G_{vol}(s) = \frac{5.335\times10^{3}}{s(9.55\times10^{-5}s+1)} \tag{7.12}$$

and the PI-regulated outer-voltage closed-loop transfer function, $G_{vcl}(s)$, is then given by:

$$G_{vcl}(s) = \frac{5.335\times10^{3}}{9.55\times10^{-5}s^{2}+s+5.33\times10^{3}} \tag{7.13}$$

The resulting compensated closed-loop response is plotted in Figure (7.7), where it is compared with the response of the uncompensated closed loop. The plots show that the compensator does eliminate the steady-state error, but it also causes a slight (albeit negligible) decrease in the closed-loop bandwidth.

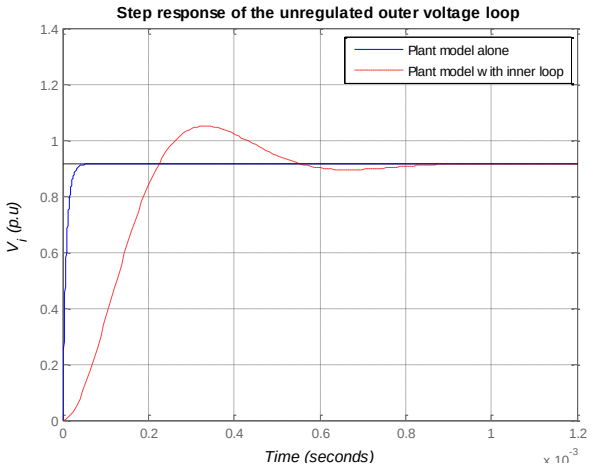


**Figure 7.6:** **Effect of the inner current loop on the transient response of the outer voltage control loop.**

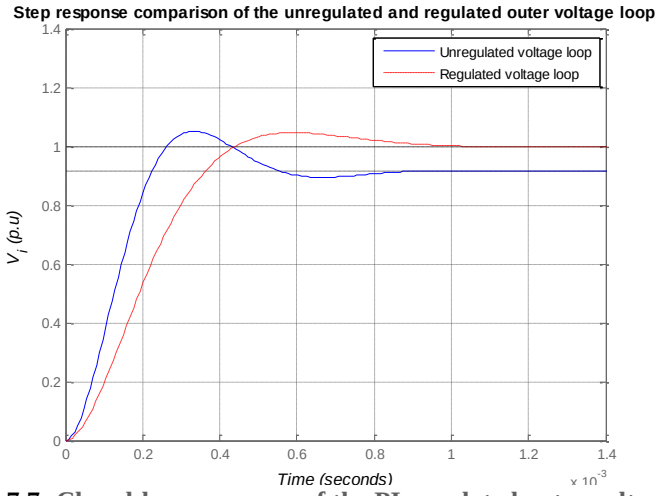


**Figure 7.7:** **Closed-loop response of the PI-regulated outer voltage loop.**

### 7.3.2. Voltage-mode stationary reference (αβ) frame PR control

The second method considered for the voltage-mode control is the *Proportional-plus-Resonant* (PR) regulation technique implemented in the *αβ* reference frame. The reason for

considering the second method is that although dq-frame PI control of the outer voltage loop is attractive for the DC nature of the controlled signals, this feature comes at a cost of significant decoupling and feed-forward compensation channels which, besides adding to the computational burden of the control processing, may also lead to unsatisfactory performance, especially under the operating conditions that the DPG-inverter may operate in the autonomous mode. Proportional-Resonant control is an alternative method that can achieve performance comparable to that of the dq-frame scheme, except with no need of the decoupling and feed-forward compensation needed for the dq-based method (Monreal *et al.*, 2009), which is an advantage.

#### 7.3.2.1. Structure of the αβ-frame PR controller

The strategy of the PR regulator, as briefly discussed in Section 6.5.2, is to incorporate into the regulator imaginary-axis double poles, placed at the frequency corresponding to that of the (periodic) signal to be regulated. In this way, the regulator adds infinite gain to the loop at the frequency of the regulated signal, which allows the periodic reference signal to be tracked with zero steady-state error. This is in accordance with the internal model principle (Teodorescu *et al.*, 2011; Yazdani & Iravani, 2010; Timbus *et al.*, 2009).

Although obtaining infinite gain at the resonant frequency from the ideal PR regulator, given by Equation (6.15) (rewritten here in Equation 7.14 and designated by $G_{PR\_1}(s)$) may be desirable to ensure a null steady-state error, it was explained in Section 6.5.2 that this infinite gain is associated with system stability concerns. Hence it is more common to use the non-ideal PR regulator, $G_{PR\_2}(s)$, ( Teodorescu *et al.*, 2011) expressed by Equation (7.15).

$$G_{PR\_1}(s) = K_p + \frac{s}{s^2 + \omega_o^2} \tag{7.14}$$

$$G_{PR\_2}(s) = K_p + \frac{2K_I\omega_c s}{s^2 + 2\omega_c s + \omega_o^2} \tag{7.15}$$

where $K_p$ is the PR regulator's proportional gain, $K_I$ is the integral gain term (commonly referred to as the PR regulator's resonant gain), $\omega_c$ is referred to as the PR regulator's equivalent bandwidth, and $\omega_o$ is the angular line frequency ($100\pi\ rad/sec$). The proportional gain contributes to the system gain at all frequencies of the system, and has a significant bearing on system dynamics (bandwidth and stability margins). The resonant gain may be tuned so as to provide specific gain at the frequency of interest; adjusting it shifts the system open-loop gain response vertically, and has negligible impact on the system bandwidth. The equivalent bandwidth allows adjusting the compensator's bandwidth as required, a feature that is not present in the ideal PR compensator. The resonant gain of the non-ideal PR

compensator, although finite, can still be high enough to ensure minimal tracking error of the reference signal (Chen, 2011).

#### 7.3.2.2. Parameter tuning for the αβ-frame PR-based voltage-mode controller

As in the preceding case (of the PI regulator), parameter selection begins with the consideration of the inner current loop. With the plant represented by a simple L-filter (first-order transfer function), the inner loop may be regulated by a PI- PR- or even pure P-compensator, provided that the outer loop is regulated by the PR compensator. Maknouninejad *et al*. (2011) showed that a proportional compensator suffices to provide the desired response characteristic of the inner current loop. The gain value must be carefully selected to ensure the inner loop bandwidth falls well below the LCL filter resonance frequency (Chen, 2011), and does not lead to excessive amplification of the high-frequency harmonic components stemming from the outer loop (responsible for setting the reference for the inner loop).

For the system considered in this study, an inner-loop proportional gain of 1 was found to provide acceptable response in terms of sufficiently large bandwidth, while limiting the harmonic level that may be caused by an excessive gain value.

For the outer voltage loop, some guidelines have been recommended for the selection of the parameter values for the PR regulator, discussed for instance in Chen (2011), and can be outlined as:

- The choice of the value for the proportional gain, $K_p$, is dictated by the required closed-loop system gain for the desired closed-loop bandwidth; because it affects the system gain at all frequencies, it may not be set too high;
- the resonant gain, $K_I$, is used to adjust the gain at the resonant frequency; it's value can also not be arbitrarily set to be very high, because high resonant gain values decrease the phase margin; and then
- the equivalent bandwidth, $\omega_c$, is used to slightly smoothen the (otherwise sharp) gain at the resonance frequency, and is so set as to slightly widen the (PR) controller bandwidth, without affecting the system phase response excessively.

In choosing the parameter values for the PR regulator, it is useful to observe the open-loop frequency response of the regulator for a range of values of the regulator parameters to be determined. This facilitates taking into account the above-mentioned guidelines. The PR regulator's frequency response for a range of proportional gain ($K_p$) values is depicted in Figure (7.8a). The figure also depicts the response of the ideal PR regulator (Equation 7.14, with $K_p$ set to 1), and shows that the ideal PR regulator exhibits very high gain and phase characteristics at the resonance frequency, whereas it contributes neither magnitude nor phase to the system response at all other frequencies. From the responses in Figure (7.8a), it can be

observed that the proportional gain value far below unity or far above unity would contribute negatively to the magnitude or phase of the PR regulator (and hence to the system it regulates).

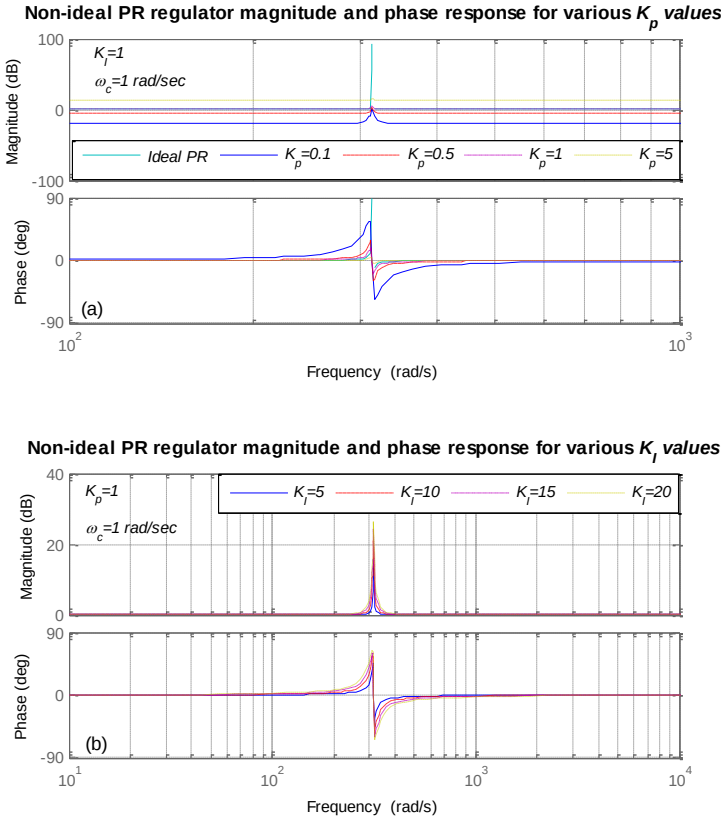


**Figure 7.8: Magnitude and phase response of the non-ideal PR regulator for various values of (a) the Proportional gain ($K_p$) and (b) the Resonant gain ($K_I$.**

The PR regulator's frequency response for a range of resonant gain ( $K_I$ ) values is depicted in Figure (7.8b). The plots reveal that the PR regulator's gain at the resonance frequency increases as $K_I$ is increased, which is what is desired. However, higher resonant gain magnitudes also tend to decrease the phase margin, which has to be avoided.

Figure (7.9a) illustrates the effect on the PR regulator's magnitude and phase response of varying the equivalent bandwidth parameter, $\omega_c$. The plots illustrate this parameter's bandwidth-widening effect on the PR regulator response mentioned earlier, but also show that its influence on the phase response can become significant when set quite high.

From the foregoing analysis, it can be observed that the positive characteristics of the PR regulator come at the cost of requiring the fine tuning of the regulator parameters, in order to ensure satisfactory perfomance.

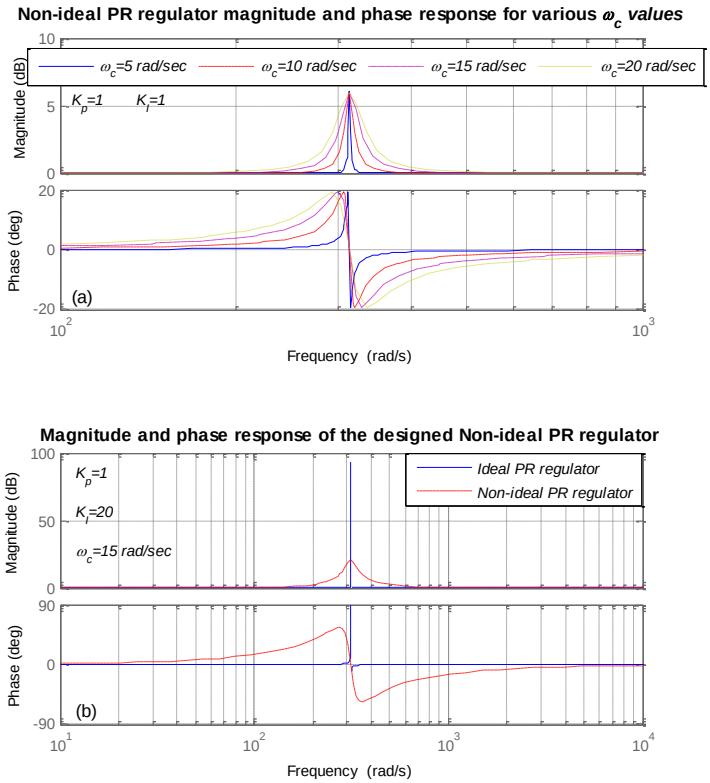


**Figure 7.9: Magnitude and phase response of the non-ideal PR regulator (a) for various values of the equivalent bandwidth ( $\omega_c$ ) and (b) for the designed parameters, compared with the ideal PR regulator.**

Taking the guidelines outlined earlier and the frequency response characteristics of the PR regulator presented above into account, the following parameters have been selected for the outer voltage loop regulator for the voltage-mode control implemented in the stationary reference frame:

$$K_p = 1, \qquad K_I = 10, \qquad \omega_c = 15\,rad/sec$$

The magnitude and phase response of the non-ideal PR regulator (Equation 7.15) with the parameters listed above is depicted in Figure (7.9b), together with that of the ideal PR regulator (Equation 7.14, again with $K_p = 1$). The designed PR regulator has moderate gain at the resonance frequency, to guarantee satisfactory overall system response (at the risk of slight (certainly negligible) steady-state error).

### 7.3.3. Comparison of the performance of the designed compensators

A number of scenarios have been simulated so as to evaluate characteristics of the dq-frame PI and the αβ-frame PR regulators for the voltage-mode control of the DPG-inverter's autonomous-mode operation. The system has been modeled for simulation in Simulink, as depicted in Figure (7.10).

#### 7.3.3.1. Rated active power supply

The first case examined is when the inverter is supplying rated active power (15 kW), with particular attention given to the controllers' ability to regulate the terminal voltage and simultaneously meet the load demand.

The performance of the dq-frame PI regulator is illustrated in Figure (7.11). The control strategy employed is voltage-oriented control (VOC), in which the d-axis voltage component ( $V_{id}$ ) is aligned with the terminal voltage vector amplitude ( $\hat{V}_i$ ) (i.e., $\hat{V} = 1 \cdot V_{id} + j \cdot 0 \cdot V_{iq}$ ), so that the q-axis voltage component ( $V_{iq}$ ) is regulated at zero. Figures (7.11a) and (7.11b) compare the outer-loop reference values with the actual outputs, and demonstrate that the regulators succeed in regulating the terminal voltage at the desired set-points. The phase-A-neutral voltage ( $V_{ian}$ ) and phase-A current ( $i_{ia}$ ) are plotted in Figure (7.11c), while the active ( $P_i$ ) and reactive ( $Q_i$ ) power outputs are as shown in Figure (7.11d) , which demonstrate that the current regulation is also well achieved by the synchronous-frame PI regulator.

The corresponding analysis done for the αβ-frame PR-regulated system is depicted in Figure (7.12). As can be inferred from the figure, control in the αβ frame involves the regulation of sinusoidal signals. This is in contrast with the control implemented in the dq frame, in which the regulated signals are DC quantities, and this distinction is worth noting, because it affects the principle of operation of the controller for the two techniques. The α- and β-axis reference and actual output signals are plotted in Figures (7.12a) and (7.12b) respectively. The phase-A-neutral voltage ( $V_{ian}$ ) and phase-A ( $i_{ia}$ ) current are plotted together in Figure (7.12c), while the active and reactive powers are plotted together in Figure (7.12d).

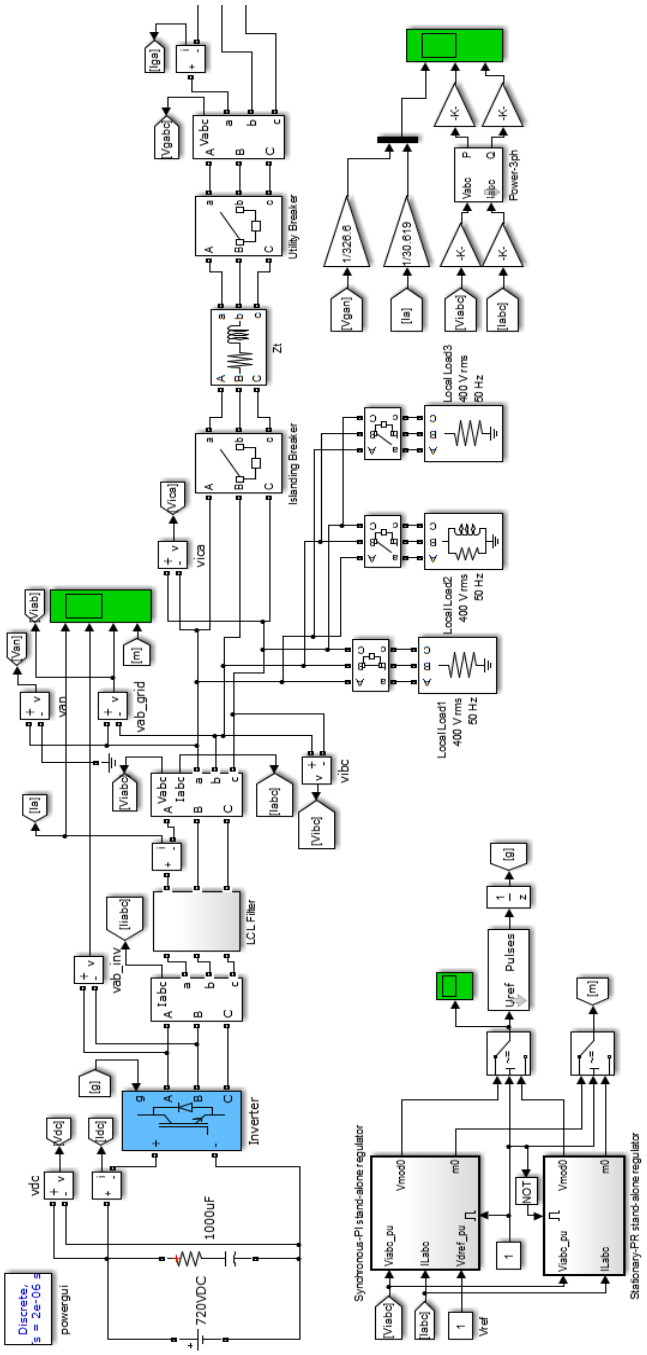


**Figure 7.10: Simulink block diagram of the stand-alone operation of the inverter-interfaced DPG.**

The PR regulator also shows good reference-tracking ability. Compared with the PI compensator though, a tracking error (of about 5%) occurs in both the outer (voltage) loop and inner (current) loop, which is more noticeable in the active power plot of Figure (7.12d) than in the voltage and current responses. This steady-state error may be explained by the fact that a non-ideal PR regulator that has been implemented in this system has been designed to have relatively moderate gain at the resonance frequency (to avoid the adverse consequences of having a very high resonance-frequency gain), whereas the zero-steady-state-error tracking of a sinusoidal signal theoretically requires the closed-loop system to exhibit infinite gain at the frequency of the sinusoidal signal to be tracked. The steady-state error in the simulation was

observed to decrease when the resonant gain was increased, but as explained, undesirable side-effects such as overshoots and slightly higher harmonic content were also associated with higher values of the resonant gain.

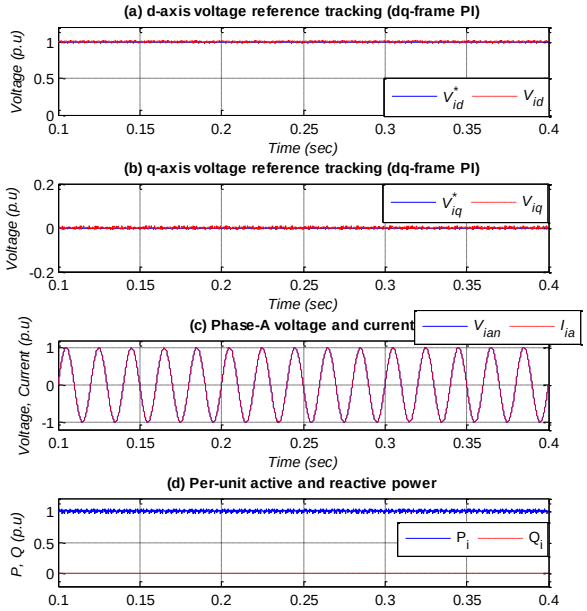


**Figure 7.11: dq-frame PI voltage-mode control of the stand-alone operation of the DPG-inverter; system response for unity-power-factor, rated-output operation.**

### 7.3.3.2. Step load changes and non-unity power-factor operation

The ability of the controllers to perform effective terminal voltage regulation when subjected to step load changes and non-unity-power factor load demand was analyzed; with the inverter initially supplying an active power load equal to 0.333 per-unit (of the inverter rated output; that is, 5 kW), the following sequence of events was initiated into the system:

- 0.10 sec: step load increase to (0.8 +j0.4) per-unit
- 0.30 sec: step load reduction to 0.5 per-unit
- 0.40 sec: end of simulation

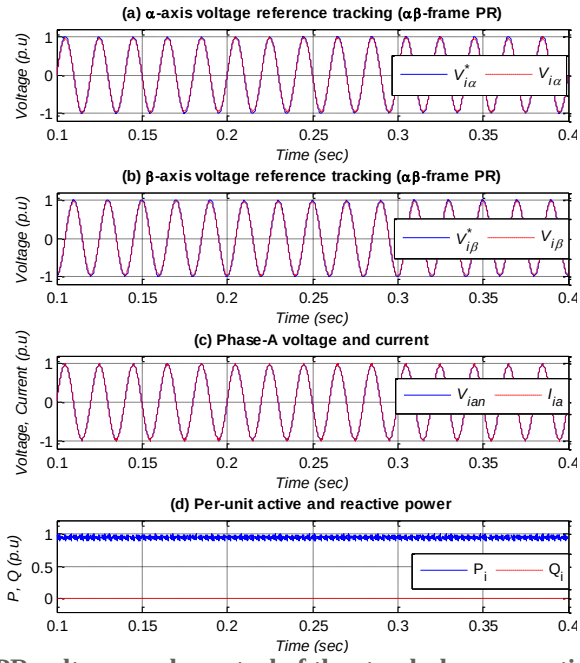


**Figure 7.12:** **αβ-frame PR voltage-mode control of the stand-alone operation of the DPG-inverter; system response for unity-power-factor, rated-output operation.**

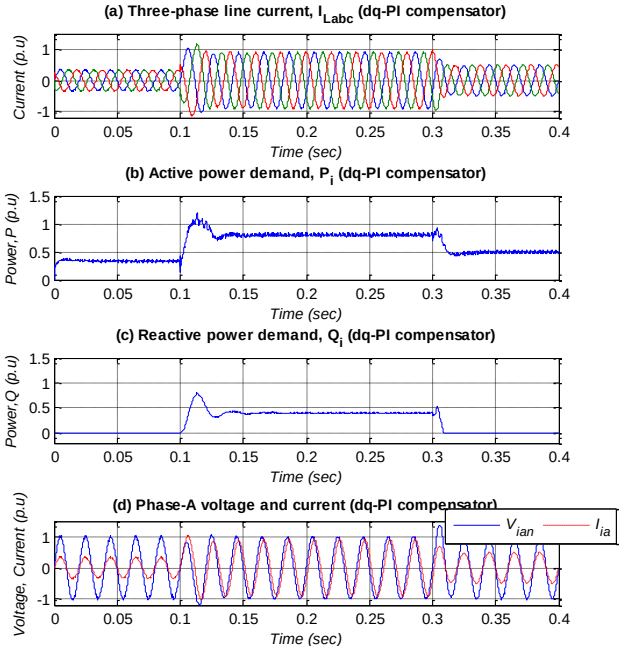


**Figure 7.13:** **Voltage, current, and power response of the dq-PI-compensated stand-alone-mode DPG-inverter operation.**

The performance of the PI compensator under the conditions outlined above is shown in Figure (7.13). The three-phase line current is depicted in Figure (7.13a), Figures (7.13b) and (7.13c) portray the per-unit active and reactive power responses respectively, and the phase-A voltage and current are plotted together in Figure (7.13d).

It can be seen from the figure that the reactive power demand in the time interval 0.1-0.3 seconds (Figure 7.13c) results in the current lagging the voltage, as depicted in Figure (7.13d), indicating a non-unity power factor operation of the inverter. The plots in Figure (7.13)

demonstrate that the dq-PI compensator performs quite well in responding to step changes in the load demand, except for the overshoot exhibited by both the active and reactive power responses as the inverter starts supplying reactive power at 0.1 sec (Figures 7.13b & 7.13c). This overshoot may be attributed to the fact that, despite the decoupling of the d-axis and q-axis loops that has been performed, a slight measure of cross-coupling between the two loops does in fact exist, and is readily seen when the inverter operates at non-unity power factor. The overshoot is momentary, nonetheless, and the steady-state values of both the active and reactive powers correspond to the commanded values.

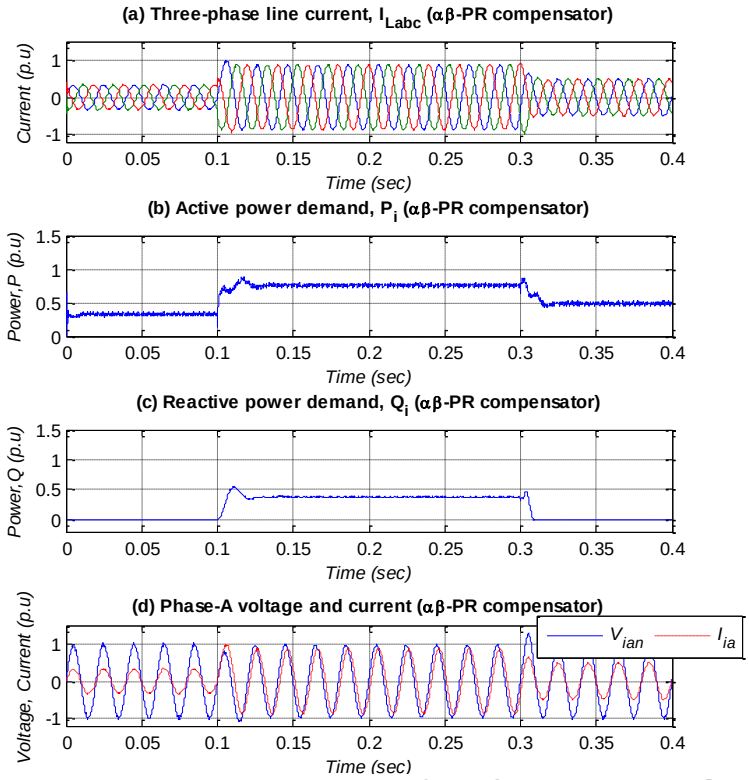


**Figure 7.14:** **Voltage, current, and power response of the αβ- PR-compensated stand-alone-mode DPG operation.**

The performance of the αβ-PR compensator for the same simulation case as described above is depicted in Figure (7.14). Comparison of the corresponding plots in Figures (7.13) and (7.14) attests to the fact that the two compensators (dq-PI & αβ-PR) have very comparable performance responses. The one distinguishing aspect of the performances of the two controllers is that the αβ-PR-compensated system does not exhibit the power output overshoot that is apparent in the dq-PI-compensated system. This is one advantage of the αβ-PR compensator over the dq-PI compensator, because the overshoot and its possibly disrupting effect on the system are avoided.

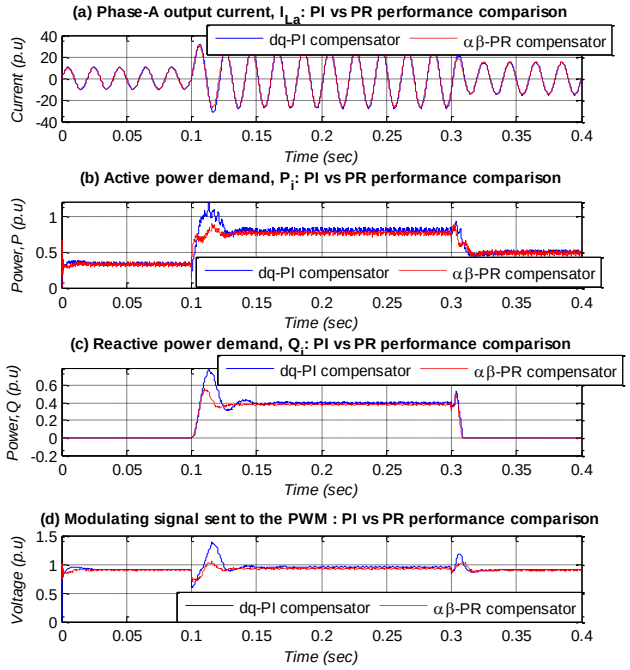


**Figure 7.15:** dq-PI vs. αβ-PR compensator performance comparison for the autonomous-mode DPG operation.

A comparison of the performance of the two compensators for the voltage-mode control of the autonomous-mode operation of the DPG-inverter is further depicted in Figure (7.15). It can be seen from the comparisons that the αβ-PR compensator only outperforms the dq-PI compensator in its not having the overshoot that is evident in the response of the dq-PI-compensated system. Moreover, unlike the dq-PI compensator, it does not need any decoupling or feed-forward compensation, and thus tends to be relatively less computation-intensive. The voltage harmonic distortion is depicted in Figures (7.16) and (7.17) for the dq-PI and αβ-PR-compensated systems respectively. The harmonic spectrum analysis reveals that the αβ-PR compensator additionally leads to relatively lower total voltage harmonic distortion.

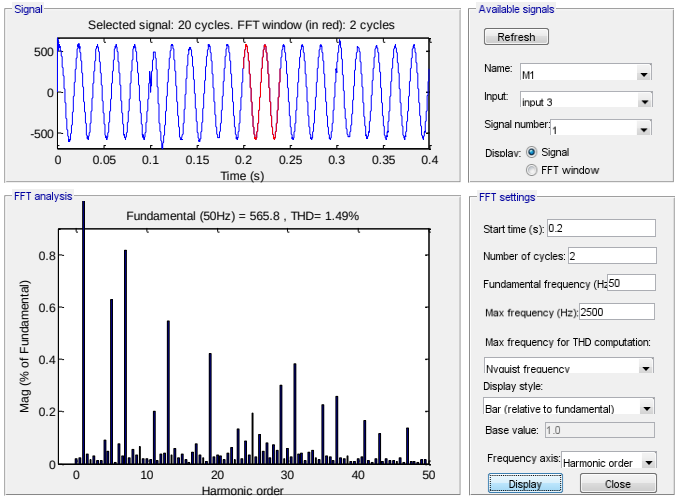


**Figure 7.16:** Voltage harmonic spectrum for the PI-compensated system (up to 50th harmonic component).

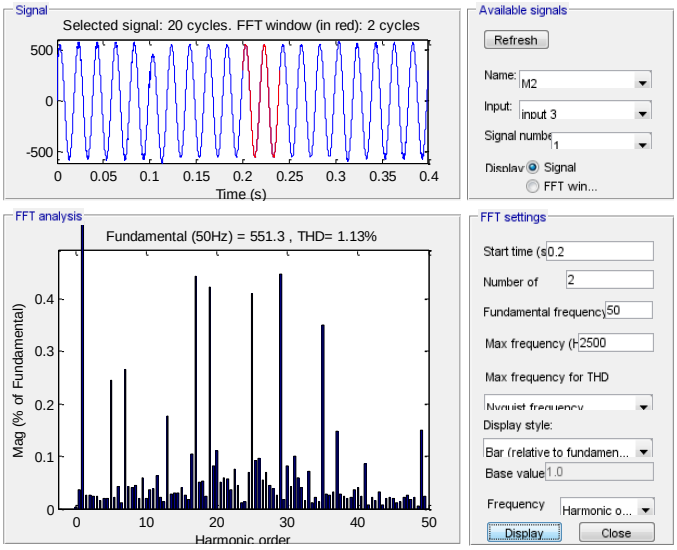


**Figure 7.17: Voltage harmonic spectrum for the PR-compensated system (up to 50th harmonic component).**

The next section looks at the operational mode transition of the DPG-inverter between the grid-mode and the autonomous mode. Procedures are suggested for achieving a seamless transition both from the grid mode to the autonomous mode and from the autonomous mode to the grid mode.

The αβ-PR compensator is considered as the voltage-mode controller for the autonomous-mode operation, as the performance comparison carried out above has shown it to slightly outperform the dq-PI compensator. The current-mode controller use is that developed in Chapter 6.

## 7.4. Mode transitioning (between grid-connected and stand-alone)

Successful operation of the inverter in both grid-connected and stand-alone modes requires that the transition between the two operational modes be properly coordinated, to ensure as smooth a transition process as possible so as to reduce the impact on the load (Wang *et al.*, 2012 ; Tirumala *et al.*, 2002). The inverter is required to be disconnected from the grid soon after the grid ceases to energize the Point of Common Coupling (PCC). If it is to carry on supplying the local load independently, it should be able to quickly set up across its terminals the voltage magnitude and frequency required by the load. The inverter then has to be controlled by a voltage-mode controller, such as that developed in Section 7.3.

In transitioning from grid-connected to stand-alone operational mode, the objective of the mode transitioning logic is to ensure that the local load sees minimal transients in the supply terminal characteristics (current, voltage magnitude and frequency). In moving from stand-alone to grid-connected mode, on the other hand, it is necessary to see to it that the inverter voltage is properly synchronized with that of the grid, both in terms of magnitude and frequency. Here, the two transition cases are considered separately.

### 7.4.1. Grid-connected to stand-alone mode

The transition of the inverter from grid-connected to stand-alone mode is highly influenced by the grid-connected system's operating conditions just prior to the disconnection of the inverter from the grid. While the inverter operates in grid mode, it is controlled to supply power at unity power factor by a current-mode regulator, and can supply up to its rated output. In terms of the system power balance following grid loss, three scenarios can be considered, which are:

1. positive power balance, when there is power transfer from the inverter to the grid;
2. perfect power balance, when power flow between the inverter and the grid is zero; and
3. negative power balance, when the grid is supplying part of the DPG's local load

These possible conditions do not only affect the detectability of the occurrence of the island, but also have an impact on the transients associated with the transition of the DPG-inverter from the grid-mode to the autonomous-mode of operation.

Assuming that the local load demand does not exceed the inverter rating, the inverter is able to sustain supply to the load independently of the grid if controlled properly, and provided that there is sufficient generation from the DPG (which is the assumption made here, so as to focus on the transients associated with the mode transition). The main issue of concern then is the minimization of these transients.

Critical to guaranteeing a seamless transition is to ensure that the control output signals of the voltage-mode regulator, which assumes the role of controlling the inverter in the autonomous operational mode, are brought to the desired steady-state, and are as close in value to the grid-mode regulator's control output signals as possible, prior to the controller changeover. This ensures that the controller changeover is accompanied by minimal transients.

The requirement to bring the voltage-mode regulator's control signals to the desired steady state before the control mode changeover implies that both (grid-mode and autonomous-mode) controllers are enabled during the transition interval, and the grid-mode regulator remains the active controller for some short interval into the islanded operational mode, the interval during which the voltage-mode controller output signals are brought to the required state. Under these circumstances, the transitioning behavior exhibits significant dependence on the pre-island power balance, according to the three scenarios outlined above, as discussed below and further investigated by means of simulations.

The analysis reveals that in the positive power balance case, the transition period is characterized by an initial over-voltage, followed by an under-voltage, which can be associated with the drop in the load demand caused by the loss of the grid load (the grid represents a sink for the fraction of the inverter power in excess of that demanded by the local load).

When the inverter output closely matches the local load (near-zero power flow between inverter- and grid-side), the transition period transients exhibit well-damped behavior, mainly because in this case the inverter supply corresponds to the load demand, and the presence or absence of the grid makes little difference to the inverter operation.

The negative power balance case is one where the pre-island inverter supply does not fully cover the entire load demand, and the deficit is supplied by the grid. Loss of grid thus implies a loss of supply, and consequently the power demand exceeds the power supply in the newly formed island, a situation that leads to severe transients, beginning with an under-voltage, followed by significant over-voltage.

The foregoing analysis suggests that the transition period transients can be partly mitigated by adjusting the grid-mode regulator set-points for the cases of power imbalance immediately following the loss of the grid. This, in conjunction with well-defined changeover logic, significantly improves the smoothness of the mode transition. The grid-connected to stand-alone operational mode transition sequence may thus be outlined as follows:

1. Upon island detection:
    a. Adjust grid-mode regulator references, to account for the absence of the grid supply/load
    b. Activate the voltage-mode regulator, with the voltage reference signals set to the pre-island grid voltage, and ramped to the nominal value if initially non-nominal; feed-forward of the (grid-mode) voltage reference signals speeds up the time for the regulator output signals to reach the required state
    c. Disconnect inverter from the grid;
2. A short interval following step 1 (one line-frequency cycle considered here), change the inverter control to voltage-mode control;
3. A sufficient interval following step 2 (two line-frequency cycles considered):
    a. Change the voltage-mode regulator reference signal to an independently generated reference signal; in the autonomous-mode operation of the DPG-inverter, an oscillator is used to generate the signal (of the required magnitude and frequency) that acts as the reference signal for the voltage-mode controller's outer control loop (Yazdani and Iravani, 2010);
    b. Deactivate the grid-mode regulator.

### 7.4.2. Stand-alone to grid-connected mode

The main issue of concern in the transition of the DPG-inverter from the autonomous-mode to the grid-mode of operation is ensuring that the inverter voltage is properly synchronized with the grid voltage prior to instituting the reconnection process (Srinivas *et al.*, 2013). Here again, the controller changeover from the voltage-mode to the current-mode controller is necessary

(because in the grid-connected mode the inverter may not regulate its terminal voltage, since the grid is normally a stiff one), and must be properly coordinated to ensure smooth inverter reconnection, so that undesirable transients upon reconnection are avoided.

A transitioning sequence from the autonomous-mode to the grid-mode of operation may thus be formulated as:

1. Upon detection of grid restoration (normally through monitoring the grid voltage magnitude and frequency), synchronize the inverter output voltage with the grid voltage by changing the voltage-mode controller reference to the sensed grid voltage;
2. Once the inverter voltage is in synchronicity with the grid voltage, and following some (interconnection standard-stipulated) waiting period:
    a. Activate the grid-mode regulator, reference currents set according to the pre-reconnection local load demand
    b. Change the inverter control from voltage-mode to current-mode control
    c. Close the interface circuit breaker to reconnect the inverter to the grid
3. A short interval following step 2, the voltage-mode controller can be deactivated; this helps to keep the (inactive) controller's output signals from deviating too much from the desired states.

## 7.5. Performance analysis of the designed scheme

The performance of both the grid-mode and autonomous-mode controllers for the control of the inverter in the grid-connected and autonomous modes, respectively, has been evaluated and their ability to meet the control objectives ascertained. Grid-mode operation was considered in Chapter 6, while the autonomous-mode operation has been analyzed in Section 7.3 of this chapter. In this section, attention is given to the ability of the DPG-inverter to seamlessly transition between the two operational modes, using the transition strategies discussed in Section 7.4.

### 7.5.1. Grid-mode to stand-alone mode transition

Three cases have been analyzed for the grid-mode to stand-alone mode transition, to examine the influence on transitioning transients of the pre-island power flow.

The first case considered is when the inverter output corresponds to the local load demand, such that power flow to or from the grid is zero. The load is set at two-thirds of the inverter rated output (*i.e.* 10 kW).

A grid disturbance is simulated by initiating a grid voltage collapse at 0.06 seconds, which leads to the grid voltage dropping to zero within 3 line-frequency cycles. The islanding detection logic detects the grid disturbance after about 11 milliseconds, and the response of the voltages, currents and powers are depicted in Figure (7.18).

From Figure (7.18a), it is observed that upon successful detection of the grid disturbance, the sequential transition to the stand-alone mode operation outlined in Section 7.4.1 is instituted, leading to the recovery of the inverter voltage within a cycle following the disturbance inception, while the grid voltage gradually reduces to zero. The plot of the inverter voltage in Figure (7.18b) displays some initial voltage sag that follows the grid voltage collapse, which is followed by a slight momentary over-voltage at the instant of control changeover. Figure (7.18c) shows that the momentary voltage sag is accompanied by a corresponding over-current, and this is due to the P-Q control nature (expressed by Equations 6.24e and 6.25e) of the grid-mode controller. The active and reactive power responses in Figure (7.18d) show little variation between the two operational modes, and only exhibit slight deviations from the steady-state values during the mode transition interval.

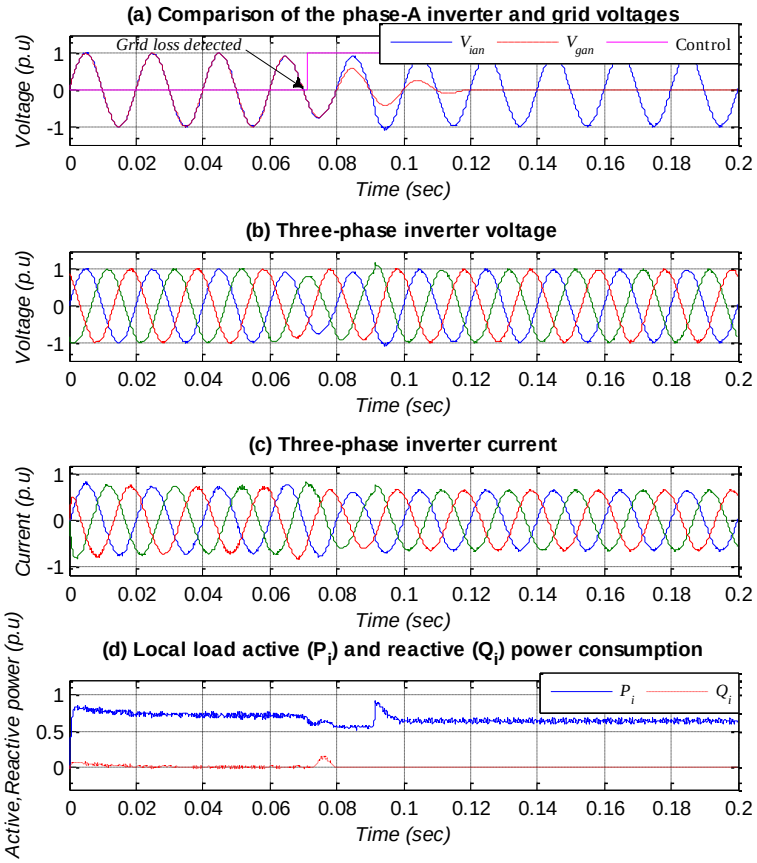


**Figure 7.18:** **Grid-mode to autonomous-mode transition of the inverter-interfaced DPG; null pre-island power flow to the grid.**

The results of the simulation case considered above demonstrate that the zero-power-transfer case (in which the inverter output power perfectly matches the DPG's local load immediately before the grid disturbance) undergoes quite a smooth transition from the grid-mode to the autonomous-mode operation. This is seen from the fact that the transition interval is void of any potentially disruptive transients, and that the pre-transition voltage, current, and power output values of the inverter match the corresponding post-transition values in the steady-state.

To investigate the conjectured influence of the nature of the pre-transition power flow (between the inverter and the grid) on the characteristics of the mode transition interval, the inverter is firstly controlled to supply its rated output (15 kW) prior to the occurrence of the grid disturbance, keeping the local load demand at 10 kW, and making no adjustments to the controller following the island formation. The results of this simulation case are depicted in Figure (7.19). This scenario implies a partial loss of load (in the form of the power sunk by the grid while present), and leads to a positive power imbalance (at least during the short transition interval).

As is noticeable from Figure (7.19), the transition interval is accompanied by significant transients that could potentially interfere with the DPG-inverter's ability to successfully transition into autonomous operation.

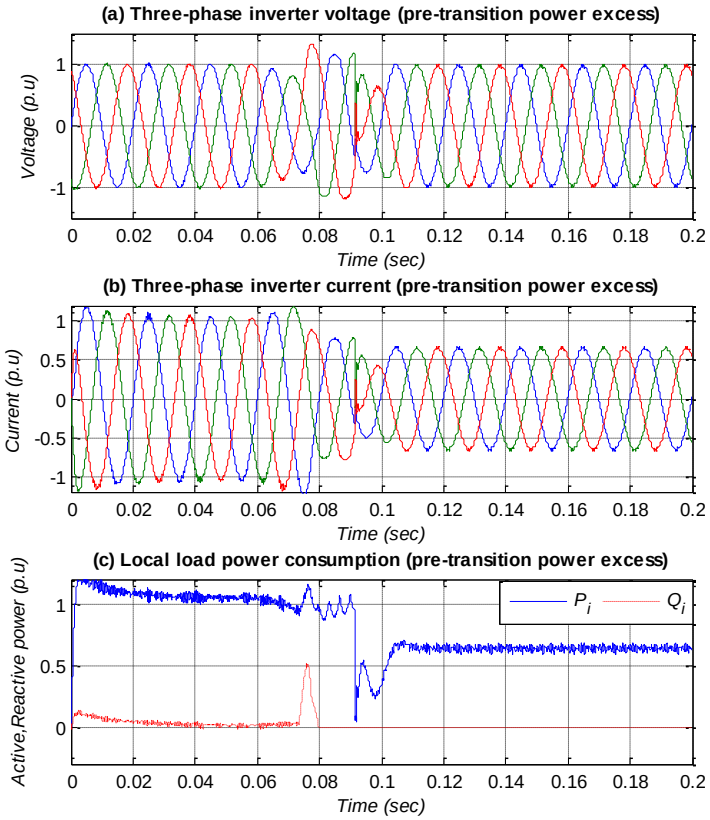


**Figure 7.19: Mode transition from grid- to autonomous operational mode, with supply excess prior to the transition; excess supply not taken into account in the controller.**

Both the voltage and the current experience a considerable surge, and the instant of controller changeover to the voltage-mode controller exhibits high (current, voltage) distortion. Both the active and reactive power responses are also characterized by significant deviation from the steady-state values.

Applying the suggested correction in the current-mode controller for the loss of load, which takes effect once the grid disturbance has been detected, leads to the simulation results depicted in Figure (7.20). A comparison of the corresponding plots in Figures (7.19) and

(7.20) reveals that correcting for the partial loss of load in this simulation case does improve the transition-interval characteristics of the considered system. Particularly, the over-voltage and over-current are considerably reduced (Figures 7.20a 7.20b respectively), and the excursions of the power outputs about the steady-state values are also significantly dampened (Figure 7.20c).

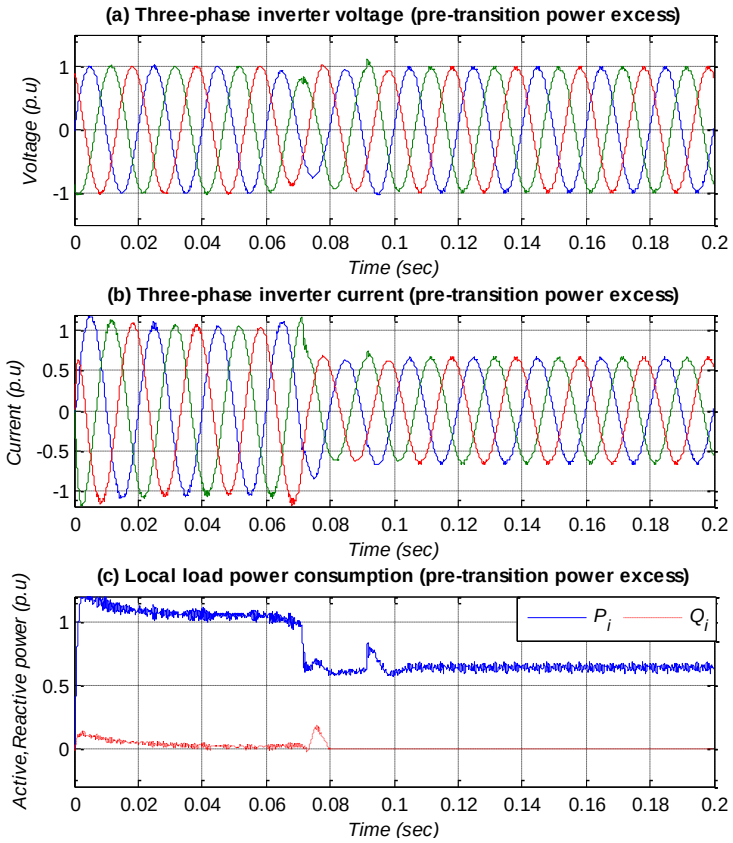


**Figure 7.20: Mode transition from grid- to autonomous operational mode, with supply excess prior to the transition; correction for the excess supply made in the controller.**

The last case considered for the grid-mode to stand-alone mode transition is when the inverter output is lower than the local load demand, supplying only a third of its rated output, while the local load is kept at 10 kW. The loss of the grid under these circumstances implies supply deficit in the newly formed island. The response of system voltages, currents and power when the pre-transition supply deficit has not been compensated for in the current-mode controller is as depicted in Figure (7.21).

In this case, while the response remains fairly well-damped during the short interval that the grid-mode controller remains the active controller as the voltage-mode controller is brought to the desired state, the voltage-mode controller exhibits excessive over-modulation, caused by the higher demand from the load on account of the lost grid supply. Transition from current-mode to voltage-mode control is thus characterized by distortion and overshoot in both the current and the voltage. The active power also manifests significant deviation from the steady-state value.

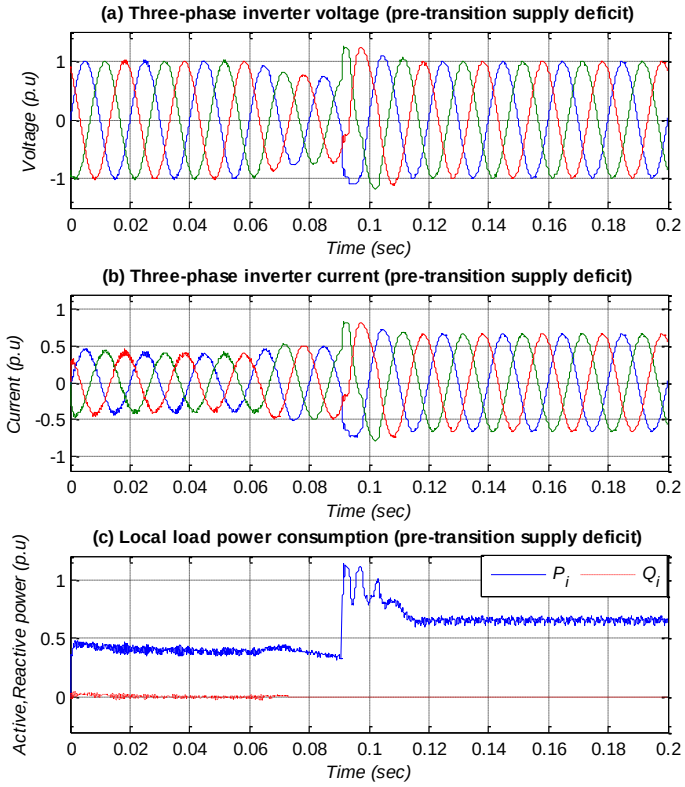


**Figure 7.21:** **Mode transition from grid- to autonomous operational mode, with supply deficit prior to the transition; supply deficit not taken into account in the controller.**

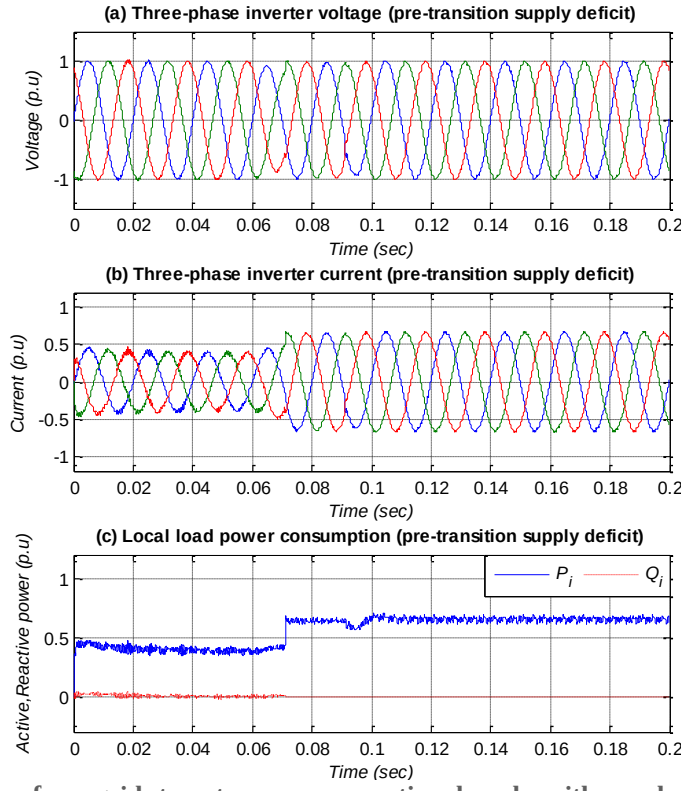


**Figure 7.22:** **Mode transition from grid- to autonomous operational mode, with supply deficit prior to the transition; correction for the supply deficit made in the controller.**

The system response in Figure (7.21) can be contrasted with that in Figure (7.22), generated by the simulation in which correction has been made for the supply deficit that immediately

follows the loss of the grid supply. Similar to the previous case of the pre-transition power surplus, the correction made in the grid-mode controller eliminates overshoots in the voltage and current, and smoothes the overall transition process, as can be inferred from Figure (7.22).

The simulations carried out above demonstrate the effectiveness of the transition strategy suggested in Section 7.4.1 in ensuring the seamless grid-mode-to-autonomous-mode operation transition and controller changeover, which is additionally decoupled from the nature of the pre-transition power flow.

### 7.5.2. Stand-alone to grid-mode transition

The inverter may be reconnected to the utility grid once it is established that the grid has been restored to normal operation; that is, when both the voltage magnitude and frequency satisfy pre-determined threshold values, and following a specified waiting period. A critical prerequisite for reconnecting the inverter to the grid is that the inverter output voltage be synchronized with the utility voltage in magnitude, frequency and phase angle. Failure to satisfy this requirement (for instance out-of-phase reconnection) would lead to the mode transition being accompanied by undesirable transients, which could possibly have damaging effects on the system operation, especially for a sufficiently large-size DPG system.

A transition of the inverter from stand-alone to grid-mode operation has been simulated for the same system considered in Section 7.5.1. Initially, the inverter operates in stand-alone mode, independently supplying a local load with a demand of two-thirds of the inverter rated output, purely active (*i.e.* 10 kW). It is assumed that the grid is recovering from a sustained voltage sag event, and only assumes the nominal voltage magnitude at 0.1 second in the simulation. Figure (7.23) illustrates the voltages and currents before and after the inverter is reconnected to the grid. In Figure (7.23a), the inverter phase voltage ($V_{ian}$) is plotted along with the corresponding waveform for the grid voltage ($V_{gan}$) to show the synchronization process. It can be observed from the figure that the voltages differ only in magnitude, having no phase displacement, and as soon as the set thresholds for the magnitude and phase differences are satisfied, the logic signaling the satisfaction of the requirements for the inverter reconnection becomes logic high (at 0.1185 seconds). A delay of one line-frequency cycle has been applied prior to reconnecting the inverter to the grid, in accordance with the procedure outlined in Section 7.4.2. From Figures (7.23b) and (7.23c), it can be seen that the transition to the grid-connected operational mode takes place without any disruptive transients, and the moderate current increase (Figure 7.23c) that occurs at the instant of the controller changeover (from voltage-mode to current-mode) is momentary. The seamless reconnection of the inverter to the grid is thus accomplished, using the step-by-step procedure outlined in Section 7.4.2.

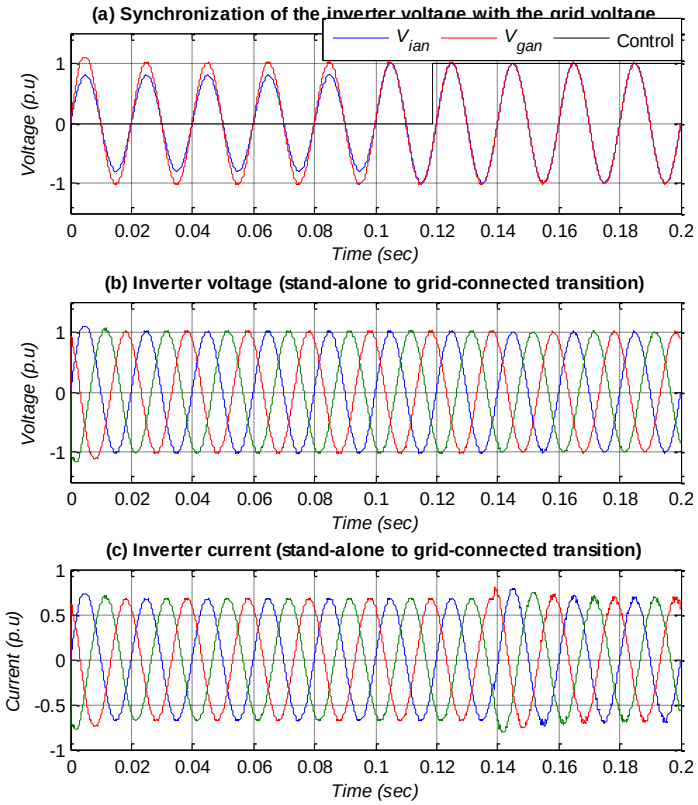


**Figure 7.23: Autonomous-to-grid-mode transition of the DPG-inverter; system voltages and currents prior to and following the transition.**

## 7.6. Conclusion

An inverter capable of interfacing the Distributed Power Generation (DPG) system both to the grid and to an autonomous load (*i.e.* a dual-mode inverter) requires an effective control strategy that takes into account the distinct control objectives of the two modes of operation. The main focus of this chapter was the design of a controller for the autonomous-mode operation of the DPG-inverter. Two other pertinent aspects of the dual-mode operation of the inverter that have been addressed in this chapter are a technique for quickly detecting the development of an island condition in the grid-connected system, and a procedure to ensure seamless transition between the grid-connected and autonomous modes of operation.

Because the inverter has to regulate the load voltage magnitude and frequency when operating independently of the grid, the dual-loop voltage-mode control strategy was discussed and developed for the autonomous-mode control of the inverter. The inner loop has been designed with the objective of regulating the inverter output current, whereas the outer loop regulates the terminal voltage at the desired magnitude and frequency.

Various steady-state scenarios of the operation of the grid-connected DPG-inverter have been considered in the simulations to analyze the performance of the designed control scheme, including the controllers, the islanding detection logic, and the mode transition procedure. The simulation results demonstrate that the presented control strategy satisfies the design

objectives of effectively controlling the inverter to meet the power demand of the load in the autonomous mode of operation, as well as seamlessly transitioning between the grid-connected and autonomous modes of operation.

In the concluding chapter of this thesis that follows, a coherent discussion of the important results from the work covered in the various parts of the thesis is presented, in light of the research objectives as set out in the introductory chapter, as well as the envisaged extensions to the work covered in this thesis.

# CHAPTER 8

# CONCLUSION AND FUTURE WORK

## 8.1. Introduction

This thesis has presented the development of an integrated control strategy for an inverter-based grid-integrated Distributed Power Generation (DPG) system that enables the DPG to operate both in the grid-connected mode as well as in the autonomous mode, with the ability to seamlessly transition between the two operational modes. The intention has been to realize a DPG whose operation approximates that of an online Uninterruptible Power Supply (UPS) system, which may find useful application in cases requiring higher power supply reliability than that obtainable from the grid supply, especially for sensitive loads for which even momentary power supply interruptions may be intolerable. When realized, such a dual-mode operation of the DPG also enables the fuller exploitation of the potential of Distributed Energy Resources (DER) to contribute to electric power supply reliability.

A comprehensive design approach has been taken in developing the dual-mode inverter control strategy in this work, where all the pertinent aspects of the grid-mode as well as the autonomous-mode control of the inverter-based DPG have been treated in a detailed manner. This has included, among other aspects, the development of the inverter plant model for current controller design; the judicious selection of the filter interface for the dual-mode operation of the inverter as well as the parameter design and dynamic response analysis of the selected (LCL) filter; the design of the relevant controllers for the two operational modes of the inverter; and the development of a procedure to ensure smooth transition of the inverter-based DPG between the grid-connected and the autonomous operational modes.

The control objectives to be satisfied in the two operational modes are distinct. In the grid-connected operational mode, the inverter is required to regulate the current injected into the grid, to ensure that the minimum power quality requirements as stipulated by the grid codes are satisfied; and in most cases (certainly the one considered here), it may not regulate its output voltage, which is normally imposed by the grid. A current-mode control technique was thus employed for the grid-mode control of the inverter, so as to satisfy these control objectives. As for the autonomous operational mode, the inverter is responsible for ensuring that the autonomous load (current) demand is adequately met, while at the same time regulating the load voltage magnitude and frequency. To achieve these control objectives, a voltage-mode control technique was used for the autonomous-mode control of the inverter.

The approach taken was thus to develop the controllers for the two operational modes separately, and then to integrate them by devising a procedure for the controller changeover, as part of the seamless operational mode transition process. Along with each controller design task (treated in separate chapters), a number of simulation cases were conducted to evaluate

the performance of the designed controller. From the perspective of the controller, the focus of the analysis was on the steady-state and dynamic performance of the controllers (*i.e.* the ability to track the commanded reference with zero steady-state error, the speed of response, and overshoot magnitude). From the perspective of the actual output voltages and currents, the emphasis was on ascertaining whether the power quality requirements were met. The power quality was evaluated by means of the harmonic spectrum analysis of the voltages and currents.

In the following paragraphs, the main results of this thesis work are briefly outlined. The possible applications of the results of this research, and the envisaged future extensions to this thesis work are also then discussed.

## 8.2. Thesis deliverables

The following subsections briefly discuss the main outcomes of this research, in light of the projected research outputs as enumerated in Section 1.10, Chapter 1.

### 8.2.1. Research output 1: Literature review on Distributed Power Generation Systems (Chapters 2 & 3)

For the review of the previous work related to the grid-integration of inverter-based Distributed Power Generation (DPG) systems, the following tasks were accomplished:

- the comprehensive comparative analysis of the literature in the field of DPG systems was conducted, with the focus being mainly on the topics:
    1. *PV and WEC systems modeling and MPPT control*
    2. *control of the Distributed Power Generation inverter interface*
    3. *dual-mode control of the grid-interactive inverter*
- the discussion of the main characteristics, technologies and typical applications of the commonly studied renewable and non-renewable Distributed Energy Resources (DER); and
- the consideration of the role of Hybrid Distributed Power Generation (HDPG) systems, both in rural and urban areas, with regard to the enhanced renewable energy harvesting and electric power supply reliability improvement.

Comment on the outcome: the contribution to the study of grid-interactive inverter-based DPG systems resulting from the accomplishment of this outcome has been to present a concise yet thorough review of the literature on the key aspects of the DPG system's dual-mode operation, as enumerated above. Moreover, the reviewed work has been logically presented and comparatively analyzed, highlighting both the main objectives and the various approaches that are commonly employed in the analysis and design of dual-mode DPG systems. The work may thus provide a basic understanding of the analysis, design and operation of the DPG

systems, as well as be a good source of reference material for the researchers in the field, from all the reviewed work that has been referenced.

### 8.2.2. Research output 2: PV and WEC systems modeling and MPPT control (Chapter 4)

For the Photovoltaic (PV) energy conversion system, the following tasks were accomplished:

- A mathematical model of the PV cell, based on the five-parameter, single-diode PV model, was developed and implemented in Matlab/Simulink; the unknown model parameters (shunt and series resistances) were determined numerically using the Newton-Raphson method for the solution of nonlinear equations; temperature and irradiance effects were also incorporated into the model, to better approximate the physical PV cell characteristics; the BP MSX 120 PV module data were used to implement the developed model in Matlab/Simulink, and the comparison of the simulation results with the characteristic curves provided in the manufacturer datasheets confirmed the accuracy of the developed model; and
- various methods for the Maximum Power Point Tracking (MPPT) control of PV generation systems were discussed; then the Incremental Conductance MPPT technique was implemented together with the developed PV model, and an assessment was made of the percentage increase in the power yield by comparing the output of the MPPT-controlled PV module with that without the MPPT controller.

For the Wind Energy Conversion (WEC) system, the following tasks were accomplished:

- the detailed discussion of the theory of the Horizontal-Axis Wind Turbine (HAWT), which is the most commonly used wind turbine configuration in modern wind power generation systems;
- the detailed discussion of the main subsystems of the WEC system in terms of their characteristics and functionalities, and the treatment of their mathematical modeling; and
- the modeling and simulation of a small-scale Permanent Magnet Synchronous Generator (PMSG)-based fixed-pitch, variable speed WEC system. Data for the Gaia-11 kW small wind turbine was used for the modeling, and the simulation analysis was carried out in Matlab/Simulink.

Comment on the outcome: the contribution to the study of grid-interactive inverter-based DPG systems resulting from the accomplishment of this outcome consists in the detailed treatment of the theory of operation, modeling and maximum-power-extraction control of PV and WEC systems. The close correlation that has been established between the simulation results and the manufacturer datasheet in both (PV and WEC systems) cases

has demonstrated the validity of the developed models and methods, such that they can be used confidently in the study of PV and Wind-based power generation systems.

### 8.2.3. Research output 3: Inverter model and filter parameter determination (Chapter 5)

For the inverter model development and filter interface parameter design, the following tasks were accomplished:

- The inverter plant model for the current controller design was developed, considering both the (inverter input) DC-link voltage and the (inverter output) AC current dynamics; this facilitated the development of a dual-loop grid-mode inverter current control system, as discussed in the third research output; and
- a systematic and detailed procedure for the LCL filter parameter design was also presented, which included the dynamic performance analysis of the designed filter, with the focus being on the effectiveness of the employed passive resonance damping, which is important from the control system stability point of view. The dynamic response analysis confirmed that the all design requirements for the filter were met.

Comment on the outcome: the contribution to the study of grid-interactive inverter-based DPG systems resulting from the accomplishment of this outcome is in the form of developing a detailed dynamic model of the inverter interface, encompassing both the DC-link voltage dynamics and the AC-side filter dynamics, which influence the generated power regulation and the accuracy (and power quality) of the inverter current control respectively. The simulation results have been confirmed to be in good agreement with those obtained by previous researchers.

### 8.2.4. Research output 4: Integrated dual-mode inverter controller design (Chapters 6 & 7)

By virtue of its relation to the main aim of this research work, the accomplishment of this objective may be said to be one of the main research outputs. As mentioned in Section 8.1, two distinct controllers were designed for the inverter control in the two operational modes, and the main results are discussed here accordingly.

#### 8.2.4.1. Grid-mode operation of the inverter (Chapter 6)

The control scheme designed for this operational mode encompassed the following:

- A Phase-Lock Loop (PLL) circuit for synchronizing the inverter voltage with the grid voltage; and
- a dual-loop current-mode inverter controller comprising of:
    - an inner current loop compensator; and
    - an outer (DC-link) voltage loop regulator

Two simulation cases were considered for evaluating the performance of the designed controller; one in which the inverter injects purely active power into the grid (i.e. unity-power factor (pf) operation), and another in which the inverter operates at non-unity power factor. Further details of the controllers and the simulation cases are provided in Tables (8.1) and (8.2) respectively.

**Table 8.1: Developed methods for the grid-mode inverter controller.**

| Method | Description of the method |
|---|---|
| SRF-PLL loop filter | PI-based loop filter with a 2nd order characteristic; phase-tracking error and speed of response design was based on the Wiener filter optimization method |
| Inner current loop compensator | dq-frame PI compensator; gain parameters were determined according to the Modulus Optimum compensator design method |
| Outer voltage loop regulator | 2nd order compensator, comprised of an integrator and a lead compensator; designed by means of open-loop frequency response methods |

**Table 8.2: Performance description of the grid-mode inverter operation with the designed controllers.**

| | Performance description | Current Total Harmonic Distortion (THD) |
|---|---|---|
| Case 1: unity-pf operation | Well-damped, negligible-steady-state error response to controller reference step changes | 1.05% (in steady state) |
| Case 2: non-unity-pf operation | Transient response following controller reference and load adjustments was characterized by significant overshoot, but the commanded signals were tracked with zero steady-state error; the undesirable transients showed that there is some (slight) cross-coupling between the d-axis and q-axis control loops for the non-unity-pf operation | 1.53% (in steady state) |

Comment on the outcome: the contribution to the study of grid-interactive inverter-based DPG systems resulting from the accomplishment of this outcome has been to develop a comprehensive controller that addresses the main control aspects of the grid-mode operation of the inverter, which are the proper synchronization of the inverter output with the grid voltage, and the control of the inverter to inject high-quality current into the grid. The steady-state and dynamic responses of the controllers, and the harmonic distortion analysis of the inverter output current, have all attested to the effectiveness of the developed methods, which moreover are in very good agreement with the results obtained by previous authors.

8.2.4.2. Autonomous-mode operation of the inverter (Chapter 7)

The following were designed in connection with the inverter controller for the autonomous-mode operation:

- An active anti-islanding detection scheme;
- a dual-loop voltage-mode inverter controller comprising of:
    - an inner current loop compensator; and
    - an outer (load) voltage loop regulator; two compensators were considered for the outer voltage loop regulation, then one chosen (based on the performance analysis) for incorporation into the overall control scheme; and
    - a procedure for ensuring the smooth transition of the operational mode of the inverter, both from grid-connected to autonomous mode, and from autonomous to grid-connected mode.

Further details of the designed controllers and the simulation cases conducted to evaluate the performance of the controllers are provided in Tables (8.3) and (8.4) respectively.

**Table 8.3: Developed methods for the autonomous-mode inverter controller.**

| Method | Description of the method |
|---|---|
| Islanding detection logic | dq-frame-based positive feedback method, based on the d-axis current reference perturbation by the d-axis grid voltage |
| Control scheme option 1 | dq-frame PI compensator was used for both the inner current and outer voltage loop compensators; the (stable) pole cancellation method was used to improve the overall system transient and steady-state response |
| Control scheme option 2 | dq-frame-based Proportional compensator was used for the inner current loop; αβ-frame-based PR compensator was used for the outer voltage loop regulation (the scheme chosen for the integrated control scheme) |

**Table 8.4: Performance description of the autonomous-mode inverter operation with the designed controllers.**

| | Performance description | Voltage THD |
|---|---|---|
| Case 1: rated power, unity-pf operation: comparison of schemes 1 & 2 | The two schemes exhibited comparable (and satisfactory) transient and steady-state behavior; there was only a slight steady-state error in the PR-compensated system | |
| Case 2: non-unity-pf operation: comparison of schemes 1 & 2 | The transient response of the αβ-PR scheme was relatively better than that of the dq-frame PI scheme, apparently due to the slight cross-coupling that characterizes the dq-frame scheme when operating at non-unity-pf | dq-PI: 1.49%<br>αβ-PR: 1.13% |
| Case 3: mode transition: grid-connected to autonomous mode | The pre-island power mismatch (between the inverter output and the load demand in the autonomous mode), whether an excess or a deficit, was found to influence the mode transition dynamics; by accounting for this in the control scheme, a smooth mode transition was realized | |

| | | |
|---|---|---|
| Case 4: mode transition: autonomous to grid-connected mode | A smooth mode transition was accomplished also in this case by means of the devised mode transition procedure, which ensured that the inverter output was properly synchronized with the grid prior to the reconnection | |

Comment on the outcome: the accomplishment of this outcome has contributed to the study of grid-interactive inverter-based DPG systems in the form of thoroughly considering the main aspects related to the effective control of the grid-inverter in the autonomous operational mode. The developed methods have covered the island phenomena detection, the effective voltage regulation and current control, and the smooth transitioning of the operational mode. The effectiveness of the developed methods has been supported by the extensive simulations conducted to evaluate their performance, whose results compare very well with those of the previous researchers.

From the discussion of the main research outputs presented above, it can be said that the main aim of the research (as stated in Section 1.4, Chapter 1) has been effectively accomplished.

### 8.2.5. Software programs developed in the thesis

**Table 8.5: Software programs developed in the thesis.**

| Program description | File type | Appendix |
|---|---|---|
| PV module initialization commands for unknown model parameter estimation | Matlab script file | C.1.3 |
| PV module Simulink implementation | Simulink simulation diagram | C.1.4 |
| Wind turbine performance curves based on numerical approximation | Matlab script file | C.2.3 |
| Wind turbine aerodynamic model Simulink implementation | Simulink simulation diagram | C.2.4 |
| LCL filter parameter design and dynamic response analysis | Matlab script file | D |
| PLL circuit design and dynamic response analysis | Matlab script file | E.1 |
| Grid-mode current controller design and dynamic response analysis | Matlab script file | E.2 |
| Grid-mode DC-link voltage regulator design and dynamic response analysis | Matlab script file | E.3 |
| Autonomous-mode inner-loop current controller design and analysis | Matlab script file | F.1 |
| Autonomous-mode PI-based voltage regulator design and analysis | Matlab script file | F.2 |
| Autonomous-mode PR-based voltage regulator design and dynamic response analysis | Matlab script file | F.3 |

## 8.3. Applications of the research output

### 8.3.1. Practical applications

Although the dual-mode control scheme discussed in this thesis was not experimentally implemented so as to evaluate its practical performance, the underlying concept is nonetheless very relevant to the prevailing (and most likely also future) needs in the field of the effective interfacing of distributed power generation systems to the electric grid. The need for reliable electric power supply can only be expected to increase, as the amount of mission-critical applications requiring uninterruptible power supply continues to grow. These applications would significantly gain from advances in the greater capabilities of distributed power generation systems made possible by more effective control methods.

### 8.3.2. Academic/research applications

The comprehensive manner in which the subject matter of this thesis has been treated, with a detailed and systematic presentation of the various fundamental aspects relevant to distributed power generation systems and their control, may serve a significant pedagogical function to students and researchers in the field of distributed generation systems. The results of the research presented here may also be used as a basis for extended research into the effective control of grid-integrated distributed generation systems, where more advanced controllers or other control strategies may be explored, and thus improve on the theoretical results obtained in this thesis.

## 8.4. Future work

Extensions to the work covered in this thesis could take any one or more of the following directions:

1. experimental implementation of the dual-mode grid-inverter control strategy developed in this thesis, so that the practical performance can be correlated with the obtained theoretical (simulation) results, and relevant improvements made to the suggested scheme;
2. the control strategy discussed in this thesis was developed with the assumption of the grid operating conditions being devoid of any anomalies, which is obviously not the case in practice; using the same integrated dual-mode controller concept presented here, advanced controllers (such as adaptive or optimal controllers) may be considered, which may be able to better deal with the non-nominal grid operating conditions, and thus enhance the practical realizability of the suggested control scheme;
3. extension of the concept to a dual-mode microgrid (*i.e.* a grid-interactive microgrid, with islanded operation capability), having multiple primary energy sources, energy storage, loads, and a power management system, which would especially be useful for enhanced renewable energy harvesting; and

4. consideration of the grid-integration of distributed power generation systems on the basis of advanced communication protocols, such as the *IEC 61850 International Communication Standard for Power Utility Automation*, in line with the smart grid objectives.

## 8.5. Publications

1. Mataifa, H., Raji, A.K. & Tzoneva, R., "Grid-mode Controller Design for a Dual-mode Inverter Interface for a Distributed Generation Source," *Proceedings of the International Conference on the Industrial and Commercial Use of Energy (ICUE)*, pp.317-324, Cape Town, South Africa, 2015.
2. Mataifa, H. & Tzoneva, R., "Integrated controller design for a dual-mode grid-inverter to ensure high-quality power supply in both operational modes," submitted to the *IET Renewable Power Generation Journal, January 2016.*

# REFERSENCES


Abdeddaim, S. & Betka, A., "Optimal tracking and robust power control of the DFIG wind turbine," *Electrical Power and Energy Systems 49, pp.234-242, Elsevier*, 2013.

Ackerman, T., Andersson, & G., Söder, L. 2001. "Distributed generation: a definition". Electric Power Systems Research 57, pp 195-204.

Ackermann, T. (Editor). 2005. "Wind power in power systems", 1st Ed., John Wiley & Sons, UK, 2005.

Ahmed, K.H., Finney, S.J. & Williams, B.W. 2007. "Passive filter design for three-phase inverter interfacing in distributed generation", in: *Compatibility in Power Electronics, CPE'07, IEEE, pp. 1-9*.

Ali, S., Pearsall, N. & Putrus, G., "Impact of High Penetration of Grid-Connected Photovoltaic Systems on the UK Low Voltage Distribution Network," *Int. Conf. on Renewable Energies and Power Quality, ICREPQ'12*, Mrach 28-30 2012.

Alternative Energy. n.d. "*Fuel Cells*", http://www.altenergy.org/renewables/fuel_cells.html. [March 31, 2014].

Anderson, P.M. & Bose, A., "Stability simulation of wind turbine systems," *IEEE Transactions on Power Apparatus and Systems, vol.102, pp.3791-3795*, December 1983.

Angquist, L. & Lindberg, L., "Inner phase angle control of voltage source converter in high power applications," *Power Electronics Specialists Conference, 1991. PESC '91 Record., 22nd Annual IEEE* , vol., no., pp.293,298, 24-27 Jun 1991.

Araújo, S.V., Engler, A. & Antunes, F.L.M. 2007. "LCL filter design for grid-connected NPC converters in offshore wind turbines", *The 7th International Conference on Power Electronics, October 22-26, 2007, EXCO, Daegu, Korea.*

Awad, B., Wu, J. & Jenkins, N. 2008. "Control of distributed generation", *Elektrotechnik & Informationstechnik*, 125 (12): 409-414.

Babu, N.R. & Arulmozhivarman, P., "Wind Energy Conversion Systems-A Technical Review," *Journal of Engineering Science and Technology, vol.8, No.4, pp.493-507,* 2013.

Bajracharya, C., Molinas, M., Suul, J.A. & Undeland, T.M. 2008. "Understanding of tuning techniques of converter controllers for VSC-HVDC", Nordic Workshop on Power and Industrial Electronics, June 9-11, 2008.

Barakati, S.M., Kazerani, M. & Aplevich, J.D., "Maximum Power Tracking Control for a Wind Turbine System Including a Matrix Converter," IEEE Transactions on Energy Conversion, vol.24, No.3, September 2009.

Barsali, S., Ceraolo, M. & Pelacchi, P., ''Control techniques of dispersed generators to improve the continuity of electricity supply,'' *in Proc. PES Winter Meeting, vol. 2,* pp. 789—794, 2002.

Bellini, A., Bifaretti, S., Iacovone, V. & Cornaro, C., "Simplified model of a photovoltaic module," *Applied Electronics International Conference*, pp.47-52, 2009.

Benadli, R., Khiari, B. & Sellami, A., "Three-phase grid-connected photovoltaic system with maximum power point tracking technique based on voltage-oriented control and using sliding mode controller," *6th International renewable Energy Congress (IREC),* 2015.

Bisoyi, S.K., Jarial, R.K. & Gupta, R.A., "Modeling and Analysis of Variable Speed Wind Turbine quipped with PMSG," *International Journal of Current Engineering & Technology, Special Issue 2*, 2014.

Blaabjerg, F., Teodorescu, R., Liserre, M. & Timbus, A.V. 2006. "Overview of Control and Grid Synchronization for Distributed Power Generation Systems", *IEEE Trans. Ind. Electron. 53, 1398-1409,* 2006

Boukhezzar, B. & Siguerdidjane, H., "Nonlinear control of variable-speed wind turbines without wind speed measurement," *Proceedings of the 44th IEEE Conference on Decision and Control, and the European Control Conference, Seville, Spain*, 12-15 December 2005.

Brambilla, A., Gambarara, M., Garutti, A. & Ronchi, F., "New approach to photovoltaic arrays maximum power point tracking," *30th Annual IEEE Power Electronics Specialists Conference, PESC 99, vol.2, pp.632-637,* 27

June-1 July 1999.

Burton, T., Sharpe, D., Jenkins, N. & Bossanyi, E. 2011. "Wind Energy Handbook", [Chapter 2], 2nd Edition, John Wiley & Sons, Ltd.

CADER. n.d. "Fuel Cells", [online]. Available at: www.cader.org/fuel-cells.html. Accessed May, 10 2012.

Carnieletto, R., Suryanarayanan, S., Simoes, M.G. & Farret, F.A. 2009. "A Multifunctional Single-Phase Voltage Source Inverter in Perspective of the Smart Grid Initiative", *Industry Applications Society Annual Meeting*. LAS 2009. IEEE, vol., no., pp. 1-7.

Carrasco, J.M., Franquelo, L.G., Bialasiewicz, J.T., Galvan, E., Guisado, R.C.P., Prats, M.A.M., Leon, J.I. & Morena-Alfonso, N., "Power electronics systems for the grid integration of renewable energy sources," *IEEE Transactions on Industrial Electronics, vol.53, no.4*, Aug. 2006.

Castañer, L. & Markvart, T. 2003. "Practical Handbook of Photovoltaics: Fundamentals and Applications", Elsevier Advanced Technology, Oxford.

Chen, C.-L. 2011. "Design, implementation and analysis for an improved multiple inverter microgrid system", *phD Thesis, Virginia Polytechnic Institute and State University*, 2011.

Chen, C-L., Jih-Sheng, L., Yu-Bin, W., Sung-Yeul, P. & Miwa, H., "Design and Control for LCL-Based Inverters with Both Grid-Tie and Standalone Parallel Operations," *IEEE Industry Applications Society Annual Meeting, (IAS'08)*, pp.1-7, 2008.

Chen, J-F. & Chu, C-L., "Combination voltage-controlled and current-controlled PWM inverters for UPS parallel operation," in *Power Electronics, IEEE Transactions on*, vol.10, no.5, pp.547-558, Sep 1995.

Chung, S.-K. 2000. "A phase tracking system for three phase utility interface inverters", *IEEE Transactions on Power Electronics*, vol. 15, No. 3.

CIGRE, "Modeling New Forms of Generation and Storage, TF38.01.10, November 2000.

Coelho, R.F., Concer, F. & Martins, D.C., "A proposed photovoltaic module and array mathematical modelling destined to simulation," in *Proc. IEEE Int. Symp. Ind. Electron.*, pp.1624-1629, 2009.

Cultura A.B. & Salameh, Z.M., "Modeling and Simulation of a Wind Turbine-Generator System," *Power and Energy Society General Meeting, IEEE*, 2011.

de Brito, M.A.G., Sampaio, L.P., Luigi, G., eMelo, G.A. & Canesin, C.A., "Comparative analysis of MPPT techniques for PV applications," *Int. Conf. Clean Electrical Power (ICCEP), pp.99-104*, 14-16 Jue 2011.

Dell'Aquila, A., Lecci, A. & Liserre, M. 2003. "Microcontroller-based fuzzy logic active filter for selective harmonic compensation," in *Proc. IAS 2003*, Oct. 12–16, vol. 1, pp. 285–292.

DeWinkel, C.C. & Lamopree, J.D. 1993. "Storing power for critical loads", *IEEE Sprectrum*, pp. 38-42, June 1993.

Di Piazza, M.C. & Vitale, G. 2013. "Photovoltaic Sources, Modeling and Simulation", Springer-Verlag, London.

Dida, A. & Benattous, D., "Modeling and control of a DFIG via back-to-back multilevel converters using fuzzy logic controller," *3rd International Conference on Control, Engineering & Information Technology (CEIT)*, 2015.

Ding, F., Li, P., Huang, B., Gao, F., Ding, C. & Wang, C., "Modeling and simulation of grid-connected hybrid photovoltaic/battery distributed generation systems," *China Int. Conf. on Electricity Distribution (CICED)*, pp.1-10, 13-16 Sept. 2010.

Ding, J.J. & Buckeridge, J.S., "Design Considerations for a Sustainable Hybrid Energy System", [online], *Transactions of the Institution of Professional Engineers New Zealand: Civil Engineering Section*, vol. 27, no. 1, Nov 2000: 1-5.

Dingguo, W. & Zhixin, W., "Modeling and Design of Control System for Variable Speed Wind Turbine in All Operating Region," *International Journal of Systems and Applications, Engineering & Development, vol.1, issue*

*3*, 2007.

Directive 2001/77/EC of the European Parliament and of the Council of 27 September 2001 on the promotion of electricity produced from renewable energy sources in the internal electricity market", *Official Journal of the European Communities, L 283/33*.

Dondi, P., Bayoumi, D., Haederli, C., Julian, D. & Suter, M. 2002. "Network integration of distributed power generation", Journal of Power Sources, vol. 106, pp 1-9.

Dulău, L.I., Abrudean, M. & Bică, B., "Effects of Distributed Generation on Electric Power Systems," *Procedia Technology*, vol.12, pp.681-686, 2014.

El-Khattam W. & Salama, M.M.A., "Distributed generation technologies: definitions and benefits", *Electric Power Systems Research*, 71, pp.119-128, 2004.

Elmer, T. & Riffat, S.B. 2012. "*State of the art: fuel cell technologies in the domestic built environment*", [online]. Available at: http://trisofc.files.wordpress.com/2012/09/fuel-cells-in-the-built-environment-state-of-the-art-review-set-paper1.pdf. Accessed March 31, 2014.

Encyclopaedia Britannica Online. 2014. "Photoelectric effect", available online at: http://www.britannica.com/EBchecked/topic/457841/photoelectric-effect. Accessed June 13, 2014.

EPRI, 2010. "Electrical energy storage technology options: a white paper primer on applications, costs, and benefits", Palo Alto, CA, 1020676.

Erickson, R.W., "Fundamentals of Power Electronics", 2nd Edn., Norwell, M.A., Springer, 2001.

Eskom standards division. 2010. *Grid Interconnection of Embedded Generation, Part 2: Small-scale embedded generation, NRS 097-2-1: 2010*.

Eskom, 2008. *Distribution Standard for the Interconnection of Embedded generation*. Eskom's guideline document, DST 34-1765. [Online]. Available at: http://www.eskom.co.za/content/DST34-1765r0EGInterconnectionStandard.pdf. Accessed February 5, 2011.

Esram, T. & Chapman, P.L. 2007. "Comparison of Photovoltaic Array Maximum Power Point Tracking Techniques", *in Energy Conversion, IEEE Transactions on*, vol. 22, no. 2, pp.439-449, June 2007.

Esram, T., Kimball, J.W., Krein, P.T., Chapman, P.L. & Midya, P., "Dynamic Maximum Power Point Tracking of Photovoltaic Arrays Using Ripple Correlation Control," *IEEE Trans. Power Electron., vol.21, no.5, pp1282-1291*, Sept. 2006.

Eurelectric, "Active Distribution System Management: A key tool for the smooth integration of distributed generation," www.eurelectric.org/media/74356/asm_full_report_discussion_paper_final-2013-030-0117-01-e.pdf. [May 01, 2015].

Evju, S.E. 2007. "Fundamentals of grid-connected photovoltaic power electronic converter design", Master Thesis, Norwegian University of Science and Technology.

FAA, 2012. "Helicopter Flying Handbook, Chapt. 2: Aerodynamics of Flight", *FAA-H-8083-21A, US Department of Transportation, Federal Aviation Administration, AFS-630, Oklahoma City*.

Femia, N., Petrone, G., Spagnuolo, G. & Vitelli, M. "Optimization of perturb and observe maximum power point tracking method," IEEE Trans. Power Electron., vol. 20, no. 4, pp. 963–973, Jul. 2005.

Fox, B., Flynn, D., Bryans, L., Jenkins, N., Milborrow, D., O'Malley, M., Watson, R. & Anaya-Lara, O., "Wind Power Integration: connection and system operational aspects", *The Institution of Engineering and Technology*, London, 2007.

Friedman, N.R. 2000. "Microturbine Technology & Business Developments", presentation at the *World Energy Engineering Congress 2000*, Atlanta, Georgia.

Frohr, F. & Orttenburger, F. 1982. 1982. "Introduction to Electric Control Engineering*",* Berlin &

Munchen: Heyden & Son Ltd., London.

Gao, F. & Iravani, R. “A Control Strategy for a Distributed Generation Unit in Grid-Connected and Autonomous Modes of Operation”, *IEEE Transactions on Power Delivery*, vol.23, no.2, April 2008.

Gardner, F.M. 1967. “Phase lock techniques”, 2nd Edition, Wiley, New York.

Gellings, C.W. 2009. “The Smart Grid: Enabling Energy Efficiency and Demand Response”, Fairmont Press, Lilburn, GA.

*Global Wind Report. Annual Market Update* 2012 (2013), GWEC. Available at: http://www.gwec.net/wp-content/uploads/2012/06/Annual_report_2012_LowRes.pdf. Accessed April 03 2014.

Goldstein, L., Hedman, B., Knowles, D., Freedman, S.I., Woods R. & Schweizer, T., ";Gas-fired distributed energy resource technology characterizations," *National Renewable Energy Laboratory*, *NREL/TP-620-34783*, Nov. 2003.

Gomathy, S., Saravanan, S. & Thangavel, S., “Design and Implementation of Maximum Power Point Tracking (MPPT) Algorithm for a Standalone PV System,” *International Journal of Scientific & Engineering Research, vol.3, Issue 3*, March 2012.

Gonzalez, L.G., Figueres, E., Garcera, G. & Carranza, O., “Dynamic Response Analysis of Small Wind Energy Conversion Systems (WECS) operating with Torque Control versus Speed Control,” Int. Conf. on Renewable Energies and Power Quality (ICREPQ’09), 15-17 April 2009.

Gow, J.A. & Manning, C.D., “Development of a photovoltaic array model for use in Power Electronics simulation studies,” *IEE Proceedings on Electric Power Applications*, vol.146, no.2, pp.193-200, March 1999.

Green, M.A., “Photovoltaic Principles,” *Physica E: Low-dimension Systems and Nanostructures, vol.14.*, April 2002, pp.11-17.

Gu, H., Yang, Z., Wang, D. & Wu, W., "Research on Control Method of Double-Mode Inverter with Grid-Connection and Stand-Alone," *CES/IEEE 5th* International *Power Electronics and Motion Control Conference, IPEMC* , vol.1, pp.1-5, 14-16 Aug. 2006.

Gundtoft, S. 2009. “Wind Turbines”, *University College of Aarhus, Denmark*.

Gupta, J. & Kumar, A., “Fixed-Pitch Wind Turbine-Based Permanent Magnet Synchronous Machine Model For Wind Energy Conversion Systems,”, *Journal of Engineering and Technology, vol.2, issue 1*, Jan-Jun. 2012.

Hansen, A.D., Soeren, P., Hansen, L.H. & Bindner, H., “Models for a Stand-Alone PV System,” *RISOE-R-1219 (EN)/SEC-R-12*, Dec. 2000.

Hansen, W.C., Luketa-Hanlin, A. & Stein, J.S., “Sensitivity of Single-diode Models for Photovoltaic Modules to Method Used for Parameter Estimation,” *28th European Photovoltaic Solar Energy Conference, Paris, France*, 2013.

Hersch, P. & Zweibel, K., “Basic Photovoltaic Principles and Methods,” *Golden, Colorado: Solar Energy Research Institute (SERI), Technical Information Office*, 1982.

Hetthéssy J., Barta A., & Bars R. 2004. “Dead beat controller design”, *Ebook, 2004*.

Hirsh, R.F., Sovacool, B.K. & Badinelli, R.D. 2005. “*Distributed Generation and Momentum Change in the American Utility System: A Social-science systems Approach*”, [online]. Available at: http://www.history.vt.edu/Hirsh/NSF-chapter-Hirsh-ver6-combined.pdf. Accessed March 26, 2014

Hohm, D.P. & Ropp, M.E., “Comparative Study of Maximum Power Point Tracking Algorithms Using an Experimental, Programmable, Maximum Power Point Tracking Test Bed,” *Progress in Photovoltaics: Research and Applications, vol.11, pp47-62,* 2003.

Holtz, J. 1992. “Pulsewidth modulation-A survey”, *IEEE Transactions on Industrial Electronics, vol. 39, No. 5*.

House of Commons. 2008. “Renewable electricity-generation technologies”, Fifth Report of Session 2007-08, Volume I, *Innovation, Universities, Science and Skills Committee*.

Hudson, R.M, Behnke, M.R., West, R., Gonzalez, S. & Ginn, J. 2002. "Design considerations for three-phase

grid connected photovoltaic inverters," *Photovoltaic Specialists Conference, 2002. Conference Record of the Twenty-Ninth IEEE* , vol., no., pp.1396,1401, 19-24 May 2002.

Hughes, T.P., "Networks of Power: Electrification in Western Society, 1880-1930," Johns Hopkins University Press, Baltimore 1983.

Huskey, A., Bowen, A. & Jager, S., "Wind turbine generator system power performance test report for the Gaia-Wind 11-kW wind turbine," *Technical Report NREL/TP-500-46151*, December 2009.

IEA Wind. 2013. "*Long-term research and development needs for the time-frame 2012-2030*", available at: http://www.ieawind.org/index_page_postings/100313/IEA%20Long%20Term%20R_D_Approved%20July%2023%202013.pdf. Accessed April 02 2014.

IEA. 2002. "Distributed Generation in Liberalized Electricity Markets", International Energy Agency, Paris, France.

IEC, 2011. "Electrical energy storage white paper", *The International Electrotechnical Commission, Geneva*.

IEEE Std 929-2000, *IEEE Recommended Practice for Utility Interface of Photovoltaic (PV) Systems*, April 2000.

*IEEE std. P1547.2*. 2008. "Draft Application Guide for IEEE Standard 1547, Interconnecting Distributed Resources with Electric Power Systems".

IEEE. 2003. "IEEE Standard for Interconnecting Distributed Resources with Electric Power Systems", *IEEE Std. 1547-2003*.

IET. 2009. "Fuel cells", *The Institution of Engineering and Technology*, available at: http://www.theiet.org/factfiles/energy/fuel-cells-page.cfm. Accessed April 03, 2014.

Jenkins, N., Ekanayake, J.B. & Strbac, G. 2010. "Distributed Generation", IET, London.

Kachhiya, K., Lokhande, M. & Mukesh, P., "Matlab/Simulink Model of a Solar PV Module and MPPT Algorithm*," Proc. Nat. Conf. Recent Trends in Eng. & Tech.*, 2011.

Kalmikov, A. & Dykes, K. 2010. *Wind Power Fundamentals*. http://web.mit.edu/windenergy/windweek/Presentations/Wind%20Energy%20101.pdf. [May 19, 2015].

Kariniotakis, G.N., Soultanis, N.L., Tsouchnikas, A.I., Papathanasiou, S.A. & Hatziargyriou, N.D., "Dynamic modeling of microgrids," *Int. Conf. on Future Power Systems*, 18 November 2005.

Kawabata, T., Miyashita, T. & Yamamoto, Y., "Dead beat control of three phase PWM inverter," *IEEE Transactions on Power Electronics, vol.5, no.1*, Jan. 1990.

Kazmierkowski, M. & Malesani, L. 1998. "Current control techniques for three-phase voltage-source PWM converters: A survey", *IEEE Transactions on Industrial Electronics, vol. 45, No. 5, October 1998*.

Keller, J. & Kroposki, B, "Understanding fault characteristics of inverter-based distributed energy resources", Tech. Rep. NREL/TP-550- 46698, *National Renewable Energy Laboratory*, January 2010.

Kesraoui, M., Korichi, N. & Belkadi, A., "Maximum power point tracker of wind energy conversion systems," *Renewable Energy Journal, vol.36, pp.2655-2662, Elsevier*, 2011.

Kim, J.E. & Hwang, J.S. 2000. "Islanding detection method of distributed generation units connected to power distribution system," *in Proc. 2000, IEEE Power System Technology Conference, pp. 643-647*.

Kim, S-E., Mun Song, B. & Lee, K.Y., "Modeling and Analysis of a Grid-Connected Wind Energy Conversion System Using PSCAD/EMTDC," *Innovative Smart Grid Technologies (ISGT), pp.1-6*, 2010.

Kim, S-K., Jeon, J-H., Cho, C-H., Ahn, J-B. & Kwon, S-H., "Dynamic modeling and control of a grid-connected hybrid generation system with versatile power transfer", *IEEE Transactions on Industrial Electronics, vol. 55, No.4*, April, 2008.

King, D.L., Dudley, J.K., Kratochvil, J.A. & Boyson, W.E., "Temperature coefficients for PV modules and arrays: measurement methods, difficulties, and results," in *Proceedings, 25th IEEE Photovoltaics Specialist Conference*, 1997, pp.1183-1186.

Kiran, N., Kumar, V.A. & Dhanamjaya, A.R., "Design of quadratic optimal regulator system for state space model of single-phase inverter both in standalone and grid-tie modes," *Bulletin of Electrical Engineering and Informatics, vol.3, no.4, pp.265-272*, December 2014.

Kobayashi, K., Takano, I. & Sawada, Y., "A study on a two stage maximum power point tracking control of a photovoltaic system under partially shaded insolation conditions," *IEEE Power Engineering Society General Meeting*, 2003, pp. 2612–2617.

Kramer, W., Chakraborty, S., Kroposki, B. & Thomas, H. 2008. "Advanced power electronic interfaces for distributed energy systems", *NREL/TP-581-42672 Technical Report.*

Kroposki, B., Pink, C., DeBlasio, R, Thomas, H., Simoes, M. & Sen, P.K. 2006. "Benefits of power electronic interfaces for distributed energy systems," *Power Engineering Society General Meeting, 2006. IEEE*, vol., no., pp.8.

Labouret, A. & Villoz, M., "Solar Photovoltaic Energy", 4th Ed., *The Institution of Engineering and Technology*, London, 2010.

Lasseter, R.H. 2002. "MicroGrids," *Power Engineering Society Winter Meeting, 2002. IEEE* , vol.1, no., pp.305,308 vol.1, 2002.

Leithead, W.E, de la Salle, S. & Reardon, D., "Role and Objectives of Control for Wind Turbines," in in *IEE Proceedings, Generation, Transmission and Distribution, vol.138, no.2, pp.135-148*, Mar. 1991.

Leithead, W.E. & Dominguez, S., "Coordinated Control Design for Wind Turbine Systems," *Proc. EWEC 2006*, Athens.

Lettl, J., Bauer, J. & Linhart, L. 2011. "Comparison of different filter types for grid connected inverter", PIERS Proceedings, Marrakesh, Morocco.

Li, H., Chen, Z. & Pedersen, J.K., "Optimal Power Control Strategy of Maximizing Wind Energy Tracking and Conversion for VSCF Doubly Fed Induction Generator System," in *International Power Electronics and Motion Control Conference, IPEMC, vol.3, pp.1-6*, 14-16 Aug. 2006.

Li, X., Shadmand, M.B., Balog, R.S. & Abu Rub, H., "Model Predictive Decoupled Power Control for Single-phase Grid-tie Inverter", *IEEE Power and Energy Conference at Illinois (PECI)*, pp.1-7, 2015.

Liserre, M., Blaabjerg, F. & Hansen, S. 2005. "Design and control of an LCL-filter-based three-phase active rectifier", *IEEE Transactions on Industry Applications, vol. 41, No. 5.*

Liserre, M., Sauter, T. & Hung, J.Y. 2010. *"Future Energy Systems: integrating renewable energy systems into the smart power grid through industrial electronics", IEEE Industrial Electronics Magazine, March 2010.*

Liu, S., Zhu, W. & Xing, B., "A Model Predictive Control Scheme for Parallel-connected Inverter-based Distributed Generation in Microgrids", *23rd Mediterranean Conference on Control and Automation (MED)*, 16-19 June, 2015, Torremolino, Spain.

Liu, S.M., Bi, T.S., Xue, A.C. & Yang, Q.X., "An optimal method for designing the controllers used in grid-connected PV systems," *International Conference on Power Systems Technology (POWERCON), pp.1-6*, Oct. 30-Nov.2 2012.

Loh, P.C., Newman, M.J., Zmood, D.N. & Holmes, D.G., "A comparative analysis of multi-loop voltage regulation strategies for single and three-phase UPS systems," *IEEE Transactions on Power Electronics, vol.18, no.5*, September 2003.

Lopes, J.A.P., Moreira, C.L., & Madureira, A.G., "Defining control strategies for MicroGrids islanded operation," in *Power Systems, IEEE Transactions on*, vol.21, no.2, pp.916-924, May 2006.

Lorenz, R.D. & Lawson, D.B. 1987. "Performance of feedforward current regulators for field oriented induction machine controllers," *IEEE Trans. Ind. Applicat.*, vol. IA-23, pp. 597–602, July/Aug. 1987.

Lorenzo, E. 1994. "Solar electricity: engineering of photovoltaic systems", Artes Graficas Gala, S.L., Spain.

Louzazni, M. & Aroudam, E., "State feedback linearization control approach of three-phase photovoltaic

inverter," *International Journal of Innovation and Applied Studies, vol.8, no.3, pp.1377-1389,* Sept. 2014.

Luna-Rubio, R., Trejo-Perea, M., Vargas-Vazquez, D. & Rios-Moreno, G.J., "Optimal sizing of renewable hybrids energy systems: a review of methodologies", *Solar Energy, 86*, pp.1077-1088, 2012.

Lupu, L., Boukhezzar, B. & Siguerdidjane, H., "Pitch and Torque Control Strategy for Variable Speed Wind Turbines," in *European Wind Energy Conference Proceedings, Athens, Greece*, 2006.

Mahat, P., Chen, Z. & Bak-Jensen, B. 2008. "Review of islanding detection methods for distributed generation," *Electric Utility Deregulation and Restructuring and Power Technologies, 2008. DRPT 2008. Third International Conference on* , vol., no., pp.2743,2748, 6-9 April 2008.

Maknouninejad, A., Godoy Simoes, M. & Zolot, M., "Single phase and three phase P+Resonant based grid connected inverters with reactive power and harmonic compensation capabilities," *IEEE International Conference on Electric Machines and Drives, IEMDC'09, pp.385-391*, 3-6 May 2009.

Maknouninejad, A., Kutkut, N., Batarseh, I., Zhihua, Q. & Shoubaki, E. 2011. "Detailed analysis of inverter linear control loops design". *In: IEEE Twenty-Sixth Annual Applied Power Electronics Conference and Exposition (APEC).*

Manwell, J.F., McGowan, J.G. & Rogers, A.L., "Wind energy explained: theory, design and application", 1st Ed., John Wiley & Sons Ltd., Amherst, 2002.

Markvart, T. & Castañer, L. (eds), "Practical Handbook of Photovoltaics: fundamentals and applications," Elsevier, Oxford, UK, 2003.

Martin, J. 2009. "Distributed vs. Centralized Electricity Generation: Are We Witnessing a Change of Paradigm? An Introduction to Distributed Generation". HEC, Paris.

Martinez, J. 2007. "Modeling and control of a wind turbine", Master Thesis, Imperial College London, 2007.

Marwali, M.N. & Keyhani, A. 2004. "Control of distributed generation systems-Part I: Voltages and currents control," *Power Electronics, IEEE Transactions on* , vol.19, no.6, pp.1541,1550, Nov. 2004.

Massawe, H.B. 2013. "Grid connected photovoltaic systems with SmartGrid functionality", Masters thesis, Norwegian University of Science and Technology.

Mathworks, 2013. SimPowerSystems (PLL (3ph)), Documentation Centre, 2013.

MathWorks®, 2010. "SimPowerSystems™ 5: User's Guide", *The MathWorks, Inc., Natick, Massachusetts, USA.*

Mauri, M., Frosio, L. & Marchiegiani, G. 2011. "Integration of hybrid distributed generation units in power grid, Electrical generation and distribution systems and power quality disturbances", InTech.

Midya, P., Krein, P.T., Turnbull, R.J., Reppa, R. & Kimball, J., "Dynamic maximum power point tracking for photovoltaic applications," in *Proc. 27th Annu. IEEE Power Spec. Conf.*, pp.1710-1716, 1996.

Milosevic, M. 2003. "Decoupling control of d and q current components in three-phase voltage source inverter", ETH, Zurich.

Mohan, N., Undeland, T. & Robbins, W., "Power Electronics: Converters, Applications, and Design", 3rd Ed., New Jersey, John Wiley & Sons Inc., 2003.

Monreal, J., Benítez, I., Morena, L., Lluna, A. & Díaz, I. 2009. "A review of linear advanced current control techniques for grid connected PV inverters", *International Conference on Renewable Energies and Power Quality (ICREPQ'10), March 2009*.

Muljadi, E. & Butterfield, C.P., "Pitch-controlled variable-speed wind turbine generation," IEEE Trans. Ind. Applicat., vol.37, pp.240-246, 2001.

Neacsu, D.O. 2001. "Space vector modulation- An introduction", *Tutorial at IECON'01, 27th Annual Conference of the IEEE Industrial Electronics Society, 2001*.

Nehrir, M.H., Wang, C., Strunz, K., Aki, H., Ramakumar, R., Bing, J., Miao, Z. & Salameh, Z. 2011. "A Review of Hybrid Renewable/Alternative Energy Systems for Electric Power Generation: Configurations, Control, and

Applications," *Sustainable Energy, IEEE Transactions on* , vol.2, no.4, pp.392,403, Oct. 2011.

Nigim, K.A. & Hegazi, Y.G. "Intentional Islanding of Distributed Generation for Reliability Enhancement", *International Symposium on Quality and Security of Electric Power Delivery Systems*, Oct. 8-10, pp.208-213, 2003.

Nise, N.S. 2004. "Control systems engineering", 4th ed., John Wiley & Sons, Inc., New Jersey.

Novak, P., Ekelund, T., Jovik, I. & Schmidtbauer, B., "Modeling and control of variable-speed wind-turbine drive-system dynamics," in *Control Systems, IEEE*, vol.15, no.4, pp.28-38, Aug. 1995.

Novak, P., Jovik, I. & Schmidtbauer, B., "Modeling and identification of drive-system dynamics in a variable-speed wind turbine," *Proceedings of the Third IEEE Conference on Control Applications, vol.1, pp.233-238, 24-26* August 1994.

Ogata, K., "Modern Control Engineering", 4th Ed., New Jersey, Prentice Hall, 2001.

O'Kane, P. & Fox, B. 1997. "Loss of mains detection for embedded generation by system impedance monitoring," *in Proc. Sixth International Conference on Developments in Power System Protection, pp. 95-98, March 1997*.

Omari, O., Ortjohann, E., Mohd, A. & Morton, D. 2007. "An Online Control Strategy for DC Coupled Hybrid Power Systems," *Power Engineering Society General Meeting, 2007. IEEE* , vol., no., pp.1,8, 24-28 June 2007.

Óskardottir, M.Ó. 2014. "A General Description and Comparison of Horizontal Axis Wind Turbines and Vertical Axis Wind Turbines", Master Thesis, University of Iceland.

Osorio, C. 2011. "Modeling and simulation of PV power inverters". *Webinar*.

Pao, L.Y. & Johnson, K.E., "A Tutorial on the Dynamics and Control of Wind Turbines and Wind Farms," *2009 American Control Conference, St. Louis, MO, USA*, June 10-12 2009.

Patel, R.M. 2006. "Wind and solar power systems: design, analysis and operation", 2nd Ed., CRC Press.

Peas Lopes, J.A., Moreira, C.L., & Madureira, A.G., "Defining control strategies for MicroGrids islanded operation," in *Power Systems, IEEE Transactions on*, vol.21, no.2, pp.916-924, May 2006.

Peña, R. & Medina, A. 2010. "Capacity estimation methods applied to mini hydro plants", in *Distributed Generation*, In-Tech, Vukovar.

Pepermans, G., Driesen, J., Haeseldonckx, D., D'haeseleer, W. & Belmans, R. (2003). "Distributed generation: definition, benefits and issues".

Perdana, A., "Dynamic models of wind turbines", Ph.D. dissertation, Chalmers University of Technology, Gottenberg, Sweden, 2008.

Price, A. 2000. "The future of energy storage in a deregulated environment", *Panel session at IEEE, PES Summer Meeting*, 16-20 July 2000, Seattle, Washington.

Prodanovic, M. & Green, T.C. 2003. "Control and filter design of three-phase inverters for high-power quality grid connection", *IEEE Transactions on Power Electronics, vol. 18, No. 1*.

Ragheb, M., "Components of wind machines", [online], available at: http://mragheb.com/NPRE%20475%20Wind%20Power%20Systems/Components%20of%20Wind%20Machines.pdf., accessed May 01, 2015.

Resource Dynamics Corporation. 2005. "Distributed Generation: Technologies", [online]. Available at: www.distributed-generation.com/technologies.htm. Accessed May 24, 2012.

Reznik, A. 2013. "Analysis and design of a smart-inverter for renewable energy interconnection to the grid", Masters Thesis, *Colorado School of Mines*.

Rocabert, J., Luna, A., Blaabjerg, F. & Rodríguez, P. 2012. "Control of power converters in AC microgrids", *IEEE Transactions on Power Electrnics, vol. 27, No. 11, November 2012*.

Rogner, H.H. 2012. "World energy demand and supply", *International Atomic Energy Association*, [online].

Available at: http://www.iaea.org/nuclearenergy/nuclearknowledge/schools/NEM-school/2012/AbuDhabi/PDFs/day1/04_Rogner_World_Energy_D%26S.pdf. Accessed March 26, 2014.

Ropp, M.E., Begovic, M., Rohatgi, A., Kern, G. & Bonn, R. 2000. "Determining the relative effectiveness of islanding detection methods using phase criteria and non-detection zones," *IEEE Transaction on Energy Conversion, vol. 15, no. 3, pp. 290-296, Sept. 2000*.

RTDS Technologies, 2006. "Small Time-step Simulation: An Introductory Tutorial", *VSC Small Times-step Modeling Manual, Winnipeg, Manitoba, Canada*.

Salameh, Z.M. & Davis, A.J. 2003. "Case study of a residential-scale hybrid renewable energy power system in an urban setting," *Power Engineering Society General Meeting, 2003, IEEE* , vol.4, no., pp.,2322 Vol. 4, 13-17 July 2003.

Salhi, M. & El-Bachtri, R., "Maximum Power Point Tracker for Using Fuzzy Control for Photovoltaic System," *International Journal of Research and Reviews in Electrical and Computer Engineering, vol.1, no.2, pp.69-75*, June 2011.

Santosh, B.R., Kumar, V. & Sumathi, S., "Implementation of Perturb & Observe and Fuzzy logic Control MPPT of PV System Uisng SEPIC Converter," *International Journal of Innovative Science, Engineering & Technology (IJISET), vol.1, Issue 4*, 2014.

Schoeman, J.J. & van Wyk, J.D. 1982. "A simplified maximal power controller for terrestrial photovoltaic panel arrays," *Proceedings of the 1982 Power Electronic Specialists Conference (PESC)*, pp. 361 - 367.

Schubel, J.P. & Crossley, J.R. 2012. "Wind Turbine Blade Design", Energies 2012, vol.5, pp.3425-3449. www.mdpi.com/journal/energies. [May 01, 2015].

Sera, D., Teodorescu, R. & Rodriguez, P., "PV panel model based on datasheet values," in *Proc. IEEE International Symposium on Industrial Electronics (ISIE)*, pp.2392-2396, 2007.

Servansing, A., Pahlevaninezhad, M. & Jain, P.K., "A review of hybrid distributed generation systems," *IEEE 34th International Telecommunications Energy Conference (INTELEC)*, 2012.

Sharifzadeh, M.E. & Jalilian, A., "Investigation of Small Signal Dynamics of Inverter-Based Distributed Generation in Grid-Connected and Autonomous Modes of Operation", *2nd Power Electronics, Drive Systems and Technologies Conference, IEEE*, 2011.

Sharma, P. & Agarwal, V. 2008. "Optimization of Operational Energy Cost in a Hybrid Distributed Generation System," *Industrial and Information Systems, ICIIS 2008. IEEE Region 10 and the Third international Conference on*, vol., no., pp.1,6, 8-10 Dec. 2008.

Singh, M. & Santoso, S. "Dynamic models for wind turbines and wind power plants". *Subcontract report to NREL, The University of Texas at Austin*, October 2011. http://www.nrel.gov/docs/fy12osti/52780.pdf. [May 18, 2015].

Slootweg, J.G., de Haan, S.W.H., Polinder, H. & Kling, W.L., "General Model for Representing Variable Speed Wind Turbines in Power System Dynamics Simulations," *IEEE Transactions on Power Systems, vol.18, no.1*, 2003.

Sozer, Y & Torrey, D.A., "Modeling and Control of Utility Interactive Inverters," *IEEE Transactions on Power electronics, vol.24, no.11*, Nov. 2009.

Srinivas, C.H. & Reddy, M.R.P., "Control of grid-connected and intentional islanding operations of photovoltaic system," *International Journal of Electrical, Electronics and Telecommunications Engineering, vol.44, Special Issue 3*, 2013.

Strauss, P. & Engler, A. 2003. "AC coupled PV hybrid systems and microgrids-state of the art and future trends," *Photovoltaic Energy Conversion, 2003. Proceedings of 3rd World Conference on* , vol.3, no., pp.2129,2134 Vol.3, 18-18 May 2003.

Sun, Z. & Zhang, X.-y., "Advances on distributed generation technology," *Int. Conf. on Elec. Power & Energy*

*Systems, Energy Procedia 17*, pp.32-38, 2012.

Swiegers, W. & Ensling, J.H.R., "An integrated maximum power point tracker for photovoltaic panels," *IEEE Int. Symp. Indust. Electron., ISIE '98, vol.1, pp.40-44*, 7-10 July 1998.

Tafticht, T. & Agbossou, K., "Development of a MPPT method for photovoltaic systems," Canadian Conference on Electrical and Computer Engineering, pp. 1123– 1126, 2004.

Teachergeek, 2006. *Wind Turbine Types*. http://www.teachergeek.org/wind_turbine_types.pdf. [May 15, 2015]

Teja, R.S. 2013. "Analysis of grid synchronization techniques for distributed generation system during grid abnormalities", MTech thesis, National Institute of Technology, Rourkela, India.

Teodorescu, R. & Blaabjerg, F., "Flexible Control of Small Wind Turbines with Grid failure Detection Operating in Stand-Alone and Grid-Connected Mode", *IEEE Transactions on Power Electronics*, vol.19, no.5, September, 2004.

Teodorescu, R., Blaabjerg, F., Liserre, M. & Loh, P.C., "Proportional-resonant controllers and filters for grid-connected voltage-source converters," *Electric power Applications, IEE Proceedings, vol.153, no.5, pp.750-762*, Sept. 2006.

Teodorescu, R., Liserre, M. & Rodrígues, P. 2011. "Grid Converters for Photovoltaic and Wind Power Systems", John Wiley & Sons, Ltd, West Sussex.

Thiringer, T. & Linders, J., "Control by Variable Rotor Speed of a Fixed-Pitch Wind Turbine Operating in a Wide Speed Range," *IEEE Transactions on Energy Conversion, vol.8, no.3*, Sept. 1993.

Tian, B., Mao,C., Lu, J., Wang, D., He, Y. & Zhou, B., "Seamless transfer control strategy for grid-interactive inverters," *Electric Power Components and Systems, vol.42, pp.1587-1597*, 2014.

Timbus, A., Liserre, M., Teodorescu, R. & Blaabjerg, F. 2005. "Synchronization methods for three phase distributed power generation systems - An overview and evaluation," *Power Electronics Specialists Conference, 2005. PESC '05. IEEE 36th* , vol., no., pp.2474,2481, 16-16 June 2005

Timbus, A., Liserre, M., Teodorescu, R., Rodriguez, P. & Blaabjerg, F. 2009. "Evaluation of current controllers for distributed power generation systems", *IEEE, Transactions on Power Electronics, vol. 24, No. 3, March 2009*.

Tirumala, R., Mohan, N. & Henze, C. 2002. "Seamless transfer of grid-connected PWM inverters between utility-interactive and stand-alone modes," *Applied Power Electronics Conference and Exposition, 2002. APEC 2002. Seventeenth Annual IEEE* , vol.2, no., pp.1081,1086 vol.2, 2002.

Trykozko, R. 1997. "Principles of photovoltaic conversion of solar energy", Opto-Electr. Rev 5., No. 4, 1997.

Twining, E. & Holmes, D.G., "Grid current regulation of a three-phase voltage source inverter with an LCL input filter," *IEEE Transactions on Power Electronics, vol.18, no.3*, May 2003.

UL Std 1741, *Inverters, Converters, and Controllers for Use in Independent Power Systems*, Underwriters Laboratories Inc. US, 2001.

Van Gerwen, R. 2006. "Distributed Generation and Renewables-Introduction", [online]. Available at: www.leonardo-energy.org/files/root/2006/AN_8_1_Introduction-to-distributed-generation-and-renewables.pdf. Accessed May 15, 2012.

van Rooij, R. 2001. "Offshore Wind Farm Energy: Terminology, Reference Systems and Conventions", http://ocw.tudelft.nl/fileadmin/ocw/courses/OffshoreWindFarmEnergy/res00062/Terminology.pdf.

[April 29, 2015].

van Werven, M.J.N. & Scheepers, M.J.J. 2005. "The changing role of distribution system operators in liberalized and decentralizing electricity markets", *Future Power Systems International Conference*.

Villalva, M.G., Gazoli, J.R. & Filho, E.R., "Comprehensive approach to modeling and simulation of photovoltaic arrays," *IEEE Trans. Power Electron., vol.24, no.5*, pp.1198-1208, May 2009.

Vlad, C., Munteanu, I., Bratcu, A.I. & Ceangã, E., "Anticipative Control of Low-power Wind Energy Conversion Systems for Optimal Power Regime," *Control Engineering and Applied Informatics, CEAI, vol.11, no.4, pp.26-35*, 2009.

Walker, G. 2001. "Evaluating MPPT converter topologies using a Matlab PV model", J Electr. Electron Eng Aus, 21 (1): 45-55.

Wang, C. 2006. "Modeling and control of hybrid wind/photovoltaic/fuel cell distributed generation systems", PhD Thesis, Montana State University.

Wang, C., Nehrir, H., Lin, F. & Zhao, J. 2010. "From hybrid energy systems to microgrids: Hybridization techniques, configuration, and control," *Power and Energy Society General Meeting, 2010 IEEE* , vol., no., pp.1,4, 25-29 July 2010.

Wang, C.S., Li, X.L., Guo, L. & Li, Y.W., "A seamless operation mode transition control strategy for a microgrid based on master-slave control," *Science China Technological Sciences, vol.55, no.6, pp.1644-1654*, June 2012.

Wasynczuk, O., Man, D. & Sullivan, J., "Dynamic behavior of a class of wind turbine generators during random wind fluctuations," *IEEE Transactions on Power System Apparatus and Systems*, vol.PAS-100, no.6, pp. 2837-2845, Jun. 1981.

Weiler, S. 2014. "From Smart Grids to the Internet of Energy," Master Thesis, York University, Ontario, Canada.

Wheeler, M., Cunningham, J. & Rockwell, S. "'The History of Alternating Current," [online]. Available at: http://www.edisontechcenter.org/AC-PowerHistory.html. Accessed May 01, 2015.

Wichert, B. 1997. "PV-Diesel hybrid energy systems for remote area power generation –a review of current practice and future developments", in *Renewable and sustainable energy reviews*, vol., 1, NO. 3, pp. 209-228.

Xiao, W. & Dunford, W.G. 2004. "A modified adaptive hill climbing MPPT method for photovoltaic power systems," in *Proc. 35th Annu. IEEE Power Electron. Spec. Conf.*, 2004, pp. 1957–1963.

Xiao, W., Dunford, W.G. & Capel, A., "A novel modeling method for photovoltaic cells," *in Proc. IEEE 35th Annual Power Electronics Specialist Conference (PESC)*, vol.3., pp.1950-1956, 2004.

Xu, W., Mauch, K., and Martel, S. 2004. "An Assessment of DG Islanding Detection Methods and Issues for Canada", *Report # CETC-Varennes 2004-074 (TR), CANMET Energy Technology Centre – Varennes, Natural Resources Canada, July 2004, 53 pp*.

Xue, Y., Chang, L., Kjaer, B.S., Bordonau, J. & Shimizu, T. 2004. "Topologies of signle-phase inverters for small distributed power generators: an overview", *Power Electronics, IEEE Transactions on*, vol. 19, no. 5, pp. 1305-1314.

Yazdani, A. & Iravani, R. 2010. "Voltage-Sourced Converters in Power Systems: modeling, control and applications", John Wiley & Sons, Inc., New Jersey.

Ye, Z., Walling, R., Garces, L., Zhou, R., Li, L. & Wang, T. 2004. "Study and Development of Anti-islanding Control for Grid-connected Inverters," *National Renewable Energy Laboratory, Golden, CO, Rep. SR-560-36243, May 2004*.

Ying-Yi, H., Shiue-Der, L. & Ching-Sheng, C., "MPPT for PM wind generator using gradient approximation," *Energy Conversion and Managament, vol.50, pp.82-89, Elsevier*, 2009.

Yuan, X., Merk, W., Stemmler, H. & Allmeling, J. 2002. "Stationary-frame generalized integrators for current control of active power filters with zero steady-state error for current harmonics of concern under unbalanced and distorted operating conditions" *IEEE Transactions on Industrial Applications, vol. 38, no. 2, Mar./Apr. 2002*.

Zeineldin, H., El-Saadany, F. & Salama, M.M.A. "Intentional Islanding of Distributed Generation," in *Proc. IEEE Power Eng. Soc. Gen. Meeting*, vol.2, pp.1496-1502, 2005.

Zeineldin, H., Marei, M.I., El-Saadany, E.F. & Salama, M.M.A., "Safe controlled islanding of inverter based distributed generation," in *Power Electronics Specialists Conference, 2004. PESC 04. 2004 IEEE 35th Annual*, vol.4, pp.2515-2520, 2004.

Zhou, L., Yang, M., Liu, Q. & Guo, K., "New control strategy for three-phase grid-connected LCL inverters without a phase-locked loop," *Journal of Power Electronics, vol.13, no.3*, May 2013.

Zuo, S. & Zhang, X.-y., "Advances on distributed generation technology," *Int. Conf. on Elec. Power & Energy Systems, Energy Procedia 17*, pp.32-38, 2012.

# APPENDIX A: MODEL TRANSFORMATIONS IN THREE-PHASE SYSTEMS

## A.1. Introduction

Because an inverter converts DC voltage and current into AC power, controlling this conversion process implies the control of both DC and AC signals. However, satisfactory *tracking control* of AC signals may necessitate the design of complex, high-order compensators with large bandwidths (Yazdani & Iravani, 2010). Moreover, for a three-phase system, voltage and current control of the AC signals would imply employment of at least six independent controllers (two per phase, for all three phases), which may be undesirable from a design point of view.

One commonly implemented solution to this issue is the transformation of the three-phase system into an equivalent two-phase system, either stationary (Clarke transformation) or rotating (Park transformation). These transformations are based on the fact that a balanced three-phase system has only two independent phase quantities, whereas the third quantity can be expressed in terms of the two independent ones (Evju, 2007).

The concept of axis transformation has its origin in electrical machine theory, where it is effectively utilized to minimize the complexity associated with the modeling and transient simulation of the AC machines having coupled electrical quantities, and enables decoupled control of machine flux and torque (Kramer *et al.*, 2008). Based on the work of Yazdani and Iravani (2010), derivations of the three-axis to two-axis system transformation are presented in this section.

A three-phase signal $V_{abc}(t)$ (using voltage as an instance; all quantities considered are functions of time, the time argument is only omitted for simplicity) can be defined as:

$$V_{abc} = \begin{bmatrix} v_a \\ v_b \\ v_c \end{bmatrix} = V_m \begin{bmatrix} \cos(\omega\omega + \theta) \\ \cos(\omega\omega + \theta - 2\pi/3) \\ \cos(\omega\omega + \theta - 4\pi/3) \end{bmatrix} \quad \text{(A.1)}$$

where $V_{abc}$ is the three-phase voltage, $v_a$, $v_b$ and $v_c$ are the instantaneous phase voltages for phases **A, B** and **C** respectively, $V_m$ is the amplitude of the three-phase voltage, $\omega$ and $\theta$ are the angular frequency and phase angle of the three-phase system respectively. The three-phase system is then expressible in the form of an equivalent space phasor ($\vec{V}$), defined by:

$$\vec{V} = \frac{2}{3}\left[v_a + \alpha v_b + \alpha^2 v_c\right] \quad \text{(A.2)}$$

where $\alpha$ is the phasor rotation operator, defined by:

$$\alpha = e^{j2\pi/3} \tag{A.3}$$

The space phasor expressed by Equation (A.2) is a complex-valued time-varying vector that can be expressed in polar form according to the following expression, valid for a three-phase balanced system with time-invariant angular frequency:

$$\vec{V}(t) = Ve^{j\omega t} \tag{A.4}$$

where:

$$V = V_m \angle \theta \tag{A.5}$$

with $V_m$, $\theta$ and $\omega$ representing the amplitude, phase angle and angular frequency respectively, of the three-phase system.

## A.2 Stationary (αβ) reference frame transformation

The complex-valued space vector representation of a three-phase system defined by Equation (A.2) above can be mapped onto the Cartesian plane, as shown in Figure (A.1), which is effectively a decomposition of the vector into its real and imaginary components as shown in the figure. This two-phase representation is commonly referred to as the αβ-frame representation of a three-phase system.

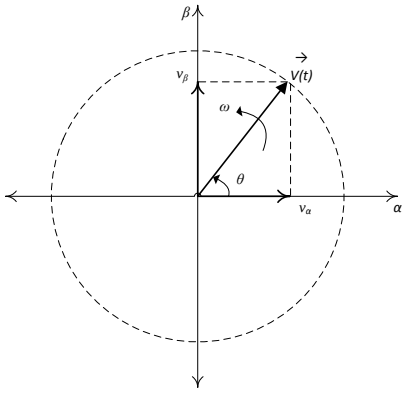


**Figure A.1: Representation of a space phasor in a cartesian coordinate (αβ) system.**

Assuming a symmetrical three-phase system, the mathematical expression for the αβ-frame representation is given by (Yazdani & Iravani, 2010):

$$\vec{V} = v_\alpha + jv_\beta \tag{A.6}$$

where $v_\alpha$ and $v_\beta$ are the real and imaginary (or the alpha- and beta) components of the space phasor respectively. The relation between the components of the space phasor and the phase voltages of the corresponding three-phase system can be expressed in a vector matrix form as:

$$\begin{bmatrix} v_\alpha(t) \\ v_\beta(t) \end{bmatrix} = \frac{2}{3} T_{\alpha\beta} \begin{bmatrix} v_a(t) \\ v_b(t) \\ v_c(t) \end{bmatrix} \tag{A.7}$$

where $T_{\alpha\beta}$ is the model transformation matrix, given by:

$$T_{\alpha\beta} = \begin{bmatrix} 1 & -1/2 & -1/2 \\ 0 & \sqrt{3}/2 & -\sqrt{3}/2 \end{bmatrix} \tag{A.8}$$

The transformation matrix (Equation A.8) is orthonormal. The inverse transformation (*i.e.* αβ-abc) is thus easily accomplished by using the transpose of Equation (A.8) as follows:

$$\begin{bmatrix} v_a(t) \\ v_b(t) \\ v_c(t) \end{bmatrix} = \begin{bmatrix} 1 & 0 \\ -1/2 & \sqrt{3}/2 \\ -1/2 & -\sqrt{3}/2 \end{bmatrix} \begin{bmatrix} v_\alpha(t) \\ v_\beta(t) \end{bmatrix} \tag{A.9}$$

Expressions for the instantaneous real ($P_{\alpha\beta}$) and reactive ($Q_{\alpha\beta}$) power a three-phase system represented in the αβ-frame can also be easily derived from the space-phasor representation of the three-phase system, and are stated below as (voltages and currents being phase-neutral values):

$$P_{\alpha\beta} = \frac{3}{2}[v_\alpha \cdot i_\alpha + v_\beta \cdot i_\beta] \tag{A.10}$$

$$Q_{\alpha\beta} = \frac{3}{2}[-v_\alpha \cdot i_\beta + v_\beta \cdot i_\alpha] \tag{A.11}$$

## A.3. Rotating (dq) reference frame

The αβ-frame representation discussed above is a *stationary* two-axis system. When made to rotate at an angular frequency $\boldsymbol{\omega}$, and having an initial angular position $\boldsymbol{\theta}$, a rotating-frame two-axis system representation is obtained, commonly known as the *dq reference frame*. In a grid-connected system for instance, the angular frequency and phase angle of the dq-frame are typically made equal to (or synchronized with) those of the grid voltages, leading to the common designation of this system as a synchronous reference frame (Teodorescu *et al*., 2011). The signals so synchronized then assume constant values (or become time-invariant) with respect to the grid voltages and currents. In this way, the dq-frame representation effectively serves to transform the system coupled to the grid from a system of time-varying (three-phase) signals into an equivalent system of time-invariant (two-axis) signals. The implication of this transformation is considerable simplification of the analysis and control design of the system.

Both the αβ- and the dq reference frames are projections of the space-phasor vector onto the two-axis Cartesian coordinate system, and are thus easily related to each other mathematically by (Yazdani & Iravani, 2010):

$$V_{dq} = V_{\alpha\beta} e^{-j\theta} \tag{A.12}$$

$$\begin{bmatrix} v_d \\ v_q \end{bmatrix} = \begin{bmatrix} cos(\theta) & sin(\theta) \\ -sin(\theta) & cos(\theta) \end{bmatrix} \begin{bmatrix} v_\alpha \\ v_\beta \end{bmatrix} \tag{A.13}$$

Figure (A.2) provides a graphical depiction of the relation between the αβ- and dq-frame representations, with the d-axis aligned with the space phasor, making the magnitude of the q-axis component null (a technique often applied in the voltage-oriented current control of the grid-connected inverter).

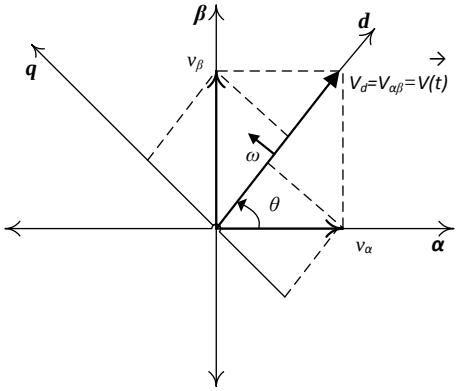


**Figure A.2:** **Graphical representation of the αβ and dq reference systems. (Adapted from Evyu, 2007)**

Obtaining the αβ-frame representation given the dq-frame representation can be accomplished by using Equation (A.13). As with the αβ-frame, the dq-frame can also be directly related to the original three-phase system by:

$$\begin{bmatrix} v_d \\ v_q \end{bmatrix} = \frac{2}{3} T_{dq} \cdot \begin{bmatrix} v_a \\ v_b \\ v_c \end{bmatrix} \tag{A.14}$$

where the transformation matrix ($T_{dq}$) is given by:

$$T_{dq} = \begin{bmatrix} cos(\theta) & cos(\theta - 2\pi/3) & cos(\theta - 4\pi/3) \\ sin(\theta) & sin(\theta - 2\pi/3) & sin(\theta - 4\pi/3) \end{bmatrix} \tag{A.15}$$

As in the case of the αβ-frame, the three-phase system representation may be obtained from the dq-frame representation by multiplying the left-hand-side of Equation (A.14) by the transpose of the matrix expressed in Equation (A.15).

The instantaneous real and reactive power values of the three-phase system expressed in the dq-frame are obtained from the following expressions (voltages and currents being phase-neutral values):

$$P_{dq} = \frac{3}{2}\left[v_d \cdot i_d + v_q \cdot i_q\right] \quad \text{( A.16)}$$

$$Q_{dq} = \frac{3}{2}\left[-v_d \cdot i_q + v_q \cdot i_d\right] \quad \text{( A.17)}$$

# APPENDIX B: INTERCONNECTION REQUIREMENTS FOR GRID INVERTERS

## B.1. Introduction

The necessity of the requirements stipulated for Distributed Generation (DG) in the grid interconnection standards can be understood in the light of the fact that DG systems are largely based on non-conventional technologies from the perspective of electric power generation, and their interaction with the grid may often have an adverse impact on the normal operation of the grid. Most of them have to be interfaced to the grid by means of power electronics interfaces because they generate power at the voltage magnitude and frequency not directly compatible with the grid voltage. These interfaces are also non-conventional from the grid's perspective, and their interaction with the grid often implies operational and protection adjustments. Grid codes are thus there to lay down specifications for the DG in terms of (Teodorescu *et al.*, 2011) (list is representative rather than exhaustive):

- General requirements to be met (such as safety, earthing, galvanic isolation, etc)
- When they may remain connected to the grid and when required to disconnect
- Fault ride-through capabilities (for certainDG systems)
- Anti-islanding prevention and test specifications for satisfying this requirement
- Technical requirements to be met at the point of connection and applicable test specifications
- Power quality (DC current injection, current harmonics) and (often) power factor specifications
- Response to abnormal grid conditions
- Protection reaction time-frame specifications in the event of deviations of voltage and frequency from the nominal values

Many interconnection standards have been developed, both at national and international level, and much effort has been made in recent times to harmonize these standards, so that they both address all the requirements for grid-connected DG systems, and be applicable internationally. The main standards bodies that may be considered to be developing authoritative international grid interconnection requirements are the *Institute of Electrical and Electronics Engineers* (IEEE), the *International Electrotechnical Commission* (IEC), and the *German Commission for Electrical, Electronic and Information Technologies of DIN and VDE* (DKE) (Teodorescu *et al.*, 2011).

These organizations have developed separate standards which, although largely similar in terms of the requirements addressed, may exhibit slight differences in certain definitions, limitations, technical specifications and/or test procedures, among others.

When it comes to the application of these international standards for DG grid integration at national level, local utilities generally adapt the standard specifications to the needs and

requirements of the local grid. The sole electric utility in the *Republic of South Africa* is Eskom, and adheres to the standards developed by the *South African National Standards (SANS)* organization. For the South African electric grid, two documents (yet to be confirmed as national standards) pertaining to the integration of DG into the Eskom grid have thus far been issued, namely:

- DST 34-1765r0-2008, Distribution Standard for the Interconnection of Embedded Generation (Eskom distribution, 2008)
- NRS 097-2-1: 2010, Grid Interconnection of Embedded Generation, Part 2: Small-scale embedded generation (Eskom standards division, 2010)

The *DST 34-1765r0* document, based on an Eskom guideline (ESKAGAA2) that was developed from the British standard *G.59, "Recommendations for the Connection of Private Generating Plant to the Electricity Boards' Distribution Systems*", provides generic interconnection requirements for distributed generation of various technologies that is integrated into the Eskom distribution network. The document states that it is applicable to generation connected to the medium- and high-voltage networks.

In response to requests from small-scale independent power producers for access to the network for their own generation, the document *NRS 097-2-1* has been drafted. It is meant to be the first in a series of three documents providing a framework for the interconnection of small-scale distributed generation (not exceeding 100 kW in capacity) to the low-voltage network (Eskom Standards Division). The *NRS 097-2-1* document focuses on the interface between the utility and the distributed generator, and although aiming to be technology-independent, it is envisaged to be largely applicable to inverter-interfaced generation technologies.

Both the *DST 34-1765* and *NRS 097-2-1* documents are significantly harmonious with the international interconnecting standards, which are discussed further in the following sections, to provide a general overview of interconnection requirements.

## B.2. Main international standards

Some of the main standards that have already been developed and are in application are:

- IEEE 929-2000: Recommended Practices for Utility Interface of Photovoltaic Systems (IEEE, 2000)
- UL 1741: Standard for Inverters, Converters and Controllers for use in Independent Power Systems (Underwriters Laboratories Inc., 2001)
- IEEE 1547-2003: Standard for Interconnecting Distributed Resources with Electric Power Systems (IEEE, 2003)
- IEC 61727: Photovoltaic (PV) Systems-Characteristics of the Utility Interface (IEC, 2004)

- VDE 0126-1-1-2006

The *IEEE 929-2000* standard addresses requirements for residential and other small-scale generation systems with an inverter interface (mainly PV, fuel cells, energy storage and dispersed generation). The same requirements have largely been incorporated into the *UL 1741* standard, which covers grid performance requirements for grid-tied inverters and addresses issues concerning construction, electrical safety as well as the principles found in the *National Electric Code* (NEC).

While the *IEEE 929* and *UL 1741* standards are mainly developed for inverter-interfaced technologies, the *IEEE 1547-2003* standard can be seen as an attempt to devise a single set of interconnection standards stipulating mandatory requirements for the grid integration of all generation technologies, with a maximum capacity of 10 MW. Developed on the foundation of previous *IEEE* and *IEC* interconnection standards, it addresses all the requirements outlined in the previous sub-section that must be covered by an interconnection standard. This is a suite of standards, the various parts dealing with specific aspects of the requirements, and some even providing application guidelines, such as the *IEEE P1547-2* document (2008), which interprets the requirements stipulated in other parts of *IEEE 1547-2003* in terms of how they can practically be realized.

*IEC 61727* is the European standard developed by the technical committee *TC-82* of the *International Electrotechnical Commission* (IEC) for non-islanding inverter-interfaced grid-connected PV systems. It is backed by IEC 62116 (Ed.1), which details the testing procedures for satisfying the requirements stated in IEC 61727.

*VDE 0126-1-1*, the German standard issued by *DKE*, mainly focuses on safety, and stipulates requirements for the protective interface of the grid-connected distributed generation system in terms of how it should react to abnormal voltage magnitude, frequency and current conditions. Requirements for a safety device are also clearly stipulated, which should be able to quickly detect a specified grid impedance jump (indicative of an ensuing grid abnormality) and act to sever the connection between the distributed generation system and the grid (thus implementing islanding prevention).

## B.3. Power quality and protection specifications

Power quality requirements stipulate the nominal ranges within which electrical parameters at the Point of Common Coupling (PCC) of the utility and the distributed generation system are to be constrained under normal operating conditions. These parameters include voltage magnitude, frequency, current magnitude, power factor, as well as such anomalies as voltage flicker, DC current injection and current harmonic distortion.

Protection requirements specify the required reaction times for the interconnection protection following voltage magnitude, frequency and current magnitude deviations from the nominal values that suggest an abnormal grid state, and thus necessitate the severing of the interconnection.

Comparison of the major international interconnection standards in respect of power quality and protection specifications reveals considerable agreement. Such a comparison has been performed for instance by Teodorescu *et al* (2011: 32). Because of this, and in addition with the fact that the technical specifications in *DST 34-1765r0* (Eskom's DG interconnection guideline) harmonize very well with those of the *IEEE 1547-2003* standard, the specifications of *IEEE 1547-2003* are considered as representative in this thesis, and are presented in the following sub-sections.

### B.3.1. Voltage

The voltage ranges for the normal operation of the interconnected distributed generator are specified in *IEEE 1547-2003 §4.2.3*, where the response to abnormal voltage conditions are also specified, in terms of the voltage ranges (as percentage of the base voltage) and the required reaction times of the protection. This is depicted in Table (B.1) (DR stands for "*Distributed Resource*").

Monitoring of each phase-to-phase voltage is specified in the case of a three-phase interconnected generator, in the case where the interface transformer configuration is not *grounded wye-wye*. Any voltage falling out of the nominal range should trigger the disconnection of the interconnected generator within the clearing times as detailed in Table (B.1). Clearing time has been defined as the time between the beginning of the abnormal condition and the interconnected generator ceasing to energize the grid.

**Table B.1**: **Interconnection system response to abnormal voltages**

| Voltage range (% of base voltage [a]) | Clearing time (sec)[b] |
|---|---|
| $V < 50$ | 0.16 |
| $50 \leq V < 88$ | 2.00 |
| $110 < V < 120$ | 1.00 |
| $V \geq 120$ | 0.16 |

[a]Base voltages are the nominal system voltages stated in ANSI C84.1-1995, Table 1.
[b] $DR \leq 30\,kW$, maximum clearing times; $DR > 30\,kW$, default clearing times

### B.3.2. Frequency

The nominal operating range along with reaction times for the system frequency falling out of the nominal range are specified in *IEEE 1547-2003 §4.2.4*. These requirements pertaining to the frequency are shown in Table (B.2). The interconnected generator is required to cease energizing the grid within the clearing times indicated in the table.

It is apparent from the table that the capacity of the interconnected generator has a bearing on the specified response time; the larger the generator, the greater influence it may have on the system's normal behavior, and consequently slightly less stringent requirements (relative to those of smaller generators) may be applied, to enhance system stability. The point is made that where protection settings for non-nominal frequency are adjustable, the settings should be coordinated with the grid.

**Table B.2**: **Interconnection system response to abnormal frequencies**

| DR size | Frequency range (Hz) | Clearing time (sec)[a] |
|---|---|---|
| ≤ 30 kW | > 60.5 | 0.16 |
| | < 59.3 | 0.16 |
| > 30 kW | > 60.5 | 0.16 |
| | < {59.8 – 57.0} (adjustable set point) | Adjustable 0.16 to 300 |
| | < 57.0 | 0.16 |

[a] DR ≤ 30 kW, maximum clearing times; DR > 30 kW, default clearing times.

### B.3.3. DC current

The current injected into the grid by the grid-connected distributed generator is required to limit the DC component to 0.5% of the generator's rated current at the point of generator connection.

### B.3.4. Harmonics

Keeping current harmonic distortion levels in the current injected into the grid by the interconnected generator as low as possible forms a vital part of power quality requirements for grid-integrated distributed generation. This requirement ensures that no adverse effects resulting from poor power quality are propagated into the system. Limits of permissible harmonic distortion in the injected current as defined in *IEEE 1547-2003 §4.3.3* are depicted in Table (B.3). Both total as well as individual current harmonic distortions (for odd harmonics) are specified, as can be deduced from the table.

**Table B.3**: **Maximum harmonic current distortion in percent of current**[a]

| **Individual harmonic order h (odd harmonics)** [b] | $h < 11$ | $11 \le h < 17$ | $17 \le h < 23$ | $23 \le h < 35$ | $35 \le h$ | **Total Demand Distortion (TDD)** |
|---|---|---|---|---|---|---|
| Percent (%) | 4.0 | 2.0 | 1.5 | 0.6 | 0.3 | 5.0 |

[a] I=the greater of the Local EPS maximum load current integrated demand (15 or 30 minutes) without the DR unit, or the DR unit rated current capacity (transformed to the PCC when a transformer exists between the DR unit and the PCC).
[b] Even harmonics are limited to 25% of the odd harmonic limits above

### B.3.5. Reconnection

The interconnected generator may not be energizing the point of common coupling at the instance that grid supply is restored. Reconnection to the grid may only be instituted once both the terminal voltage magnitude and frequency satisfy the nominal operating values as specified in Tables (B.1) and (B.2) respectively.

A delay of at least five minutes between the time that the terminal parameters of the distributed generator fall within the specified nominal ranges and reconnection is stipulated.

## B.4. Anti-islanding requirements

Most interconnection standards do not allow the interconnected generator to continue energizing the PCC in the event that grid supply is lost, whether due to system faults or as a maintenance procedure. The reason for this specification has to do with concern over the safety of grid personnel (who may be unaware of the continued energized state of the grid as they respond to a system disturbance, for instance) as well as prevention of coordination problems between the grid supply and the interconnected generator (Teodorescu *et al.*, 2011).

A situation where the interconnected generator continues to energize the PCC in the absence of grid supply is termed “Islanding”, and prevention of the phenomenon is addressed as *anti-islanding requirements* in the interconnection standards.

The *IEEE 1547-2003/UL 1741* standards specify that the islanded state of the interconnected generator should be detected and the interconnection severed within two seconds of the formation of an island. The corresponding IEC standard (draft standard *IEC 62116-2006*) stipulates a similar requirement as regards the response time of the islanding prevention system.

In terms of testing the anti-islanding system functionality, a resonant RLC circuit resonating at nominal system frequency and having a specified quality factor may be used between the grid supply and the interconnected generator. Further details of the test set-up specifications may be obtained by consulting the standards’ documents.

# APPENDIX C: DATA AND SOFTWARE PROGRAMS FOR CHAPTER 4

## C.1. PV modeling-related information

### C.1.1. Electrical characteristics of the BP MSX 120 PV module

Electrical Characteristics[1]

| | MSX 120 | MSX 110[4] |
|---|---|---|
| Maximum power ($P_{max}$)[2] | 120W | 110W |
| Voltage at $P_{max}$ ($V_{mp}$) | 33.7V | 33.6V |
| Current at $P_{max}$ ($I_{mp}$) | 3.56A | 3.3A |
| Minimum $P_{max}$ | 114W | 105W |
| Short-circuit current ($I_{sc}$) | 3.87A | 3.6A |
| Open-circuit voltage ($V_{oc}$) | 42.1V | 41.6V |
| Temperature coefficient of $I_{sc}$ | (0.065±0.015)%/°C | |
| Temperature coefficient of $V_{oc}$ | -(80±10)mV/°C | |
| Temperature coefficient of power | -(0.5±0.05)%/°C | |
| NOCT[3] | 47±2°C | |
| Maximum system voltage | 600V (U.S. NEC rating)<br>1000V (TÜV Rheinland rating) | |
| Maximum series fuse rating | 20A | |

### C.1.2. Current-voltage curves of the BP MSX 120 PV module

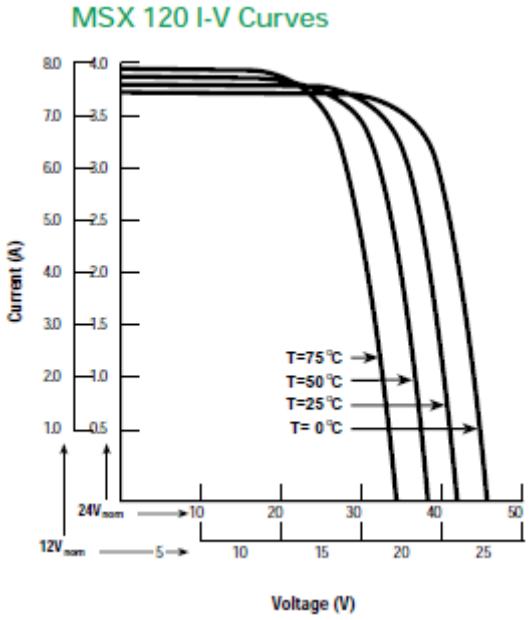


### C.1.3. PV module initialization command for unknown parameter estimation

```
clear Rsa Rpa
clc
Kt=(NCOT-20)/800;              % coefficient of temperature for NCOT
Tref=25;
k=1.3806e-23;                  % Boltzmann constant
q=1.602e-19;                   % electron charge
VTfactor=nCells*nid*k/q;       % diode thermal vooltage factor
```

```
VTref=VTfactor*(Tref+273.2);        % diode thermal voltage at Tref
 % estimation of Rs, Rp
err=1e6;                % tolerance initialization
X(1)=.005*nCells;       % initial value of Rs
X(2)=10*nCells;         % initial value of Rp
 iter=0;                % counts No. of iterations
maxiter=40;             % maximum number of iterations
 while (err>1e-9 && iter<=maxiter)   % loop to compute Rs, Rp
   iter=iter+1;
   x1=X(1);
   x2=X(2);
   % Function definition
   e=exp((Vmpp-Voc+Impp*x1)/VTref);
   f(1)=-Impp+Isc-(Vmpp-x1*(Isc-Impp))/x2-(Isc-(Voc-Isc*x1)/x2)*e;
   f(2)=Isc-(2*Vmpp-Isc*x1)/x2-(1+Vmpp/VTref)*(Isc-(Voc-Isc*x1)/x2)*e;
   %Jacobian matrix elements computation
   J(1,1)=(Isc-Impp)/x2+(Isc/x2-(Isc-(Voc-Isc*x1)/x2)*Impp/VTref)*e;
   J(1,2)=(Vmpp-x1*(Isc-Impp)-(Voc-Isc*x1)*e)/x2^2;
   J(2,1)=Isc/x2-(Isc/x2+(Isc-(Voc-Isc*x1)/x2)*Impp/VTref)*(1+Vmpp/VTref)*e;
   J(2,2)=(2*Vmpp-Isc*x1-(Voc-Isc*x1)*(1+Vmpp/VTref)*e)/x2^2;
   %compute delta (ratio of f to f-prime for each iteration)
   delta=-J\f';
   X=X+delta';     % new values of the variables
   err=sqrt(delta(1)^2+delta(2)^2);
end
 if (iter>maxiter)
   s=sprintf('***Did not converge within %3.0f iterations. Attempt to adjust initial
estimations.***', maxiter);
   disp(s)
end
 Rsa=X(1)*nSer/nPar
Rpa=X(2)*nSer/nPar
VTrefa=VTref*nSer;
Isca=Isc*nPar;
Voca=Voc*nSer;
```

### C.1.4. Simulink implementation of the PV module

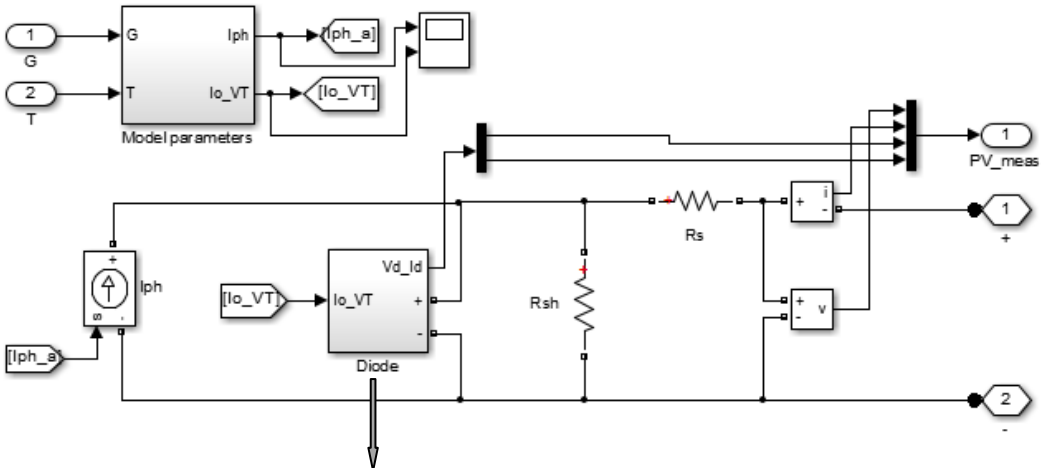


***Diode subsystem***

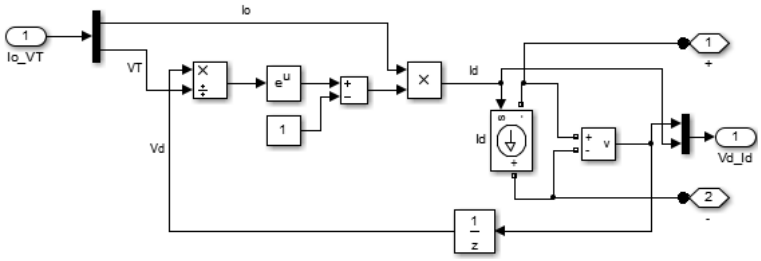


## C.2. WEC system-related information

### C.2.1. Characteristic data for the Gaia-Wind 11kW turbine

Table 1. Test turbine configuration

| | |
|---|---|
| Turbine make, model, serial number, production year | Gaia-Wind 11-kW, 10711114, 2007 |
| Rotor diameter (m) | 13 |
| Hub height (m) | 18.2 |
| Tower type | Tubular |
| Rated electrical power (kW) | 11 |
| Rated wind speed (m/s) | 9.5 |
| Rotor speed range (rpm) | 56–62 |
| Fixed or variable pitch | Fixed blade, variable tip |
| Number of blades | 2 |
| Blade tip pitch angle (deg) | 90 |
| Blade make, type, serial number | Gaia-Wind T202, glass fiber, centrifugally activated tip brake, 2007/22 |
| Control system (device and software version) | Gaia-Wind IC-1000, Rev.1:P00515\031020 |

### C.2.2. Measurement test data for the Gaia-Wind 11kW turbine

Table 6. Performance at sea-level air density, 1.225 kg/m³

| Measured Power Curve (Database A) | | | | | | | |
|---|---|---|---|---|---|---|---|
| Reference Air Density: 1.225 kg/m³ | | | | | Category A Standard Uncertainty (kW) | Category B Standard Uncertainty (kW) | Combined Standard Uncertainty (kW) |
| Bin (m/s) | Wind Speed (m/s) | Normalized Power Output (kW) | $C_p$ | Number of 1-Minute Data Sets | | | |
| 3 | 3.00 | –0.10 | –0.05 | 7347 | 0.00 | 0.06 | 0.06 |
| 3.5 | 3.49 | –0.11 | –0.03 | 6270 | 0.00 | 0.06 | 0.06 |
| 4 | 3.99 | 0.31 | 0.06 | 5193 | 0.01 | 0.11 | 0.11 |
| 4.5 | 4.49 | 1.15 | 0.16 | 3951 | 0.01 | 0.20 | 0.20 |
| 5 | 4.99 | 2.28 | 0.23 | 3021 | 0.02 | 0.29 | 0.29 |
| 5.5 | 5.49 | 3.67 | 0.27 | 2381 | 0.03 | 0.38 | 0.38 |
| 6 | 5.99 | 5.00 | 0.29 | 2017 | 0.03 | 0.40 | 0.40 |
| 6.5 | 6.49 | 6.27 | 0.28 | 1706 | 0.03 | 0.41 | 0.41 |
| 7 | 7.00 | 7.57 | 0.27 | 1455 | 0.03 | 0.44 | 0.44 |
| 7.5 | 7.49 | 8.70 | 0.25 | 1358 | 0.03 | 0.42 | 0.42 |
| 8 | 7.99 | 9.80 | 0.24 | 1142 | 0.03 | 0.43 | 0.43 |
| 8.5 | 8.49 | 10.77 | 0.22 | 970 | 0.03 | 0.41 | 0.41 |
| 9 | 9.00 | 11.67 | 0.20 | 873 | 0.03 | 0.39 | 0.39 |
| 9.5 | 9.50 | 12.36 | 0.18 | 713 | 0.04 | 0.32 | 0.32 |
| 10 | 10.00 | 13.12 | 0.16 | 604 | 0.04 | 0.37 | 0.37 |
| 10.5 | 10.49 | 13.69 | 0.15 | 520 | 0.03 | 0.30 | 0.30 |
| 11 | 11.00 | 14.15 | 0.13 | 417 | 0.04 | 0.25 | 0.25 |
| 11.5 | 11.49 | 14.59 | 0.12 | 336 | 0.04 | 0.26 | 0.26 |
| 12 | 12.00 | 14.80 | 0.11 | 317 | 0.04 | 0.15 | 0.15 |
| 12.5 | 12.49 | 14.90 | 0.09 | 280 | 0.06 | 0.11 | 0.13 |
| 13 | 13.00 | 15.00 | 0.08 | 225 | 0.05 | 0.11 | 0.12 |
| 13.5 | 13.49 | 14.93 | 0.08 | 187 | 0.06 | 0.10 | 0.12 |
| 14 | 13.99 | 14.80 | 0.07 | 180 | 0.07 | 0.13 | 0.15 |
| 14.5 | 14.48 | 14.60 | 0.06 | 146 | 0.08 | 0.16 | 0.18 |
| 15 | 15.00 | 14.40 | 0.05 | 117 | 0.10 | 0.17 | 0.19 |
| 15.5 | 15.48 | 14.49 | 0.05 | 100 | 0.10 | 0.11 | 0.15 |
| 16 | 16.03 | 14.42 | 0.04 | 87 | 0.09 | 0.10 | 0.14 |
| 16.5 | 16.50 | 14.15 | 0.04 | 70 | 0.13 | 0.24 | 0.27 |
| 17 | 16.99 | 14.24 | 0.04 | 66 | 0.10 | 0.12 | 0.16 |
| 17.5 | 17.50 | 14.13 | 0.03 | 59 | 0.10 | 0.13 | 0.16 |
| 18 | 17.99 | 14.08 | 0.03 | 53 | 0.10 | 0.10 | 0.14 |
| 18.5 | 18.48 | 13.91 | 0.03 | 31 | 0.07 | 0.17 | 0.18 |
| 19 | 18.99 | 14.00 | 0.03 | 25 | 0.08 | 0.12 | 0.14 |
| 19.5 | 19.45 | 14.11 | 0.02 | 13 | 0.11 | 0.14 | 0.18 |
| 20 | 19.92 | 13.74 | 0.02 | 10 | 0.10 | 0.38 | 0.39 |

| Wind speed | m/s | 0.5 | 1 | 1.5 | 2 | 2.5 | 3 | 3.5 | 4 | 4.5 | 5 | 5.5 | 6 | 6.5 | 7 |
|---|---|---|---|---|---|---|---|---|---|---|---|---|---|---|---|
| Rotor speed | rpm | 0.3 | 1.4 | 3.8 | 8.5 | 13.6 | 20.8 | 30.7 | 37.4 | 45.3 | 51.9 | 57.1 | 59.0 | 59.4 | 60.2 |

| Wind speed | m/s | 7.5 | 8 | 8.5 | 9 | 9.5 | 10 | 10.5 | 11 | 11.5 | 12 | 12.5 | 13 | 13.5 | 14 |
|---|---|---|---|---|---|---|---|---|---|---|---|---|---|---|---|
| Rotor speed | rpm | 60.6 | 60.7 | 60.8 | 60.8 | 60.8 | 60.9 | 61.0 | 61.0 | 61.1 | 61.1 | 61.0 | 61.1 | 61.1 | 61.1 |

| Wind speed | m/s | 14.5 | 15 | 15.5 | 16 | 16.5 | 17 | 17.5 | 18 | 18.5 | 19 | 19.5 | 20 | 20.5 | 21 |
|---|---|---|---|---|---|---|---|---|---|---|---|---|---|---|---|
| Rotor speed | rpm | 61.1 | 61.1 | 61.1 | 61.1 | 61.1 | 61.0 | 61.0 | 61.0 | 61.0 | 61.0 | 61.1 | 61.0 | 61.0 | 61.1 |

### C.2.3. Program listing for the generation of the performance and rotor speed-wind speed curves for the WEC system

```
close all
%%Power coefficient-Tip-Speed Ratio characteristics for different pitch
%%angle values
%%Based on the numerical approximation:
%%Cp(lambda,beta)=c1(c2/lambdai-c3*beta-c4)exp(-c5/lambdai)+c6*lambda.
c1=.5176; c2=116; c3=.4; c4=5; c5=21; c6=.0068;
beta=0:5:20;
lambda=0:.05:18;
lambdaiinv1=(lambda+.08*beta(1)).^-1-.035/(beta(1)^2+1);
lambdaiinv2=(lambda+.08*beta(2)).^-1-.035/(beta(2)^2+1);
lambdaiinv3=(lambda+.08*beta(3)).^-1-.035/(beta(3)^2+1);
lambdaiinv4=(lambda+.08*beta(4)).^-1-.035/(beta(4)^2+1);
lambdaiinv5=(lambda+.08*beta(5)).^-1-.035/(beta(5)^2+1);

Cp1=c1*(c2.*lambdaiinv1-c3*beta(1)-c4).*exp(-c5.*lambdaiinv1)+c6.*lambda;
Cp2=c1*(c2.*lambdaiinv2-c3*beta(2)-c4).*exp(-c5.*lambdaiinv2)+c6.*lambda;
Cp3=c1*(c2.*lambdaiinv3-c3*beta(3)-c4).*exp(-c5.*lambdaiinv3)+c6.*lambda;
Cp4=c1*(c2.*lambdaiinv4-c3*beta(4)-c4).*exp(-c5.*lambdaiinv4)+c6.*lambda;
Cp5=c1*(c2.*lambdaiinv5-c3*beta(5)-c4).*exp(-c5.*lambdaiinv5)+c6.*lambda;
plot(lambda,Cp1,lambda,Cp2,lambda,Cp3,lambda,Cp4,lambda,Cp5);
axis([0 18 0 .5]);
grid
text(10.3,.4,'\beta=0^o')
text(14.5,.2,'\beta=5^o')
text(10.2,.2,'\beta=10^o')
text(8.1,.15,'\beta=15^o')
text(6.5,.1,'\beta=20^o')
title('C_p vs \lambda for various values of \beta','FontSize',12);
xlabel('Tip-speed ratio (\lambda)','FontSize',12);
ylabel('C_p(\lambda,\beta)','FontSize',12);
clear all

clc
% Performance curve and rotor speed-wind speed for the Gaia-Wind 11kW turbine
Vw=3:.5:20;
C_p1=[-.05 -.03 .06 .16 .23 .27 .29];
C_p2=[.28 .27 .25 .24 .22 .20 .18];
C_p3=[.16 .15 .13 .12 .11 .09 .08];
C_p4=[.08 .07 .06 .05 .05 .04 .04];
C_p5=[.04 .03 .03 .03 .03 .02 .02];
C_p=[C_p1 C_p2 C_p3 C_p4 C_p5];
 p1=[-.1 -.11 .31 1.15 2.28 3.67 5];
p2=[6.27 7.57 8.70 9.80 10.77 11.67 12.36];
p3=[13.12 13.69 14.15 14.59 14.80 14.90 15.00];
```

```
p4=[14.93 14.80 14.60 14.40 14.49 14.42 14.15];
p5=[14.24 14.13 14.08 13.91 14.00 14.11 13.74];
P=[p1 p2 p3 p4 p5];
 wsp1=[20.8 30.7 37.4 45.3 51.9 57.1 59.0];
wsp2=[59.4 60.2 60.6 60.7 60.8 60.8 60.8];
wsp3=[60.9 61.0 61.0 61.1 61.1 61.0 61.1];
wsp4=[61.1 61.1 61.1 61.1 61.1 61.1 61.1];
wsp5=[61.0 61.0 61.0 61.0 61.0 61.1 61.0];
wsp=[wsp1 wsp2 wsp3 wsp4 wsp5];
 figure(3);
subplot(2,1,1);
title('Performance and power curves for the Gaia-Wind 11kW Wind Turbine');
xlabel('Wind speed (m/s)');
[haxes, hl1, hl2]=plotyy(Vw,C_p,Vw,P,'plot');
axes(haxes(1)); axis([0 20 0 .3]); ylabel('C_p');
axes(haxes(2)); axis([0 20 0 16]); ylabel('Normalized power (kW)');
grid;
subplot(2,1,2);
title('Rotor speed vs. wind speed curve for the Gaia-Wind 11kW Wind Turbine');
xlabel('Wind speed (m/s)');
plot(Vw,wsp); grid; xlabel('Wind speed (m/s)'); ylabel('Turbine rotor speed (rpm)');
```

### C.2.4. WEC system data initialization and aerodynamic subsystem implementation in Simulink

```
%Data initialized in the aerodynamic subsystem Simulink block
Vw=3:.5:20;
C_p1=[-.05 -.03 .06 .16 .23 .27 .29];
C_p2=[.28 .27 .25 .24 .22 .20 .18];
C_p3=[.16 .15 .13 .12 .11 .09 .08];
C_p4=[.08 .07 .06 .05 .05 .04 .04];
C_p5=[.04 .03 .03 .03 .03 .02 .02];
C_p=[C_p1 C_p2 C_p3 C_p4 C_p5];
 OmegaT1=[20.8 30.7 37.4 45.3 51.9 57.1 59];
OmegaT2=[59.4 60.2 60.6 60.7 60.8 60.8 60.8 ];
OmegaT3=[60.9 61.0 61.0 61.1 61.1 61.0 61.1];
OmegaT4=[61.1 61.1 61.1 61.1 61.1 61.1 61.1];
OmegaT5=[61.0 61.0 61.0 61.0 61.0 61.1 61.0];
OmegaT=[OmegaT1 OmegaT2 OmegaT3 OmegaT4 OmegaT5];
```

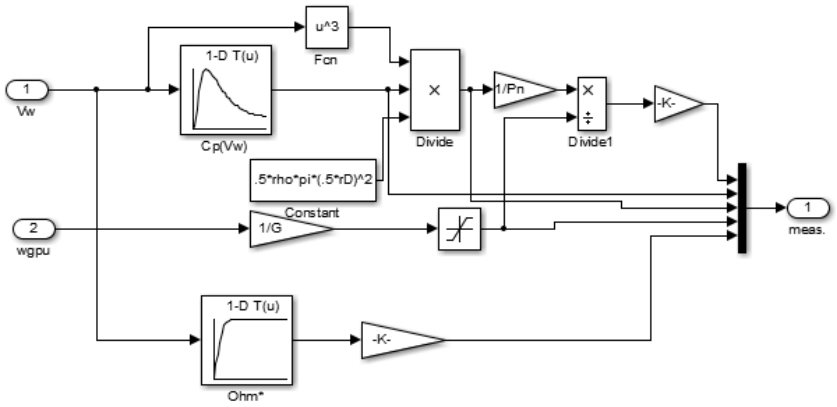

## APPENDIX D: SOFTWARE PROGRAMS FOR CHAPTER 5

### D. LCL filter design dynamic simulation program

#### D.1. Program listing for generating the plot of the current ripple attenuation factor

```
clear all
close all
clc
r=0.2:.1:2.2;
L=2.11e-3;
Cb=298.4e-6;
w=2*pi*20e3;
x=.03;
a=L*Cb*w^2;
rr=1./abs((1+r.*(1-L*Cb*w^2*x)));
rr1=1./abs(1-r.*a*x);
figure(1)
plot(r,rr1,'r*')
axis([0.1 2.2 0 .05]);
xlabel('Ratio of Grid Inductor to Inverter Inductor (r)')
ylabel('Ripple attenuation factor (|Ig/Ii|)')
title('Current Harmonic Attenuation (as a function of Grid to Inverter Inductor ratio)')
```

#### D.2. Program listing for the LCL filter dynamic response analyis

```
%clear all
close all
clc
% Filter parameters
L=2.11e-3;
Lg=0.95e-3;
C=8.95e-6;
Rd=2.85;
ri=.25;
rg=.25;
R=ri+rg;
%Transfer functions
Gpi2=tf([5.1  833.33],[1  0]);        % PI regulator (compensated for discretization and computational delay)
Gd=tf(1,[3e-4 1]);            % Control loop delay transfer function
Gf=tf(1,[3.06e-3 .1]);         % L-filter transfer function
a=L*Lg*C;
b=Rd*C*(L+Lg)+C*(L*rg+Lg*ri);
c=L+Lg+Rd*C*R+C*ri*rg;
d=R;
n3=[Lg*C C*(Rd+rg) 1];
d3=[a b c d];
sysdd=tf(n3,d3);
% Different values of damping resistor
Ts=5000^-1;
r=0:.5:3;
na=[Lg*C r(1)*C 1];
da=[L*Lg*C r(1)*C*(L+Lg) L+Lg 0];
sysa=tf(na,da);
```

```
Gao=Gpi2*Gd*sysa;
Gac=feedback(Gao,1);
Gacs=c2d(Gac, Ts);
nb=[Lg*C r(2)*C 1];
db=[L*Lg*C r(2)*C*(L+Lg) L+Lg 0];
sysb=tf(nb,db);
Gbo=Gpi2*Gd*sysb;
Gbc=feedback(Gbo,1);
Gbcs=c2d(Gbc, Ts);
nc=[Lg*C r(3)*C 1];
dc=[L*Lg*C r(3)*C*(L+Lg) L+Lg 0];
sysc=tf(nc,dc);
Gco=Gpi2*Gd*sysc;
Gcc=feedback(Gco,1);
Gccs=c2d(Gcc, Ts);
nd=[Lg*C r(4)*C 1];
dd=[L*Lg*C r(4)*C*(L+Lg) L+Lg 0];
sysd=tf(nd,dd);
Gdo=Gpi2*Gd*sysd;
Gdc=feedback(Gdo,1);
Gdcs=c2d(Gdc, Ts);
ne=[Lg*C r(5)*C 1];
de=[L*Lg*C r(5)*C*(L+Lg) L+Lg 0];
syse=tf(ne,de);
Geo=Gpi2*Gd*syse;
Gec=feedback(Geo,1);
Gecs=c2d(Gec, Ts);
nf=[Lg*C r(6)*C 1];
df=[L*Lg*C r(6)*C*(L+Lg) L+Lg 0];
sysf=tf(nf,df);
Gfo=Gpi2*Gd*sysf;
Gfc=feedback(Gfo,1);
Gfcs=c2d(Gfc, Ts);
ng=[Lg*C r(7)*C 1];
dg=[L*Lg*C r(7)*C*(L+Lg) L+Lg 0];
sysg=tf(ng,dg);
Ggo=Gpi2*Gd*sysg;
Ggc=feedback(Ggo,1);
Ggcs=c2d(Ggc, Ts);
%-----------------------------------------------
Gs1=Gpi2*Gd*Gf;
Gs1c=feedback(Gs1,1);
Gss=c2d(Gs1c,5000^-1);
sysL=tf(1,[L+Lg R]);
Gdao=Gpi2*Gd*sysd;  % open-loop damped system
Gdac=feedback(Gdao,1);      % closed-loop damped system
%-------------------------------------------------
%% Plots
figure(1)
bode(Gao,'b',Gdo,'r',Ggo,'m');
title('LCL filter magnitude and phase response for various damping resistor values');
legend('Rd=0 Ohm','Rd=1.5 Ohm','Rd=3.0 Ohm');
grid
figure(2');
bode(sysdd,sysL);
title('Open-loop magnitude and phase response comparison of L and LCL filters');
```

```
legend('LCL filter','L filter');
grid
figure(3);
bode(Gs1c,Gdac);
title('Closed-loop response of L and LCL filters');
legend('L filter','LCL filter');
grid
figure(4);
step(Gss,Gdac);    % comparison of L and LCL filter responses
title('Closed-loop step response comparison of L and LCL filters');
legend('L filter','LCL filter');
grid
figure(5);
pzmap(Gacs,'r',Gbcs,'y',Gccs,'g',Gdcs,'m',Gecs,'c',Gfcs,'b',Ggcs,'k');
title('LCL filter poles and zeros for various damping resistor values');
legend('Rd=0    Ohm','Rd=0.5    Ohm','Rd=1.0    Ohm','Rd=1.5    Ohm','Rd=2.0    Ohm','Rd=2.5
Ohm','Rd=3.0 Ohm');
grid
```

# APPENDIX E: SOFTWARE PROGRAMS FOR CHAPTER 6

## E.1. Program listing for the PLL circuit-dynamic response analysis

```
close all; clc;
z=2^-.5;
wn=100*pi*2;
n1=[2*z*wn wn^2];
n2=[1 0 0];
d=[1 2*z*wn wn^2];
Gco=tf(n1,[1 0 0]);
Gcc=tf(n1,d);
Gec=tf(n2,d);
Ts=5000^-1;
Gccs=c2d(Gcc,Ts);
figure(1); bode(Gco); grid;
title('PLL \theta_o(s)/\theta_i(s) open-loop magnitude and phase response')
figure(2); bode(Gcc); grid;
title('PLL \theta_o(s)/\theta_i(s) closed-loop magnitude and phase response')
figure(3); bode(Gec); grid;
title('PLL \delta_{PLL}(s)/\theta_i(s) closed-loop magnitude and phase response')
figure(4); step(Gcc, Gec, 'r--'); grid;
title('PLL \theta_o(s)/\theta_i(s) and \delta_{PLL}(s)/\theta_i(s) step response (degrees)')
legend('\theta_o(t)','\delta_{PLL}(t)')
xlabel('Time (seconds)')
ylabel('Amplitude (degrees)')
figure(5)
pzmap(Gccs,'r')
grid
title('PLL \theta_o(s)/\theta_i(s) closed-loop pole-zero location')
t=PLL.time;
e=PLL.signals(1,2).values;
wt1=PLL.signals(1,4).values(:,1);
wt2=PLL.signals(1,4).values(:,2);
f1=PLL.signals(1,3).values(:,1);
f2=PLL.signals(1,3).values(:,2);
figure(6)
subplot(2,1,2)
plot(t,f1,'r',t,f2,'b--')
legend('Input signal frequency (f_i)','Output signal frequency (f^*)')
title('PLL Frequency response for an undisturbed input signal')
xlabel('Time (sec)')
ylabel('Frequency (Hz)')
grid
axis([0 .5 45 55])
 subplot(2,1,1)
plot(t,wt1,'r',t,wt2,'b--')
grid
title('PLL Phase angle response for an undisturbed input signal')
legend('Input signal phase (\theta_i)','Output signal phase (\theta_o)')
xlabel('Time (sec)')
ylabel('\theta (degrees)')
axis([0 .5 0 8]);
 figure(7)
plot(t,e)
title('Phase error for an undisturbed input signal (degrees)')
```

```
xlabel('Time (sec)')
ylabel('Phase error (degrees)')
grid
axis([0 .5 -.1 .1])
```

## E.2. Program listing for the grid-mode current controller design analysis

```
close all
clc
 Gpc=tf(5e5,[1 1e3 5e5]);
Gf=tf(1, [3.06e-3 .1]);
Gfc=feedback(Gf,1);
 figure(1);
rlocus(Gf);
title('Root locus of the current control plant'); grid;
 figure(2);
step(Gfc);
title('Closed-loop step response of the unregulated current control plant'); grid;
 figure(3);
bode(Gpc);
title('Current control system closed-loop magnitude and phase response');
grid
 figure(4);
step(Gpc);
title('Current control system closed-loop step response');
grid
axis([0 .05 0 1.2])
```

## E.3. Program listing for the grid-mode DC-link voltage regulator design analysis

```
 close all
clc
Gvol=tf(10e5,[1 500 0 0])
Gl=tf([1 23.1],[1 433.15]);
Gvol1=Gvol*Gl;
Gvol2=22.13*Gvol1;
Gvcl=feedback(Gvol2,1);
figure(1)
bode(Gvol)
title('Voltage-loop magnitude and phase response with integral compensator ')
grid
figure(2)
bode(Gvol1,'--',Gvol2,'r')
title('Compensated voltage-loop magnitude and phase response')
legend('Gvol(s) before gain adjustment','Gvol(s) after gain adjustment')
grid
figure(3)
bode(Gvcl)
title('DC-link voltage closed-loop magnitude and phase response')
grid
figure(4)
step(Gvcl)
title('DC-link voltage closed-loop step response')
grid
```

# APPENDIX F: SOFTWARE PROGRAMS FOR CHAPTER 7

## F.1. Program listing for the autonomous-mode inner-loop current controller analysis

```
close all; clc;
 Li=2.11e-3;
Lg=.95e-3;
Cf=8.95e-6;
Rd=2.85;
Zl=10.667;
Lt=3.06e-3;
R=.1;
 Gp=tf(1,[Lt R]);
Gpu=feedback(Gp,1);
Gpc=tf(1e3,[1 1e3]);
 figure(1); subplot(2,1,2); step(Gpu,'b--',Gpc,'r');
title('Inner-loop current control response'); grid;
legend('Uncompensated','Compensated');
xlabel('time (sec)'); ylabel('Amplitude'); axis([0 .04 0 1.2]);
 subplot(2,1,1); bode(Gpu,'b--',Gpc,'r');
title('Inner-current closed-loop magnitude and phase response'); grid;
legend('Uncompensated','Compensated');
```

## F.2. Program listing for the autonomous-mode PI-based voltage regulator analysis

```
close all; clc;
Gpvc=tf(10.67, [9.55e-5 11.67]);
Gvclu=tf(10670, [9.55e-5 1.095 11670]);
Gvclc=tf(5335, [9.55e-5 1 5335]);
 figure(1); step(Gpvc,Gvclu,'r--'); grid;
title('Step response of the unregulated outer voltage loop',...
    'FontWeight','bold', 'FontSize',10);
legend('Plant model alone','Plant model with inner loop');
xlabel('Time','FontAngle','italic', 'FontSize',10);
ylabel('V_{i} (p.u)','FontAngle','italic', 'FontSize',10);
 figure (2); step(Gvclu, Gvclc, 'r--'); grid;
title('Step response comparison of the unregulated and regulated outer voltage loop',...
    'FontWeight','bold', 'FontSize',10);
legend('Unregulated voltage loop','Regulated voltage loop');
xlabel('\itTime', 'FontSize',10);
ylabel('V_{i} (p.u)','FontAngle','italic', 'FontSize',10);
```

## F.3. Program listing for the autonomous-mode PR-based voltage regulator analysis

```
close all; clc;
Kp=[0 .1 .5 1 5];
Ki=[1 5:5:20];
wc=[1 5:5:20];
wo=314.16^2;
% Ideal PR regulator
h=tf([Kp(4) 1 Kp(4)*wo],[1 0 wo]);
 % Varying equivalent bandwidth (wc)
n1=[Kp(4) 2*wc(1)*(Kp(4)+Ki(1)) wo*Kp(4)];
d1=[1 2*wc(1) wo];
h1=tf(n1,d1);
 n2=[Kp(4) 2*wc(2)*(Kp(4)+Ki(1)) wo*Kp(4)];
```

```
d2=[1 2*wc(2) wo];
h2=tf(n2,d2);
 n3=[Kp(4) 2*wc(3)*(Kp(4)+Ki(1)) wo*Kp(4)];
d3=[1 2*wc(3) wo];
h3=tf(n3,d3);
 n4=[Kp(4) 2*wc(4)*(Kp(4)+Ki(1)) wo*Kp(4)];
d4=[1 2*wc(4) wo];
h4=tf(n4,d4);
 % Varying proportional gain
n5=[Kp(2) 2*wc(1)*(Kp(2)+Ki(1)) wo*Kp(2)];
d5=[1 2*wc(1) wo];
h5=tf(n5,d5);
 n6=[Kp(3) 2*wc(1)*(Kp(3)+Ki(1)) wo*Kp(3)];
d6=[1 2*wc(1) wo];
h6=tf(n6,d6);
 n7=[Kp(4) 2*wc(1)*(Kp(4)+Ki(1)) wo*Kp(4)];
d7=[1 2*wc(1) wo];
h7=tf(n7,d7);
 n8=[Kp(5) 2*wc(1)*(Kp(5)+Ki(1)) wo*Kp(5)];
d8=[1 2*wc(1) wo];
h8=tf(n8,d8);
 % Varying resonant gain
n9=[Kp(4) 2*wc(1)*(Kp(4)+Ki(2)) wo*Kp(4)];
d9=[1 2*wc(1) wo];
h9=tf(n9,d9);
 n10=[Kp(4) 2*wc(1)*(Kp(4)+Ki(3)) wo*Kp(4)];
d10=[1 2*wc(1) wo];
h10=tf(n10,d10);
 n11=[Kp(4) 2*wc(1)*(Kp(4)+Ki(4)) wo*Kp(4)];
d11=[1 2*wc(1) wo];
h11=tf(n11,d11);
 n12=[Kp(4) 2*wc(1)*(Kp(4)+Ki(5)) wo*Kp(4)];
d12=[1 2*wc(1) wo];
h12=tf(n12,d12);
 n13=[Kp(4) 2*12*(Kp(4)+Ki(3)) wo*Kp(4)];
d13=[1 2*12 wo];
h13=tf(n13,d13);
 figure(1)
 subplot(2,1,1)
bode(h,'c',h5,'b',h6,'r--',h7,'m-.',h8,'y:')
title('Non-ideal PR regulator magnitude and phase response for various \itK_{p} values',...
    'FontWeight','bold','FontSize',10);
legend('\itIdeal PR','\itK_{p}=0.1','\itK_{p}=0.5','\itK_{p}=1','\itK_{p}=5')
grid
text(105,-70,'(a)','FontSize',10)
text(110,300,'\itK_{I}=1','FontSize',8);
text(110,260,'\it\omega_{c}=1 rad/sec','FontSize',8);
 subplot(2,1,2)
bode(h9,'b',h10,'r--',h11,'m-.',h12,'y:')
title('Non-ideal PR regulator magnitude and phase response for various \itK_{I} values',...
    'FontWeight','bold','FontSize',10);
legend('\itK_{I}=5','\itK_{I}=10','\itK_{I}=15','\itK_{I}=20')
grid
text(12,-70,'(b)','FontSize',10)
text(12,295,'\itK_{p}=1','FontSize',8);
text(12,240,'\it\omega_{c}=1 rad/sec','FontSize',8);
```

```
figure(2)
 subplot(2,1,1)
bode(h1,'b',h2,'r--',h3,'m-.',h4,'y:')
title('Non-ideal PR regulator magnitude and phase response for various \it\omega_{c} values',...
   'FontWeight','bold','FontSize',10);
legend('\it\omega_{c}=5 rad/sec','\it\omega_{c}=10 rad/sec','\it\omega_{c}=15 rad/sec',...
   '\it\omega_{c}=20 rad/sec')
grid
text(105,50,'\itK_{p}=1','FontSize',8);
text(135,50,'\itK_{I}=1','FontSize',8);
text(105,-16,'(a)','FontSize',10)
 subplot(2,1,2)
bode(h,'b',h13,'r--')
grid
title('Magnitude and phase response of the designed Non-ideal PR regulator',...
   'FontWeight','bold','FontSize',10);
legend('\itIdeal PR regulator','\itNon-ideal PR regulator');
text(12,-70,'(b)','FontSize',10)
text(12,290,'\itK_{p}=1','FontSize',8);
text(12,230,'\itK_{I}=20','FontSize',8);
text(12,170,'\it\omega_{c}=15 rad/sec','FontSize',8);
```